Wrocław University
of Science and Technology

Department of the Experimental Physics
Faculty of Fundamental Problems of Technology

PHD THESIS

GaAs-based quantum dots grown by MBE on metamorphic buffers as a platform for single-photon emitters in the telecommunication spectral range

Paweł Wyborski

Supervisor: prof. dr hab. inż. Grzegorz Sęk,
Supporting supervisor: dr hab. inż. Paweł Podemski, prof. PWr

Advisor from the partnering university: prof. Sven Höfling,
(University of Würzburg)

A thesis submitted for the degree of Doctor of Philosophy at Wroclaw University of Science and Technology

Keywords: semiconductor quantum dots, InAs/GaAs, metamorphic buffer layer, telecommunication spectral range, single-photon sources

Wrocław, 2023

"InterDok – Programy Interdyscyplinarnych Studiów Doktoranckich na Politechnice Wrocławskiej" Grant No. POWR.03.02.00-00-I003/16

The doctoral thesis co-financed by the European Union under the European Social Fund

ABSTRACT

Semiconductor quantum dots (QDs) can serve as efficient, near-perfect sources of single photons, as has been repeatedly demonstrated experimentally. Modern epitaxial growth technologies allow controlling the morphological and optical properties of the dots, including tuning of the emission wavelength. In order to achieve emitters in the telecommunications range, i.e., in the spectral region of the minimal transmission losses in fiber-optic networks, it is necessary to select semiconductor materials appropriately. One of the most technologically mature is the InAs/GaAs system. However, due to the significant difference in crystal lattice constants, quantum dots in this material system emit typically around 1 μm or below. Shifting the optical transitions to the telecommunication range requires special technological approaches aiming at band structure and strain engineering. One of the options is the use of an additional metamorphic buffer layer preceding the quantum dot layer, which reduces the strain and hence shifts the emission to infrared. This work aims at characterizing InAs QDs grown by molecular beam epitaxy (MBE) on a metamorphic InGaAs buffer, for its different composition gradients, to connect the dots' structural, electronic and optical properties. In particular, the work focused on obtaining single-photon emission from such quantum dots, including especially the range of the third telecommunication window as the most application-demanded, while at the same time the most difficult to obtain within the GaAs-based technology.

In the thesis, there was demonstrated that by modifying the metamorphic buffer layer composition it is possible to control the QD emission wavelength over a wide spectral range, reaching also the 1.55 μm window, and beyond. The results of spectroscopic measurements confronted with electronic structure calculations utilizing the collected morphological parameters of such dots allowed identifying the main factors responsible for shifting the optical transitions. In addition, a non-zero value of the degree of linear polarization of the emission was obtained, resulting from the mixing of valence states due to anisotropy of the carrier confinement potential in the plane of the dot and enhanced by the low strain and shallow confinement conditions. The temperature dependence of photoluminescence indicated fingerprints of carrier redistribution between QDs and allowed identifying the escape of carriers into the buffer layer as the main thermal loss mechanism and quenching of emission intensity. Observation of the increase in photoluminescence intensity in the range of low temperatures for single quantum dots confirmed the presence of shallow carrier trapping states in their surroundings. Measurements of photoluminescence in a function of excitation power density and polarization initially identified the fundamental charge (excitonic) complexes confined in single QDs, origin of which was confirmed in the second order correlation function via cross-correlating events of emission from different complexes. Results on the exciton and biexciton lifetimes derived from time-resolved measurements suggested the intermediate confinement regime in such dots, which was also supported in calculation of the excitonic states. Whereas low exciton fine structure splitting indicated slight anisotropy of the confinement potential in the plane perpendicular to the growth direction.

Photon autocorrelation measurements proved of unequivocally single-photon character of emission, including both the second and third telecom windows, thus demonstrating that this type of quantum dots grown by the MBE can compete with other single-photon emitters in this spectral range. The lineshape of the measured second-order autocorrelation functions in the pulsed regime confirmed the occurrence of trapping and carrier release processes from charge states in the vicinity of the dots, in agreement with the results of previous experiments, which also indicates the direction for further optimization of these nanostructures.

STRESZCZENIE

Jak wielokrotnie dowiedziono eksperymentalnie, półprzewodnikowe kropki kwantowe mogą służyć jako wydajne, niemal idealne źródła pojedynczych fotonów. Ponadto współczesna technologia wzrostu metodami epitaksjalnymi pozwala na kontrolę właściwości morfologicznych i optycznych, umożliwiając, między innymi, sterowanie długością fali emitowanego promieniowania. W celu uzyskania emiterów w zakresie telekomunikacyjnym, czyli w obszarze widmowym przypadającym na minima strat przy transmisji w sieciach światłowodowych, konieczny jest odpowiedni dobór materiałów półprzewodnikowych. Jednym z najbardziej dopracowanych technologicznie jest układ InAs/GaAs, jednakże ze względu na znaczną różnicę w stałych sieci krystalicznej, kropki kwantowe w tym układzie materiałowym emitują zwykle poniżej 1 μm. Przesunięcie emisji do zakresu telekomunikacyjnego wymaga dodatkowych zabiegów technologicznych oraz związanej z tym inżynierii struktury pasmowej i naprężeń. Jednym z podejść jest zastosowanie dodatkowej metamorficznej warstwy buforowej pozwalającej na zredukowanie odkształceń w warstwie kropek kwantowych, co skutkuje przesunięciem emisji w kierunku podczerwieni. Celem niniejszej pracy było scharakteryzowanie właściwości optycznych oraz powiązanie ich z własnościami strukturalnymi dla kropek kwantowych z materiału InAs na podłożu z GaAs, otrzymywanych metodą epitaksji z wiązek molekularnych (MBE) i wytwarzanych na metamorficznej warstwie buforowej z InGaAs o różnym gradiencie składu. W szczególności prace koncentrowały się na określeniu warunków przesunięcia emisji do zakresu trzeciego okna telekomunikacyjnego oraz na uzyskaniu emisji pojedynczych fotonów z takich kropek kwantowych.

W rozprawie wykazano doświadczalnie możliwość sterowania długością fali emisji w szerokim zakresie widmowym poprzez modyfikacje metamorficznej warstwy buforowej, osiągając emisję również w zakresie okna 1.55 μm. Wyniki pomiarów spektroskopowych skonfrontowane z obliczeniami struktury energetycznej wykorzystującymi zgromadzone parametry morfologiczne dla takich kropek, pozwoliły na wskazanie głównych czynników odpowiadających za zmianę energii przejść optycznych. W szczególności, uzyskano niezerową wartość stopnia polaryzacji liniowej emisji, wynikającą z mieszania stanów walencyjnych wskutek występowania anizotropii potencjału wiążącego nośniki w płaszczyźnie kropki, dodatkowo wzmocnioną przez zredukowane odkształcenia oraz spłycony potencjał wiążący. Zależność fotoluminescencji od temperatury wskazała na możliwość występowania redystrybucji nośników pomiędzy kropkami kwantowymi oraz pozwoliła określić ucieczkę nośników do warstwy buforowej jako główny mechanizm strat termicznych i spadku intensywności fotoluminescencji. Obserwacja wzrostu intensywności emisji w zakresie niskich temperatur dla pojedynczych kropek kwantowych powiązana została z obecnością płytkich stanów pułapkowych w strukturze. Pomiary w funkcji gęstości mocy pobudzania i polaryzacji pozwoliły zidentyfikować podstawowe kompleksy ładunkowe (ekscytonowe), a ich pochodzenie zostało potwierdzone poprzez wyznaczenie funkcji korelacji drugiego rzędu aktów emisji z różnych kompleksów (korelacji wzajemnej różnych linii emisyjnych). Wyniki charakteryzacji czasów życia ekscytonu i biekscytonu oraz obliczeń struktury energetycznej wskazały na występowanie tzw. pośredniego ograniczenia przestrzennego ekscytonów w badanych kropkach. Zaś niewielkie wartości energii rozszczepienia struktury subtelnej ekscytonu potwierdziły występowanie nieznacznej anizotropii potencjału wiążącego w płaszczyźnie prostopadłej do kierunku wzrostu.

Pomiary autokorelacji emisji fotonów potwierdziły jednoznacznie jej jednofotonowy charakter. W szczególności, uzyskano emisję pojedynczych fotonów o dużej czystości w zakresie zarówno drugiego jak i trzeciego okna telekomunikacyjnego, dowodząc tym samym, że ten rodzaj kropek kwantowych wytwarzanych metodą MBE może konkurować z innymi emiterami jednofotonowymi w tym zakresie spektralnym. Rezultaty pomiaru funkcji autokorelacji drugiego rzędu w reżimie impulsowym potwierdziły występowanie procesów wychwytu i uwalniania nośników przez pułapki z otoczenia kropek, w zgodzie z

wynikami wcześniejszych eksperymentów, co też wskazuje na kierunek dalszej optymalizacji tych nanostruktur.

ACKNOWLEDGMENTS

At the very beginning, my biggest thanks go to my supervisors, Professors Grzegorz Sęk and Paweł Podemski, for their enormous help at each stage of this research, preparation of publications, and for performing all other university duties. I would like to thank them for the time and the trust they have given to me. I am extremely grateful for their insight, comments, and all the suggested revisions when preparing my dissertation. The knowledge I have gained, the uncountable amount of guidance that still helps me develop, and the support I have received all allowed me to keep moving forward in life and work, inspired by their example. Thanks to them I have reached the place where I am now.

Realization of this work would not have been possible without the great support from Prof. Sven Höfling leading the Technische Physik (TEP) department at University of Würzburg where the samples I have studied were fabricated, as well as the always friendly assistance of many experienced researchers from TEP during my internships there: Piotr Wroński, Fauzie Jabeen, Johannes Michl, Tobias Huber-Loyola, Magdalena Dusanowska and Łukasz Dusanowski.

Great thanks also go to Michał Gawełczyk for sharing the results of his calculations and for all the fruitful discussions which helped me interpret the experimental data. In addition, I would like to express my admiration to his physics knowledge interacting with which was an amazing experience, inspiring for further developments. In addition, many thanks for all the criticism and constructive feedback on the dissertation draft.

I would also like to express my gratitude to the colleagues from the Laboratory of Optical Spectroscopy of Nanostructures at Wroclaw University of Science and Technology. The innumerable conversations on both scientific and life topics, the shared lunches, and the atmosphere of working together enabled the working hours to always pass in an excellent atmosphere. In particular, I would like to thank Anna Musiał, Marcin Syperek and Wojciech Rudno-Rudziński who let me use their measurement setups and shared their experience on spectroscopic measurements. In addition, I would like to express my sincere thanks to Paweł Holewa for crossing the PhD studies time together, sharing responsibilities and overcoming numerous challenges, and having countless discussions on various scientific and non-scientific topics.

I would also like to thank Prof. Krzysztof Ryczko for contacting me with my supervisor Prof. Grzegorz Sęk already in the first year of my studies. Without this, nothing would have started. In addition, I would also like to thank Aleksander Maryński, Anna Musiał, and Paweł Podemski for their time, help in understanding and learning the basics of spectroscopy when I was making my first steps.

Finally, I would like to express my deep gratitude to my family for their patience, understanding and support, giving me a chance to realize my dreams.

CONTENTS

INTRODUCTION

Recent progress in the development of epitaxial technologies allowed for the practical implementation of epitaxially-grown self-assembled quantum dots (QDs)[1], characterized by excellent structural quality, as structures emitting radiation arising from the recombination of both types of carriers: the electron and the hole trapped within a QD [1]. The interacting carriers form a correlated pair of the electron and the hole from now on called an exciton. Due to the full quantization of the QD energy structure, exciton recombination leads to the emission of radiation with precisely defined energy. A fully discrete energy structure provides a two-level exciton system for which the single-photon emission has been demonstrated, i.e., emission statistics showing at most the emission of a single photon at a time [2]. These properties led to using QDs as radiation sources in secure quantum communication as an element of quantum cryptography realization [2]. Furthermore, thanks to confining carriers with charge and spin degrees of freedom, QDs allow for the manipulation of spin and charge states using optical excitation and external electric or magnetic fields, finding applications in quantum information processing [3], including QD spin-qubit implementations [3]. In addition, thanks to their optical properties, QD structures are also used as emitters in many kinds of photonics structures, e.g., as active areas of laser diodes, broadband radiation sources, optical amplifiers, or detectors [4].

An important QD feature is the possibility of selecting the material from which the structures are made and controlling their size and shape [5]. This results in the ability to tune the QD parameters, including the emission wavelength, where matching the second (~1300 nm) and third (~1550 nm) telecommunications windows is the most demanded. It provides the highest optical transmission of silica fibers allowing for the implementation of long-haul ultra-secure quantum telecommunication. These two spectral windows can be covered by InAs QDs based on InP or GaAs substrates [6].

The growth on the InP substrate naturally leads to QDs emitting in the telecommunication spectral range [1]. Moreover, the possibility of using such QDs as single-photon sources has already been demonstrated [6]. The more mature and developed technology of GaAs-based QD growth provides dots with unprecedented optical and structural quality, also in the context of applications in quantum technologies. However, their emission wavelength has a natural upper bound of 1200 nm. Therefore, strain-engineering approaches have been pursued to shift GaAs-based QDs emission to the telecommunication range [7]. In addition, single-photon emission in the second and third telecommunication windows has also been shown in recent years [5].

This work concerns systematic characterization of optical properties of a new type of QDs, grown by molecular beam epitaxy (MBE). The QDs were formed from InAs on GaAs substrate, however preceded by a InGaAs metamorphic buffer layer (MBL) allowing for strain engineering. The main goal was to demonstrate the tuning of the QD emission into the spectral range of telecommunication windows and to analyze the impact of the MBL on dot parameters and electronic and optical properties of such nanostructures. The study also examines the single dot properties, including exciton complexes and single-photon emission statistics focusing especially in the telecommunication spectral range.

In that respect, the following research goals have been defined in this doctoral thesis:

- Demonstration of the spectral control of the emission from GaAs-based InAs QDs up to the telecom range, including the third window at 1.55 um.

[1] List of all abbreviations is attached at the end of the thesis.

- Determination of the main factors affecting the energies of optical transitions in structures employing MBL via comparison of the obtained results of optical and structural characterization with the results of theoretical modeling.
- Analysis of the fundamental optical properties of the QD ensemble, including the energy band structure details, the polarization of emission, thermally-activated carrier loss mechanisms, and carrier dynamics.
- Observation and characterization of single QD emission in the telecommunication range and the analysis of the main factors responsible for the single dot properties: optical/structural quality of the dots and impact of non-radiative processes; the influence of the QD charge environment and changes in the excitation scheme on the spectral linewidth; the effect of exciton-phonon coupling driven by the temperature.
- Identification of the fundamental charge complexes (excitonic complexes) confined in the studied dots and contributing to the single-dot emission spectra, determination of their binding energies as well as the exciton fine structure splitting and the degree of linear polarization of emission.
- Characterization of emission dynamics for QD ensembles as well as individual exciton complexes, including analysis of the quantum confinement regime.
- Experimental proof of single-photon emission from the studied dots, especially in the second and the third telecommunication windows, through measurements of photon emission statistics from individual exciton complexes.

AUTHOR CONTRIBUTION

The investigated structures were fabricated by **Piotr Wroński** at the Applied Physics Department (Technische Physik), University of Würzburg, led by **Prof. Sven Höfling**, who is also the advisor of this thesis from the side of the University of Würzburg.

All spectroscopic measurements were carried out by the author of the thesis in the Laboratory for Optical Spectroscopy of Nanostructures (LOSN) at the Department of Experimental Physics, Faculty of Fundamental Problems of Technology, Wrocław University of Science and Technology under the supervision of **Prof. Grzegorz Sęk** and **Dr. Paweł Podemski**.

Atomic force microscopy (AFM) and scanning electron microscopy (SEM) measurements for reference dots were mostly performed and provided by **Piotr Wroński**, where the author had the opportunity to assist in a significant part of measurements during his three one-month research stays at the University of Würzburg. Part of the AFM measurements was performed by the author.

For the buried QD parameters, characterization using scanning transmission electron microscopy (STEM) was carried out in two independent laboratories: by **Dr. Mirosława Pawlyta** at the Materials Testing Laboratory at the Faculty of Mechanical Engineering of Silesian University of Technology in Gliwice and by **Dr. Sandeep Gorantla** at Łukasiewicz Research Network – PORT Polish Center for Technology Development. In both cases, the author assisted in these measurements. In addition, the author also participated in the complete process of fabricating the lamellas for STEM characterization performed at **NANORES**, Wrocław.

Calculations, which served as a reference for interpreting an important part of the obtained spectroscopic results, were performed by utilizing two different software platforms. The dependence of the QD ground state transition energy on the modifications in the MBL were carried out by the author using the commercial software **NEXTNANO**. In addition, more advanced calculations of QD properties including the excitonic effects were performed by **Dr. Michał Gawełczyk**,[MG] who employed codes written by **Dr. Krzysztof Gawarecki**.

[MG] This footnote within the entire thesis refers to results of calculations performed by Dr. Michał Gawełczyk from Institute of Theoretical Physics, Wrocław University of Science and Technology.

1. QUANTUM DOT

1.1. QUANTUM DOT AS A ZERO-DIMENSIONAL STRUCTURE

The epitaxial growth of semiconductor QDs is based on the mismatch of the dot and substrate materials' lattice constants. To form confinement for carriers, materials showing a difference in the band gap are chosen. Such QDs are characterized by limited in-plane dimensions, typically below 50 nm, and height below 10 nm, thus providing a zero-dimensional confinement. Due to the higher potential in the material surrounding the dot, the movement of carriers in all three directions is limited, resulting in crucial quantum effects including full quantization of the energy structure, analogous to atoms [8]. The density of QD states, describing the number of states per unit of energy, also illustrates this quantization. It takes a discrete form, depending only on the energies of states bound in the dot, as a series of Dirac delta peaks [9]:

$$\rho^{0D-QD}(E) = \sum_{i=1}^{n} \delta(E - E_i), \tag{1.1}$$

where E_i is the energy of the ith quantized level. Figure 1.1 shows such a QD discrete density of states compared to a continuous function corresponding to a bulk material.

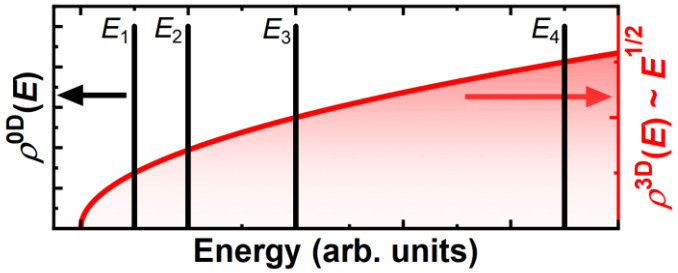

Figure 1.1. The density of states for a semiconductor QD (black) and bulk material (red).

The energy structure depends on the confinement potential, which depends directly on the QD size and the strain associated with the mismatch of the crystallographic structure of the dot and the substrate materials. In analogy to the quantum well with infinite energy potential barriers, energy levels are approximately inversely proportional to QD size ($\sim 1/L^2$) [10], which results in lowering the energy and reducing the splitting of the states by increasing the QD size. This analogy is only a simple approximation, as it is crucial to consider, e.g., the deformation of the dot, which also significantly modifies the energy structure. Nevertheless, it indicates the possibility of controlling the QDs' emission energy by modifying QD geometry. However, for QDs growth under a large difference in lattice constants, a significant strain hinders the possibility of changing the sizes in a wide range. Additionally, the quality of the dots deteriorates due to increased strain and correlated defects creation. In addition, the high strain increases the energy distance of the energy levels, significantly reducing the possibility of lowering the emission energy [5].

1.2. EPITAXIAL GROWTH OF OPTICALLY-ACTIVE QDS

Semiconductor quantum dots for applications as optical sources are produced primarily using epitaxial growth, in which the substrate's crystal lattice is maintained during successive layers' deposition. The indicated approach allows for acquiring high structural quality, making it possible to use QDs as radiation emitters with a minimized number of defects in the crystallographic structure. Another epitaxial growth method for realizing zero-dimensional structures, for example, is the production of dots based on thin quantum well lithography. However, structure modification during the lithography process results in poorer crystallographic quality, with an increased number of defects. Therefore, due to the optical properties, the

epitaxial growth is usually carried out in the self-assembly mode, ensuring high structural quality with minimized defects [8].

Growth in the self-assembly mode is based on energy minimization (volume energy of the material, surface energy, strains). The growth driver is the mismatch of lattice constants of the materials being grown. For the zero or nearly zero mismatches, the undefected high-quality layers growth occurs, which can be controlled over a wide range of layer thicknesses. This type of growth is called the Frank-van der Merve (FM) mode, characterized by the formation of epitaxial monolayers. When the mismatch of lattice constants increases, the strain of the lattice of the growing material increases, causing significant stresses in the structure that results in the growth of imperfect layers or force the creation of three-dimensional islands forming quantum dots. The Volmer-Weber (VW) growth mode is characterized by the growth of islands of material directly on the substrate layer for significant differences in lattice constants. In the intermediate case between the VM and FM modes, for smaller differences in the lattice constants than for VM mode, there is the Stranski-Krastanov (SK) mode characterized by the growth of a few monolayers in the initial stage. Then, after crossing the critical thickness, the transition to the three-dimensional islands' formation occurs due to stress increase resulting in the growth of QDs. A schematic comparison of the described growth modes is shown in Figure 1.2A. QDs grown in the VM mode have less regular position and size distributions and more defects that negatively affect the optical properties. Moreover, the higher strain in the dots negatively affects the ability to control their parameters, including their emission energy.

On the other hand, the SK growth mode, resulting in the initial epitaxial layer called the wetting layer (WL), leads to better structural quality with fewer defects. Furthermore, the WL enhances the regularity of dot parameters, including spatial orientation, shape, size, and composition. All this contributes to the better properties of the dots grown in the SK mode for use as radiation sources.

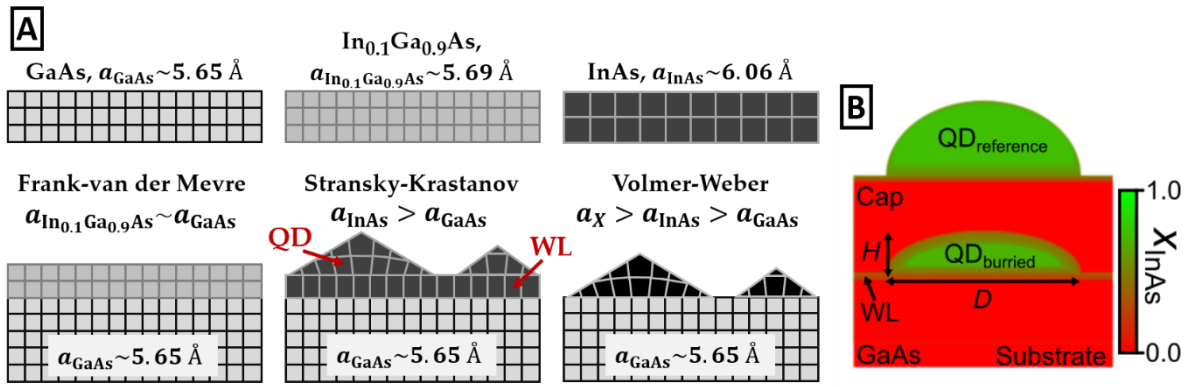

Figure 1.2. (A) Scheme of epitaxial growth of layers under various lattice constant mismatch conditions leading to layer and island growth modes. (B) Scheme of an epitaxially grown quantum dot, considering the effect of material intermixing and the capping layer affecting the differences between buried and reference dots.

The QDs grown in the self-assembly process are then covered with another epitaxial layer (capping layer) characterized by a larger energy gap compared to QDs to limit the movement of the carriers and thus create the full confinement potential. In addition, the capping layer protects the dots against the influence of the environment, particularly the degradation processes of the crystallographic structure, resulting in the deterioration of the QDs' optical properties. This layer may also modify the QD parameters by admixing its material to the existing dots, resulting in changes in QD size, shape, and composition [11]. In addition, the different lattice constant of the covering material creates additional strain. All this leads to a complex picture of the dot strain and possible changes in the structural QD parameters in the presence of a capping layer. In addition, intermixing between the substrate layer and the dot is also likely, leading to a gradient composition of the dot, especially at material interfaces. Figure 1.2B shows a schematic image of a QD highlighting the indicated effects of mixing materials and modifications of the dot parameters due to the

presence of the capping layer. Marked modification effects result in the difference between buried QDs and the reference dots formed on the structure's surface.

The QDs properties, particularly the confinement potential and the associated emission energy, depend on many parameters, such as size, shape, or material composition. In the epitaxial growth, besides the material mismatch, several parameters affect the dot-forming layer properties and the diffusion of materials, including the substrate temperature, the ratio of the appropriate components forming the layers, the dynamics of component delivery, or the layer thickness. Controlling of indicated constraints allows the adjustment of QD features in a wide range, allowing for structures characterized by, among others, low surface density, elongated size in one direction, or tuning the emission energy in a wide spectral range. Moreover, the choice of materials for the substrate, dots, and capping layer is crucial in the context of strain occurring in QDs and controlling the QD emission energy. The most popular structures for obtaining the emission in the telecommunication range are InAs QDs grown on InP and GaAs. These systems differ in the lattice constant mismatch, which naturally results in differences in strain affecting the QD emission energy [5]. As a result, emission in the 1200–2000 nm range is achievable for the InAs/InP structures, while for the InAs/GaAs structures emission ranging only up to 1200 nm has been demonstrated structures due to higher strain [1]. However, it is possible to use strain engineering and modify QD parameters in analogy to the possibility of modifying the dots due to the special capping layer. This approach is discussed in more detail in Chapter 3, presenting the emission from InAs/GaAs dots in the telecommunication range thanks to QD growth modifications reducing the dot strain.

Nevertheless, QD growth is complex, and many parameters affect the resultant QD structural and optical properties. Among epitaxial growth techniques, two are the most popular: high-vacuum molecular beam epitaxy and metalorganic vapor phase epitaxy (MOVPE) [12]. Both allow for obtaining high-quality QDs with application potential [2]. The MOVPE growth is faster and allows for large-scale applications. On the other hand, MBE growth allows using additional methods to control subsequent layers' growth, ensuring the material's high structural quality.

1.3. QDs AS QUANTUM EMITTERS

Due to three-dimensional confinement, the energy structure of QDs shows full quantization of energy levels for both electrons and holes. Their positions depend mainly on the confinement potential, which is also influenced by the strain [13,14]. A simplified diagram of the QD level structure is shown in Figure 1.3A. Discrete energy levels lead to similarly discrete emission lines characterized by a precisely defined energy for recombining an electron with a hole. The spectral width of the QD emission has a lower bound specified by the emission decay time. For InAs QDs, recombination times are about 1 ns [14], and the resulting Lorentzian broadening is typically less than 1 μeV. In addition, carriers confined in a QD may also interact with nearby fluctuating charges in the structure, which results in non-uniform Gaussian broadening due to the spectral diffusion effect [15]. Due to fluctuations in the electrical environment, the energy structure of the dot fluctuates continuously around the average energy value. Moreover, the coupling of the exciton with crystal lattice vibrations (phonons) also contributes to the energy broadening.

In addition, due to the mixing of QD hole states formed from different valence-band subbands, the contribution of both the heavy hole (HH), light hole (LH), and spin-orbit split-off states can be distinguished. Compressive deformations occurring in QDs with a larger lattice constant relative to the substrate, apart from increasing the energy distance between states, also lead to larger subband separation. Mixing LH-HH states, affecting the QD emission polarization properties, seems particularly important [16]. For standard InAs dots, a hole state with a majority of HH contribution is observed [17]. However, the strain reduction and increased QD size result in a modification of the mixing, leading to an increase in the LH contribution in the hole ground state. This results in an increased degree of linear polarization of the emission, which would be zero for a pure HH state [16].

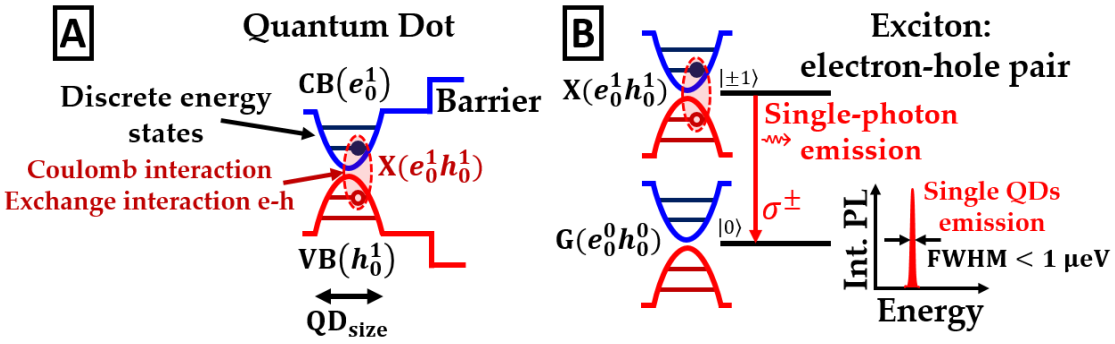

Figure 1.3. (A) Energy diagram of a quantum dot with marked discrete energy states for the electron and hole and the interacting electron-hole pair forming the exciton. (B) Scheme of an exciton with recombination of an electron-hole pair leading to the emission of a single photon with defined emission energy with broadening related to the exciton lifetime. The symbol e_0^1 or h_0^1 indicates one electron or hole in its lowest energy state (0).

Self-assembled growth allows obtaining dots characterized by similar size, composition, shape, and strain. However, due to parameter fluctuations, an inhomogeneous ensemble of QDs is observed (emission energy distribution) for a larger surface of the structure [18]. The inhomogeneous broadening of the QD ensemble emission results in the possibility of using such structures as broadband optical amplifiers [19,20]. In addition, considering the possibility of growth of different QD distributions during a single growth, a significantly wide range of the emission is achievable, which makes it possible to apply these emitters as broadband radiation sources [21–23]. In addition, QDs can be used as an active region of lasers due to the large differential gain, large modulation bandwidth, and the reduced dependence of the laser action threshold current on temperature and its low values [24–28].

On the other hand, QDs can accumulate strain in the structure and be used as specific strain filters, especially for significantly mismatched lattice constants of the grown materials [4]. Indicated behavior allows for implementing good-quality layers grown on substrates with very different lattice constants. The possibility of using structures containing QDs as detectors [7,25] and in solar cells [29,30] has also been demonstrated. However, these applications are mainly based on QD ensembles, not fully exploiting the advantages associated with full quantization of the energy structure.

The key QD property is also that the QDs' emission is associated with recombining a correlated electron-hole pair within the dot. For QDs, the increased localization favors a presence interaction of carriers, where exciton effects become crucial [31], and the dots' emission shows an excitonic character (although strong quantization reduces the impact of carrier pair correlation effects). Figures 1.3A and 1.3B show a schematic view of an exciton (X) with an outline of the energy structure. The interaction affects the emission energy, and the QD emission parameters primarily depend on the exciton complex properties, described in more detail in Chapter 2. Additionally, the exciton in the dot can be considered a two-level system, where there is a state associated with the presence of an exciton and the state of an empty dot [2]. The exciton recombination results in the emission of radiation, which is a single-photon emission. Therefore, the emission associated with exciton in a single dot can also be used as a source of single photons for applications in secure quantum communication. In addition, QDs should enable the implementation of more advanced information transmission protocols due to the possibility of emitting pairs of entangled photons and indistinguishable photons together with on-demand mode operation in both cases [32]. These structures have also been historically associated with the possibility of implementing quantum bits for quantum computing due to the full quantization of the energy structure and for the quantum state control [33]. The prospects of QDs as spin memories and manipulation of the spin state [3] have been demonstrated so far.

The application possibilities of QDs are still hindered due to limited efficiency and the lifetime of carriers. The main restriction is the low extraction efficiency of QD emission without additional photonic

structures. In addition, the lifetime of the emission also limits the possibility of obtaining a high repetition of single-photon emissions. Several structures have shown a significant improvement in emission efficiency and a reduction in emission decay time due to the coupling with an optical cavity [18]. However, still, record applications concern structures emitting below the telecommunication range [18].

2. EXCITONIC COMPLEXES IN QD

2.1. SINGLE EXCITON IN QD

The Coulomb interaction forming the exciton[2] changes the energy of the entire system, where the energy distance of the electron and hole states is insufficient to determine the carrier recombination energy. In the simplest picture accounting for interaction, based on the Hartree-Fock (HF) theory, the exciton energy is defined by the energy distance of the non-interacting states of the electron and the hole reduced by the energy of the direct Coulomb interaction and the energy of the exchange interaction for spins of the carriers [34]. In the HF approximation for the lowest exciton energy level, this can be written as follows:

$$E_{\mathrm{X}} = (E_{\mathrm{e}} - E_{\mathrm{h}}) + E_{\mathrm{C,eh}} + E_{\mathrm{ex}}, \tag{2.1}$$

where E_{e} and E_{h} are single-particle electron and hole energies, $E_{\mathrm{C,eh}}$ is the Coulomb interaction energy, and E_{ex} is the energy of the electron-hole exchange interaction. A more accurate approach beyond the HF approximation leads to an additional correction to the exciton energy due to the admixtures of higher configurations of electron and hole single-particle states. In particular, for dots characterized by high Coulomb interaction energy between carriers, comparable to (or higher than) the quantization energy, it is necessary to consider corrections to the HF approximation in the form of Coulomb correlations ($\Delta E_{\mathrm{C,corr}}$) in the configuration-interaction formalism CI [14,35]. The energy of a photon emitted as a consequence of the radiative recombination of such an interacting electron-hole pair is equal to the total energy of the exciton: $\hbar\omega_{\mathrm{X}} = E_{\mathrm{X}}$. The binding energy of the exciton is defined as the difference of the energy of non-interacting electron and hole and their interacting pair [14]:

$$\Delta E_{\mathrm{X}} = (E_{\mathrm{e}} - E_{\mathrm{h}}) - E_{\mathrm{X}}. \tag{2.2}$$

This binding energy is crucial for figuring out the carrier confinement regime discussed in the following section. The experimental determination of the exciton binding energy is difficult because the energies of non-interacting carriers are unknown. The exciton binding energy also allows for the existence of an interacting pair of carriers under the influence of the temperature-dependent distribution of phonons. Higher exciton binding energy makes possible observation of excitonic properties at higher temperatures.

The X energy depends not only on the Coulomb interaction but also on the electron-hole exchange interaction [36]. The wave functions of the electron and the hole also contain their spin (or total band angular momentum) parts depending on the value of the total angular momentum projection on the structure growth direction. Its value for an electron can be $\pm 1/2$ (denoted by $|\uparrow\rangle$ or $|\downarrow\rangle$), and for heavy holes $\pm 3/2$ (denoted by $|\Uparrow\rangle$ or $|\Downarrow\rangle$). A simplified diagram of the QD level structure is shown in Figure 2.1A. The hole ground state is a heavy hole state based on the implicitly higher effective mass for these states and the compressive strain in InAs QDs [17,31,36], resulting in lower energy for states with a large, even close to total HH contribution, as opposed to states with a larger LH contribution. The indicated values of the angular momentum for carriers lead to the total angular momentum for the exciton equal to ± 1 or ± 2. Therefore, for a purely heavy-hole exciton, two bright states $|\mp 1\rangle = |\pm 1/2, \mp 3/2\rangle$ ($|\uparrow\Downarrow\rangle$ or $|\downarrow\Uparrow\rangle$) and two dark states $|\pm 2\rangle = |\pm 1/2, \pm 3/2\rangle$ ($|\uparrow\Uparrow\rangle$ or $|\downarrow\Downarrow\rangle$) can be distinguished [18] (see Figure 2.1B). Dark states, due to the change in the total angular momentum equal to ± 2 needed for recombination, cannot interact with light and are optically inactive.

[2] The exciton in a quantum dot is not a standard quasiparticle formed only by the Coulomb interaction of carriers as in the case of bulk material. The carrier confinement potential for the dot leads to the localization of carriers in a limited space which favors the occurrence of Coulomb interaction of carriers, i.e. the creation of the interacting pair of carriers occurs as a result of the localization of carriers rather than Coulomb interaction. Nevertheless, within this work, an interacting pair of carriers localized in the QD will be called an exciton.

The electron-hole exchange interaction depends on the total angular momentum, resulting in the splitting of the exciton energy depending on the angular momentum of a given state. Three different splittings of the energy structure are involved: splitting between bright and dark states ($\delta_{|\pm1\rangle,|\pm2\rangle}$), between bright states ($\delta_{|\pm1\rangle}$), and between the dark states ($\delta_{|\pm2\rangle}$). The corresponding Hamiltonian has the following form (for symmetry of a QD reduced from cylindrical D_{2d} to C_{2v}) [36]:

$$H_{\mathrm{ex}} = \frac{1}{2}\begin{pmatrix} \delta_{|\pm1\rangle,|\pm2\rangle} & i\delta_{|\pm1\rangle} & 0 & 0 \\ i\delta_{|\pm1\rangle} & \delta_{|\pm1\rangle,|\pm2\rangle} & 0 & 0 \\ 0 & 0 & -\delta_{|\pm1\rangle,|\pm2\rangle} & \delta_{|\pm2\rangle} \\ 0 & 0 & \delta_{|\pm2\rangle,} & -\delta_{|\pm1\rangle,|\pm2\rangle} \end{pmatrix}. \tag{2.3}$$

The individual splittings are related to the coupling of electron and hole angular momenta along different crystallographic directions. For InAs dots, the bright and dark states are always split, leading to the lower energy of the dark states. In addition, the dark states are also always split [36]. The splitting of bright and dark states is associated only with the coupling in the direction of structure growth, regardless of the in-plane symmetry (cylindrical or lower symmetry), resulting in the separation of these states [36]. The splitting of individual bright and dark states is related to the in-plane angular momenta coupling (see Figure 2.1B). Regardless of in-plane symmetry, dark states are split due to the summation of the spin coupling contributions for orthogonal directions in the plane. However, in the case of bright states, the splitting $\delta_{|\pm1\rangle}$ called fine structure splitting (FSS), depends on the difference of coupling constants for orthogonal in-plane directions, which leads to the dependence of the splitting on the asymmetry of the confinement potential in the plane. The reduction of the cylindrical symmetry (D_{2d}) to the broken symmetry in the plane (C_{2v} or lower) leading to a non-zero FSS (see Figure 2.1C) is related to the QD shape and strain anisotropy [36] or the position anisotropy of the atoms building the dot [37].

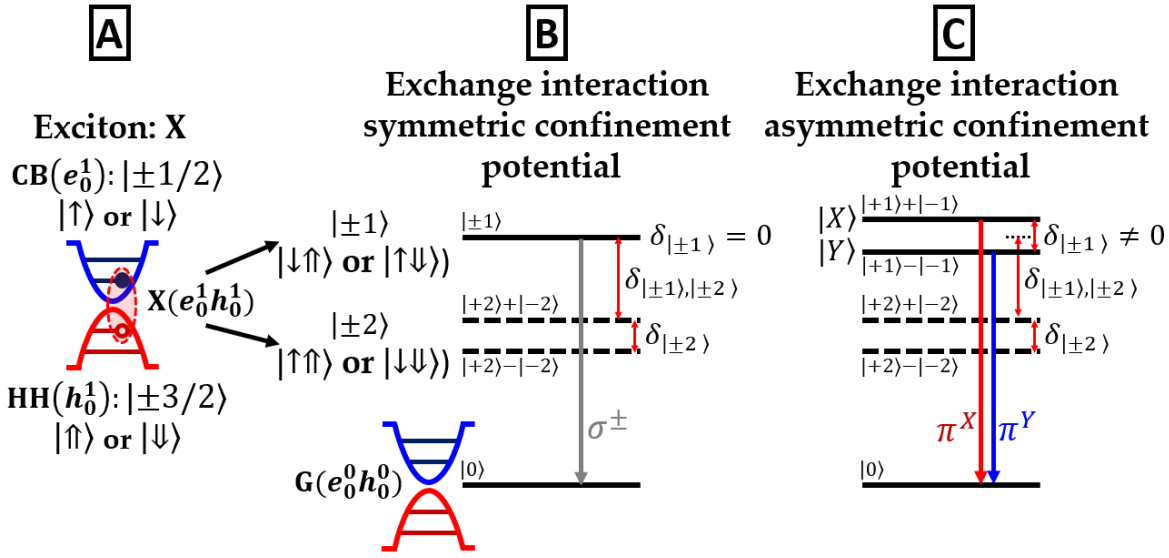

Figure 2.1. (A) Diagram of the energy structure of a QD with a marked pair of electron-hole carriers forming an exciton, including the angular momentum value for individual carriers and exciton. Diagram of exciton energy levels, including the exchange interaction for (B) the symmetry of the dot confinement potential (cylindrical symmetry) and (C) the asymmetry of the confinement potential (elongated QD). Optical transitions for individual exciton bright states and individual splitting values for particular states.

For QDs based on materials from the III-V group, in most cases, the asymmetry of the crystallographic structure in the plane usually leads to the observation of non-zero FSS [38,39]. The FSS value depends on the level of the in-plane potential asymmetry. The lower the asymmetry, the smaller the energy separation between the two bright states (therefore, also called anisotropy splitting). Additionally, due to the influence

of external electric [40–43] or magnetic fields [35,36] and strain conditions [44–46], it is possible to control the anisotropy of the potential and thus influence also the value of FSS. An essential element is the influence of the wave functions of both the electron and the hole on the exchange interaction. The splitting depends on the asymmetry of their overlap [47]. Thus, it is possible to observe small FSS values when asymmetry occurs only for one of the carriers. In addition, the electron-hole exchange interaction for anisotropic in-plane confinement (C_{2v} of lower symmetry) also results in the mixing of $|\pm 1\rangle$ states [16]. The new bright eigenstates are $|X\rangle = \frac{1}{i\sqrt{2}}(|+1\rangle - |-1\rangle)$, $|Y\rangle = \frac{1}{\sqrt{2}}(|+1\rangle + |-1\rangle)$, where the total angular momentum projection for the exciton is 0. These states are split by the FSS energy. The schematic exciton structure, depending on the confinement potential in-plane asymmetry, is shown schematically in Figures 2.1A, B and C.

Optical transitions for an electron-hole pair in semiconductor structures depend on the electron (ψ_i) and hole (ψ_j) wave functions composed of the envelope functions (orbital part) and the Bloch function at the Gamma point. The exciton transition probability can be described based on Fermi's Golden Rule (described in more detail for optical transitions in Section 2.4). For this, the matrix element of interaction in the dipole approximation can be used. For a transition between confined states of the electron (i) and the hole (j), it takes the form [14,48]:

$$M_{ij} = \langle \psi_j | \hat{e} \cdot \bar{p} | \psi_i \rangle, \tag{2.4}$$

and, apart from the electron and hole wave functions, also involves the momentum operator ($\bar{p}$). The latter acting on a state (derivative) changes its parity. Optical transition is possible only for a non-zero M_{ij}, which thus occurs for different parity of electron and hole wave functions (including both the envelope functions and the Bloch function). Hence, as the parity of the electron and hole Bloch functions is opposite (based on the symmetry of p-type valence states and s-type conduction states), the selection rules for exciton optical transitions indicate the non-zero overlap of electron and hole envelopes and conserved total band angular momentum.

For the emission due to the recombination of bright states $|\pm 1\rangle$ without superposition, there is a total change in angular momentum equal to ± 1, corresponding to photons with circular polarization ($\sigma^{\pm}$). For the superposition of bright states, zero change in total angular momentum implies linear polarization ($\pi^{X,Y}$) [16,18]. Accordingly, there is also a natural assignment of dark states as optically inactive due to the change in total angular momentum equal to ± 2, for which there is no possible interaction with light. The complicated image of the QDs' energy structure may result in the lack of full strictness of the indicated rules. However, they reveal the most intensive optical transitions. Among other things, the mixing of hole states can significantly complicate the picture of selection rules and emission polarization.

For purely light-hole states, there are transitions associated with the angular momentum of holes $\pm 1/2$ (denoted by $|\Uparrow_{\mathrm{LH}}\rangle$ or $|\Downarrow_{\mathrm{LH}}\rangle$) and resultant bright light-exciton states $|\pm 1\rangle_{\mathrm{LH}} = |\pm 1/2, \pm 1/2\rangle$ ($|\uparrow\Uparrow_{\mathrm{LH}}\rangle$ or $|\downarrow\Downarrow_{\mathrm{LH}}\rangle$). Similarly to transitions for HH states, circular polarization occurs. However, it is opposite for the same initial state of the electron (respectively $|\uparrow\rangle \rightarrow |\Downarrow\rangle: -1\ (\sigma^-), |\uparrow\rangle \rightarrow |\Uparrow_{\mathrm{LH}}\rangle: +1\ (\sigma^+)$). As a result of HH-LH mixing, the nominally HH exciton states become $|\mp\tilde{1}\rangle = \sqrt{1-\beta^2}|\pm 1/2, \mp 3/2\rangle + \beta e^{\pm 2i\theta}|\pm 1/2, \pm 1/2\rangle$ (respectively: $\sqrt{1-\beta^2}|\uparrow\Downarrow\rangle + \beta e^{\pm 2i\theta}|\uparrow\Uparrow_{\mathrm{LH}}\rangle$) [16]. Accordingly, the first term relates to the HH content, and the second to the LH one, the parameter β describes the mixing, and θ describes its phase. Due to the hole contribution imbalance (higher HH contribution for the InAs QD), mixing results in two elliptical polarizations for transitions. Moreover, adding the possible anisotropy in the electron-hole exchange interaction, the mixing of these states $|\mp\tilde{1}\rangle$ results in: $|\tilde{X}\rangle = \frac{1}{i\sqrt{2}}\left(|+\tilde{1}\rangle - e^{2i\alpha}|-\tilde{1}\rangle\right)$, $|\tilde{Y}\rangle = \frac{1}{\sqrt{2}}\left(|+\tilde{1}\rangle + e^{2i\alpha}|-\tilde{1}\rangle\right)$, where α is the angle formed between the direction of the

anisotropy of QDs emission polarization relative to the crystallographic direction. Due to the LH and HH mixing, the QDs characterized by potential anisotropy show a linear emission polarization and an emission intensity imbalance for the two polarizations. This results in a non-zero degree of linear polarization (DOLP) defined based on the relationship:

$$\mathrm{DOLP} = (I_{\max} - I_{\min})/(I_{\max} + I_{\min}), \tag{2.5}$$

where the intensities $I_{\max}$ and $I_{\min}$ correspond to the intensity for orthogonal polarizations with maximum and minimum emission intensity [16].

DOLP can be shown to depend directly on the QD parameters [49,50], in particular on the in-plane dimensions (longer dimension D_{long}, shorter dimension D_{short}) and a phenomenological parameter having the meaning of the energy separation between the HH and LH states (i.e., states with dominant HH or LH contributions; $\Delta E_{\mathrm{HH-LH}}$):

$$\mathrm{DOLP} \sim 1/\Delta E_{\mathrm{HH-LH}}(D_{\mathrm{short}}^{-2} - D_{\mathrm{long}}^{-2}). \tag{2.6}$$

The value of $\Delta E_{\mathrm{HH-LH}}$ is related mainly to QD height and strain conditions. An increase in the height of the dots favors an increase in mixing hole states, causing a higher value of DOLP. Additionally, the crucial factor contributing to the increase in DOLP is the asymmetry of the dot shape in the plane. However, the mixing of hole states is significant in the case of high dots, even for their slight asymmetry (exhibiting low FSS).

2.2. CONFINEMENT REGIME FOR A QD EXCITON

Based on the relation between the energy separations of the single particle electron (ΔE_{e}) and hole states (ΔE_h) and the exciton binding energy (ΔE_{X}) three different confinement regimes in QDs are typically distinguished: strong, intermediate, and weak [51,52]. For the strong carrier confinement regime, the influence of the Coulomb interaction is negligible compared to confinement, i.e., the energy of the Coulomb electron-hole interaction is smaller than the separation of electron and hole states ($E_{\mathrm{C,eh}} \ll \Delta E_{\mathrm{e}}, \Delta E_{\mathrm{h}}$). In the case of the intermediate confinement regime, the indicated condition occurs only for one of the carriers ($E_{\mathrm{C,eh}} < \Delta E_{\mathrm{h}}$ and $E_{\mathrm{C,eh}} > \Delta E_{\mathrm{e}}$ or $E_{\mathrm{C,eh}} < \Delta E_{\mathrm{e}}$ and $E_{\mathrm{C,eh}} > \Delta E_{\mathrm{h}}$), i.e., the quantization of states is stronger than the Coulomb interaction for only one of the carriers forming the exciton. Eventually, for the weak confinement regime, the single-particle splittings are smaller than the exciton binding energy for both electron and hole ($E_{\mathrm{C,eh}} \gg \Delta E_{\mathrm{e}}, \Delta E_{\mathrm{h}}$). It results in the dominance of correlations effects (spatial correlation of the electron and hole wave functions) over the carrier quantum confinement [53]. This description can also be connected to the Bohr radius of a bulk exciton, where the strong confinement regime corresponds to the case when the dot size is much smaller than the Bohr radius of the exciton. In contrast, it is the opposite in the weak confinement regime. The intermediate confinement regime applies when the dot size is usually comparable to the exciton Bohr radius (or, more properly, the dot volume similar to a volume of a sphere with a Bohr radius) [51]. The determination of the QD confinement potential regime is not related to an actual physical quantity. It is rather an indication of the set of characteristic properties of the exciton based on the interplay of the carrier confinement potential and the exciton binding energy.

For InAs QDs on a GaAs substrate, the exciton binding energy for standard structures (without any sophisticated strain engineering) is about (10–20) meV [8,14,17]. Due to the significant separation of electron states above 50 meV and hole states above 10 meV, these structures usually show a strong (or close to) confinement regime. However, hole states have weaker carrier confinement, which may result in the intermediate confinement regime. It may occur due to increasing the QD size or reducing the strain resulting in exciton emission energy shift and a decrease of the states' distance. In addition, the modification of the dot material, or the barrier itself, affects the confinement regime of the carriers due to the dependence of the Coulomb interaction on the material's dielectric constant.

2.3. OTHER EXCITONIC COMPLEXES

QD confinement potential can contain not only a single pair of carriers (forming exciton) but also their higher number bound by Coulomb interaction. These include the negatively or positively charged excitons (CX) formed due to the presence of an additional electron or hole, respectively. Moreover, there is the biexciton (XX) for two electron-hole pairs [18]. In the characterization of the QD emission, it is possible to observe also complexes higher than the biexciton. However, interpreting such data is often difficult due to the density of the emission spectrum (also in the presence of emission from other dots) as well as the complicated energy patterns for individual complexes. An example diagram of the energy structure of a dot with different numbers of carriers for successive basic complexes is shown in Figure 2.2A.

As for the exciton, the energy of higher exciton complexes can be estimated based on the Hartree-Fock theory, considering the energy of additional carriers and the energy of the Coulomb interaction between all the carriers. The electron-hole exchange interaction energy for the basic exciton complexes (CX, XX) is zero due to the zero value of the total angular momentum of electrons or holes. Due to the exchange interaction, higher complexes' energy structure becomes more complicated.

The emission energy of higher exciton complexes is related to recombining a single pair of carriers as the most probable and allowed process. Therefore, additional carriers remain in the dot afterward. An extra electron or hole remains in QD for charged exciton, while for biexciton, it is the whole electron-hole pair. The excitonic complexes emission leads to a similar notation as for the exciton [14]:

$$\begin{aligned} \hbar\omega_{+\mathrm{CX}} &= E_{+\mathrm{CX}} + E_{\mathrm{h}}, \\ \hbar\omega_{-\mathrm{CX}} &= E_{-\mathrm{CX}} - E_{\mathrm{e}}, \\ \hbar\omega_{\mathrm{XX}} &= E_{\mathrm{XX}} - E_{\mathrm{X}}, \end{aligned} \tag{2.7}$$

where the binding energies of individual complexes relative to the exciton energy can be determined as the energy necessary to bind additional carriers to the basic exciton (in other words, break the complex into an exciton and additional carriers) [14]:

$$\begin{aligned} \Delta E_{+\mathrm{CX}} &= (-E_{\mathrm{h}} + E_{\mathrm{X}}) - E_{+\mathrm{CX}} = \hbar\omega_{\mathrm{X}} - \hbar\omega_{+\mathrm{CX}}, \\ \Delta E_{-\mathrm{CX}} &= (E_{\mathrm{e}} + E_{\mathrm{X}}) - E_{-\mathrm{CX}} = \hbar\omega_{\mathrm{X}} - \hbar\omega_{-\mathrm{CX}}, \\ \Delta E_{\mathrm{XX}} &= 2E_{\mathrm{X}} - E_{\mathrm{XX}} = \hbar\omega_{\mathrm{X}} - \hbar\omega_{\mathrm{XX}}. \end{aligned} \tag{2.8}$$

The presented definition of the binding energy allows ease determination of binding energies of exciton complexes based on the measurement of the emission energy and the subsequent determination of the energy difference between the emission lines related to the complexes. The indicated binding energies of individual complexes depend on the confinement potential for the carriers in the dot, particularly on the wave functions and their overlapping. In the case of reduced confinement towards the weak confinement regime, it is necessary to consider the correction for the energies of the Coulomb correlations, which additionally modifies the energies [14]. Positive and negative energies indicate either the binding or anti-binding nature. For standard InAs/GaAs QDs, the binding energies of exciton complexes are usually not higher than a few meV of absolute value, e.g., for the biexciton in the −4.8 meV to 3.0 meV range, for +CX in the 0.9 meV to 15.2 meV range, and for −CX in the −3.0 meV to −8.9 meV range [54]. Typically, +CX is characterized by positive binding energy, i.e., an anti-bonding state, while −CX and XX are characterized by a binding state. However, changes in the confinement potential associated with dot size, strain, and composition can significantly modify the confinement for individual carriers, leading to a different confinement regime and interaction energies between individual carriers, favoring different binding energies for complexes higher than the exciton. Apart from attraction interactions, there is also a repulsion interaction, and it is often necessary to include the contribution of higher-energy single-particle states in the ground states of complexes, which changes their energy [14].

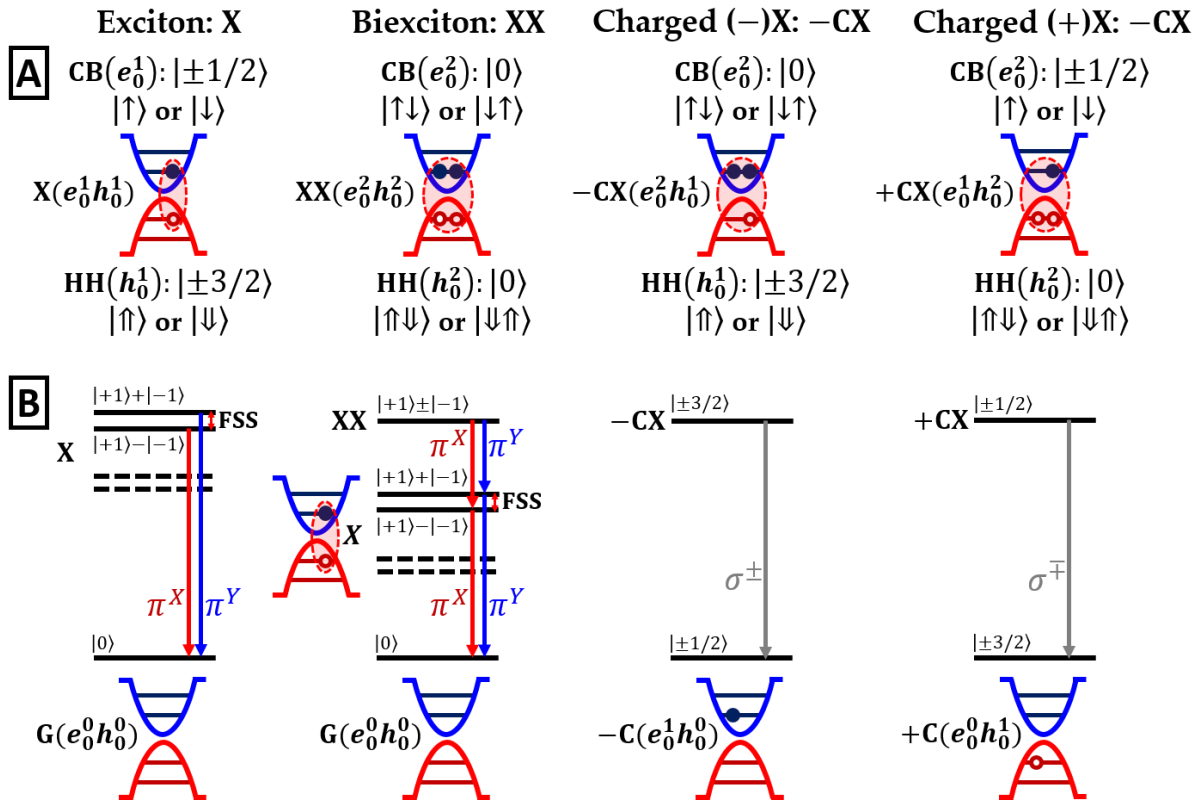

Figure 2.2. (A) Diagrams of the energy structure of exciton complexes in a QD with the angular momentum projection values for the individual carriers and complexes. (B) Energy level diagrams for exciton complexes with optical transitions for individual complexes together with the diagrams of the QD after the transition.

Figure 2.2B shows the individual complexes' optical transitions, including the final states, e.g., the exciton after the biexciton recombination and the remaining electron or hole after charged exciton recombination. Due to the total angular momentum for electrons or holes equal to zero for the biexciton and charged excitons (two carriers with opposite spins), there is no exchange interaction. Therefore there is no fine structure in the ground state.

Considering the recombination of a single electron-hole pair in neutral XX, the remaining exciton is in one of the bright states depending on the spin configuration of carriers that recombined. Taking into account the asymmetry of the confinement potential resulting in eigenstates being the superpositions of bright states $|\pm 1\rangle$, the emission for XX leads to transitions with orthogonal linear polarizations ($\pi^{X,Y}$). Considering the FSS, it is possible to distinguish the appropriate energies of the transitions with the corresponding linear polarization. There is identical polarization for the lower-energy exciton transition and the higher-energy biexciton transition and identical polarization for the opposite pair of transitions (higher-energy exciton, lower-energy biexciton, see Figure 2.2). In the absence of confinement potential anisotropy or due to the introduced magnetic field (in Faraday configuration), the bright states for XX and X are characterized by orthogonal circular polarizations ($\sigma^{\pm}$), as in Figure 2.1.

For charged exciton complexes, possible transitions for an exciton included in these complexes with a total change of angular momentum equal to ± 1, cause emission with circular polarizations ($\sigma^{\pm}$) due to the lack of exchange interaction [18]. There may also be an additional mixing of the HH and LH states, resulting in an approximately identical non-zero value of the DOLP independently of the exciton complex (for XX or CX), depending on the QD parameters, as shown for the exciton. In these cases, the charged exciton shows elliptical orthogonal polarizations, and the biexciton exhibits orthogonal linear polarizations.

Regardless of the anisotropy of the QD confinement potential, the occurrence of a non-zero FSS value is correlated with the opposite dependence of the emission energy on polarization for particular XX and X

states and allows for easier identification of these transitions compared to charged excitons showing no FSS. However, identification becomes more difficult for the neutral X and XX with FSS values close to zero. Then the solution can be correlation measurements combined with other experiments (power-dependent and polarization-resolved characterization) or the measurements in the magnetic field (Voight configuration), where different neutral and charged states splitting schemes allow for the identification [36,55].

2.4. KINETICS OF OPTICAL TRANSITIONS

For exciton complexes in a QD, the rate of an optical transition can be described by Fermi's golden rule [14]. In the dipole approximation, the rate of the transition from state i in the conduction band to state j in the valence band can be written in the form:

$$P_{ij}(\hbar\omega) = \frac{ne^2\hbar\omega}{3\pi\hbar^2c^3\varepsilon_0 m_0^2}\sum_{ij}\left|\langle\psi_j|\hat{e}\cdot\bar{p}|\psi_i\rangle\right|^2\delta(E_j - E_i \pm \hbar\omega), \tag{2.9}$$

where e is the elementary charge, n is the refractive index, c is the speed of light in vacuum, ε_0 is the vacuum permittivity, E_i and E_j are the initial and final energies, $\delta(x)$ is the Dirac delta relating to QD density states (formula 1.1), while the matrix element of the dipole moment $\langle\psi_j|\hat{e}\cdot\bar{p}|\psi_i\rangle$ is evaluated with the electron and hole wave functions (analogous to formula 2.4 for radiative recombination). Correspondingly, photon absorption is related to the additional energy ($-\hbar\omega$) delivered to the dot, while the emission is associated with the energy emitted as a photon ($+\hbar\omega$). To simplify the relationship, one may express it in terms of the Kane energy (E_P) determined for various semiconductor materials [56], and introduce an additional quantity called oscillator strength:

$$f_{ij}(\hbar\omega) = \frac{\left|\langle\alpha_j|\alpha_i\rangle\right|^2 E_P}{2\hbar\omega}, \tag{2.10}$$

where, $\langle\alpha_j|\alpha_i\rangle$ is the overlap of the respective envelope functions associated with the initial and final states. With this, the transition rate is as follows [57]:

$$P_{ij}(\hbar\omega) = \frac{ne^2 f_{ij}(\hbar\omega)}{6\pi\hbar^2c^3\varepsilon_0 m_0}(\hbar\omega)^2 \tag{2.11}$$

Considering the emission energy dependence of the oscillator strength ($f_{ij}(\hbar\omega) \sim (\hbar\omega)^{-1}$), the optical transition rate depends linearly on the emission energy in the strong confinement regime. On the other hand, in the case of weaker carrier confinement regime within the QD, it is necessary to consider the additional admixture of higher configurations of single-particle states.

The radiative recombination rate for an exciton determines the radiative recombination rate, leading to the transition from the correlated electron-hole pair state to an empty dot. Based on the inverse of the transition rate, the lifetime of the exciton is determined: $\tau_{i,j}(\hbar\omega) = P_{i,j}(\hbar\omega)^{-1}$. Furthermore, the exciton lifetime is inversely related to the emission energy ($\tau_{i,j}(\hbar\omega) \sim (\hbar\omega)^{-1}$) [58]. In particular, the close overlapping of the exciton and hole wave functions for the strong carrier confinement regime simplifies the dependence. However, this dependence is more complex for the weak confinement regime due to the additional dependency of the oscillator strength on the dot size, which is also indirectly related to the emission energy [58].

The exciton emission decay time is generally not equivalent to the exciton radiative lifetime due to the additional impact of non-radiative processes [57,59]. The combination of these two processes decides the overall emission decay times. In addition, besides the lack of transition rate dependence on the state occupation (formula 2.9), emission dynamics depends on the occupations of the initial and final states [14]. Therefore, to determine the radiative lifetime of an exciton, using the lowest possible excitation power density in photoluminescence (PL) measurements is necessary to avoid occupying excited states of the

exciton. Additionally, the possible non-radiative escape of carriers to trap states (e.g., defects near the dots) or other thermally-activated processes also change the decay time, which is generally independent of temperature.

Thus, in the strong confinement regime, the exciton radiative lifetime is inversely proportional to the emission energy if the excitation is weak enough and if it is possible to neglect the non-radiative recombination processes. In this regime, for the biexciton, the Coulomb interaction between the two excitons forming biexciton is weak compared to exciton binding energy (Coulomb interactions only slightly perturb the exciton states). The decay time can approximately be considered as for two separate excitons, the XX decay time being twice shorter than X based on twice the number of allowed decay channels [56,60]. The lifetime of charged excitons is similar to the exciton lifetime in the strong confinement regime. In the weak confinement regime, the oscillator strength of the transition for an exciton is proportional to the volume of the quantum dot, resulting in an inverse proportionality of the lifetime to both the emission energy and the dot size [58]. In this case, the Coulomb interactions between individual carriers become significant compared to quantization energy, introducing changes in the lifetimes of individual complexes depending on the admixture of higher single-particle states. Due to the increased interaction of carriers, for X, there is a reduction in lifetime. At the same time, for XX, there is an increase in lifetime relative to the strong confinement regime (reduction in the lifetime ratio, nominally equal to about 2 for the strong confinement regime) [56]. Similarly, charged complexes also have significant differences in lifetimes compared to the exciton [60].

The dependence of the decay time on the occupation of individual states leads to the necessity of considering the full dynamics of processes possible for excitonic states. The system of kinetic rate equations for individual states allows for determining of the occupation of states. They have the form of coupled first-order differential equations for the occupation n_i of states for each state i involved [61–65]:

$$\frac{dn_i}{dt} = \frac{n_{i+1}}{\tau_{i+1\to i}} - \frac{n_i}{\tau_{i\to i-1}} + g_{\mathrm{e/h/eh}} n_{i-1} - g_{\mathrm{e/h/eh}} n_i, \tag{2.12}$$

where n_i is the state occupation, $\tau_{i\to i-1}$ is the recombination time from state i to $i-1$, $g_{\mathrm{e/h/eh}}$ is the rate of carrier (electron-hole pair or one of them) capture (including excitation processes). Continuous excitation leads to a stationary state, where there is no change in the occupation of states, i.e., $\frac{dn_i}{dt} = 0$. Then occupations depend only on the recombination times and the excitation of carriers $g_{\mathrm{e/h/eh}}$. The emission intensity is related to the state occupation and the recombination time:

$$I_{ij} \sim \frac{n_i}{\tau_{ij}} \tag{2.13}$$

For the three-level system (see Figure 2.3A) with the levels of the empty dot, exciton, and biexciton, the following emission intensity dependencies can be determined assuming a cascade scheme of transitions [66]:

$$I_{\mathrm{X}} = \frac{g_{\mathrm{eh}}}{1 + P\tau_{\mathrm{X}} + P^2\tau_{\mathrm{X}}\tau_{\mathrm{XX}}},$$
$$I_{\mathrm{XX}} = \frac{{g_{\mathrm{eh}}}^2\tau_{\mathrm{X}}}{1 + P\tau_{\mathrm{X}} + P^2\tau_{\mathrm{X}}\tau_{\mathrm{XX}}}. \tag{2.14}$$

In the range of low powers continuous-wave (CW) excitation, there is a linear dependence of the exciton emission intensity on the excitation and a quadratic one for the biexciton. For a four-level system with an additional level above the XX state, there are other processes of supplying and depleting the XX state. They allow for describing the decrease in the XX emission intensity in the range of high excitation powers [66].

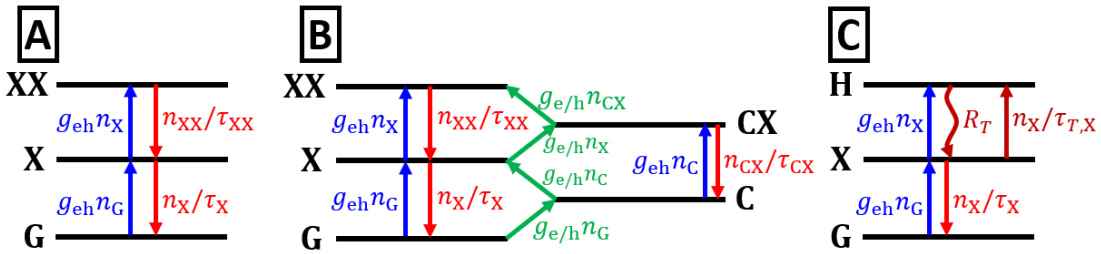

$$(A): \frac{dn_X}{dt} = \frac{n_{XX}}{\tau_{XX}} - \frac{n_X}{\tau_X} + g_{eh}n_G - g_{eh}n_X$$

$$(B): \frac{dn_X}{dt} = \frac{n_{XX}}{\tau_{XX}} - \frac{n_X}{\tau_X} + g_{eh}n_G - g_{eh}n_X + g_{e/h}n_C - g_{e/h}n_X$$

$$(C): \frac{dn_X}{dt} = R_T - \frac{n_X}{\tau_X} - \frac{n_X}{\tau_{T,X}} + g_{eh}n_G - g_{eh}n_X$$

Figure 2.3. (A) A scheme of a three-level system including exciton, biexciton, and empty QD state with marked individual processes of carrier recombination (red arrows) and carrier capture (electron-hole pairs: blue arrows). (B) Diagram of a five-level system including a charged exciton. Indication of other capture processes of single carriers (green arrows). (C) Scheme of a three-level system for an exciton and a state from the environment of a quantum dot with higher energy in the range of available thermal energies. Indication of the additional exciton transition process to a higher state due to non-zero thermal energy (brown arrow) and fast relaxation from a higher state (wavy brown arrow).

In addition, for a cascade that also includes charged excitons, if single carriers can be captured and not only pairs of carriers are considered (see Figure 2.3B) [67], it is possible to modify the individual complexes build-up coefficients and the relative intensities of emission from complexes due to possible charge imbalance and capture processes. This can be caused by, e.g., unintentional doping or defects effectively capturing single carriers of one type. This effect may lead to a variable ratio of the emission intensity of charged complexes to neutral ones and differences in the intensity build-up coefficients. For pulsed excitation, there is no stationary state. After excitation, all carriers go to higher states and then return to the lowest states, where radiative recombination and the associated emission decay occur.

Due to the Heisenberg uncertainty principle, the radiative recombination time is directly related to the homogenous emission line broadening for exciton complexes. For dots characterized by radiative recombination time of 1–2 ns [14,68,69], this broadening is below 1 μeV (also called zero-phonon linewidth, ZPL) – see Figure 2.4A. In a real system, an exciton in a QD may interact with phonons via inelastic scattering processes due to the non-zero temperature of the sample (temperature-dependent phonon distribution) and with the charge environment, in particular with the fluctuations of the electric field (excitation-induced charging and discharging of traps/defects in the dot vicinity). The latter modifies the energies of carrier states over time, resulting in the spectral diffusion effect. The phonons' influence is negligible in the low-temperature range (e.g., around 5 K) due to the small reservoir of available phonons. In this temperature range, the dominant factor is spectral diffusion, resulting in the inhomogeneous broadening of QD emission lines (see the brown line in Figure 2.4A) [15,70]. This factor is the primary source of QDs line broadening observed at the low-temperature (usually 1-2 orders of magnitude larger linewidths than those related to the finite exciton lifetime [71]), besides the spectral resolution of the measurement system limitations (which, however, can reach single μeV values in the current spectroscopic systems). At higher temperatures, the influence of phonons increases, resulting in additional sidebands coming from recombination processes involving phonon absorption and emission, increasing the spectral broadening of QD emission lines (see the red line in Figure 2.4A) [72]. In this case, the change in the broadening is connected to the temperature-dependent distribution of phonons. As the temperature increases, the contribution of emission associated with the interaction with phonons increases, extending inhomogeneous broadening (see Figure 2.4B). In general, these processes result in the loss of the coherence

of the electron-hole pair forming an exciton, even for coherent resonant excitation into the exciton state, thus avoiding the relaxation from higher states [15]. For non-resonant excitation, despite the coherent exciton formation, the relaxation processes lead to the loss of coherence due to scattering and the carriers with exciton interaction.

Another issue is the possible presence of additional higher states at a small energetic distance. If such states lay in the vicinity of QDs and are a few meV above the exciton state (see Figure 2.3C), carriers can be transferred there (e.g., via phonon-assisted tunneling) from the X state even with the low thermal energy available at T = 5 K ($k_B T$ ~ 0.4 meV). In this case, the standard single-exponential decay of an exciton is accompanied by an additional decay process with dynamics appropriate for the temperature-dependent rate of carrier transfer to a higher state (charge traps) and then relaxation towards the QD exciton state.

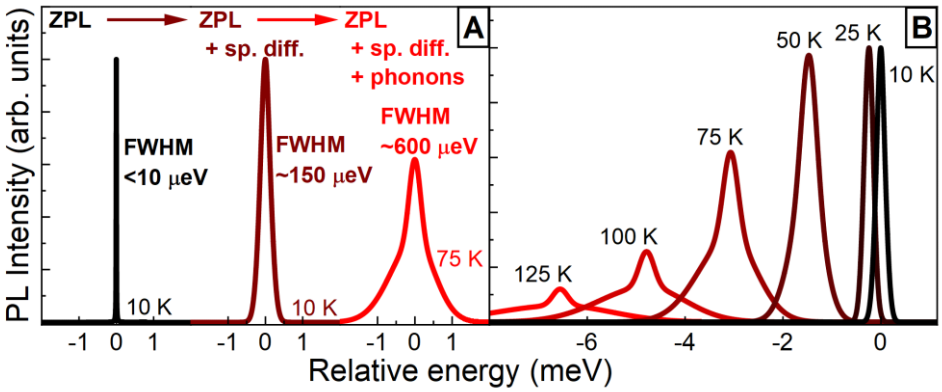

Figure 2.4. (A) PL spectra of QD for ZPL related to exciton recombination time (black line), with the influence of spectral diffusion (brown line) and including interactions with phonons at higher temperature (red line). (B) Diagram of changes in QD emission spectra showing broadening due to the spectral diffusion process and interactions with phonons for subsequent temperatures (10–125 K) based on Ref. [71,72].

2.5. STATISTICS OF EMISSION

The exciton radiative recombination leads to a single-photon emission, which results in the possibility of using such emitters as non-classical light sources. A photon is a particle with a specific energy depending on the exciton emission energy with a slight energy broadening, for which the number of photon states equals 1 (precisely one photon in case of detection). The second-order correlation function allows the determination of the statistical properties of the investigated radiation, including the distribution of the number of photons recorded in the measurement (which may distinguish between 0, 1, and more phonons) [8]. In general, it can be written in terms of photon annihilation $\hat{a}_i$ and creation $\hat{a}_i^+$ operators for two modes (non-monochromatic radiation: i and j) of a time-dependent electric field at one spatial point and for a specific delay τ:

$$g_{ij}^{(2)}(t,\tau) = \frac{\langle \hat{a}_i^+(t)\hat{a}_j^+(t+\tau)\hat{a}_j(t+\tau)\hat{a}_i(t)\rangle}{\langle \hat{a}_i^+(t)\hat{a}_i(t)\rangle\langle \hat{a}_j^+(t)\hat{a}_j(t)\rangle}. \tag{2.15}$$

For a monochromatic wave, the modes are identical, $i = j$, leading to the autocorrelation function. For different modes $i \neq j$, this function describes the cross-correlation of two different fields [73].

For stationary source at steady state (only significant difference in times τ) the $g^{(2)}(\tau)$ function can be related to the probability $P(n;t)$ of emitting n photons in a period of length t. Thanks to this, sources with multi-photon emission can be distinguished (non-zero probability of emission of more than one photon at the same time), as well as sources with emission of single photons (zero probability of such events). For emitters with a near-zero probability of emitting more than one photon (in particular, two photons), the emission probability can be directly related to the second-order correlation function. For the zero time delay,

a value close to zero is observed and associated with the probability of emission of more than one photon, and for longer delays, it takes values equal to 1 [18]:

$$g^{(2)}(0) = \frac{2P(2;t)}{[P(1;t)]^2}. \tag{2.16}$$

The second-order correlation function for time delays close to zero determines the degree of photon bunching, i.e., the tendency of photons to occur at close time distances. Therefore, it is possible to indicate whether there is a bunching of photons for small time intervals ($g^{(2)}(\tau = 0) > g^{(2)}(\tau \gg 0)$) or antibunching of photons ($g^{(2)}(\tau = 0) < g^{(2)}(\tau \gg 0)$) [8]. For coherent radiation sources, characterized by Poisson statistics of the photon number, emitters show neither bunching nor antibunching of photons, and the correlation function takes the value $g^{(2)}(\tau) = 1$ in the full range of time delays. In this case, $g^{(2)}(\tau)$ can be connected to the average number of photons $\mu_n = \langle \hat{n} \rangle$ in the act of emission, as well as the variance of the number of photons: $\sigma_n^2 = \langle \hat{n}^2 \rangle - \langle \hat{n} \rangle^2$. Then, the autocorrelation function can be written as:

$$g^{(2)}(0) = 1 + \frac{\sigma_n^2 - \mu_n}{{\mu_n}^2}. \tag{2.17}$$

Accordingly, for a Poissonian source, the average number of photons is equal to the variance, $\langle \hat{n} \rangle = \langle \hat{n}^2 \rangle - \langle \hat{n} \rangle^2$, showing an autocorrelation value of 1 for zero delay. However, for sub-Poissonian statistics, $g^{(2)}(0) < 1$ can be observed where the variance is smaller than the average number of photons, $\langle \hat{n} \rangle > \langle \hat{n}^2 \rangle - \langle \hat{n} \rangle^2$. This situation corresponds to the photon antibunching. Similarly, super-Poissonian statistics with photon bunching can be considered. The ideal source of single photons has sub-Poissonian statistics with an average number of photons equal to $\mu_n = 1$ and zero variance, showing the value $g^{(2)}(0) = 0$. The finite efficiency of a measurement system, extraction of photons from a QD, as well as the reduction of the single-photon emission probability ($P(1) = \mu_n < 1$) due to, e.g., non-radiative recombination, lead to observing an average number of photons less than 1 reduced to even very low values. However, maintaining $g^{(2)}(0) = 0$ still corresponds to an ideal source of single photons but with limited generation efficiency. For the correlation value $g^{(2)}(0) > 0$, emission acts involving more than single photons can occur (at least for some of the emission/detection acts), which limits the purity of the single-photon emission. The limiting criterion of $g^{(2)}(0) < 0.5$ was adopted for the classification of the emission as single-photon, where the value $g^{(2)}(0) = 0.5$ corresponds to a source with a strictly defined number of photons equal to 2 (ideal source of double photons) [2,8]. However, for practical applications, the value of $g^{(2)}(0)$ should be as low as possible (below 0.01). The possibility of obtaining the highest possible single-photon emission purity indicates the potential of a particular emitter for practical application.

The second-order correlation function is determined experimentally, usually using the Hanbury Brown and Twiss (HBT) configuration (see Figure 2.5B) [18]. The radiation from the source is divided using a beam splitter and then hits two detectors, which can record single photons. The measurement comprises observation of acts of collective detection on the two detectors and determination of the time distance between the act of detection on one detector (D1-START) and the act of detection on the other (D2-STOP) in a given time interval. The count of coincidences is recorded for a given time delay between the two detectors. The control of delay and detection acts is carried out using an electronic system that operates as a correlator. The details of the used emission statistics measurement system are described in Subsection 4.2.2. The correlation function $g^{(2)}(\tau)$ is directly related to the number of coincidences for a given time delay. The temporal resolution for the correlation function measurement is connected to the used time bin width (the time width of discrete time intervals that build the time scale) and the limited system temporal resolution (optical system and detectors). For the correlation function changes at time scales shorter than the system resolution, the result of the measurement is a convolution of $g^{(2)}(\tau)$ with the instrument

response function (IRF) characterizing the time resolution of the system. Then, the deconvolution of the IFR signal allows for obtaining the exact $g^{(2)}(\tau)$, although it is reasonable only for fast changes in the correlation function. An additional limitation is the number of detector counts in time. A low number of counts (related to the number of coincidences) limits the measurement speed, naturally extending the time necessary to obtain the assumed level of coincidences (to obtain meaningful statistics). Moreover, the technique has limitations related to the detectors used, which often cannot determine the amount of photons incident on them. This hinders the ability to correctly determine the statistics, allowing only for distinguishing single-photon acts from multi-photon ones without seeing the exact distribution and statistics [73]. The solution to this problem is to use detectors that can precisely detect the number of incident photons [74].

The dependence of $g^{(2)}(\tau)$ obtained experimentally (for CW excitation) is fitted using the delay dependence for a two-level system (including changes in the state's occupation over time). For an exciton (see Figure 2.5A without the XX state) [75], characterized by single-photon emission, it takes the form:

$$g^{(2)}(\tau) = 1 - exp\left(-\frac{|\tau|}{\tau_{\mathrm{D}}}\right), \tag{2.18}$$

where τ_{D} is the exciton state evolution time. In general, the probability of coincidences for the zero-time delay is low, which is associated with zero or close to zero correlation value, $g^{(2)}(0) \cong 0$, for a single-photon emitter. However, with increasing delay, the correlation function increases to a value equal to 1 for times longer than τ_{D}. From the rate equations for the two-level system, it appears that the dynamics of occupation of the X state is also dependent on the excitation conditions, resulting in a reduction of τ_D with increasing excitation ($1/\tau_{\mathrm{D}} = g_{\mathrm{eh}} + 1/\tau_{\mathrm{X}}$), thus increasing the rate of changes in $g^{(2)}(\tau)$. Therefore, τ_{D} is referred to as the rise time due to the significant influence of the generation rate (process g_{eh}, see Figure 2.3A) [76].

The QD can be considered as a two-level system with a state containing an exciton (excited state) and a state with an empty dot (ground state). Then, recombination leads to the emission of a single photon, and the system switches to the ground state. Actual QD structures are more challenging than theoretical concepts, resulting in limitations in observing ideally-pure single-photon emission. The finite QD emission intensity can limit the accuracy of purity determination based on the need for long measurements of emission statistics. The registered QD emission can also be affected by the occurrence of emission from the QD surroundings with an identical spectral range. For emission from the background, the emission purity is reduced by the observation of additional photons not connected to the examined dot, with the possibility of recording two photons simultaneously. In addition, with an increase in excitation power, the background emission signal can increase, resulting in a deterioration of the purity of single photon emission. Moreover, the influence of the electric environment and the associated QD emission spectral diffusion causing an increase in the QD emission spectral width may also translate into limitations in filtering single QD emission from background emission (spectral selection of single QD emission). On the other hand, there is also the possibility of recording scattered photons of the excitation laser, also reducing the purity of the emission. Furthermore, the short $g^{(2)}(\tau)$ signal rise time (dependent on the excitation power and exciton decay time), as well as the finite time resolution of the measurement system, can also limit the accuracy of the determination of $g^{(2)}(0)$ due to the high dynamics of changes in the $g^{(2)}(\tau)$ function depending on the time delay. In addition, the rise time reduction with the increasing excitation power enhances the changes in $g^{(2)}(\tau)$ (reducing the antibunching signal time width), favoring a reduction of the accuracy of determining the purity of single-photon emission.

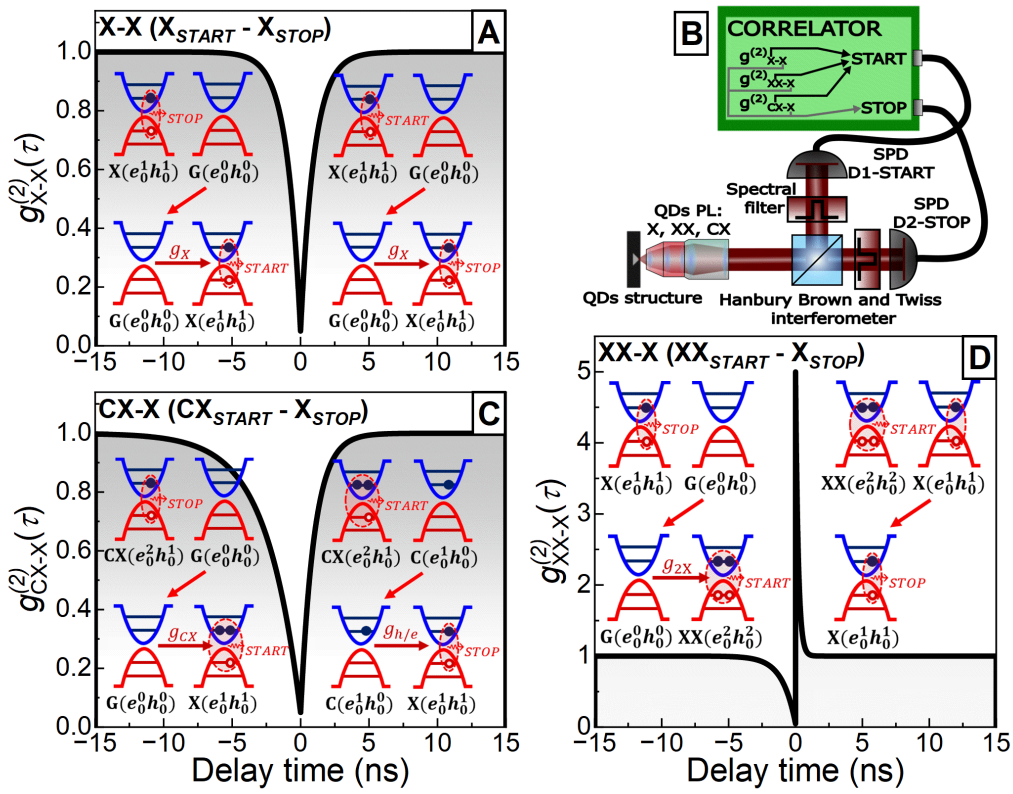

Figure 2.5. (A) Graph of the autocorrelation function $g^{(2)}(\tau)$ for the exciton (X-X). Individual successive recombination and exciton formation processes are described for both negative and positive delays. (B) The Hanbury Brown and Twiss interferometer scheme [18]: a beam splitter dividing the dot emission signal between two single-photon detectors (SPD), D1 and D2, respectively associated with the used correlator recording time delays between the acts of detection for the START and STOP channels. (C) Cross-correlation function $g^{(2)}(t)$ for the emission cascade CX-X and (D) XX-X. Individual successive recombination and complex formation processes are described for negative and positive delays. The curves shown are for a low excitation power range, favoring a lower probability of additional carriers excitation.

The realization of single-photon emission can also be performed based on pulsed excitation, which makes it possible to obtain triggered single-photon emission within the exciton emission decay time after pulsed excitation. This approach enables more control over the realization of single-photon emission relative to CW excitation, where the emission process is random in stationary conditions. In particular, using additional resonant excitation schemes in pulsed excitation provides a basis for realizing on-demand single-photon emission crucial toward realizing single-photon sources for quantum communication practical applications [73]. However, the use of pulsed excitation, where the emission is not observed in stationary conditions, is associated with the observation of single-photon emission in a specified time frame after the excitation pulse resulting in the need to include emission dynamics processes. In this context, there may be additional problems with the realization of single-photon emission as besides the normal emission decay driven by exciton lifetime observation of additional decay processes after the laser pulse may lead to the need to adjust the repetition of the excitation laser as well resulting in an increased background of $g^{(2)}(\tau)$ function [77]. In addition, there may be additional QD recapturing processes of carriers from the charge environment, reducing the purity of single-photon emission due to additional emission unrelated to pulse excitation and limiting the real value of $g^{(2)}(0)$ characterization [78].

In addition to autocorrelation function determination, the cross-correlation function for two non-monochromatic modes can confirm whether the emission lines originate from the same QD, which makes possible identification of exciton complexes. In this case, the different order of the series of recombination,

excitation, and carrier capture processes for the cross-correlation emission cascade characterization between different exciton complexes affects the $g^{(2)}(\tau)$ signal depending on each complex emission probability over time. Using rate equations for the state's occupation for the appropriate emission cascade for various ranges of positive and negative delays allows for examining the changes in the correlation function and analyzing the generation of exciton complexes and carrier capture [63,67,75,76,79,80].

A standard function $g^{(2)}(\tau)$ for the CX-X cross-correlation can be distinguished, as shown in Figure 2.5C. Its asymmetry is due to different times of capturing three carriers forming CX (processes: g_{CX}) after X emission and capturing one carrier (processes: $g_{\mathrm{h/e}}$) necessary to form X after CX emission. The exact dependence results from both the individual processes of capturing single carriers and the excitation conditions, leading to the need to consider the complete picture of kinetic equations. However, the asymmetry in the function $g^{(2)}(\tau)$ is generic.

In the case of the XX-X emission cascade, there is a similar asymmetry in the cross-correlation function due to the different biexciton and exciton emission times (see Figure 2.5D). After the XX recombination, there is still a pair of carriers forming an exciton in the dot, resulting in an increase in the population of this state and a high probability of X emission. This leads to high values of the correlation function for positive near-zero delays. After X emission, it is necessary to capture four carriers forming XX (processes: g_{2X}) to obtain the biexciton emission, which leads to values below 1 for the correlation function for negative near-zero delays.

3. ENGINEERING THE QDS FOR SINGLE-PHOTON EMISSION IN THE TELECOMMUNICATION RANGE

3.1. QDS AS EMITTERS IN THE TELECOMMUNICATION RANGE

The exciton emission properties for single QDs described in previous chapters make them ideal for applications in quantum information technology, especially in ultra-secure quantum telecommunication based on single-photon emission (see Section 2.5) [81]. In addition, due to other properties (also of the ensembles of nanostructures), these emitters can be used as basic components for many nanophotonic devices, including lasers, optical amplifiers, and broadband sources (see Section 1.3) [4,25,82]. In that context, an important property of QDs is the characteristic emission/absorption wavelength defining the possible applications. This dissertation concerns QDs able to emit up to around 1.6 μm in the near-infrared, i.e., covering the entire range of high-transmission windows of silica fibers commonly used in optical communication networks. There are two telecommunication windows with the lowest attenuation (see Figure 3.1): the second telecom window (1260–1360 nm) with attenuation of ~0.35 dB/km and almost zero signal dispersion, and the third telecom window (1460–1625 nm) with the lowest attenuation at ~0.20 dB/km [6,83]. The most desirable is the implementation of emitters in the third telecommunication window, enabling the transmission of information over the most extended distances, above 100 km, without signal amplification. Within the indicated windows, some useful channels for free-space optical satellite telecommunication can be distinguished (mainly the third telecom window), where the multitude of existing solutions for fiber-optic communication allows for a more straightforward realization of such applications in this area compared to other spectral ranges for free-space telecommunication [84]. In addition, the telecommunication range is attractive for applications related to the implementation of integrated photonics and quantum computing on Si-based materials, showing high transmission in this range [85,86], where integrated quantum dots can be used as radiation sources [26,87–89].

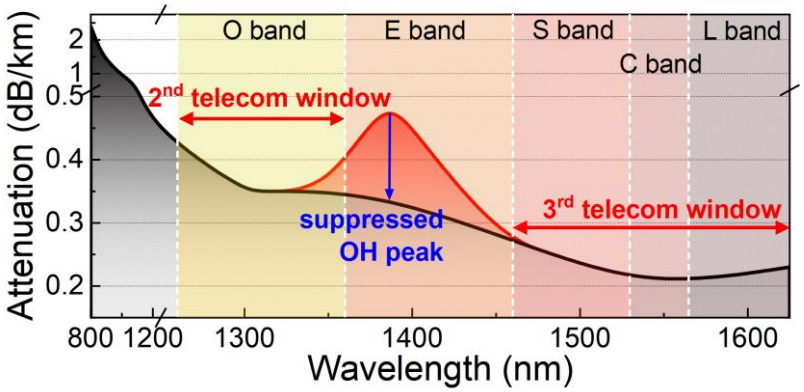

Figure 3.1. Spectral dependence of attenuation for modern silica fibers (based on data for SMF-28e fibers from Corning) [90].

For QDs, the most common systems used to reach emission in the telecommunication range are based on InAs material epitaxially grown on InP and GaAs substrates. The InAs material has an energy gap of ~0.354 eV corresponding to 3500 nm wavelength (~0.415 eV at 5 K). But, when including the quantum size effect and the compressive strain, an intrinsic property of all the self-assembled QD structures, the optical transition energy shifts up (compared to InAs bulk material). To limit this shift and get emission in the 1.3–1.55 μm range, the primary system of choice are QDs grown on InP substrates, which naturally emit in the third telecom window [91]. On the other hand, structures based on GaAs substrates, after combining the quantum confinement and strain (which is by more than a factor of 2 larger in the InAs/GaAs system),

usually show emission at a much shorter wavelength below 1200 nm [7]. For the mentioned structures, the main difference is the lattice constant of the substrate material. The InAs material has a ~3% difference in lattice constant compared to InP and ~7% to GaAs [92]. The larger compressive strain for InAs deposited on GaAs is responsible for a shift of QD ground state [7] but also affects the growth conditions and prevents the formation of islands with increased sizes [5]. As a result, the states confined in small InAs/GaAs dots experience a strong quantum size effect. Therefore, for GaAs-based structures, implementing additional growth modifications to reduce the strain (and at the same time possibly increase the QD size) is needed to shift the emission to the near-infrared, reaching telecommunication wavelengths. Modification of the QD properties to reduce the difference in the lattice constants of the InAs material relative to the substrate material showed the possibility of low-strain dot growth based on lower QD indium composition [93]. However, the accompanying reduction of the emission wavelength, associated with the lower indium content in the dots, blocks the possibility of shifting the emission to longer wavelengths due to the drastic energy gap modification toward the GaAs material [94]. It has been demonstrated that one of the most efficient ways to shift emission to longer wavelengths is strain engineering via modifications in the composition of the material surrounding the dots while maintaining the high indium composition in a QD [7].

Despite the necessary efforts to shift the emission to the telecommunication range, QDs based on GaAs material are a very good candidate for structures for applications due to the very mature technology of epitaxial growth of structures on GaAs substrates [89]. In addition, the fabrication of various photonic confinement structures is well developed for this material group, offering high extraction efficiency of emission [18]. In particular, the almost lattice-matched AlAs and GaAs create a very good pair of materials with good refractive index contrast (the difference of the refractive indices in near-infrared is ~0.5), making them suitable for the realization of high-quality distributed Bragg reflector (DBR) for advanced photonic structures and optical cavities [91]. All this indicates the legitimacy of the attempt to implement InAs QDs on GaAs substrates to obtain emitters for the telecommunication range.

3.2. ROLE OF STRAIN ENGINEERING

Several approaches have been proposed in the literature to shift the InAs QD emission to the second and even the third telecom windows. As the main limitation of the emission shift is the significant deformation of InAs grown on GaAs, two methods directly related to reducing the strain via modifying the QD environment have been proposed. These modifications are the strain-reducing layer (SRL) and metamorphic buffer layer (MBL).

The SRL method is the growth of InGaAs dots on the GaAs layer with an additional InGaAs capping layer with indium content smaller than in the dots [95–106] (including QD growth in InGaAs quantum wells). Such a layer reduces the strain [96,107] and increases the size of the structures [5,95,98], but also affects the QD composition [108], making the dots In-richer due to the natural tendency of indium to segregate/cluster [7]. The InGaAs-based SRL method makes it possible to shift the emission even to the third telecom window [109]. The use of another capping layer of InAlAs [96], GaAsSb [110–113], or InGaAsSb [112,114] also allows shifting the emission towards the telecommunication range.

The second, MBL approach is based on applying an additional layer between the substrate and QD layer, changing the base material for QD layer growth [115–119], reducing the difference between base and InAs QD lattice constants [120]. The dots grow on a material with a greater lattice constant than GaAs, resulting in reduced stress during the QD layer formation [7], which increases dot sizes [116,121]. Changing the lattice constant results in the need to relax the crystal lattice, where, by using the appropriate thickness of the MBL layer [116,122–125], it is possible to reduce the number of structural defects (misfit and threading dislocations) [126] that affect the QDs structural and optical quality, which is the main challenge of this method. The selection of InGaAs [4,127], GaAsSb [110,128], or AlGaAsSb [129] materials allowed

obtaining a reduction of strain and shifting the emission to the range of the third telecom window [7]. Most such structures were designed mainly for use in lasers [4,117,119,127,130] and other photonic devices [4,22].

Other methods can be distinguished for lowering QD deformation and shifting QD emissions. The method based on vertically-stacked QDs made it possible to limit strain, especially for subsequent layers of dots [131–136]. In this approach, the QDs and the spacer layer act as a filtering layer for strain and defects caused by stress associated with the mismatch of the crystal lattice. This method showed emission redshift to 1.3 μm and 1.5 μm for the top QD layer (including the InGaAs capping layer). The emission energy is controlled by strain and intermixing with the capping layer, whereas the density of QDs can be influenced by the seeding layer [131].

The control of the InAs QD growth rate (indium accumulation and decrease of the density of QDs [137–140]) or layer thickness (growth to the second critical InAs material thickness [141,142]) can also shift the emission up to 1500 nm. However, to sufficiently shift the emission of obtained low-density QDs, it was required to use the InGaAs capping in most cases to compensate for the increase of strain. Similarly, controlled overgrowth of InGaAs QDs improves the structural quality, also including GaAs capping layer towards realizing multilayer QD growth and QD size modification [143]. This method shows the emission shift to 1.3 μm with the improvement of QD optical properties. The alternate InGaAs QD MBE growth approach shows the emission shift up to 1.3 μm [144–147].

A completely different approach is to use the InAs QD growth with an additional small concentration of nitrogen [148], resulting in decreasing the energy gap and increasing the QD size by the reduced strain between QDs and GaAs, eventually shifting the emission to 1.3 μm. This approach also reduces the number of defects, showing a strong PL signal at room temperature [149], also for QD stacked laser structure [150]. Nitrogen incorporation can also shift the emission up to 1.5 μm, which was, however, accompanied by a decrease in the PL signal due to the low emission efficiency of these QD (incorporation of non-radiative defects) [151]. Most of the mentioned methods primarily concerned applications like lasers or amplifiers, where the active region utilizes ensembles of dots and single quantum dot properties are not in the spotlight.

At least two of the listed methods have been demonstrated as useful in fabricating single-photon emitters in the telecommunication range, based on the SRL and MBL approach on GaAs substrate [1,81]. However, for the SRL approach, the single-photon emission was demonstrated only for QDs emitting up to 1350 nm [5,6]. The only method for implementing single-photon emission from GaAs-based QDs in the third telecom window that has been demonstrated so far is based on MBL [5]. This technique was previously used mainly in the form of homogeneous MBLs grown (constant indium content) on a GaAs substrate, allowing for the reduction of strain from the growth on GaAs and making possible the growth of QDs with the emission shifted to the telecommunication range [4,7]. Due to the still significant difference in the lattice constants of the substrate and the metamorphic layer, there was a considerable strain in the structure (observation of V-shaped or closed-shaped defects and cross-hatched surface [152]), which was mainly reduced by selecting the appropriate thickness of the metamorphic layer. It still affected QD optical quality and hindered the emission shift to longer wavelengths. Nevertheless, such an approach showed the possibility of obtaining single QD emission shifted up to 1300 nm [124,153,154] and demonstrating single-photon emission [155].

Another approach based on a gradient buffer layer was also developed to improve the structural quality and shift the QD emission to longer wavelengths. It allows for a gradual change in the lattice constant, significantly reducing the difference in lattice constants at each growth stage [126,156–158]. Using the growth based on MBE, this approach allowed demonstrating the single dot emission in the third telecom window [156]. Further development of this technique using MOVPE-based growth allowed for obtaining very good quality QDs characterized by emission in the third telecom window and showing high purity of single-photon emission [5].

3.3. VARIOUS SINGLE-PHOTON SOURCES IN TELECOM RANGE

Secure quantum key distribution, or implementing quantum repeaters as part of quantum information technologies, requires a high-purity and high-brightness single-photon sources (SPS) as a fundamental element [81]. In addition, realizing long-haul communication requires operation within the high transmission windows. So far, several structures have been demonstrated that meet, at least partially, the indicated requirements [6,159]. One of the most basic and widely used SPS is based on spontaneous parametric down-conversion [160]. Using an appropriate laser source and a non-linear material ensures radiation conversion into the telecommunication range, demonstrating high-purity single-photon emission [160,161]. However, this approach is based on a probabilistic photon generation process, which makes it difficult to achieve high brightness and efficiency of single-photon emission. Moreover, the random photon generation process cannot provide the on-demand emissions necessary for implementing quantum communication [2,74,89]. Nonetheless, these emitters have demonstrated high generation rates in the telecom range [161]. In addition, the applied approaches based on heralded photon pairs allow for a partial solution to the problems with implementing the on-demand mode. However, obtaining both high repetition and high emission purity in the on-demand mode is very limited by the probabilistic photon generation process [32,89].

The application of SPS based on atomic ions was also demonstrated [162], showing relatively good single-photon emission purity. Similarly, the possibility of implementation was also presented using defects in carbon nanotubes [163], silicon carbide [164] or gallium nitride [165], and nitrogen-vacancy centers in diamond [166]. These approaches show the possibility of achieving good-quality emitters with high-purity single-photon emission. However, several technological problems prevent their straightforward application, like limited brightness, stability, scalability, and the possibility of integration with existing semiconductor platforms [2,6]. Nevertheless, approaches of this type towards the implementation of SPS are still being developed.

In comparison to indicated sources of single-photon emission, QDs as SPS in the telecommunication range show very high-purity values of single-photon emission (record low multiphoton generation probabilities [81,89]), together with the possibility of solving many of the indicated problems. QDs show good emission stability, scalability, and easy integration with existing semiconductor platforms [85,89,167,168]. In addition, numerous studies of these structures solved some problems and developed techniques that allow the implementation of QD-based SPS towards applications in quantum information technologies [32,81]. In addition, QDs showed the emission of entangled pairs of photons and indistinguishable photons, also with the on-demand generation [32,81]. Moreover, the possibility of improving the extraction efficiency of QD emission based on additional photonic structures was shown [18,77,169–173]. The deterministic fabrication of QDs integrated with photonic structures was also demonstrated [169,174]. Moreover, the opportunity of obtaining emission at elevated temperatures [1,121,171,175–178] and application-ready compact SPS were also presented [179]. Furthermore, in the context of integrating QDs with the silicon platform, several approaches have already been presented [85], especially in applying solutions for on-chip computing. In addition, transferring many of the achievements for structures based on QDs emitting below 1200 nm to the telecommunications range should further increase the capabilities of dot-based structures in this range.

Both InP and GaAs systems allowed the realization of QD-based SPS in the telecom range, particularly in the third telecom window [1,6,159]. According to what was presented in the first part of Chapter 3, the InAs/InP combination allows for the direct fabrication of emitters for the telecom windows [1,81]. High-purity single-photon emission has been presented for approaches employing the QD growth in the standard SK mode [77,80,171,180–186], but also by droplet epitaxy [177,187,188]. The latter provides, by default, a significant improvement in the shape symmetry of the dots allowing for FSS reduction [189]. The formation of elongated QDs called quantum dashes (QDashes) is typically obtained using MBE-based growth [190].

However, their high areal density significantly hinders applying them as SPS. Nevertheless, single QD [71,75,191] and single-photon emission [80,175,186] has been demonstrated, even at elevated temperatures [175]. In addition, implementing a spin memory based on these nanostructures was suggested [192,193]. Applying an additional ripening process allowed for improving the QD parameters, obtaining low-density [194], almost-symmetrical QDs [23,195], for which single-photon emission [183] has been reported, also in the triggered excitation mode [185]. For the MOCVD-based growth, more symmetrical quantum dots with better surface density control have been demonstrated using an additional "double-capping" method [180,196–201], achieving high single-photon emission purity with non-resonant [196,198] and quasi-resonant excitation [77,184,200]. Moreover, the droplet epitaxy approach showed the possibility of implementing SPS using electrical excitation within the diode structure [177] and the possibility of obtaining entangled [177,202,203] and indistinguishable photons (also at elevated temperatures) [204–206], as well as quantum teleportation of qubits [203,204] and increased emission rate based on a photonic structure [207,208]. For structures grown in the SK approach, several photonic structures providing increased emission extraction efficiency have been demonstrated [77,170,171,186,198], including the deterministic control of the photonic structure position relative to the dots and showing the emission of indistinguishable photons [173].

As presented in Section 3.2, the InAs/GaAs material system requires special additional strain engineering to realize QDs emitting at telecommunication wavelengths. For both, the MBL and SRL approaches, single-photon emission in the second telecom window has been obtained [155,179,209–212], whereas for the latter several other properties (entangled photon-pairs emission, indistinguishable photons emission, on-demand generation of photons) suitable for application in quantum technologies have also been demonstrated [81,179,213,214], including also fabrication of photonic structures increasing the emission extraction efficiency [215,216]. The implementation of GaAs-based SPS in the third telecom window has been presented, but only for a system based on MBL using MOVPE technology [5,157,158], and concerns demonstration of the entangled photon-pairs emission [46,217,218], emission of the indistinguishable photons [172,219,220], or the on-demand generation of photons [218,219]. In addition, the possibility of applying advanced photonic structures has been confirmed [221], including the application of the DBR structure [5,157], all of which improve the extraction efficiency of emission [172]. The emission tuning using precise piezo-tuning and the FSS control have also been demonstrated using QD strain control [46,158]. Therefore and on the contrary, the primary goals of this PhD thesis was a comprehensive characterization of the properties of the potentially new nanomaterial system, i.e. QDs on MBL grown by MBE (as the growth conditions are then entirely different than in MOVPE), and determination of the potential of this system in developments of efficient single-photon sources in the near infrared range, with a special focus on the third telecom window.

4. EXPERIMENTAL METHODS AND THEORETICAL CALCULATION OF QDS PROPERTIES

This chapter describes the methodology used for the experimental characterization of the materials and for modeling their electronic structure. For structural characterization, atomic force microscopy (AFM), scanning electron microscopy (SEM), and scanning transmission electron microscopy (STEM) measurements (including energy dispersive spectroscopy EDX scans) were performed. For optical characterization, several complementary spectroscopic techniques were used, like modulation spectroscopy and photoluminescence, also in high spatial and spectral resolution modes, as a function of parameters like excitation power density, sample temperature, or polarization of light. In addition, photoluminescence excitation (PLE) spectroscopy, time-resolved photoluminescence (TRPL), and photon-correlation spectroscopy were also used. For the energy structure calculations, the commercial NEXTNANO software was used to gather the basic information on the optical transitions and preliminarily interpret the experimental data for the ensembles of nanostructures.

4.1. STRUCTURAL CHARACTERIZATION

The measurements of the dots' structural properties carried out in this work were first used to evaluate the QDs and MBL structure quality versus the changes in the MBL. Secondly, and perhaps more importantly, the structural characterization results were used to determine the QD morphology, in particular sizes, in-plane shape asymmetry, and the composition of the dots and surrounding layers to enable the energy structure calculations and to support the interpretation of the optical spectra. Part of these studies (SEM and AFM) was also performed for reference dots on the sample's surface, whereas STEM measurements were made for optically-active buried QDs.

Atomic force microscopy allows imaging of the sample surface and reveals its morphology, including the dots on it. In addition, it allows for analyzing structure roughness as a one of the determinants of structure quality. The intermittent contact operating mode was used in these experiments, where the cantilever oscillates close to the resonant frequency (about 200 kHz). During the position scan of the cantilever relative to the surface, the change in cantilever vibrations' amplitude and frequency due to the interaction of the sample surface with the tip allows for surface topography characterization. The cantilever position is detected using a laser reflected from its upper surface. A commercial "Level AFM" device from Anfatec Instruments AG was used, offering an in-plane step of 2 nm and a scanning resolution of 0.2 nm for the direction perpendicular to the sample plane. The device was placed on an additional vibration-damping element to reduce the impact of surrounding vibrations. Moreover, the effect of air vibrations was also suppressed using the closure of the measurement zone through glass insulation.

Scanning electron microscopy is based on scanning a beam of electrons (with a diameter below 5 nm) focused via a complex arrangement of electromagnetic lenses. Electrons are detected as a result of the interaction of primary electrons with the sample, i.e. mainly secondary (low-energy electrons generated from the sample by ionization process caused by inelastic electrons scattering) and backscattered (high-energy electrons originating from electron beam reflected from sample atoms by elastic scattering interactions). The magnification of the scanned image depends on the size of the characterized area, including the limited resolution due to the electron beam size and the area of the interaction of electrons with the sample.

The image of the sample topography is created mainly using the signal of secondary electrons with energy below 50 eV. Due to their low energy, the signal is primarily related to small penetration depths in the sample, allowing for its imaging, especially based on the number of electrons emitted from the sample's bulges and valleys. On the other hand, the signal coming from backscattered electrons gives more information about the material composition as it depends on the atomic number of the imaged atoms. Hitachi S5000 HRSEM scanning electron microscope was used for the examined structures. A source of

electrons in the form of a field emission gun was used with an accelerating voltage of around 10 keV (30 keV possible at maximum). All this allows obtaining a resolution on the level of single nanometers sufficient to image single QDs. Reference QDs on the sample's surface, i.e., without an additional capping layer, were imaged. In addition, a special sample holder used in the microscope enabled characterizing the sample edges and imaging of the sample surface but with its position rotation.

Imaging of reference (surface) QDs has limitations due to the distorted image of the QD properties because the lack of a capping layer can result in morphology different than for buried dots. Therefore, direct characterization of buried QDs (the optically-active ones examined in optical measurements) is more valuable. Then, one of the most efficient options is to use transmission electron microscopy (TEM). This technique, in high-resolution mode, allows for obtaining more accurate imaging results on the buried QDs. For transmission microscopy, the image is created based on characterizing electrons that have passed through the sample as a parallel wide beam. Due to the shorter wavelength of the electron beam associated with higher accelerating voltages and, even more crucial, better electron beam control (including its focusing), TEM allows the imaging with better resolution (of the order of 0.1 nm) compared to standard scanning electron microscopy. Implementation of this type of measurement requires special sample preparation. It is necessary to obtain very thin so-called lamellae (below 100 nm) to allow the electron beam to be transmitted. For this purpose, preparing a sample lamella with a thickness of about 50–70 nm was used employing ion beam cutting (focused ion beam (FIB) method [222]), using double-column scanning microscopes for SEM imaging with an ion beam. The lamellae were fabricated using Xe or Ga ions and platinum as the structure-securing part. Additionally, the lamella was placed in a special transmission microscope holder, using a positioned platinum deposition and the possibility of controlling the lamella position with a special manipulator. Before introducing the sample into the microscope column, additional cleaning was performed using a low-energy argon-oxygen plasma.

Standard TEM mode using a parallel electron beam primarily allows imaging of the crystallographic structure due to the possibility of observing the diffraction pattern. It is also possible to perform imaging of the sample in the scanning mode (STEM), where a focused beam of electrons on the lamella structure scans successive positions. The signal is recorded based on the intensity of the scattered electron beam signal on detectors. The electrons scattered elastically and inelastically can be distinguished. Those scattered elastically with the atomic nuclei (mostly based on Rutherford scattering) at large angles with the direction of incidence are typically used to image the structure. Depending on the charge of the nucleus, i.e., the atomic number Z, the signal intensity varies, which allows imaging of the sample material composition ($\sim Z^2$), especially in the presence of significant differences between individual atoms. To record elastically scattered electrons in the range of high angles, the High-Angle Annular Dark Field (HAADF) detector is used in the form of a ring that increases signal collection efficiency. In addition, using this detector with a small distance to the sample, the analysis of signals is simplified due to the reduced influence of the diffraction image, making the analysis much simpler based on the image resulting mainly from the sample atomic composition. The measurements were made using the STEM mode, with HAADF detection in the range of high angles (79.5–200 mrad), completed with images obtained in the bright field. This allowed obtaining a contrast based on changes in the material composition, enabling the observation of QDs surrounded by InGaAs layers with a lower indium content. The S/TEM TITAN 80-300 microscope by TFS (Thermo Fisher Scientific), equipped with an extreme field emission gun (X-FEG) electron source module allowing for high brightness, and the STEM scanning system, together with scanning and transmission detectors, were used for these measurements. An additional spherical aberrations correction system (double Cs correctors) allows for obtaining a resolution of the microscope in the STEM mode even below 0.1 nm, which is sufficient for characterizing dots with a height of single nanometers [223].

For the QD characterization, simultaneous analysis of characteristic X-ray emission was also used. The interaction of high-energy electrons from the scanning beam with electrons of sample atoms results in characteristic radiation energies for the investigated components in the sample. The used microscope was

equipped with an energy dispersion spectrometer (EDS), allowing for the measurement of the X-ray spectrum and the subsequent identification of the sample composition.

As part of the QD characterization, two systems for STEM measurements were used, showing comparable parameters due to the similar model of the electron microscope (S/TEM TITAN 80–300 microscope by TFS). One system was equipped with the EDAX detector for the EDX characterization, while the other system was equipped with the Super-X 4-detector X-ray (TFS). In the latter case, the slightly increased sensitivity allows for more accurate characterization of the atomic composition of the studied structures.

4.2. Optical characterization

4.2.1. Optical characterization of ensembles of QDs

The essential measurement allowing for the characterization of QD emission is the photoluminescence observed due to excitation with a laser beam (in the simplest case non-resonantly). Figure 4.1 shows a respective experimental setup. It consists of a cooling system with a sample mount, a part responsible for the excitation of the sample with a laser source, and a part for emission detection.

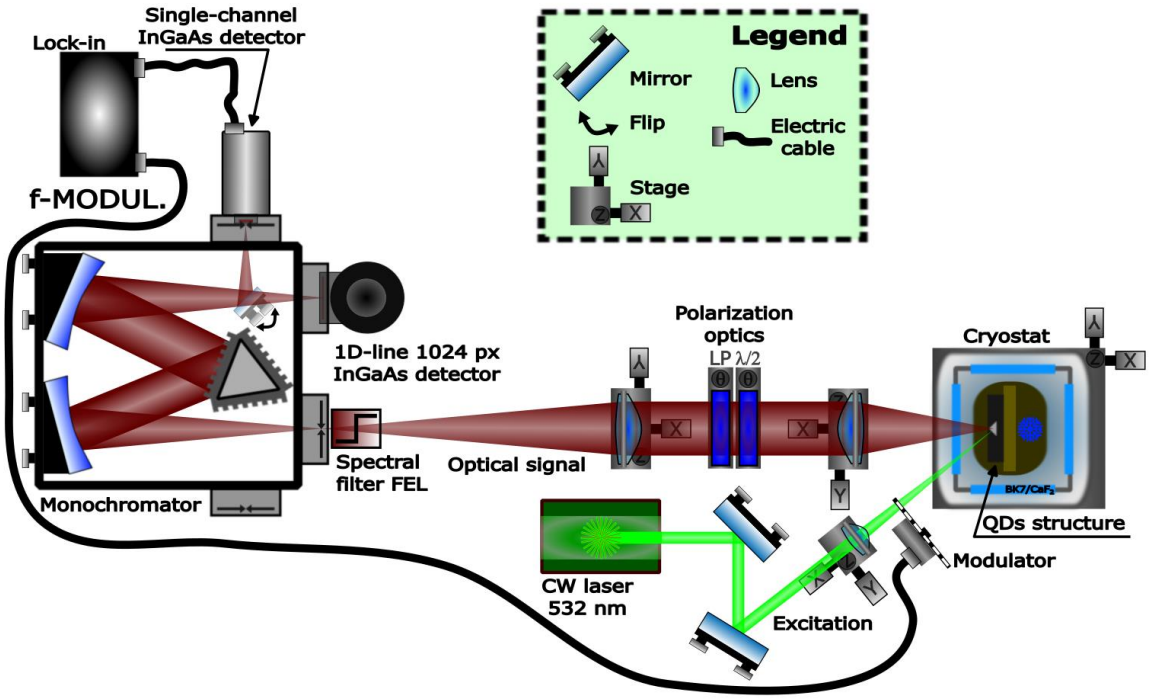

Figure 4.1. Scheme of the PL measurement system. Edge long-pass filter (for wavelength) marked as Spectral filter FEL. Laser modulation frequency (related to the excitation) directed to Lock-in marked as f-MODUL.

The investigated sample was placed in a closed-cycle helium refrigerator (thermodynamic cycle based on helium gas, Janis CCR system), giving the possibility of the sample cooling down to the temperature of about 10–12 K and temperature control in the range of 10–300 K due to the installed heater (controlled via Model 335 Cryogenic Temperature Controller from Lake Shore Cryotronics). The position of the sample in relation to the optical system was controlled using an XY stage on which a refrigerator was placed. The sample's distance from the cryostat's transmission window was relatively large (about 4 cm), which defines the focal length of the used optics. The excitation was non-resonant using typically the 532 nm line of a CW, frequency-doubled neodymium-doped yttrium aluminum garnet laser (MGL-III-532–200mW, CNI Laser, green color in Figure 4.1, about 0.2–0.5 cm diameter beam size), with a possibility to change the source (two other lasers were also available with wavelengths of 405 or 640 nm). The excitation beam was

directed off-axis through a lens (Bi-Convex 15 cm focal length, 2.54 cm diameter, uncoated N-BK7 material) and matched with the detection point on the sample (presented as the brown line in Figure 4.1). A lens collected the emission signal (Bi-Convex 10 cm focal length, 5.1 cm diameter, uncoated N-BK7 material), and then a parallel beam was directed to the detection system, where another lens (Bi-Convex 20 cm or 10 cm focal length, 5.1 cm diameter, uncoated N-BK7 material) focused it on the monochromator slit (typical width used was 0.1–0.25 mm). Then, using the reflection diffraction grating, the signal was dispersed and directed, depending on the configuration, to one of the monochromator outputs. The basic setup utilized 0.3-m focal length monochromator (Princeton Instruments Acton SP2300) equipped with grids of 150, 300 and 600 lines per mm, all with blaze at 1200 nm, i.e. well suited for measurements in the telecommunication range. For QD photoluminescence measurements, two detecting systems were used: a multi-channel, liquid-nitrogen-cooled linear array InGaAs photodetector operating in the range of 800-1600 nm (Princeton Instruments Acton OMA V InGaAs System, 1024-element, ~173 K operating temperature), and single-channel thermoelectrically-cooled InGaAs PIN photodiodes with preamplifier ensuring measurements in the range of 800–2600 nm.[3] For measurements with single-channel detectors, there was used a phase-sensitive detection with a lock-in amplifier (Stanford Research System, SR830 DSP Dual Phase Lock-In Amplifier) and additional mechanical modulation of the excitation laser beam (marked as f-MODUL in Figure 4.1) with modulation frequency $f \sim 270$ Hz, similar for all measurements. For polarization-resolved measurements, a half-wave plate (AHWP10M-1600 Thorlabs, 1100–2000 nm, marked as $\lambda/2$) and a linear polarizer (LPNIR100-MP2 Thorlabs, 650–2000 nm, marked as LP) were additionally used in the detection part of the setup, enabling transmitting selected linear polarization to the detection system, where the angle of the half-waveplate allowed for selection of certain linear polarization and to be independent of the polarization characteristics of the monochromator. In addition, a long-pass edge filter (e.g., FEL800 Thorlabs with cut-on wavelength: 800 nm, marked as FEL) was placed in front of the monochromator slit, allowing the observation of the PL signal and blocking the scattered light from the laser.

In addition, the PLE measurements were also carried out and allowed to investigate the higher-energy states via detecting an absorption-like spectrum. It also probed the occurring carrier transfers, i.e., characterized the emission signal (here set at the QD ground state transition) as a function of the variable photon energy of the excitation beam. For the excitation, a tunable pulsed titanium-sapphire laser (Mira-HP-P Coherent, additional Verdi G12 laser as pump laser) with a repetition of 76 MHz and a laser pulse width of about 2 ps, with the possibility of tuning in the range of 700–1000 nm, was used. In addition, it was possible to also tune the wavelength in the range of 980-1600 nm by employing a widely tunable optical parametric oscillator (Mira-OPO Coherent with crystals PP775 980–1350 nm or PP830 1100–1600 nm) - see the red-shaded area in Figure 4.2 showing the tunable sources. A set of variable filters was used in front of the monochromator (e.g., FELH1000 Thorlabs with cut-on wavelength: 1000 nm) to reduce the impact of the laser excitation signal on the detection part, ensuring that only the optical signal was passed through.

A modified detection system was used for time-resolved measurements. A streak camera (configuration 1 in Figure 4.2) or a superconducting NbN nanowire detector (configuration 2 in Figure 4.2) in the mode of single-photon counting (superconducting single-photon detector, marked as SSPD) were available in this setup. The operation of the streak camera (Hamamatsu C11293 model) is based on converting the time dependence of emission intensity into spatial dependence in analogy to images obtained in an oscilloscope. In addition, it simultaneously captures the time dependence of intensity in a certain spectral range (thanks

[3] Hamamatsu C12483-250 model: 800–1600 nm, typical photosensitivity 5×10^7[V/W], detectivity 6.7×10^{13}[cmHz$^{1/2}$/W], noise equivalent power (NEP) 7×10^{-14} [W/Hz$^{1/2}$], C12485-210 model: 800–2050 nm, typical photosensitivity 1.8×10^8[V/W], detectivity 2×10^{12}[cmHz$^{1/2}$/W], NEP 1×10^{-13} [W/Hz$^{1/2}$], G6122-03 model: 800-2560 nm, typical photosensitivity 1.5×10^8[V/W], detectivity 4.5×10^{11}[cmHz$^{1/2}$/W], NEP 6×10^{-13} [W/Hz$^{1/2}$].

to the used linear array of photocathodes). The optical signal is transformed into electrons, which propagate within the generated electric photocathode's field controlled by the electrodes. They deviate from the straight line of propagation in the electric field. The longer the time distance from the excitation reference signal, the greater the deviation. Finally, they are recorded by a calibrated two-dimensional camera (Digital CCD camera ORCA-ER Hamamatsu) that allows for determining emission intensity time dependence. The used semiconductor photocathode (liquid-nitrogen-cooled InP/InGaAs) allows recording the signal in the range of 1000–1650 nm, with the time resolution below 50 ps, allowing to keep the time resolution of the whole system below 100 ps.

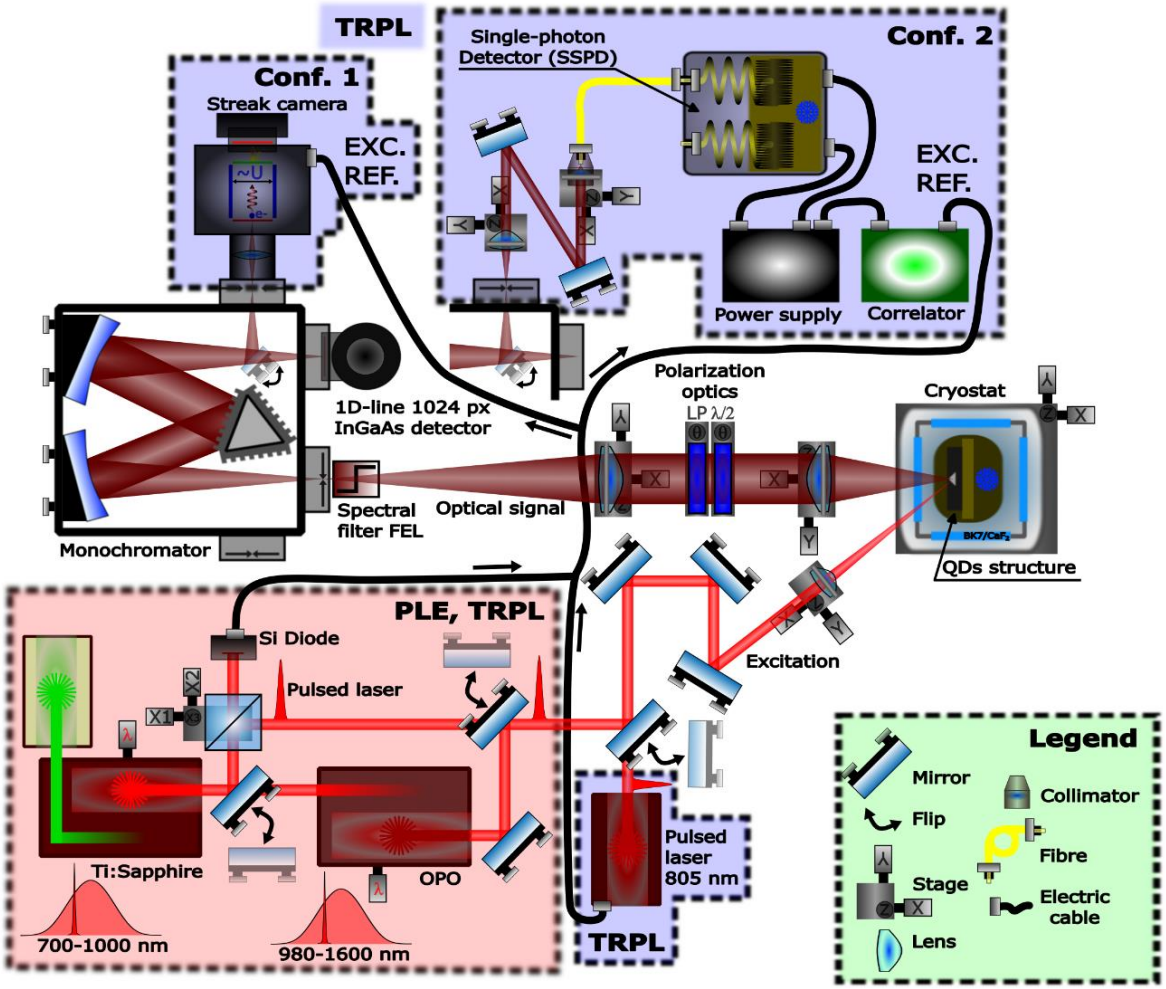

Figure 4.2. Scheme of the system for PL measurements extended by additional elements for PLE (tunable lasers) and TRPL (pulse lasers and time-resolved detectors) measurements. Detection of PL time dependencies using a streak camera (marked as Conf. 1) or superconducting single-photon detectors (marked as Conf. 2). The reference signal of pulsed laser excitation (from the reference diode or directly from the laser power supply) directed to the electronics supporting the TRPL measurement, marked as EXC. REF. Edge long-pass filter (for wavelength) marked as Spectral filter FEL.

For single-channel measurements,[4] the signal is recorded as voltage signal due to the modification of the current in the nanowires resulting from the photon absorption. The used detectors were characterized

[4] NbN nanowire, SSPD Scontel, system efficiency >50%, low-dark counts ~100 counts/s, dead time <20 ns, jitter time <50 ps, closed-cycle helium refrigerator, low-temperature ~1.8 K.

by high detection efficiency in a wide spectral range, covering the second and third telecom windows, with a time resolution of down to 50 ps, enabling the overall resolution of the system below 100 ps. The optical signal was supplied to the detectors using single-mode fibers. Therefore, after the monochromator, the signal was coupled to a single-mode fiber (SMF-28 Ultra, Thorlabs, NA = 0.14, 1260–1625 nm) using a collimator (CFC11P-C Thorlabs, adjustable 11-mm-focal-length, NA = 0.35, C-coated 1050–1620 nm), lens collecting signal from monochromator (AC254-050-C Achromatic Doublets Thorlabs, 5 cm focal length, 2.54 cm diameter, C-coated N-LAK22/N-SF6 material) and two mirrors. The measurement system was completed by a pulsed lasers: Ti-Sapphire as described above or 805 nm semiconductor pulsed diode laser with the possibility of tuning the repetition rate in the range of 2.5–80 MHz for 50 ps-long pulses (LDH-D-C-810 PicoQuant). The electrical triggering signal (EXC. REF. in Figure 4.2) coming from the laser was used to obtain a reference for the emission signal time recording (signal directly from the laser power supply or from the silicon measuring diode (TDA 200 PicoQuant or C1808-03 PIN Diode Head Trigger Hamamatsu). The time difference between the excitation laser pulse and the act of detecting a single-photon was measured using a correlator (PicoHarp 300 PicoQuant, count rate up to 10^7 counts/s, 65536 histogram time bins, 4 ps resolution, adjustable built-in electric input delay).

In addition, the measurements of photomodulated reflectivity (photoreflectance, PR) were used to detect all possible optical transitions in the entire structure. This method is based on detecting relative changes in sample reflectivity due to its electric field modulation made with a high-energy laser beam (excitation energy above the band gap of the GaAs material). The photo-generated carriers (electron-hole pairs) are becoming separated by the built-in electric fields (usually at the surface or interfaces), which change the internal distribution of the electric field, thus resulting in its modulation. Changing the electric field in the structure leads to small changes in the reflectivity coefficient (ΔR). These, in turn, are related to the changes in the dielectric function (complex permittivity) in the following way (described in numerous review works more in detail: [224–227]):

$$\frac{\Delta R}{R} = \alpha(\varepsilon_1, \varepsilon_2)\Delta\varepsilon_1 + \beta(\varepsilon_1, \varepsilon_2)\Delta\varepsilon_2, \tag{4.1}$$

where, α and β are the so called Seraphin coefficients, $\Delta\varepsilon_1$ and $\Delta\varepsilon_2$ are the modulation-induced changes of real and imaginary parts of the dielectric function, respectively. Electromodulation based on photo-generated carriers leads to a disturbance of the translational symmetry of the material, resulting in the acceleration of unbound carriers, leading to the PR line shapes resembling the third derivative of the unperturbed dielectric function (the so called low electric field limit) and being in fact an approximation of Franz-Keldysh effect for very small fields [228,229]. In this range and the presence of unbound free carriers as in bulk-like materials and assuming the Lorentzian broadening of the lines, the relative changes in reflectivity can be expressed in a simple analytical form which can be used to fit the experimental spectra and derive the transition energy, linewidth and intensity (for Gaussian broadening the line shape is much more complicated and numerical approximations are necessary for fitting) [230]:

$$\frac{\Delta R}{R}(E) = \mathrm{Re}\left[Ae^{i\varphi}\left(E - E_\mathrm{g} + i\Gamma\right)^{-m}\right], \tag{4.2}$$

where A is the signal amplitude, Γ is the spectral broadening, φ is a factor describing the phase, and m is a factor depending on the type of critical point in the Brillouin zone [230]. For slightly larger electric fields (the so called intermediate-field regime) the Franz-Keldysh oscillation (FKO) will appear on the high energy side (for $E > E_\mathrm{g}$), i.e. as above the absorption edge for a semiconductor in electric field. The period of these oscillations, when plotted in a proper scale, can be used to estimate the built-in electric fields [231–233]. On the contrary, for confined states (e.g., excitons in low-dimensional structures), the electric field modulation causes the quantum confined Stark effect resulting in PR line shapes in the form of the first derivative of

the dielectric function [234]. However, it has been shown that it can be well approximated by line shape as in Eq. (4.2), but with just different m parameter.

The modulation-induced changes in reflectivity around the critical points (optical transitions) are usually very weak ($\Delta R/R$ on the level of 10^{-7}–10^{-5}). However, in modulation spectroscopy when the spectra have a derivative-like character the response can be extracted from the background making the method very sensitive to even low-intensity transitions. For approximate determination of the energy and broadening of the optical transition from the modulation spectra one can use a simple three-point method [230], taking into account only the coordinates of the two main maxima $[E_1, (\Delta R/R)_1]$ and $[E_2, (\Delta R/R)_2]$- see Figure 4.3. Based on that the resonance energy is determined from the equation:

$$E_g = E_1 + (E_2 - E_1)\, f\left(\left|\frac{(\Delta R/R)_2}{(\Delta R/R)_1}\right|\right), \tag{4.3}$$

whereas the broadening from:

$$\Gamma = (E_2 - E_1)\, g\left(\left|\frac{(\Delta R/R)_2}{(\Delta R/R)_1}\right|\right), \tag{4.4}$$

where the functions f and g are related to the symmetry of the resonance shape determined based on the relationships presented in Ref. [230], where the influence of the type of critical point was also taken into account (see Figures 4.3B and C). In cases close to symmetrical resonance, $(\Delta R/R)_2 \approx (\Delta R/R)_1$, $f \approx 0.5$ and $g \approx 1.0$ can be obtained, allowing to basically read the transition parameters directly from the spectra.

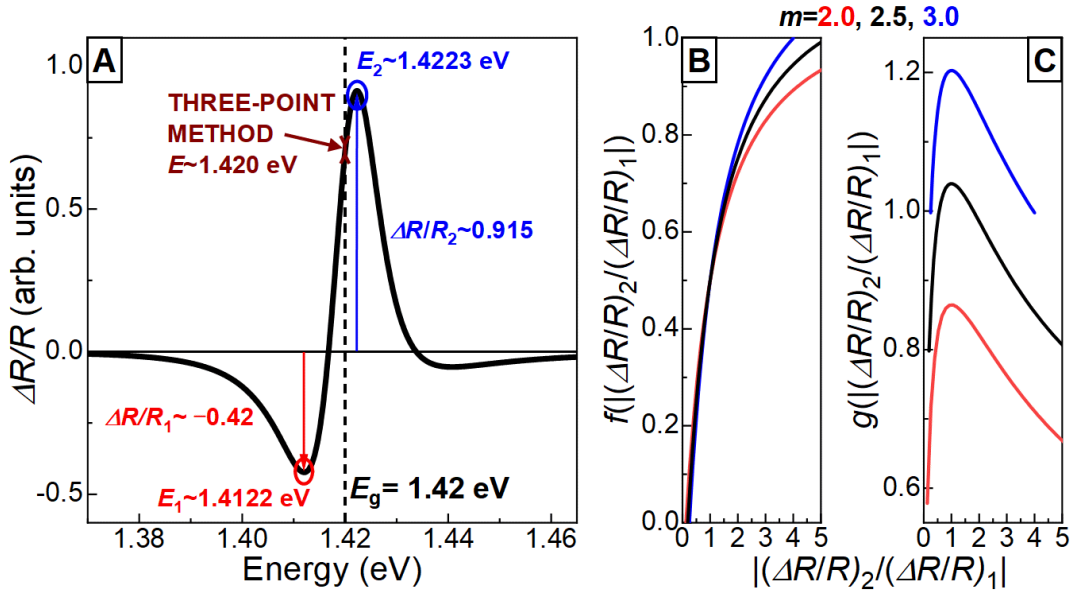

Figure 4.3. (A) The schematic resonance shape of PR signal with the third derivative line shape (solid black line; based on equation 4.2) for GaAs material energy gap at room temperature (dashed black line). The determination of the resonance energy based on the three-point method is marked with arrows. Graph of functions (B) f and (C) g depending on the value of the PR signal for the extremes [230].

A scheme of a setup for photoreflectance measurements is shown in Figure 4.4. The photomodulation with frequency $f \sim 270$ Hz was provided by a 532 nm line of a CW laser (frequency-doubled Nd-YAG MGL-III-532–200mW), directed to the sample off-axis to reduce the scattered laser light reaching the detection system. The measurement is based primarily of recording the reflection spectrum. Therefore, the sample was illuminated with spectrally broad radiation from a tungsten halogen lamp, which, after being reflected from the sample, was directed to a monochromator through a lens (Bi-Convex 5 cm focal length, 5.1 cm diameter, uncoated N-BK7 material) focusing the signal on the monochromator slit. The diameter

of the beam on the sample surface was about 2–5 mm in diameter. The size of the modulated laser beam was adjusted to the size of the white light spot on the sample surface and to match their positions spatially. A monochromator with a focal length of 0.3 m was used (Princeton Instruments Acton SP2300) with a reflection diffraction grating with 300 lines per mm (blaze wavelength: 2000 nm) or 150 lines/mm (blaze at 800 nm). The size of the slits and the related resolution of the measurements were not critically important due to rather large broadening of the observed spectral features being always significantly larger than 1 nm. Two detectors could be used. First, characterized by higher quantum efficiency, consisted of single-channel thermoelectrically-cooled InGaAs detectors, ensuring the possibility of measurement in the range of 800–1600 nm.[5] Second was a model with an extended detection range in the range of 800–2600 nm but with reduced detectivity.[6] The entire measurement was carried out using phase-sensitive detection with a lock-in amplifier synchronized by the laser modulation frequency (similar to the system for PL measurements described above). In front of the monochromator, a long-pass filter for wavelengths above 800 nm was used to cut off any residual light from the modulating laser (e.g., FEL800 Thorlabs with cut-on wavelength: 800 nm). The simultaneous recording of an AC signal (voltage) proportional to the modulation-induced changes in the reflectivity (ΔR), and a DC signal proportional to the reflectivity (R) allowed the determination of the photoreflectance spectrum ($\Delta R/R$).

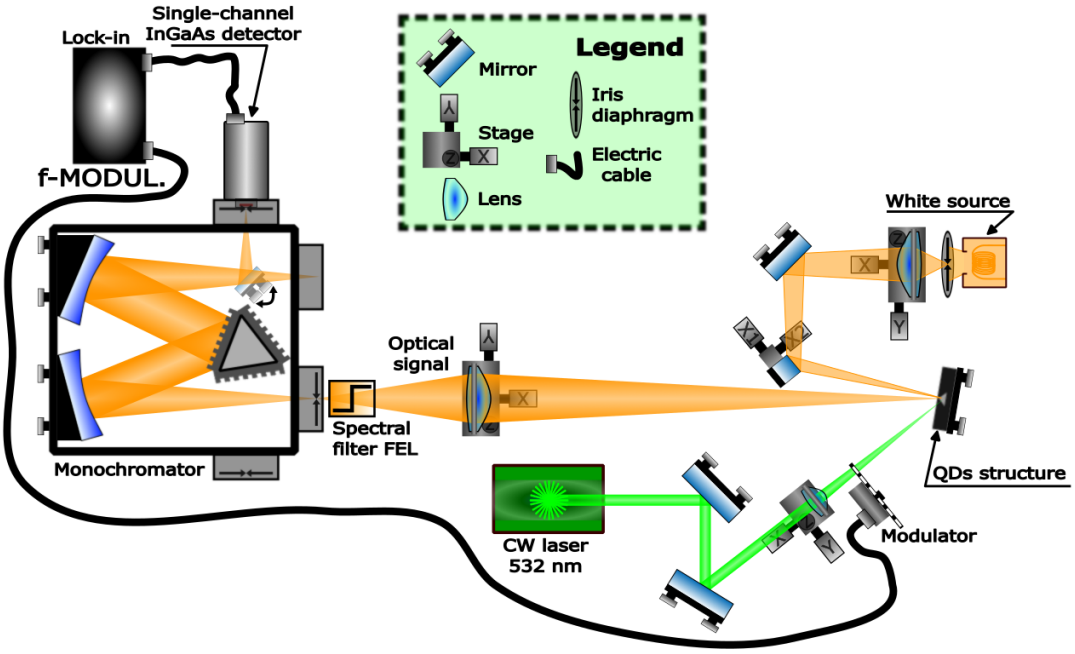

Figure 4.4. Scheme of the setup for PR measurements. Edge long-pass filter (for wavelength) marked as Spectral filter FEL. Laser modulation frequency (related to reflectivity modulation) is directed to lock-in marked as f-MODUL.

4.2.2. Optical characterization of single QDs

The optical characterization of single QD properties was performed using a high-resolution microphotoluminescence (μPL) setup – see Figure 4.5. The sample was placed in a continuous-flow liquid-helium cryostat (ST-500 JANIS), providing an operating temperature of about 5 K, with control up to 300

[5] Hamamatsu C12483-250 model: 800–1600 nm, typical photosensitivity $5 \times 10^7 [\mathrm{V/W}]$, detectivity $6.7 \times 10^{13} [\mathrm{cmHz^{1/2}/W}]$, NEP 7×10^{-14} $[\mathrm{W/Hz^{1/2}}]$

[6] Hamamatsu G6122-03 model: 800–2560 nm, typical photosensitivity $1.5 \times 10^8 [\mathrm{V/W}]$, detectivity $4.5 \times 10^{11} [\mathrm{cmHz^{1/2}/W}]$, NEP 6×10^{-13} $[\mathrm{W/Hz^{1/2}}]$

K due to the installed heater (Cryogenic Temperature Controller Model 335 from Lake Shore Cryotronics). The use of a microscopy-type cryostat with an optical window at a distance of ~10 mm from the sample allowed using a microscope objective with a sufficiently large working distance and still high numerical aperture (20x Mitutoyo Plan Apo NIR Infinity Corrected Objective, numerical aperture NA = 0.4, working distance 20 mm). Such approach, where both excitation and collection of photoluminescence are realized through the same objective, allowed obtaining a laser spot size of about 2 μm in diameter on the sample surface, limited mostly by the diffraction and hence depending on the exact excitation wavelength used. The laser was introduced to the main optical path using a 50:50 beam splitter optimized for the 1100–1600 nm range (Non-polarizing Cube Beamsplitter BS015 Thorlabs, 2.56 cm size, C-coated 1100–1600 nm N-BK7).

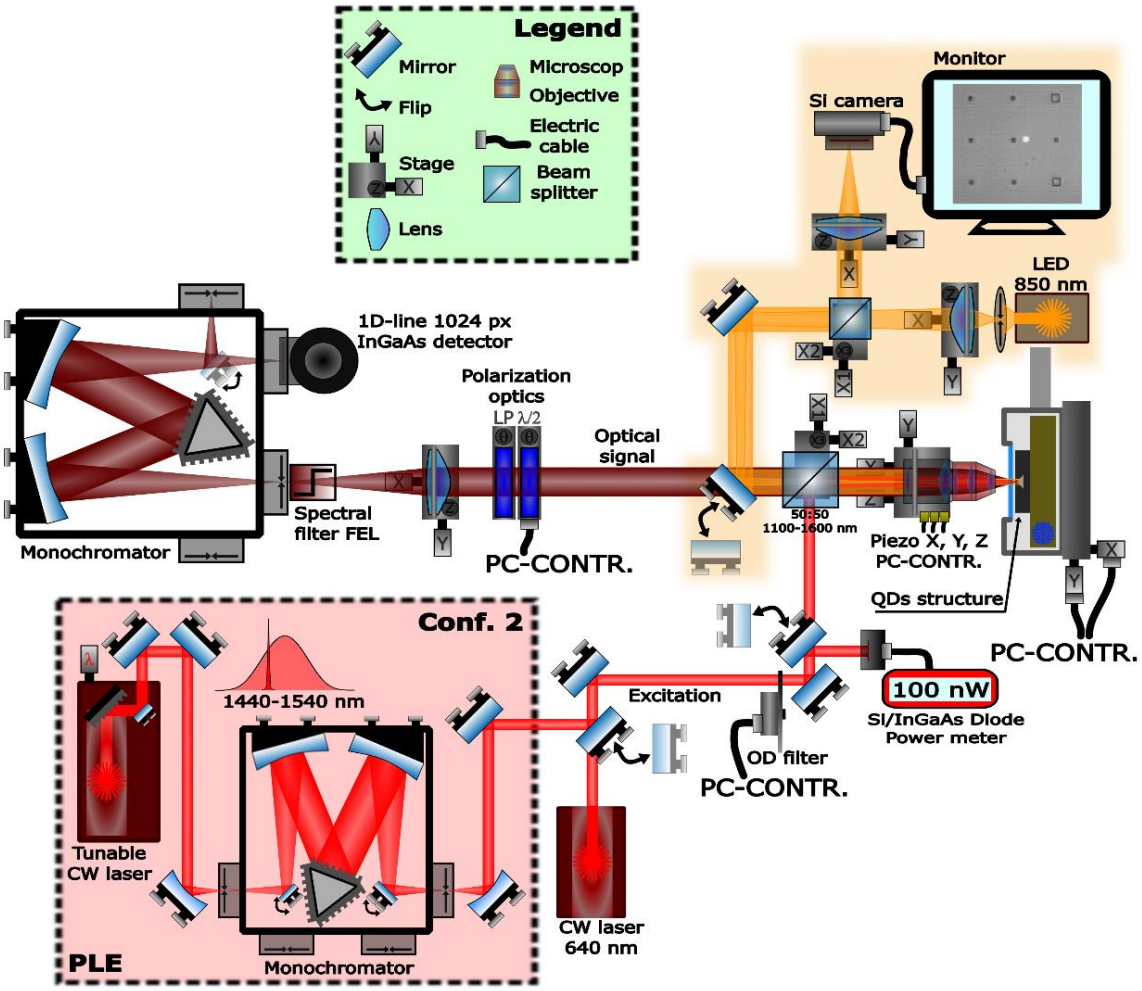

Figure 4.5. Scheme of the μPL setup, extended by additional elements for μPLE measurements (tunable laser, marked by the red box). Remote control of gradient neutral density filter (OD filter), half-wave plate ($\lambda/2$) angle, microscope objective position and cryostat position (marked as PC-CONTR.). Edge long-pass filter (for wavelength) marked as Spectral filter FEL.

An imaging system was used to view the sample surface and control the position of the focused laser spot. For the imaging, illumination from an infrared diode (Collimated LED Light Source M850L3, wavelength ~ 850 nm, power ~ 1 W) was directed using a folding mirror towards the sample. The returning image of the structure, collected by the objective, was guided to an additional beam splitter and partially directed to the imaging CCD camera (WAT-902B Watec). The detection system for μPL measurements was usually a high-resolution monochromator with a 1-m focal length (FHR1000 HORIBA Scientific), with two reflection diffraction gratings of 150 lines/mm (blaze at 1200 nm) and 600 lines/mm (blaze at 1500 nm),

providing a high-spectral resolution of at least 100 μeV (150 lines/mm) or 25 μeV (600 lines/mm). A multi-channel InGaAs linear detector was used for signal detection (Symphony II InGaAs, 1024-element, liquid-nitrogen cooling, operating temperature ~ 170 K, 800–1600 nm, pixel size 25 μm). For polarization-resolved measurements, a pair of the half-wave plate and a linear polarizer with an additional motorized rotation handle system (CONEX-PR50CC Newport) controlled by a computer were used in the detection part of the setup. As the primary excitation source, a 640 nm line from a CW laser was used (CUBE 640 nm 40 mW Laser System Coherent), with the ability to control the its power by a gradient neutral density filter (NDHN-100, OptoSigma) on a motorized rotation mount (OSMS-40YAW, OptoSigma), plus a calibrated Si photodiode (S120C Thorlabs: Si 400–1100 nm, power range 50 nW–50 mW or S122C Thorlabs: Ge 700–1800 nm, power range 50 nW–40 mW with Power Meter PM100D Thorlabs) that allows modification of the excitation power in a feedback loop. A motorized stage (2-axis of TravelMax Translation Stage LNR502E, 50 mm travel range, step resolution > 100 nm) placed under the cryostat provided the ability to move the sample relative to the optical system, allowing controlling the probed sample area. More precise control of the position of the excitation laser on the sample was carried out using a piezo stage controlling the position of the microscope objective with 4 mm mechanical travel range and 20 μm piezo travel range with 200 nm step (3-Axis NanoMax MAX312D Thorlabs).

The PLE characterization of single QDs was carried out using a CW laser tunable in the 1440–1540 nm range (External Cavity Diode Laser DL PRO Toptica, Littrow setup, power ~ 50 mW), as shown in configuration 2 in Figure 4.5. A special laser line filtering system, employing an additional 0.3-m-focal-length monochromator (similar to that described in Subsection 4.2.1), was also used. For time-resolved photoluminescence measurements, an 805 nm semiconductor diode laser (the same as described in Subsection 4.2.1) was used with the ability to adjust repetitions in the range of 2.5–80 MHz together with approximately 50 ps-long pulses, as presented in Figure 4.6.

As part of the time-resolved measurements, the detection system based on SSPDs was used (the same as described in Subsection 4.2.1). For correlation and photon-statistics measurements, the HBT configuration (as described in Section 2.5 and shown in Figure 2.5B) was used in the time-correlated single-photon counting mode, where the signal was additionally divided by a 50:50 beam splitter (BS015 Thorlabs, C-coated 1100–1600 nm) into two detection systems both based on 0.32-m-focal-length monochromators (iHR320 Horiba, reflection diffraction grating: 600 lines/mm and 1500 nm blaze wavelength. Time correlation of the photon occurrence on two superconducting detectors of the two detection arms was used to characterize coincidences versus the delay time, using a correlator (the same as described in Subsection 4.2.1), where one signal was used as initiating and the other as stopping the counting. In addition, a relative delay was also introduced electronically by a built-in delay line for one of the paths to obtain a negative delay range. The monochromators worked as spectral filters for the presented system to select the investigated emission lines (different or the same for cross- or autocorrelation measurements, respectively).

The correlation measurement allows determining the time statistics of the registered photon coincidences on two detectors by determining the delay between the indicated acts. Multiple measurements of photon pair detection acts allow the construction of a histogram that can be used to determine the second-order correlation function. However, due to the limited emission intensity in the single-dot regime (10^3–10^4 per second, depending on the excitation power and the specific QD, as well as the filtering spectral width with the use of a monochromator), it is necessary to conduct measurements for more than 2 hours. An additional limitation is the time resolution of the measurement, where the selection of the time width of the counting channel also affects the speed (and time) of building up a histogram.

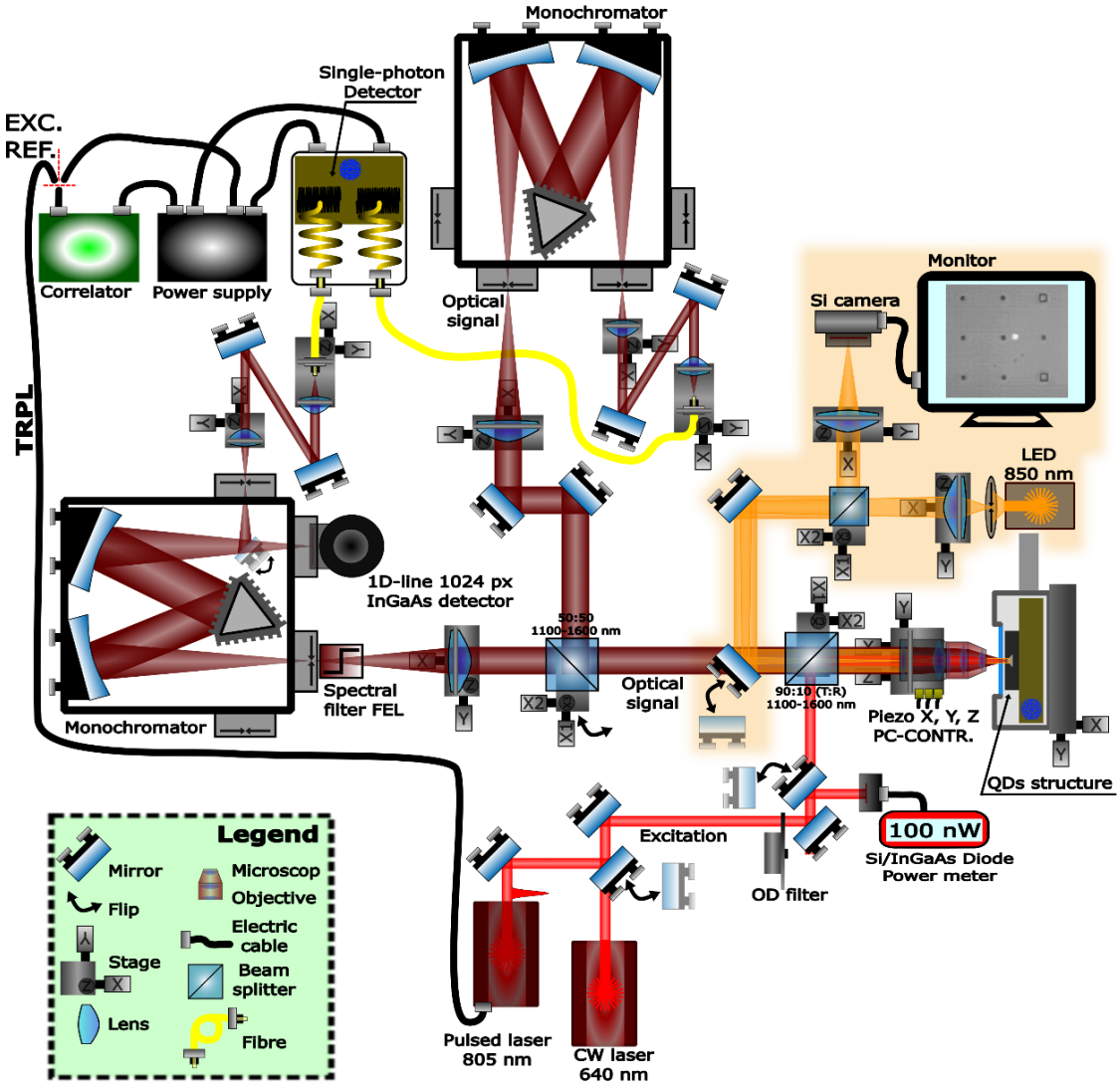

Figure 4.6. Scheme of the μPL system with a pulsed excitation laser and single-photon detectors for TRPL measurements. Extension based on the second detection system (HBT configuration, second system marked by the blue area) for correlation measurements. Edge long-pass filter (for wavelength) marked as Spectral filter FEL. The reference signal of pulsed laser excitation (from the laser power supply) is directed to the electronics supporting the TRPL measurement, marked as EXC. REF.

4.3. THEORETICAL CALCULATIONS OF QD ENERGY STRUCTURE

Numerical calculations of the energy structure of the investigated QDs were performed using the NEXTNANO (nextnano++) commercial solver [235], allowing modeling the electronic structure of various low-dimensional systems using the solution of Schrödinger equation, including the possibility to take into account the carrier density [236]. The indicated solver allows performing the calculations within the 8-band $k \cdot p$ model within envelope function approximation [236]. The calculations work along the following stages: determination of strain, finding of conduction and valence band edges using material parameters and including strain, calculation of the electrostatic potential (due to piezoelectricity) using the Poisson equation, and ends with the calculation of confined eigenstates within the obtained confinement potential based on the 8-band $k \cdot p$ theory [237]. Further, the solver also allows determining the optical properties like the optical transition energies or their intensities (oscillator strengths) [238].

For lattice-mismatched materials, existence of elastic deformations of the crystal requires to use of the Bir-Pikus Hamiltonian [239], whereas the strain tensor is determined within the linear continuum elasticity theory [236] via numerical minimization of the elastic energy [238]. The creation of piezoelectric charges due to shear strain in a piezoelectric material is also taken into account. Based on the Poisson equation, the resultant electrostatic potential is determined and included in further calculations of the eigenstates [237].

Calculations of confined states within the determined potential are carried out by diagonalizing the 8-band Hamiltonian evaluated on a discreet grid of points, which enables obtaining single-particle eigenstates for both electrons and holes [238]. The 8-band model includes the lowest conduction band and three highest valence subbands (heavy-holes, light-holes, and spin-orbit split-off band). The rest of the bands are included via perturbative corrections.

The standard nextnano++ database of material parameters was used in QD calculations for GaAs, InGaAs, and InAs. The code uses the ARPACK solver for matrix diagonalization [237]. The calculations were carried out for the assumed quantum dot model (shape, size, and composition), including the respective barrier materials.

5. QD EMISSION REDSHIFT VIA GROWTH ON METAMORPHIC BUFFER LAYERS

The self-assembled epitaxial growth of quantum dots exploits the lattice mismatch between the crystal of a substrate and the material delivered to the sample, where the occurring strain leads to the self-organization of the deposited material in the form of 3D islands forming QDs. The standard SK mode leads to a relatively narrow but still noticeable distribution of QD parameters. The strain during growth is a crucial factor that controls the QD morphology. The QD size and shape, in turn, affect the energy structure of the confined states and hence the optical transitions and the emission energy/wavelength. For InAs QDs grown on a GaAs substrate, the growth of an additional MBL on the substrate can be used to reduce the strain and shift emission to the infrared, up to the telecom range.

This chapter describes properties of InAs QDs grown on (001) GaAs in which the emission energy shift is tailored by modifications in composition of MBL affecting the QD parameters. Section 5.1 presents a scheme of the investigated structures with a description of the approach to develop the MBL and results of calculations presenting the impact of MBL composition on the QD emission energy. Sections 5.2–5.4 present three generations of structures realizing different QD emission shifts while indicating the limitations of implementing the MBL. General characterization by PL and PR measurements, confronted with structural data, is presented as a method to determine QD optical parameters and structural quality. Section 5.5 describes the QD structural characterization (results of AFM, SEM, and STEM studies), mainly aimed at determining parameters responsible for modifying the emission energy. The last Section 5.6 summarizes the results of calculations of the optical transitions with input parameters taken from the structural data. Basic calculations are performed using the commercial NEXTNANO software. In addition, results of more advanced calculations taking into account the excitonic effects and made by Dr. Michał Gawełczyk are included to complete the whole numerical simulations and give more detailed insight into the electronic structure properties.

5.1. INVESTIGATED STRUCTURES

Standard growth directly on a GaAs produces rather small In-rich QDs emitting around 1000 nm usually. Exemplary calculation results of the fundamental optical transition energy (using NEXTNANO, described in Section 4.3) are shown in Figure 5.1A for a symmetric lens-shaped QD based on GaAs substrate or on MBL, with an aspect ratio between height and diameter (H/D) equal 1/5 (height in the range of 2.5–7.0 nm), QD indium contents of 60% and 80% (parameters based on Ref. [240,241]). The critical factor shifting the emission energy to shorter wavelengths is the strain, therefore, its reduction is crucial in obtaining QDs emitting in the telecom range. This is possible by using an InGaAs MBL causing a decrease of the lattice constants between MBL and the QD material. In this work, such an MBL is used as a matrix for the QD growth, allowing strain reduction and modification of the emission energy. Adjusting MBL indium content allows for reaching the telecom range. Figure 5.1A shows the calculated emission energy shift for an InAs QD tuned by modifying the MBL composition. In addition to the MBL modification, changes in QD height and QD indium content are also considered, which may also occur due to the change in the mismatch of the materials and possible composition intermixing during the growth. It is clearly seen that achieving emission in the third telecom window is possible. Modifying the growth kinetics relative to the standard InAs/GaAs growth can change the QD geometry. Figures 5.1B and C show that the modifying QD parameters, such as the H/D ratio (aspect ratio, AR) and the ratio of the size in [1-10] and [110] directions (lateral aspect ratio, LAR), can also shift the QD emission energy. When changing the LAR, the energy shift of the emission below 50 meV is predicted. However, the certain LAR values can influence other crucial optical properties like polarization of emission or exciton FSS (see results in further chapters). Considering strain modification via MBL, structural characterization is essential to understand the actual reasons for the

emission shift. On the other hand, obtaining an MBL with good structural quality without many defects is crucial. Growing an InGaAs MBL with 40% indium directly on GaAs would be impossible due to too large lattice constants mismatch of ~2.7%. Thus, MBLs with composition gradients are used to maintain good quality and reduce strain simultaneously.

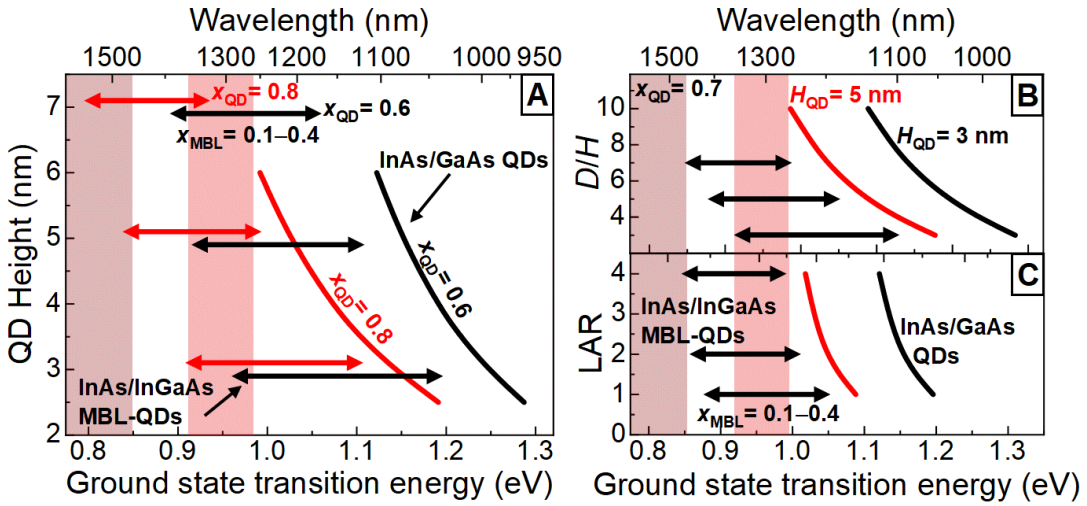

Figure 5.1. (A) Calculated ground-state exciton energy for symmetric QDs (LAR = 1.0) with different heights and indium contents (60 or 80%) for standard InAs/GaAs strained structures (lines) and structures with MBL layer for different indium contents in the range of 10-40% (horizontal arrows represent the obtained range of energies). (B) Emission energy of QDs with 70% indium content and different H/D ratios for InAs/GaAs QDs (H = 3 nm or 5 nm) and QDs grown on MBL (H = 5 nm). (C) Emission energy of MBL-based (H = 5 nm) and InAs/GaAs (H = 3 nm or 5 nm) QDs with 70% indium content and varying shape asymmetry, i.e., LAR with respect to the [1-10] direction.

The investigated structures were grown by MBE using solid elemental sources in the Eiko reactor.[7] The layer structure scheme is shown in Figure 5.2. The growth procedure starts with purifying the GaAs (001) substrate. Then an epitaxial GaAs buffer layer is deposited, allowing for obtaining a high-quality starting layer for subsequent growth. Further, the gradient MBL structure with increasing indium content is grown using a digitally alloyed approach [242]. The indium content is controlled based on the percentage composition of sublayers in the period (driven by their thickness), which includes the base layers (A) and the additional layer (B) (see the period in Figure 5.2). The average composition should be established at the intended level within an entire period due to the possible intermixing of components, where control of the relative thicknesses of individual layers (correlated A and B forming one period) allows composition modification for the entire period. Gradual modification of the thickness (the only parameter that changes) of layer A from a value equal to half the period correlated to the increase in the thickness of layer B (introducing higher indium content) allows controlling the average indium content within the period. For the studied structures, the section thickness of 30 nm was designed for a series of successive identical periods characterized by the same composition to obtain good structural quality and stress reduction between the successive increases in the indium composition by 1 percentage point. The thickness of the periods and their number within the indicated 30 nm are directly interrelated and, as presented later, will be crucial for the quality of the structure and the possibility of QD growth at higher indium content in the MBL. Depending on the period type used (differences in the material composition: GaAs, InAs, InGaAs, and thickness for layers A and B) and the aimed MBL composition, the thicknesses of the layers/periods can be in the range from single nanometers down to a submonolayer.

[7] Performed by Piotr Wroński at the University of Würzburg, led by Prof. Sven Höfling

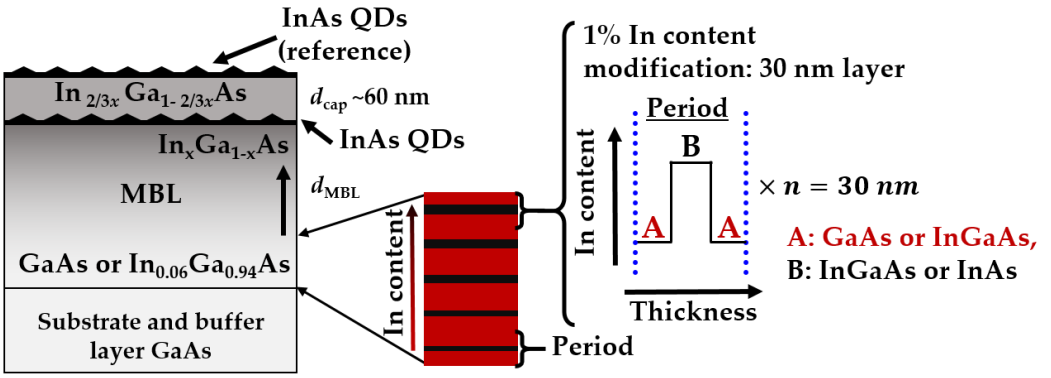

Figure 5.2. Scheme of the structure containing a gradient MBL based on changes in the thickness of individual layers that create the period, controlling the indium content. The different composition of the A and B layers corresponds to the modification of the period composition during the growth or difference for each generation of periods.

Three main series of samples were grown, for which the diagrams of the three types of periods are shown in Figure 5.3. The introduced modifications aimed, in the first place, at improving the structural and optical quality of the samples, and secondly, to extend the emission wavelength tunability.

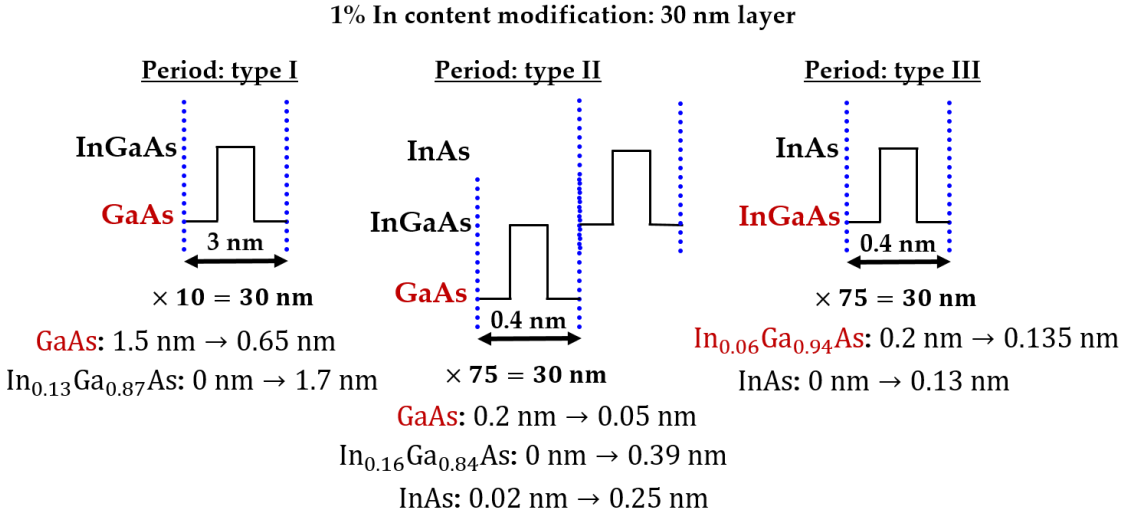

Figure 5.3. Schemes of compositions and material of the periods forming the metamorphic layer for the three types of periods with a detailed range of thicknesses of individual layers forming the period. For period type II, there is an additional modification of the composition of layers A and B above a certain MBL indium content (marked as an additional period).

The main factor limiting the QD emission redshift turned out to be the MBL indium content, where the possible processes of indium aggregation and desorption may hinder the control of the parameters of this layer. The base material was changed for subsequent generations of structures (detailed information in the following Sections). GaAs or calibrated InGaAs material (optimized parameters for direct growth of InGaAs layer with specific indium content) growth was used for a specific composition. In contrast, for the additional layer responsible for indium control, InGaAs or InAs calibrated material was used. Moreover, for the second generation of structures, the period of the GaAs/InGaAs was changed to InGaAs/InAs during MBL growth above 17% indium content in the period (marked as an additional period in Figure 5.3). During the MBL growth, the substrate temperature was varied to minimize problems with indium segregation and its incorporation into MBL. The MBL thickness was related to the final indium content at the top, keeping a constant indium composition change rate of 1 percent per 30 nm. 1.5 monolayers (ML) of InAs were

deposited on the MBL to form self-assembled QDs. Then, they were covered with about 60 nm InGaAs capping layer with indium content of about 2/3 of that at the top of MBL. The calculation shows no significant changes (emission shift below 30 meV) in ground energy transition with modified indium composition in the capping layer relative to MBL. Finally, an analogous layer of InAs was deposited on the layer covering the dots to create optically inactive reference QDs and enable their structural studies.

For optical characterization of single QDs, additional processing of the sample surface was performed for selected structures to reduce the number of probed QDs and to achieve repeatability of measurements for selected QDs. The studied area was limited using circular mesa structures or apertures in the form of holes in a thin silver layer deposited on the structure's surface. The mesas were fabricated by using electron beam lithography and chemical (wet) etching with liquid acid solutions. In contrast, using apertures allowed limiting the additional processing to only lithography while obtaining less influence on the surface. The nominal diameters of the mesas or apertures were in the range of 0.4 to 5 μm to find the optimal sizes for the spectroscopic measurements.

5.2. FIRST GENERATION OF STRUCTURES

The first generation is a series of samples with indium content for the upper part of the $\mathrm{In}_x\mathrm{Ga}_{1-x}\mathrm{As}$ MBL (x_{MBL}) ranging from 6% to 36% (see Table 5.1).[8] The period scheme is based on GaAs and InGaAs layers (type I period) or two base materials for its components (type II period: GaAs/InGaAs-InGaAs/InAs), where the thickness of the periods was set to 3 nm, and the thickness of the entire MBL is defined by the final indium content in the metamorphic layer. Modifying the MBL composition while maintaining the same QD growth parameters should allow for a shift of the emission energy to longer wavelengths driven mainly by strain changes. The samples are hereafter labeled according to the nominal values of indium composition as specified in Table 5.1.

Sample	x_{MBL}(nominal) (%)	d_{MBL}(nominal) (nm)	Period type (thickness)
In-6%	6	180	I (3 nm)
In-9%	9	270	I (3 nm)
In-12%	12	360	I (3 nm)
In-24%	24	720	II (3 nm)
In-36%	36	1080	II (3 nm)

Table 5.1. Nominal values of structure parameters: indium content x_{MBL} and MBL thickness d_{MBL}.

PL characterization of a QD ensemble (see Figure 5.4) allows the observation of the optical response changes between samples while maintaining similar measurement conditions (T = 10 K, 100 μW excitation power), i.e. a shift of the emission peak from ~1100 nm (for In-6%) to 1200 nm (for In-24%). A substantial decrease in PL intensity is noticeable for structures with x_{MBL} > 12%. For the first three structures (In-6%, In-9%, and In-12%), the peak intensities are comparable (intensity multipliers in the range of 0.87–2.1), while the following two structures have much lower emission intensities (multiplied by 124 for the In-24% sample and by 529 for the In-36% one). Even if taking into account the possible changes in the dots' density, this observation suggests a deterioration of the structural quality and increased concentration of defects working as non-radiative carrier loss channels. In addition, for the In-36%, a set of low intensity, narrower PL peaks is observed in a broad spectral range up to approximately 1250 nm, which most likely indicates a very heterogonous growth resulting in inhomogenous ensemble.

[8] Performed by Piotr Wroński at the University of Würzburg.

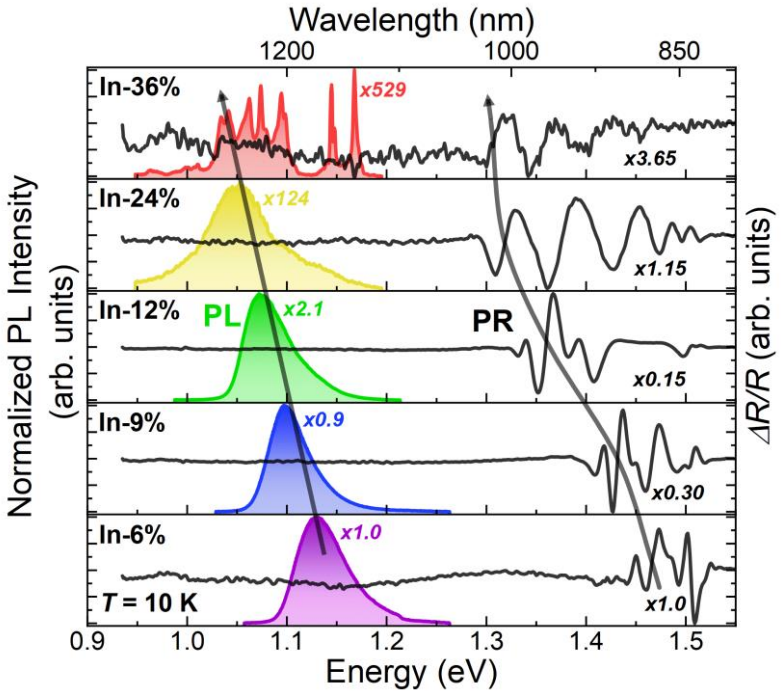

Figure 5.4. Intensity normalized PL spectra for subsequent structures measured at 10K – colored plots. Multipliers with respect to the In-6% PL signal are given near each PL peak. Normalized PR spectra (black plots) for subsequent structures. Multipliers with respect to the In-6% PR signal are given on the right. The PR spectra were measured at room temperature and then shifted to low temperature to correspond to the PL spectra. The gray arrows are guides to the eye to show the direction of the shift toward longer wavelengths of both QD emission energy and MBL energy gap with increasing indium content.

In PR spectra (see Figure 5.4), a redshift of the lowest-energy spectral feature (resonance) was observed, which is attributed to the upper part of the MBL layer (from ~1.47 eV for In-6% to ~1.32 eV for In-24%). The PR spectra measured at room temperature were shifted to a low-temperature according to the Varshni dependence for a bulk material with an indium content as in particular MBLs. Following the QD signal in PR would be difficult as it is not clearly pronounced in the spectra. This is a common observation as the total absorption of QDs is significantly lower than for a quantum well or bulk material. The PR response from QDs is further smeared out in case of inhomogeneity of the QDs parameters, which is the case for QD ensembles, especially for In-36% structure. Similarly to PL spectra, observation of a significant deterioration of the signal-to-noise ratio in PR spectra indicates a worse overall optical quality of the structure, especially for In-24% and In-36% samples. Increased concentration of defects causes trapping of carriers photogenerated by the modulation beam in the PR experiment and hence decreasing the modulation efficiency, an effect already observed previously in other systems [243]. Therefore, this chapter focuses only on the observation of the shift of MBL-related PR signal - a more detailed analysis and explanation of the origin of the entire PR spectrum will be presented in Section 6.3.

The above-described results may be confronted with SEM images of the edges and surfaces of the structures presented in Figure 5.5, showing a similar deterioration of homogeneity and incorporation of large surface undulations (more significant roughness) with increasing indium content in the MBL, probably hindering the formation of the dots (lack of QDs on the surface for In-36% sample) and also supporting the generation of threading dislocations from the edge side. Please note that these images present surface QDs grown on the cap layer.

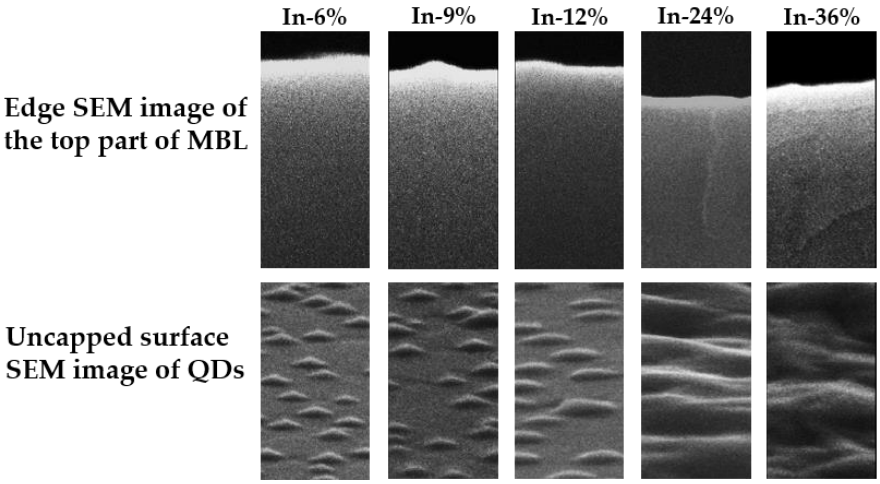

Figure 5.5. SEM images of the top edge of the structures and uncovered reference QDs grown on the capping-layer surface for subsequent structures.

All these results indicate the deterioration of the MBL structural quality with increasing indium content, starting at about x_{MBL} ~ 12%. At the same time, achieving the emission significantly above 1200 nm was impossible.

5.3. THE SECOND GENERATION: SHIFT OF EMISSION UP TO THE SECOND TELECOM WINDOW

Based on the results of the previous Section, another series of samples was fabricated[9] with modifications introduced in the period scheme: the thinner period of 0.4 nm and two base materials for its components (type II period: GaAs/InGaAs-InGaAs/InAs), aiming at improved crystal quality and control of indium incorporation. As shown in Table 5.2, the second series of samples concerns structures with indium content in the top part of MBL ranging from 18% to 36% (nominal values). For the last sample (In-29%), the indium pressure was additionally increased aiming at better In incorporation. The samples are labeled according to the actual values of indium composition determined based on optical spectroscopy. Indium composition analysis will be presented later in this section.

Sample	x_{MBL}(nominal) (%)	x_{MBL}(optical) (%)	d_{MBL}(nominal) (nm)
In-11%	18	11	540
In-15%	24	15	720
In-20%	30	20	900
In-24%	36	24	1080
In-29%	36	29	1080

Table 5.2. Structure parameters: indium content x_{MBL}(designed and determined values) and the thickness of the MBL d_{MBL} (designed values).

The emission characteristics shown in Figure 5.6A were collected at similar conditions as for the first generation of samples: T = 10 K, 100 μW excitation power. This time the QD-related PL peak shifts from ~1100 nm to ~1250 nm. Due to the natural ensemble inhomogeneity (translated into broadening of the PL peaks) emission in the range of the second telecom window was obtained in the low-energy PL tail of the In-29% sample, as seen in Figure 5.6B. For this series, a similar optical quality for all structures was observed

[9] Performed by Piotr Wroński at the University of Würzburg.

based on almost identical emission intensity (multipliers in the range of 0.7–1.0 for all spectra in Figure 5.6A), which indicates improved MBL and QD material crystal quality, regardless of MBL composition.

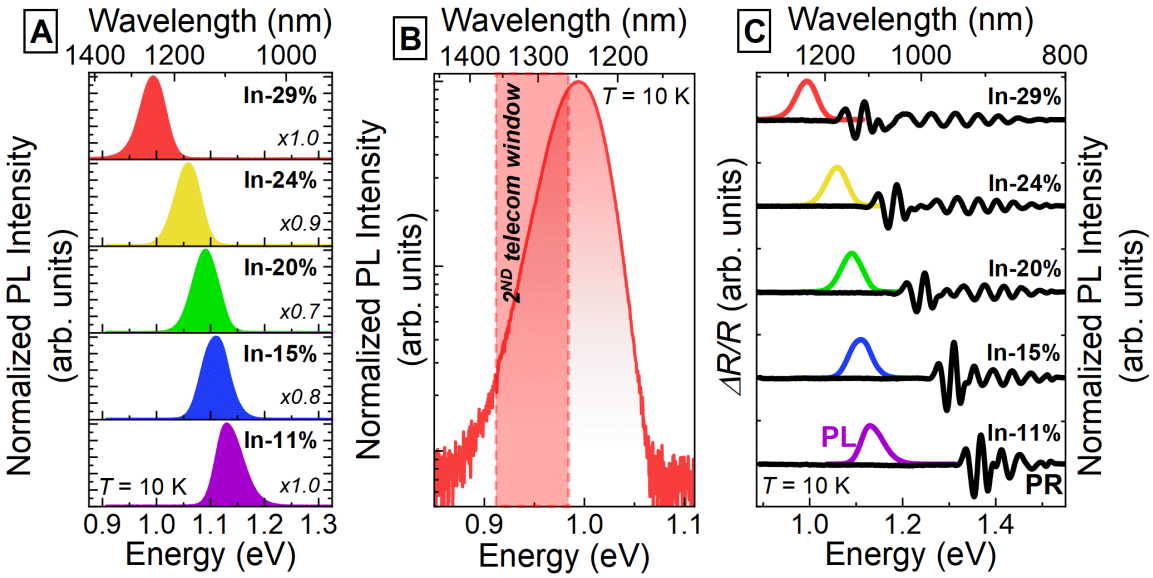

Figure 5.6. (A) Normalized PL spectra for subsequent structures (In-11%–In-29%), the multiplier in the lower right corner relative to the In-11% sample PL signal. (B) PL spectrum of In-29% structure in the logarithmic scale with the marked second telecom window. (C) PR spectra for subsequent structures compared with normalized emission.

Similarly, the analysis of the PR spectrum confirms a significant improvement in the structure quality when compared to the first generation of samples, evidenced by very good signal to noise ratio (high PR signal intensity) regardless of MBL composition. For all structures, a clear resonance on the low-energy tail of the spectrum is observed associated with the top part of MBL, as shown in Figure 5.6C. In addition, a shift of this resonance is observed with the increase in the indium content (from ~1.36 eV for In-11% to ~1.107 eV for In-29%), associated with the decrease in the MBL band gap [244]. The SEM images for the edges and surfaces of the samples (see Figure 5.7) also confirm good and similar structural quality, with reference QDs visible on the surface regardless of MBL composition. Moreover, the surface is less rough for all samples when compared to the first generation.

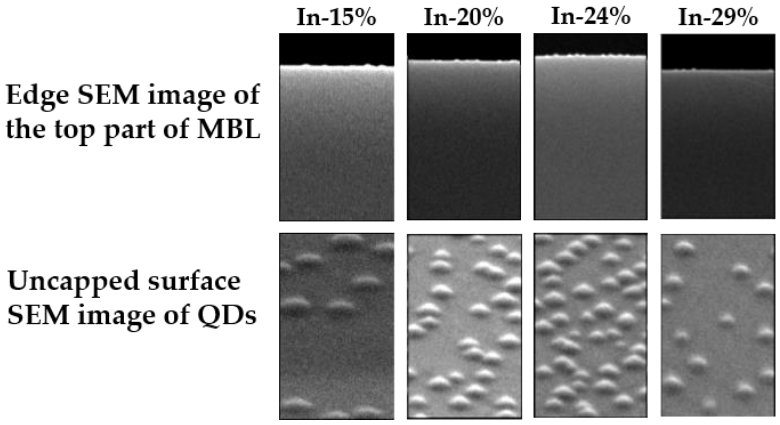

Figure 5.7. SEM images of the top edge of the structures and uncovered reference QDs grown on the capping layer surface for subsequent structures.

Next, the actual indium content is analyzed based on results in Figure 5.8A: the PR resonance position, also consistent with the absorption edges observed in the PLE spectra. When neglecting the possible residual strain, x_{MBL} is determined using the following interpolation for InGaAs energy gap [244]:

$$E_{\mathrm{g}}(\mathrm{InAs}_x\mathrm{GaAs}_{1-x}) = xE_{\mathrm{g}}(\mathrm{InAs}) + (1-x)E_{\mathrm{g}}(\mathrm{GaAs}) - x(1-x)C_{\mathrm{GaAs}}^{\mathrm{InAs}}\,, \tag{5.1}$$

where $E_{\mathrm{g}}(\mathrm{InAs}) = 0.417$ eV, $E_{\mathrm{g}}(\mathrm{GaAs}) = 1.519$ eV, $C_{\mathrm{GaAs}}^{\mathrm{InAs}} = 0.477$ [244]. Using the determined transition energy for the top of MBL, the MBL composition was calculated. As presented in Table 5.2, the indium content is always lower than the nominal values. These results also showed that the increased indium pressure during growth of the In-29% sample improved the indium incorporation (when compared to In-24%), but still, the nominal value of 36% could not be reached.

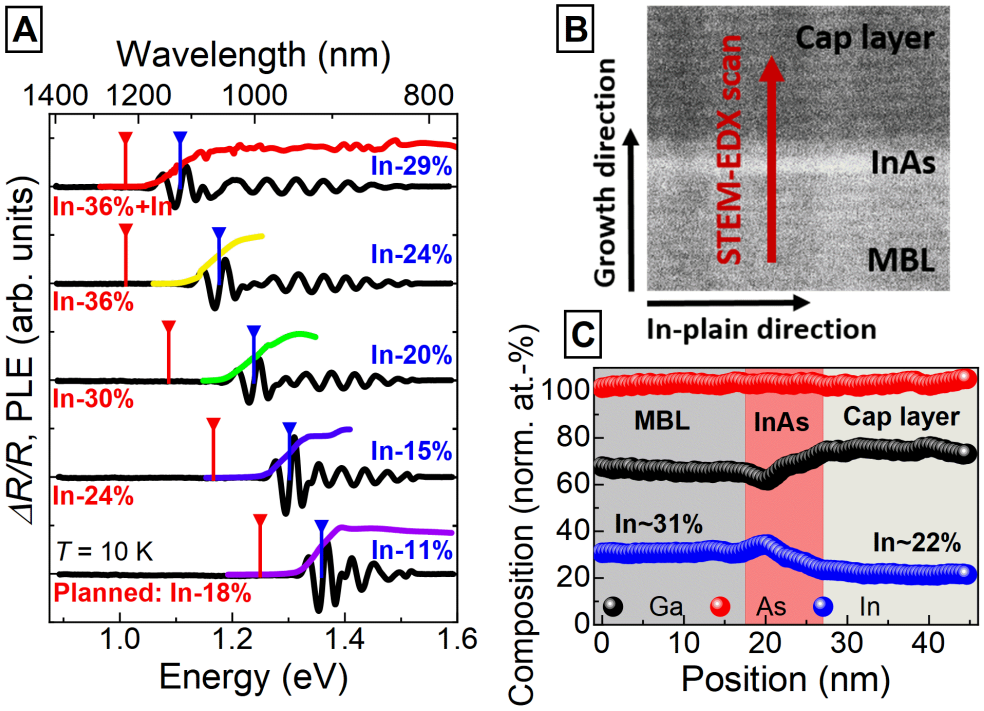

Figure 5.8. (A) PR (black lines) and PLE (colored lines) spectra for particular structures with an indication of the energy of the InGaAs material for the nominal composition of the MBL and the determined values. (B) STEM image with the marked range of linear atomic composition scan (red arrow) of EDX characterization.[10] (C) Atomic composition normalized and divided into Group III and V components.

For sample In-29%, the x_{MBL} values based on optical measurements were compared with the EDX spectroscopy scan[10] (see Figure 5.8B), showing the structure composition along the growth direction through the top part of the MBL, the InAs layer, and the cap layer. The determined compositional profile, shown in Figure 5.8C, gives approximately 31% indium in the MBL (close to 29% obtained from the optical measurements), and ~22% indium content in the QD capping layer, i.e. comparable to ~20–22% determined based on optical characterization and in good agreement with the nominal 2/3 ratio between the In contents of the cap to the top part of the MBL.

[10] STEM and EDX measurements were performed by Dr. Sandeep Gorantla at the Łukasiewicz Research Network – PORT Polish Center for Technology Development with participation of the author.

5.4. THE THIRD GENERATION: EMISSION IN THE THIRD TELECOM WINDOW

The fundamental period of the MBL growth for the third generation of samples was based only on the InGaAs as a base material with the InAs as indium control material to obtain a significantly increased indium content based exclusively on thickness control of indicated layers, i.e. InGaAs/InAs pairs. The growth of the MBL started directly from the InGaAs material with indium content of 6%, for which the lattice constant is still close to GaAs. Then, as in the case of the previous generations, subsequent sequences of InGaAs/InAs periods with 0.4 nm thickness were grown, with 1 percent of indium content increase in each step of 30 nm layer. That way, there was fabricated the MBL with a total thickness of about 1200 nm and nominal indium content of 42% at its top.[11] However, the content verified by optical studies appeared to be about 38% (see below), being the largest obtained. For further studies there was available only one such structure (which was named In-38%), which in addition contained an additional DBR structure preceding the MBL layer (see Figure 5.9).[12] The DBR consists of five pairs of GaAs/AlaAs layers with 106 nm and 120 nm thicknesses, respectively, designed for the third telecom range. However, it has not been optimized showing only about 0.5 reflectivity at 1.55 μm, so its optical impact wasn't crucial. It was mainly included to test it as a technological step in view of future photonic structures fabrication.

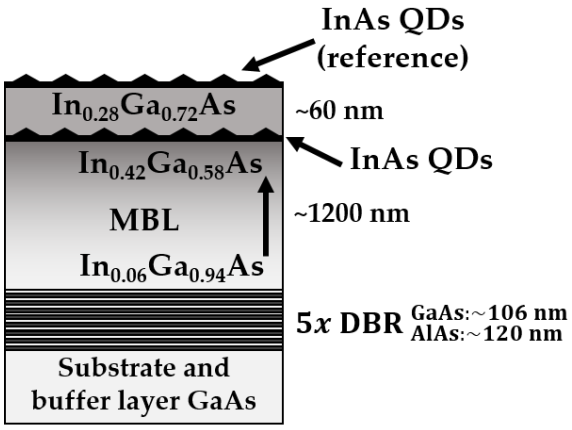

Figure 5.9. Layer scheme for the In-38% structure.

Figure 5.10A presents the results of PL measurements vs the excitation power. A shift of the main QD-related peak to approx. 1380 nm is observed, with also noticeable intensity band at longer wavelengths, i.e. in a broad range of 1450–2400 nm covering the third telecom window. Moreover, microphotoluminescence spectra (Figure 5.10B) show clear single QD lines in the range of 1450–1600 nm, confirming that one of the main goals has been achieved, namely, there is detected bright emission in the 3rd telecom window from single InAs QDs grown by MBE on InGaAs MBL.[13]

[11] Grown by Piotr Wroński at the University of Würzburg.

[12] No DBR-free structure was available.

[13] Recording single QD emission lines above 1.6 μm was not possible because a suitable multichannel detector operating at longer wavelengths is not available in our laboratory. However, as the main target spectral range has been reached, further studies concentrated on the emission around 1.55 μm.

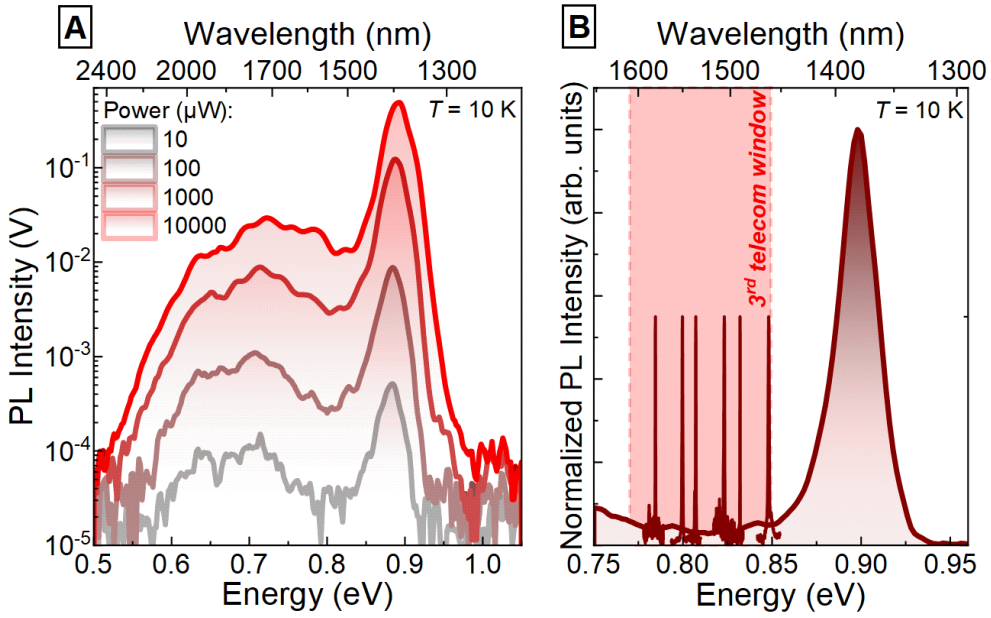

Figure 5.10. (A) PL spectra measured at 10 K for QD ensemble of the In-38% structure for different excitation powers (values measured outside the cryostat). (B) Single QD emission lines in the 3rd telecom window, overlayed with the ensemble PL spectrum.

The SEM image from the edge of the In-38% sample (see Figure 5.11A) shows a homogeneous MBL on a DBR without any extended defects. The SEM and AFM images of the sample surface (Figure 5.11A and 5.11B) show an evident heterogeneity (surface roughness), which makes difficult to distinguish the dots, however some nanometer islands are visible. Cross-sectional STEM[14] from the edge of the sample confirmed the presence of the buried dots, as seen in Figure 5.11C.

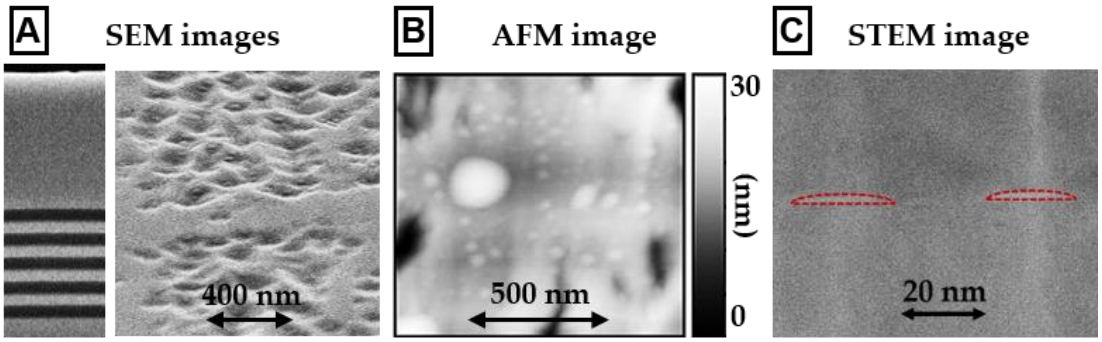

Figure 5.11. (A) SEM images of the edge and surface of the In-38% sample. (B) AFM image of the surface of the In-38% structure with reference dots. (C) STEM image[14] of buried quantum dots.

Eventually, PLE spectrum was measured at low temperature as plotted in Figure 5.12 where it is compared with the PL from the dots. A clear absorption edge could be detected in PLE related to the MBL – its energy agrees with the band gap of $In_{0.38}Ga_{0.62}As$, also marked in the figure.

[14] STEM measurements were performed by Dr. Mirosława Pawlyta at the Silesian University of Technology in Gliwice with participation of the author.

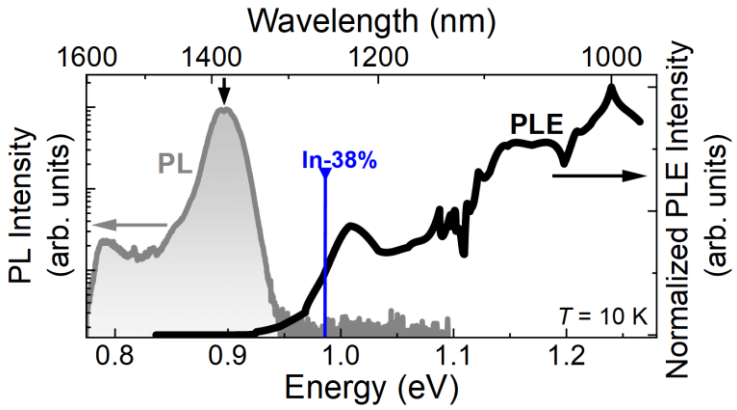

Figure 5.12. Low-temperature PL and PLE spectra for In-38% sample; black vertical arrow indicates the detection energy in PLE experiment; blue marker shows the energy gap of $In_{0.38}Ga_{0.62}As$ at low temperature agreeing with the MBL absorption edge.

5.5. MORPHOLOGICAL PROPERTIES OF THE DOTS

The next stage of the work focused on detailed investigation of the QDs morphology for selected six structures characterized by the emission range spanning from 1100 nm to 1600 nm, i.e., five structures from the second generation (In-11%, In-15%, In-20%, In-24%, In-29%) and the one structure from the third generation (In-38%). They have been chosen so as representing the broadest possible spectral range, including the telecom windows, and because they are characterized by the best optical properties in certain ranges.

In addition to strain, QD parameters like size, shape, and composition are important factors affecting the electronic structure and optical transitions energy. Reducing the lattice mismatch between QDs and MBL and thus strain introduced changes in the growth conditions, favored formation of QDs with larger size and higher indium content. First, SEM and AFM data were analyzed for reference QDs on the top of the structures. Examples of results for In-11%, In-29%, and In-38% structures are shown in Figure 5.13. For the In-11% and In-29% samples, it was possible to analyze the QD parameters directly. It was more challenging for the In-38% structure with more rough surface and worked better only for some cases from AFM.

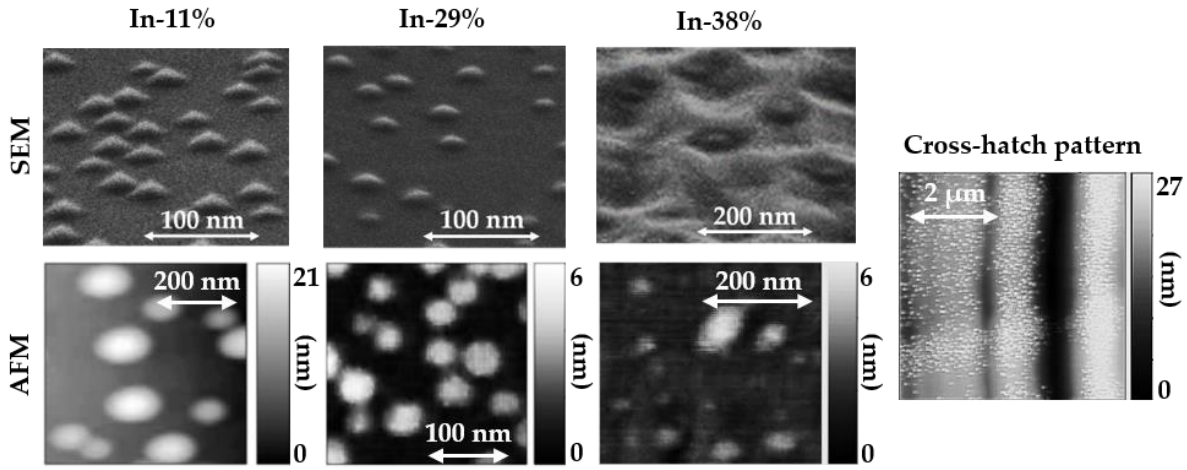

Figure 5.13. SEM and AFM images of the sample surface with reference QDs for structures In-11%, In-29%, and In-38%, and AFM image of QDs showing a cross-hatch pattern.

An important issue that should be considered is the difference between the examined optically inactive reference dots and the QDs inside the structure covered by the capping layer. The covering usually causes changes in the dots' morphology, when compared with the reference, uncapped ones on the sample surface [11]. In addition, the proper analysis of the surface QDs may also be hindered by the surface roughness or presence of cross-hatch pattern and threading dislocations, which can cause significant undulation of the QD properties – see an example in the very right image of Figure 5.13 for sample In-15%.

To analyze the parameters of the optically active, i.e. buried QDs, an additional analysis of their cross-sections was carried out using STEM imaging[15] for In-11%, In-29%, and In-38% structures, shown in Figure 5.14. The exemplary QD heights were determined to be about 5 nm for the In-11% and In-29% structures and about 3.5 nm for In-38%, whereas the diameters of about 45 nm for In-11% and about 30 nm for In-29% and In-38%.

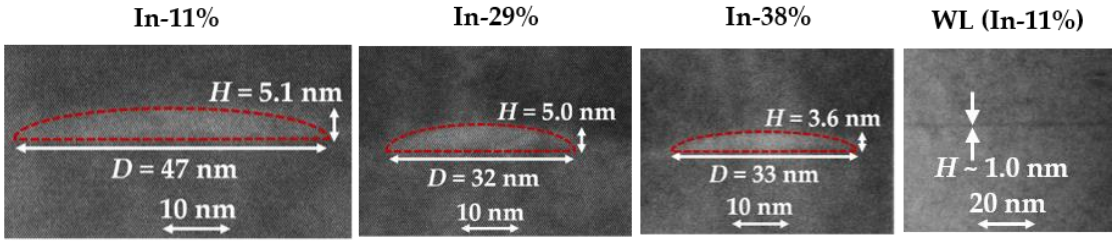

Figure 5.14. STEM images[15] of single lens-shaped QDs for In-11%, In-29%, and In-38% structures with marked QD height and diameter and a thin WL-like STEM image.

The structural measurements allowed only to characterize the dimensions for one crystallographic direction (probably [110]). The InAs material forming a undulated layer-like object was mainly observed for imaging in the perpendicular direction, which made the observation of single QDs unclear. Therefore, it was possible to determine the sizes of the dots for one crystallographic direction but without the information about their possible shape anisotropy in the plane. Besides QDs, a thin layer of InAs with a thickness of about 0.5 - 1 nm was observed for scans of In-11%, indicating the presence of WL with apparently a fluctuating thickness and indium content. It was hardly observable for the other samples with higher In composition, i.e. lower composition contrast between the top of MBL and the QD layer.

The collected QD parameters are presented in Table 5.3 (average values determined from the set of results). All structures have a similar QD surface density around $10^{10}\ \mathrm{cm}^{-2}$, with however significant density changes when traveling over the sample surface (as seen in the very right SEM image in Figure 5.13). A more detailed analysis of the surface density for optically active dots is presented in Section 7.1. The reference QD dimensions from SEM imaging of all samples are H = 3.0–4.5 nm and D = 24–35 nm, with the aspect ratio $H/D \sim 1/8$, almost independent of the sample. In the case of AFM measurements, the obtained values for height are more scattered, most likely due to complications associated with surface undulation. Nevertheless, it was possible to determine the in-plane asymmetry with LAR ~ 1.2. The STEM characterization yields QD the average dimensions of about 5 nm for height and 40 nm for diameter ($H/D \sim 1/8$) for In-11% and In-29% samples, and nearly 3 nm height and 24 nm diameter ($H/D \sim 1/8$) for In-38%. The obtained smaller size of reference dots (based on the SEM measurements) compared to the buried ones (from STEM) is expected in the absence of the capping layer for the reference dots [11].

[15] STEM measurements were performed by Dr. Mirosława Pawlyta at the Silesian University of Technology in Gliwice with participation of the author.

		In-11%	In-15%	In-20%	In-24%	In-29%	In-38%
SEM	*D* (nm)	33.3	34.6	30.6	27.6	24.0	
	H (nm)	4.1	4.3	3.6	3.8	2.9	
AFM	*X* (nm)	85	55	48	48	50	41
	Y (nm)	61	44	35	38	47	28
	H (nm)	10	7.4	4.6	6.8	2.3	2.4
TEM	*D* (nm)	40.5				36.6	20.5
	H (nm)	4.3				4.7	2.5
LAR (reference QDs)		1.40	1.25	1.38	1.26	1.06	1.46
H/*D*		$1/9.4_{TEM}$	$1/8.1_{SEM}$	$1/8.5_{SEM}$	$1/7.3_{SEM}$	$1/7.8_{TEM}$	$1/8.2_{TEM}$

Table 5.3. QD structure parameters for particular structures: height (*H*) and diameter (*D*) or in-plane dimensions (*X* and *Y*), LAR of QD shape, and the ratio of *H*/*D*.

STEM-based QD characterization of buried QDs has also limitations. Thin lamella of the material is needed for this method, and its quality and thickness significantly affect the imaging result. The possibility of characterizing the QD height is limited due to averaging electron STEM signal over the entire lamella thickness with a low signal coming from the small volume of QD material. Averaging the parameters determined for many dots was performed to reduce this effect. Due to similar QD sizes found for the extreme In-11% and In-29% structures identical QD parameters were adopted for the entire series in the modelling, which is justified also because of the same QD layer growth in all samples of the second generation. Due to the surface roughness mentioned above, reliable structural characterization of the dots in the In-38% structure (third generation) was hardly possible. The limited AFM and TEM data suggest their sizes are rather smaller than those of ODs in the second generation samples. However, due to the impossibility of separating the results for dots in the 1380 nm range from the second family emitting in the 1450-2400 nm range, it is difficult to determine the exact parameters for QDs emitting in the third telecom window. Therefore, for simplicity as a first approximation in the calculations, the geometrical parameters of the In-38% dots were assumed the same as for QDs of the second series of structures. Such assumption is also supported by optical results of single QDs emitting in the third telecom range indicating similar properties to the second series regardless of the spectral range (as presented in Chapter 7).

During the STEM measurements there was also carried the EDX characterization to determine the material composition.[16] Exemplary results are shown in Figures 5.15A and 5.15B for samples In-11% and In-29%, respectively. Their analysis was difficult mainly due to low compositional contrast between the individual layers (all created based on an InGaAs material). Just a slight contrast between QDs and the surrounding material indicates similar indium content values and can be a fingerprint of significant intermixing effect. Nevertheless, as shown in Figure 5.15A, in the case of the In-11% structure, it was possible to detect QD indium content of about 50%, consistent with the calculation results for this structure (presented in the next section). At the same time, the compositions for the top part of MBL and the cap showed higher values than it was estimated form the optical characterization. This agree better with the optical results for sample In-29% - see Figures 5.8B and C. Collecting more data for the latter structure, presented in Figure 5.15B, gave in average about 30% and below 20%, for the MBL and cap respectively, in agreement with the results of the optical characterization and with the nominal indium contents ratio. In

[16] STEM and EDX measurements were performed by Dr. Sandeep Gorantla at the Łukasiewicz Research Network – PORT Polish Center for Technology Development and also by Dr. Mirosława Pawlyta at the Silesian University of Technology in Gliwice with participation of the author.

contrast, the indium content in QDs is underestimated, with only one result above 50%, consistent with the expected indium value for this structure to obtain emission in the second telecom window (in accordance with Figure 5.1A for $H = 5$ nm and $x_{\mathrm{MBL}} = 30\%$). Due to the described limitations of EDX characterization, they were only used as some indications and the final determination of the QD indium content was performed based on a comparison of optical and calculation results for the obtained and realistic geometry: $H = 5.0$ nm, $D = 40$ nm, LAR = 1.2, assuming x_{MBL} also from the optical measurements, and 2/3 of this value for the cap layer, which found at least partial confirmation in the EDX measurements.

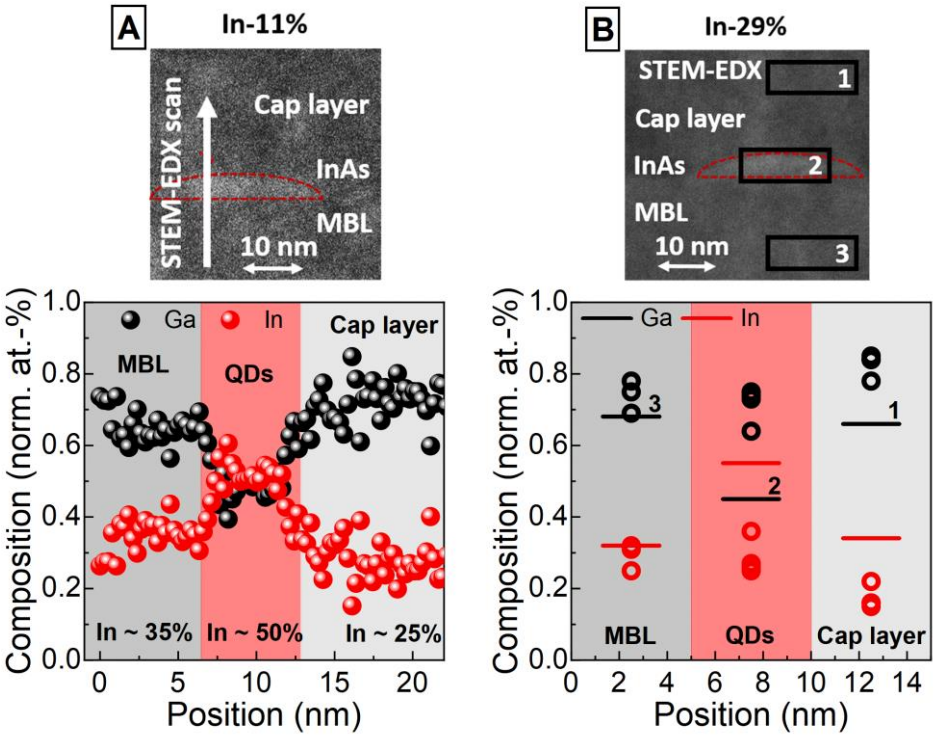

Figure 5.15. STEM image for (A) In-11% structure with line scan of the normalized atomic composition of metallic elements (gallium or indium). STEM image for (B) In-29% structure with a particular area scan of the atomic composition of metallic elements (gallium or indium).[17]

5.6. CALCULATION OF OPTICAL TRANSITIONS

Assuming the abovementioned typical lens-shaped geometry of QDs on 0.5-nm WL, and the MBL and cap layer parameters based on the results of optical characterization, numerical calculations of the emission energy for a wide range of QD indium contents (x_{QD}: 50%–100%) were performed using the NEXTNANO software (as described in Section 4.3). The model of a QD and calculation results are shown in Figure 5.16. Due to the lack of information about the composition distribution inside the dots, a uniform QD composition was assumed, with only a slight In step-like gradient over 0.5 nm at the interfaces between the dot and the surrounding layers assuming that some intermixing of materials always takes place. A series of computations for various QD indium contents was performed to estimate QD composition based on comparing the calculation results with QD ground state transition energy determined by optical characterization of second and third generation structures In-11%–In-38%. WL composition was set as

[17] STEM and EDX measurements were performed by Dr. Sandeep Gorantla at the Łukasiewicz Research Network – PORT Polish Center for Technology Development and also by Dr. Mirosława Pawlyta at the Silesian University of Technology in Gliwice with participation of the author.

$x_{WL} = x_{QD} - 0.25(x_{QD} - x_{MBL})$, including a simple-approach for material composition intermixing occurring at material interfaces. The difference in the composition between the MBL and WL and the gradient for dot edges are related to possible intermixing, lowering the indium content in the WL layer and on the edges of the dot. Due to the growth in the SK mode resulting in the presence of WL, its inclusion in the calculations seems reasonable as it may affect the properties of the dots. However, simple calculations of the energy structure for WL assumed as just a thin quantum well with asymmetric barriers, showed that confining electrons is hardly possible (for a wide range of indium contents), which suggest that the WL can be expected to be optically inactive in these structure and difficult to be detected in the spectra.

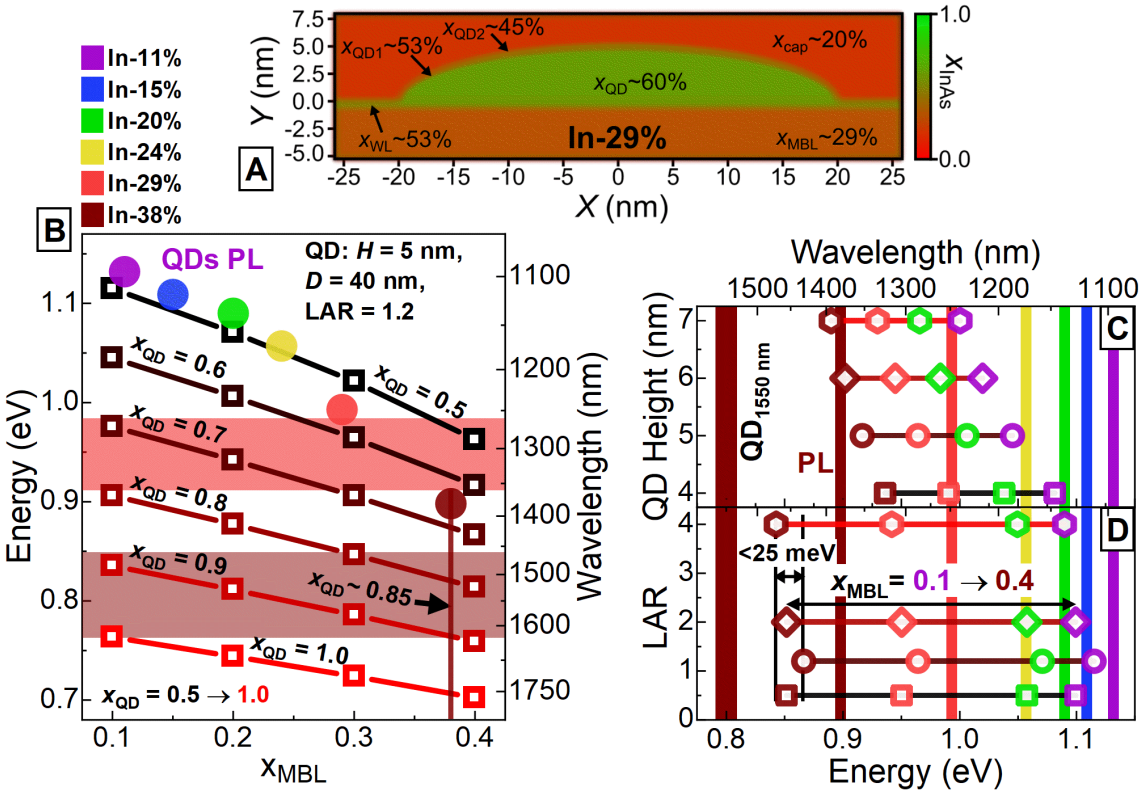

Figure 5.16. (A) Model of a QD used in calculations of the electronic structure (NEXTNANO). (B) Calculated ground state energy as a function of the MBL indium content for successive values of the indium content in a QD with H = 5 nm, D = 40 nm, and LAR = 1.2 (squares). Comparison with experimentally determined emission energy (circles for peak energies and brown line for low-energy PL tail for In-38%). Shaded areas show the second (pink; 1260–1360 nm) and third (light-brown; 1460–1625 nm) telecom windows. QD ground-state energy for (C) different QD heights and (D) different LAR values. Vertical lines show experimentally determined QD emission energies. The color of the open symbols labels the MBL indium content. QD parameters in (C): H/D = 1/8, LAR = 1.2, x_{QD} = 60%, and in (D): H/D = 1/8, H = 5 nm, x_{QD} = 50% for purple and green open symbols, x_{QD} = 60% for red open symbols, and x_{QD} = 70% for brown open symbols.

For each QD indium content, the QD ground-state energy was determined as a function of the MBL composition (Figure 5.16B), showing the expected redshift due to strain reduction. In addition, the increase in the QD indium content also shifts the emission towards lower energies due to the reduction of the energy gap of the QD material. The obtained data were compared with the experimentally determined emission energies for selected samples from the second and third generations (colored full symbols for PL peak energy for particular samples and vertical solid line for low-energy tail for In-38% in Figure 5.16B). Based on that, the estimated x_{QD} is about 50% for the first four samples. In addition, one may notice that introducing a change in the QD indium content for the In-29% and In-38% samples is necessary to obtain

agreement between the calculations and the experiment, and it then closer to 60% and 70%, respectively. For the dots emitting within the 3rd telecom window of the low-energy tail of the In-38% sample, x_{QD} is around 85%. In addition, it is seen in Figure 5.16C that assuming identical indium content in the dots ($x_{QD} = 0.6$) regardless of the MBL composition, changes in QD height do not allow reconstructing the experimentally determined emission energies, indicating the necessity of the QD indium content correction (see Figure 5.16B).

The obtained explanation of emission energy changes based on strain and QD indium content modifications can probably correlate with the introduced growth changes for the indicated structures. In the case of In-11%–In-24% samples, QD growth was carried out identically. Only the MBL composition was modified. In contrast, the only change for the sample, In-29%, was the increase in indium pressure during the entire growth, which could increase indium content in both the MBL and QDs. For the MBL, it was confirmed by optical measurements (see Figure 5.8A). For QDs, calculation-based composition determination also confirms higher indium content, a seen in Figure 5.16B. Modifying the period pattern and the increased indium content for the last structure from generation III (In-38%) resulted in further indium content increase in the QDs. Naturally, QDs emitting in the third telecom window must have different parameters than those emitting around PL peak at 1380 nm. Due to rather weak influence of the QD size changes on the ground state transition energy (within the range of realistic sizes as from the structural data), it was assumed that the main parameter shifting the emission must be the QD indium content, in agreement with the results of Figure 5.16B (for QD emitting above 1500 nm, x_{QD} ~ 85% is necessary).

A separate issue is the possibility of QD in-plane elongation, most likely along [1-10], as observed for InAs QD grown under reduced stress conditions [50,93,245]. However, the results of AFM measurements for reference QDs show nearly symmetrical dots with LAR about 1.2. Problems with observing QDs in the perpendicular direction with STEM made it impossible to directly determine the QD in-plane symmetry. In the calculations, QD elongation modifies the emission energies only slightly, as shown in Figure 5.16D. The associated changes below 25 meV are small compared to the emission energy shift between the structures differing in MBL composition, indicating that QD elongation is not the main factor responsible for the spectral shifts of the fundamental optical transition. The shape anisotropy issue is explored yet in the next chapters on the analysis of DOLP and FSS - see Sections 6.2 and 7.5.

In addition to the basic NEXTNANO calculations used mainly to determine the factors driving the changes of the QD emission energy, results of more advanced theoretical considerations performed by Dr. Michał Gawelczyk were also used and compared with the experiment. The latter are based on a similar approach to that used in NEXTNANO, but they include the Coulomb interaction and calculate the excitonic states. Based on the obtained morphological parameters, the parameters of the dot are selected, additionally introducing Gaussian averaging (here with σ = 0.9 nm) of the composition profile to account for the interdiffusion of atoms at the interfaces. For such a structure, taking into account the influence of strain, piezoelectric field, and spin-orbit interaction, the eigenstates for electrons and holes are determined using the 8-band $\boldsymbol{k \cdot p}$ method [246,247] within the envelope-function approximation [239]. By determining the basis of eigenstates for electrons and holes (here, 32 states), a configuration basis is constructed for determining the states of excitonic complexes within the configuration-interaction method. Optical transition dipole moments [248] and the oscillator strengths [249] for individual eigenstates are also calculated within the dipole approximation. Based on such calculations, it is possible to obtain single-particle and exciton states, emission energy, and binding energies for different excitonic complexes. In addition, it is also possible to determine the decay time of the emission and the degree of polarization based on dipole moments [250]. Material parameters for GaAs, InGaAs, and InAs used are based on Refs. [244,250].

A comparison of these two approaches, shown in Figure 5.17A, is discussed here to show the consistency between the models. The differences in the emission energy are insignificant (below 40 meV). They may partly result from minimal differences in the QD model (Gaussian averaging of composition

profile in the advanced approach) and additional effects taken into account in the second approach, including electron-hole interaction.

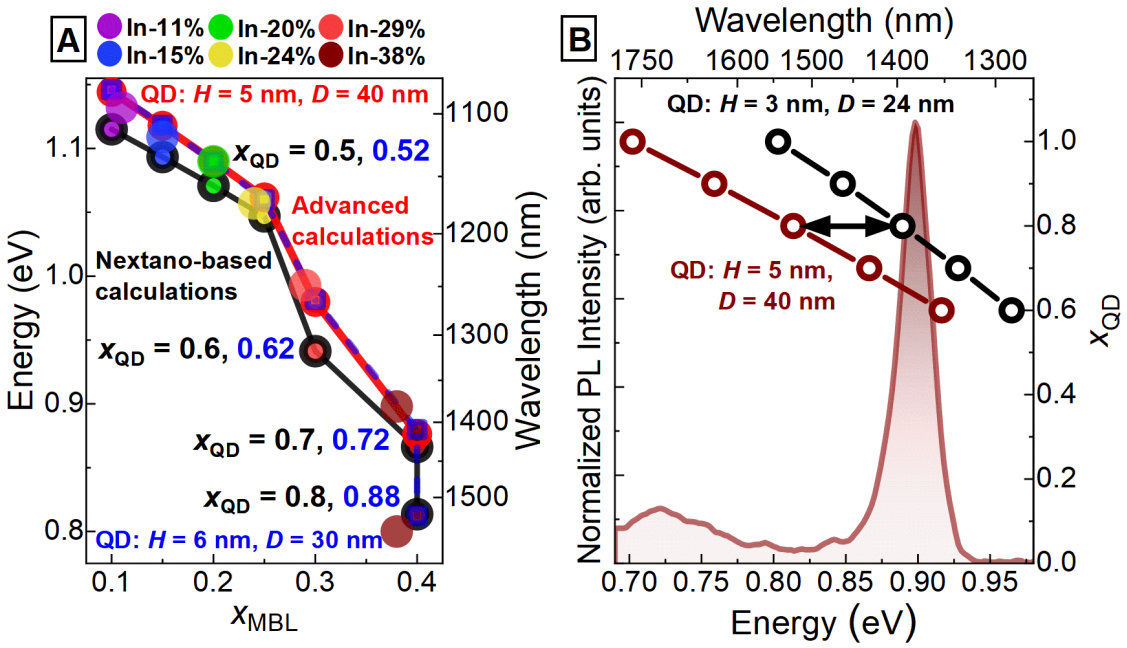

Figure 5.17. (A) Comparison of the calculation results of the QD ground state for the approach based on NEXTNANO software (black-colored points) and the more advanced approach[MG] for two QD geometries: H = 5 nm, D = 40 nm (red circles) and H = 6 nm, D = 30 nm (blue squares) with LAR = 1.2. Collation of the calculation results with the peak energy for QDs emission for successive structures (colored points). The marked indium content values (described in black for geometry H = 5 nm, D = 40 nm and in blue for geometry H = 6 nm, D = 30 nm) are determined by comparing QD emission energy determined experimentally and by calculations (see Figure 5.16). (B) Comparison of the ground-state energy calculation results (NEXTNANO-based calculations) for QDs from the In-38% structure as a function of QD indium content for two geometries: H = 5 nm, D = 40 nm (brown points) and H = 3 nm, D = 24 nm (black points) with LAR=1.2. Collation of the calculation results with the emission spectrum of the In-38% structure.

Moreover, a minimal QD geometry modification, with H = 6 nm and D = 30 nm, was also considered, which seems still possible regarding the collected structural data, especially the accuracy of STEM measurements (characterization based on the image contrast within a lamella). To maintain the agreement with the experimentally determined QD emission energy (shown in Figure 5.17A) and to compensate for the QD-size-driven blueshift, the indium content was slightly increased for all structures by 2 percentage points compared to the previous geometry (H = 5 nm, D = 40 nm). The introduced geometry seems to be still realistic but it has the advantage to be even more consistent with the results of further optical characterization of single QDs studied in Chapter 7 (see Subsection 7.5.4).

The issue which remains unclear is the inconsistency of the STEM results for the In-38% sample. It is possible that QDs with sizes determined from the structural characterization (see Table 5.3) are a separate QD family emitting at 1380 nm. Calculations performed for such QDs indicate that it could be the case for about 80% QD indium content (see Figure 5.17B). Moreover, achieving emission above 1500 nm for such small nanostructures is hardly possible because it would require assuming pure InAs in QDs, which is rather unrealistic. On the other hand, assuming the QD geometry identical to that determined for the second generation of structures: H = 5 nm, D = 40 nm (based on In-11% and In-29%), the 1500 nm emission is found for QDs with x_{QD} > 80%. This value is consistent with the above-determined indium content for the smaller QD family from TEM – for example calculations for the QD with H = 3 nm and D = 24 nm give emission around 1400 nm. Thus, it is likely that third-generation QDs emitting in the third telecom

window have geometry similar to those from the second generation, while the TEM characterization probed the morphology of another family of smaller QDs present in the structure and emitting at shorter wavelengths (around the PL maximum, most probably).

In conclusion, it was shown that the main factor shifting the emission energy in the investigated structures is strain modification due to the change in the indium content in the MBL, together with the related change in the QD composition. All QD parameter modifications affect not only the energy of the ground state but also the higher-energy states, mixing of light- and heavy-hole states, spatial carrier probability distribution, etc., which all are crucial in terms of the applicability as emitters. Therefore, studying the optical properties of QDs in more detail is crucial for these structures to fully characterize and understand their properties.

6. OPTICAL PROPERTIES OF QD ENSEMBLES

Determining the optical properties of QDs is crucial for many applications in optoelectronic devices. Modifying QD parameters (strain, size, composition) via altering the growth conditions leads to changing the confinement potential for carriers, affecting the emission energy and other optical properties, including polarization or quantum efficiency. The energy structure of the barrier material surrounding the dots also affects their properties via the electric environment, thermally activated processes, and the processes of supplying carriers after the optical excitation. In addition, natural inhomogeneity intrinsically occurring in self-assembled epitaxial growth leads to a significant distribution of QD parameters, and thus, a spectrally broad optical response for an ensemble of QDs.

Growth of InAs QDs on GaAs with an MBL provides lower mismatch of materials. It leads to a significant reduction of strain and also modifies other QD parameters (especially the size and the indium content), resulting in increasing the emission wavelength up to the third telecom window. This chapter presents the results of optical characterization performed to determine the emission properties of the investigated QDs, on the ensemble level, for the same six structures as investigated in Sections 5.5 and 5.6 from the second and third generations, with varying indium content in the MBL. Figure 6.1 shows the emission spectra for all these samples, demonstrating the emission shift from 1100 nm (In-11%) to 1600 nm and even beyond 2000 nm (In-38%).

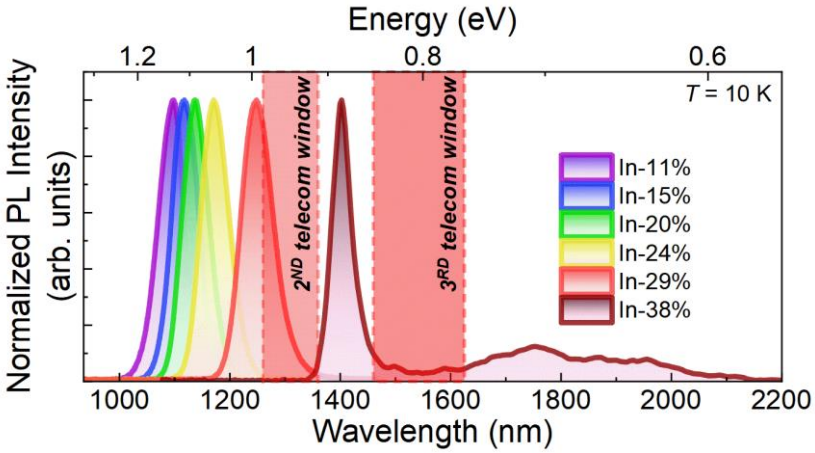

Figure 6.1. Normalized PL spectra for structures with indium content in MBL from 11% to 38%. Shaded areas mark the second and third telecommunication windows.

Characterizing the QD ensemble emission allows for determining the averaged properties of the dots without insight into the properties of individual emitters. Studying other processes occurring within an ensemble of QDs is also possible, for example, the redistribution of carriers and carrier loss channels. The first section analyzes PL for different MBL compositions and its dependence on the excitation power. In the next part, an attempt is made to determine the effect of the QD parameters on their polarization properties to explain the observed significant DOLP for nearly symmetrical QDs, as obtained from the AFM images. Further, analyzing the QD and MBL band structure makes it possible to determine the possible escape channels for the carriers, which is then compared with the results of photoluminescence temperature dependence and the obtained carrier activation energies. The last section describes the results of time-resolved PL determining the carrier dynamics. Electronic structure simulations in an advanced computational approach (performed by Dr. Michał Gawełczyk) support the interpretation of the spectroscopic data.

6.1. PROBING THE OPTICAL QUALITY VIA PHOTOLUMINESCENCE PROPERTIES

The energy of ground state emission is defined by the exciton energy, whereas the emission intensity is connected to the rate of its recombination. Modifying the QD parameters leads to changes in the energy structure of the confined states and the oscillator strength (as described in Section 2.4). The crystal quality of the MBL affects the QD emission intensity in addition, not only via modifying the oscillator strength (due to MBL-driven changes in the confinement potential) but also via structural material degradation that increases the contribution of non-radiative processes. Appearance of defects near QDs working as charge traps may also affect the emission properties, including its kinetics, due to fluctuations of the electrical environment and more complex temperature-dependent processes of carriers' transfer between the neighboring traps and the dots. Eventually, there can also occur a distribution of carriers between different dots which depends on the dots' density and details of the band structure defining the carrier transfer channels, availability of which is sensitive to the sample temperature.

In the optical characterization of QD ensembles, broad PL peaks (emission bands) are typically observed, reflecting the QD parameters distribution. Comparing the peaks linewidth and intensity for different samples with similar surface QD density and under the same excitation conditions allows judging on the relative ensemble inhomogeneities and determining the relative QD material quality (competition between the efficiency of radiative and non-radiative processes). Figure 6.2A shows as-measured low-temperature (10 K) PL spectra for the same set of structures as shown previously in Figure 6.1. The power density of the 532 nm laser excitation (CW) was about 5 W/cm^2 (laser spot diameter about 50 μm with the laser power of 100 μW). Similar integrated emission intensity for all structures is observed. When taking into account their similar QD density (see Section 5.5), it suggests similar material quality in all the samples. In the case of the In-38% sample, the diamond symbol labels a sum of intensities of the both emission bands at 1380 nm and low-energy tail in the range of 1450–2400 nm.

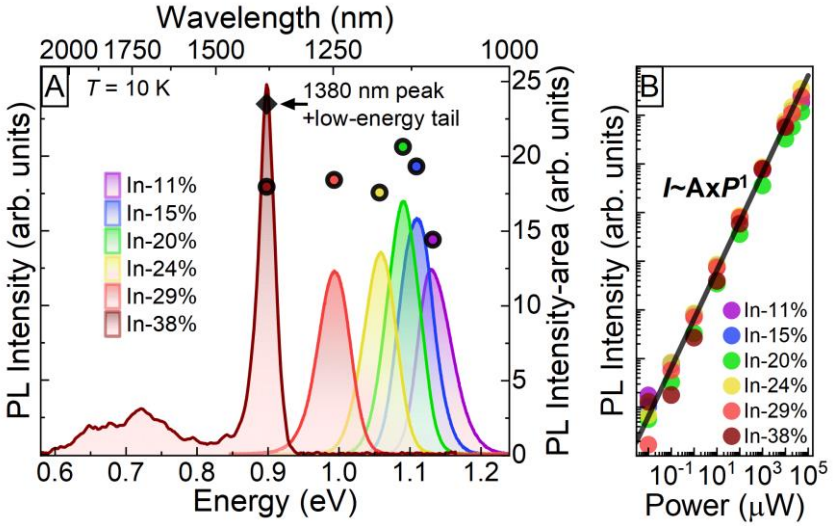

Figure 6.2. (A) Low-temperature PL spectra for a set of structures with different MBL indium content from 11% to 38% for the same excitation power density; the colored points represent integrated PL intensity; a second diamond symbol is added for sample In-38% for which the intensity of the entire low-energy tail is also included. (B) Integrated PL intensity versus excitation power (symbols) for individual structures; the line shows a power function with an exponent equal to 1.

Analyzing the changes in emission intensity as a function of excitation power gives additional insight into the nature of the optical transition – see the results in Figure 6.2B. A linear dependence was obtained for all samples in the entire range of excitation, which is expected for excitons in QDs in the low excitation regime. It also shows that the total density of QD states is not fully saturated in such conditions.

Other aspects of emission power dependence were also analyzed, like changes in the linewidth and shape of the spectra, including the observation of emission from higher QD states, or the MBL. Figure 6.3A shows the normalized emission spectra for the In-29% structure as a function of the excitation power in the range from 1 μW to 30 mW. A continuous shift of the emission maximum towards higher energies with increasing excitation power is observed (from 0.984 eV to 1.023 eV). This a very often observed effect and it is caused by an increased contribution from QDs with higher emission energy within the ensemble plus emission from higher QD states due to the state filling effect with increasing the excitons generation rates. The PL spectra in a logarithmic intensity scale are shown in Figure 6.3B. In this case, the state-filling effect is not observed as a clear appearance of separate additional peaks but rather as increased width and asymmetric shape of PL emission in the high-energy tail, most likely due to dense ladder of the confined states with energy separation lower than the inhomogeneous broadening. Figure 6.3C shows an analogous excitation-power series for the In-15% structure, where a second emission can be resolved, suspected as related to the higher QD states (energy distance between the two peaks is ~44 meV). It suggest that now the confined states separation becomes closer to the PL band width. This interpretation on the excited state emission is supported by the shown μPL spectra for two significantly different excitation powers, where single QD lines can be distinguished. When increasing the excitation, additional lines appear on the high energy side separated by about 44 meV from the lowest ones, confirming the results for the ensemble.

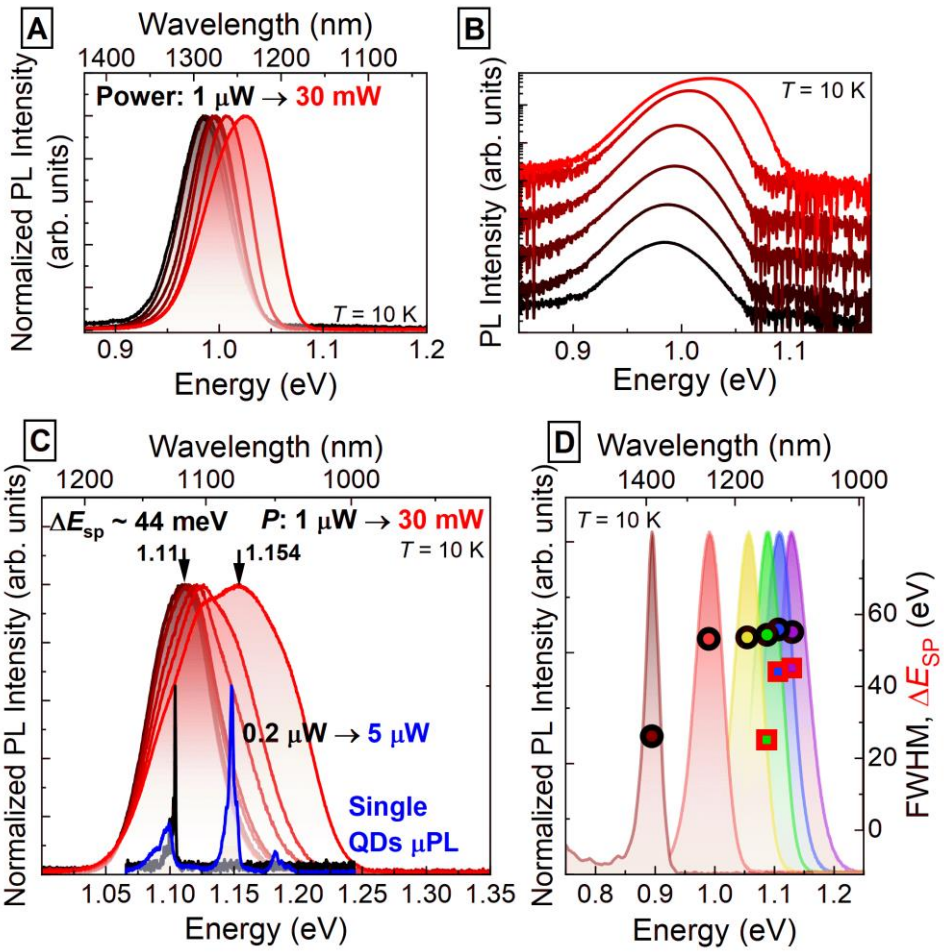

Figure 6.3. (A) Normalized PL spectra for the In-29% structure for excitation powers ranging from 1 μW to 30 mW (values measured outside the cryostat). (B) The same but in a logarithmic scale. (C) Normalized PL spectra for the In-15% structure for excitation power ranging from 1 μW to 30 mW (red lines). Normalized μPL spectra for a single QD at two excitation powers (black and blue lines). (D) Ensemble PL broadening (black-colored dots) and QD energy separation between the first higher state and ground state (red-colored squares) for individual structures (shown over normalized PL spectra).

Additional information on the QD ensemble is contained in the spectral width of PL peaks. The full width at half maximum (FWHM) shown in Figure 6.3D is ~ 55 meV for the first five structures and ~ 25 meV for the dominating peak at 1380 nm of the In-38% sample (all determined at 100 μW excitation). A similar emission bands width indicates comparable inhomogeneity of the ensembles and similar distribution of the QD parameters, except of the In-38% structure characterized by a bimodal distribution (one around 1380 nm, more homogeneous, FWHM ~ 25 meV, and the long wavelength one significantly more inhomogeneous, FWHM ~ 130 meV, as presented in Figure 6.1). The determined energy separation between the first higher state and the ground state - ΔE_{sp} (based on PL but also supported by PLE characterization discussed in the following sections) is slightly smaller than FWHM for the first three structures, which makes the observation of higher state emission difficult but possible as shown for the example of In-15% sample.

6.2. POLARIZATION PROPERTIES

The selection rules for QD optical transitions are affected by the valence-band states mixing (mainly for heavy- and light-hole states), which depends on the confinement potential, i.e. the QD shape and strain. This mixing modifies exciton oscillator strength for particular transitions (as described in Section 2.1). The compressive strain present in self-assembled dots results in an increased states separation (driven by biaxial strain component), which translates also into decreased hole states mixing when compared to unstrained case. It usually favors heavy-hole as the ground state, as it is the case for InAs QDs on GaAs. Strain reduction increases the hole states mixing causing a larger light-hole admixture in the nominally heavy-hole ground state. This mixing results in ellipticity in the polarization of emission, i.e., an imbalance between the oscillator strengths of the optical linearly polarized orthogonal transitions. Indicated elliptical polarization is manifested by changes in the emission intensity, based on which the DOLP can be determined. Moreover, any in-plane asymmetry of the QD confinement potential may further increase the degree of emission polarization ellipticity due to the increase in the oscillator strengths difference and enhanced mixing of the hole states due to reduction of the their energy separation for elongated structures. Figure 6.4A shows the PL map as a function of the linear polarization angle in the 0 to 360 degrees range for structure In-29%.

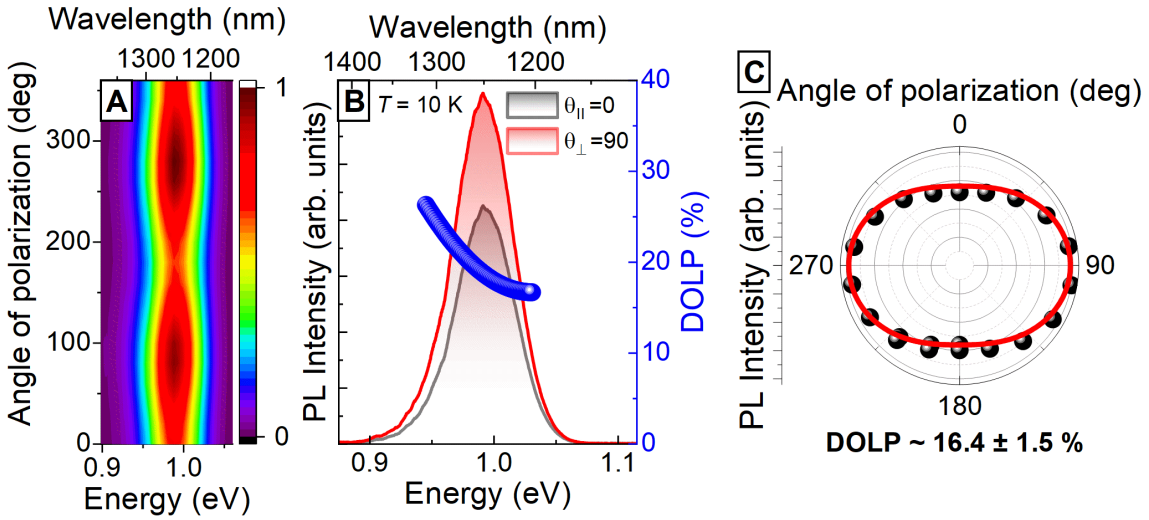

Figure 6.4. (A) The map of low-temperature PL as a function of linear polarization angle from 0 to 360 degrees for the In-29% structure. (B) PL spectra for the In-29% structure for two selected linear polarizations characterized by the highest (red line) and lowest intensity (black line). Determined DOLP value (based on Eq. (2.5)) as a function of emission energy (blue dots). (C) Integrated emission intensity for QD ensemble emission as a function of the angle of linear polarization, together with a fit based on Eq. (6.1).

Based on the analysis of the changes in emission intensity, a spectrum was selected with the highest (I_{MAX}) and lowest (I_{MIN}) PL intensity (see Figure 6.4B), the DOLP value was determined based on Eq. (2.5). In Figure 6.4B, the dispersion of DOLP within the emission distribution is added, with values ranging from 16% to over 26%. The increase of its value towards lower energy may be caused by enhanced HH-LH mixing, which would be the case for larger (higher) nanostructures emitting at longer wavelengths, even if the potential symmetry is not changed [49]. DOLP was also determined based on the changes in the total integrated PL intensity as a function of the linear polarization angle based on the following dependence [251]:

$$I(\theta) = A\big(1 + \mathrm{DOLP}\cos\big(2(\theta - \phi)\big)\big), \tag{6.1}$$

where θ is the angle of linear polarization, $I(\theta)$ is the PL intensity, A is the scaling factor, and ϕ is the angle for the maximum PL signal relative to the 0-degree mark in the setup. Figure 6.4C shows such dependence together with the fitting function according to Eq. 6.1, where DOLP above 16% was determined. Although it is an averaged signal for many dots of the ensemble, which can have slightly different geometries and orientations, the obtained value indicates significant HH-LH mixing in the investigated dots, possibly enhanced by some potential asymmetry. And actually, it is not contradictory to the data from structural characterization. Almost symmetrical QDs were found in the AFM characterization (Figure 5.13), but their sizes are larger than for typical InAs/GaAs dots, and the strain is lower, both decreasing the levels separation, so even a small shape anisotropy could induce significant valance band states mixing [49].

The influence of the excitation power and sample temperature on DOLP were also characterized, with results summarized in Figures 6.5A and 6.5B. A slight increase and then decrease in DOLP is observed with the excitation power, which may be related to the changed occupation of the higher states and hence also their possible contribution to the emission. These states may have different HH-LH mixing and DOLP values tending to rather enhance DOLP with increasing excitation [49]. However, the indicated range of DOLP changes from 15% to 19% is small, suggesting that this effect is not significant. It is also confirmed in a lack of systematic changes in DOLP (values scattered in the range of 15-20%) as a function of temperature, which also causes increased occupation of the higher states.

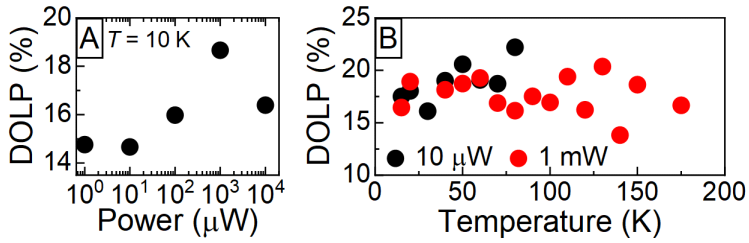

Figure 6.5. The value of DOLP determined via Eq. (6.1) as a function of (A) excitation power (values measured outside the cryostat) and (B) temperature for the In-29% sample.

The emission polarization was characterized analogically for all structures. The determined spectral dependencies of DOLP are plotted in Figure 6.6A. The DOLP increases from a few percent for the In-11% structure to about 50% for the In-38%. Thus increasing the indium content in MBL and QDs must be responsible for it. This effect may indicate an increased HH-LH mixing along with the strain reduction due to the decreased mismatch between the MBL and the InAs layer. Some changes in asymmetry of QDs may also contribute to increase in DOLP as it favors higher LH contribution. However, the results of structural characterization seems do not confirm this observation. However, the effective confinement potential does not need to have identical asymmetry axes as the QD shape asymmetry. The observed increase in DOLP may be related to the increased tendency of QDs to align along a common crystallographic orientation. Also, buried QDs may be more asymmetric than the reference ones. The strain reduction that occurs with

the indium content increase in the MBL may result in enhanced diffusion of indium for the specific crystallographic directions. All these factor may favor a strong tendency for QDs to be elongated and oriented similarly. Such an effect has been observed for low-strain InGaAs/GaAs QDs [93].

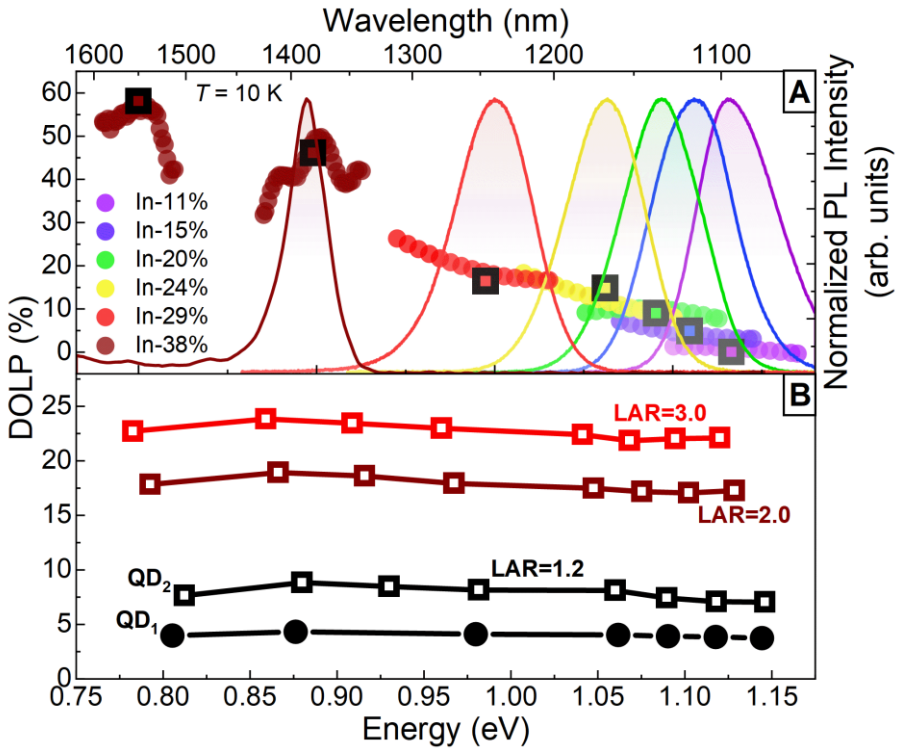

Figure 6.6. (A) DOLP values determined based on Eq. (2.5) (colored points) or (6.1) (black-colored squares) for individual samples (colored lines PL spectra) as a function of emission energy. (B) Calculated DOLP values[MG] for two dot geometries: QD_1: H = 5 nm, D = 40 nm (points), and QD_2: H = 6 nm, D = 30 nm (squares), and varying in-plane asymmetry (LAR = 1.2, 2.0, 3.0).

To understand better the influence of asymmetry and strain on DOLP, the optical characterization results were compared with calculations[MG] for the determined QD parameters, see Figure 6.6B. For both 5×40 nm and 6×30 nm geometries with LAR = 1.2 introduced in Section 5.6, no clear dependence of DOLP is observed on the emission energy and thus on the modification of strain associated with the MBL. Depending on the geometry, DOLP is above 3% for QD_1 and 6% for QD_2 for all x_{MBL}. In addition, considering possible changes in QD asymmetry, the DOLP of above 17% is expected for LAR = 2.0 and above 21% for LAR = 3.0. So, the QD geometry seems critical to get large DOLP values. Increasing height or asymmetry favors a stronger HH-LH mixing and increased DOLP. At the same time, an enlargement in the in-plane QD size (with fixed LAR) leads to a slight decrease in DOLP. A separate issue is the QD composition. The reduction of the indium content difference between MBL and QD also leads to lower strain in QDs, causing an increased LH contribution due to the smaller band splitting. Some differences between measured and calculated DOLP may be due to the limitations of the QD model based on limited structural characterization results. There are also possible residual strain conditions connected to the MBL. There is still the problem of the averaged signal from the entire QD distribution and possible differences in the orientation of individual emitters. These issues will be addressed in Subsection 7.5.3.

6.3. PROBING THE ENERGY STRUCTURE

In the investigated complex systems, details of the band structure concern, apart from QD states, also the states of WL expected to exists in the SK growth mode, plus the MBL and the capping layer, being the confinement barriers for the dots. The nominally lower indium content in the capping layer with respect to

the top part of the MBL (see explanation in Section 5.1) indicates that the MBL is the lowest potential barrier for the carriers in the dots. The presence of WL has not been fully confirmed for the studied structures. It may have a similar composition to the MBL due to the strong indium intermixing, thus hindering its recognition. The confinement potential and the entire energy structure are essential for processes of carrier supply and escape from QDs, which are crucial for the emission properties. Figure 6.7A shows the energy structure characterization results for the In-29% sample. The complex oscillations seen in PR are associated with the overlap of the response from the MBL, which is a compositional gradient structure with changing E_g, with the signal from the capping layer. The former, i.e. PR response from a semiconductor with gradually changed composition, shows usually such an oscillatory behavior [252], which in the simplest picture is an overlap of signals from different sample depths with different E_g. The cap band gap signal is expected to be superimposed with it, disturbing the oscillations but rather hard to be resolved. All this may be additionally complicated by Franz-Keldysh oscillations associated with the built-in internal electric fields at the surface and interfaces and sometimes observed above the band gaps of bulk-like materials (see Section 4.2). Therefore, the only information from this part of the PR spectra which could be derived unambiguously is the position of the lowest energy resonance associated with the band gap of the top part of MBL, which agrees well with the absorption edge observed in PLE (marked with red dashed line).

High excitation PL spectrum in Figure 6.7A shows a strong emission for energy slightly lower than the observed MBL band gap detected in the absorption-like spectra. It could potentially be connected with WL emission, very often appearing for very high excitation when all the QD states are filled up. But it is a bit contradictory to the estimations from calculations suggesting problems with confinement of electrons. Therefore, this peak is related to a transition between the weakly confined carriers in the WL, or just emission from the MBL shallow defects, agreeing with the absorption tail seen in PLE.

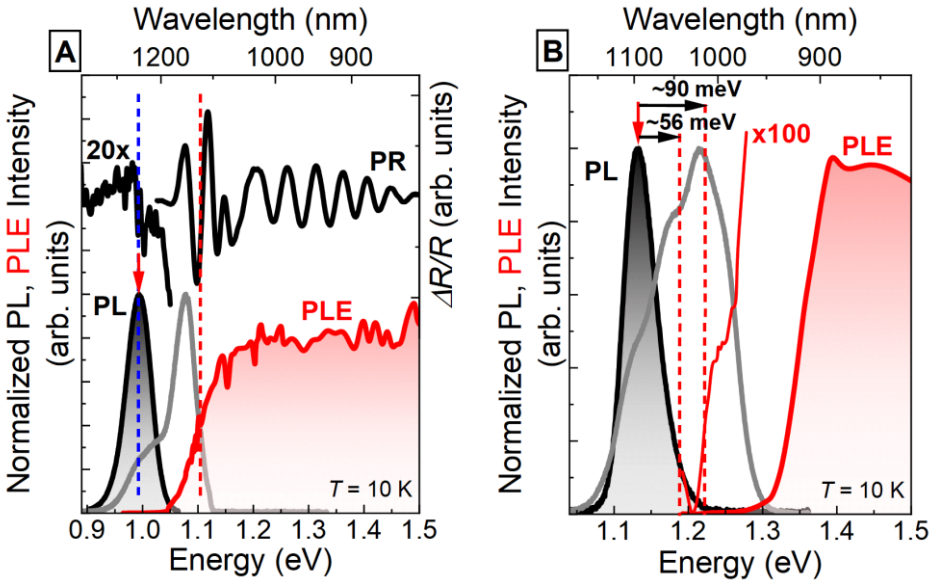

Figure 6.7. (A) Normalized PL (shaded peak), PLE and PR spectra for the In-29% sample. The vertical blue dashed line indicates the coincidence of the weak PR resonance with QD emission. The vertical red dashed line shows the coincidence of the PLE signal edge and the fundamental, most intense PR resonance. In addition, PL spectrum for the highest excitation power is shown (gray solid line). (B) Normalized PL and PLE spectra for the In-11% sample. The vertical red dashed lines indicate the excited state QD transitions in the case of PL spectrum for the highest excitation power (gray line).

After magnification, a weak signal associated with QDs is also observed in the PR spectrum (marked by the dashed blue line in Figure 6.7A). It agrees with the fundamental PL peak seen in both low and high

excitation spectra, also shown in this figure (black shaded peak and gray line, respectively). Low absorption cross-section of the dots resulting typically in low PR intensity, and hence also low signal to noise ratio [226,253], made difficult to detect higher QD states. The higher energy QD states could be observed in the high excitation PL and PLE spectra of sample In-11%, see Figure 6.7B. The lack of observation of an emission peak close to the MBL band gap in the case of this structure is perhaps related to a QD deeper confinement potential than in the case of the In-29% sample, which translates into more confined states (see also Figure 6.13 with the band structure schemes) making more difficult to fill up all the QD states. In Figure 6.7B, there is also added a 100 times magnified PLE spectrum which shows an additional weak signal, in the energy range below the MBL band gap show, approximately consistent with the higher QD transitions in the PL spectrum. The energy separation of the higher energy PL peaks with respect to the QD ground state transition are 56 and 90 meV, respectively.

Figure 6.8 shows similar results for all samples. Based on the results from PR and PLE and comparing with QD ensemble PL energy peak, the energy differences between the QD ground state and the band gap of the MBL barrier (i.e. its top part) were determined. For the In-38% structure, the analysis does not include the PR spectrum, because the signal was significantly disturbed by the presence of the DBR. The latter causes strong changes in the reflectivity, which were also modulated apparently with the carriers photogenerated by the modulating laser beam (effect know from modulation spectroscopy [226,254]). It made impossible to distinguish the MBL band gap signal.

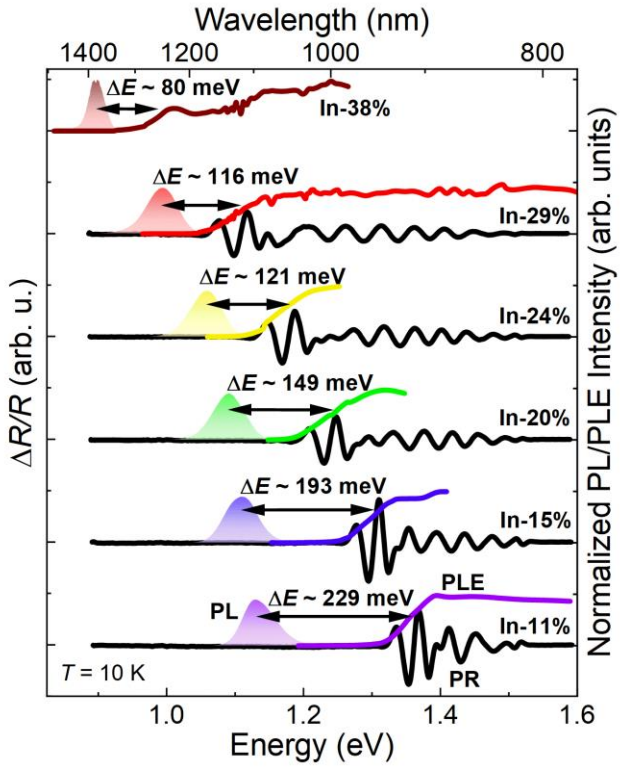

Figure 6.8. PR (black lines) spectra for particular structures and normalized PL (colored area) and PLE (colored lines) spectra. Indication of energy distances (ΔE) between MBL and QD emission energy.

The determined energy differences noticeably decrease with the increase of the indium content in the MBL (from about 230 meV for structure In-11% to about 80 meV for In-38%), i.e. the QD confinement potential gets shallower for the samples with higher MBL indium content. The main reason is that the MBL energy gap depends only on the material composition resulting in its faster change compared to QD ground state energy driven rather by changes in the strain conditions (the QD composition is approx. constant, affected perhaps by some MBL-composition-dependent intermixing, and has only changed for the last two structures). Consequences of the QD confinement modifications will be discussed yet in the next sections.

More detailed analysis of the In-38% structure shown in Figure 6.9 allows the observation of the PL signal for QDs emitting around 1380 nm and 1550 nm (vertical black and red arrows) due to the bimodal distribution of the QD parameters. Therefore, the PLE spectra were measured with detection set at both of the wavelengths. The black line represents the PLE spectrum for detection at 1380 nm. Whereas the red PLE plot corresponds to detection at 1550 nm. In this case, apart from the MBL PLE signal an additional PLE peak agreeing with the QD emission maximum at 1380 appears. It indicates clearly the existence of the energy/carriers' transfer between the two dots families. Although it is hard to indicate the exact mechanism of this transfer, it is in agreement with several other observations (described in the following sections of this Thesis) and previous reports in other QD systems [255–261].

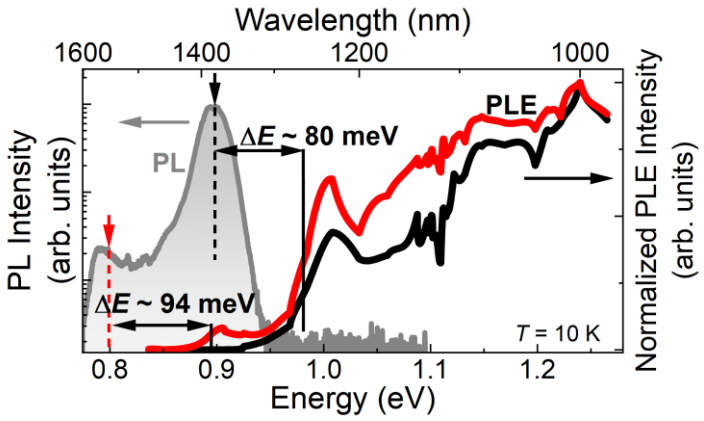

Figure 6.9. The PL spectrum and normalized PLE spectra for two detection energies (emission maxima at 1380 nm and 1550 nm for black and red plots, respectively) for the In-38% structure. Vertical dashed lines indicate the QD emission energies; solid lines mark the characteristic PLE signal; energy differences between these are marked with horizontal arrows.

6.4. TEMPERATURE DEPENDENCE OF EMISSION FROM QD ENSEMBLES

QD emission properties also depend on the temperature. First of all, with the temperature increase, the crystal structure expands, and the energy gap of the material is reduced, which results in a shift of emission to lower energy (following Varshni's dependence). Also, the thermal energy enables the excitation of carriers to higher-energy states, thus reducing the emission intensity or resulting in the redistribution of carriers within the QD ensemble. In addition, the interaction with phonons also increases the FWHM of the QD emission (as described in Section 2.4), however, this broadening is only observed in single QD emission spectra (discussed later in Section 7.3).

Figure 6.10A shows a series of selected PL spectra for the In-29% structure as a function of temperature, with the excitation power of 1 mW, providing an appreciable signal at elevated temperatures. A standard decrease in emission intensity with increasing temperature is observed due to the expected enhanced carrier losses and non-radiative processes. Changes in QDs emission as a function of temperature are analyzed based on the integrated emission intensity, the energy of PL maxima, and FWHM. Figure 6.10B shows the emission energy and the spectral linewidth versus temperature. A faster decrease in the emission energy than the standard Varshni relationship for $In_{0.6}Ga_{0.4}As$ bulk material is observed. This effect is typically interpreted by thermally-activated redistribution of carriers towards those with lower energies (larger dot size or higher indium content) [259–261]. The reduction of the spectral width of the emission supports such scenario (a subset of QDs has a narrower distribution) [262,263]. The thermal energy activating this process

is too small ($k_B T$ energy is about several meV) to promote the carriers directly to the wetting layer,[18] so other mechanism would need to be involved. One possibility can be a carrier transfer via indirect defect states, if they match energetically and their concentration is sufficient. It can need some additional thermal excitation when the QD and defect energy levels do not match exactly, which is expected for a random system. There are also reports showing the possibility of direct tunneling between the dots, which can be responsible for carriers' redistribution, if the dots' spatial separation in the plane is small enough. It can take place even for relatively low QD densities, when there are some other reasons, of e.g. technological origin, which cause clustering of the dots in some areas of the sample (see e.g. here – Ref. [256,257]). It seems also probable in the case of the investigated QD structures in their denser areas – see Figure 5.13. Another possible scenario is dipole-dipole coupling between different dots, which can become a long-distance excitation transfer when mediated by the electromagnetic field of the emitted light, and it can be observed even if the dots are not located in any cavity [255]. But in fact, the exact mechanism could not be recognized in these structures, but the experimental observations are hardly explainable without involving a redistribution processes, which already occurs at very low temperatures apparently.

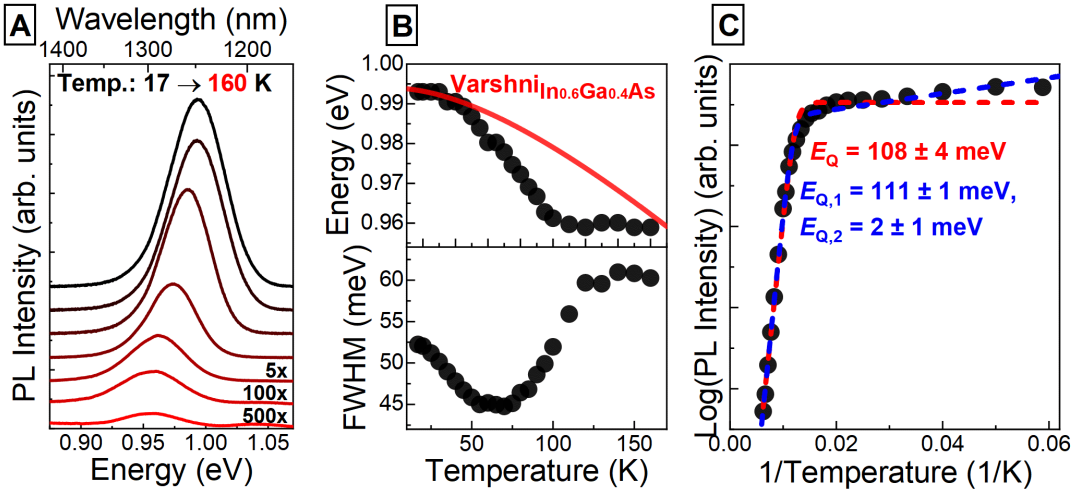

Figure 6.10. (A) PL spectra as a function of temperature from 17 to 160 K for the In-29% structure. (B) Dependence of energy (top panel) and FWHM (bottom) as a function of temperature (points). The line shows the Varshni dependence [264] for $In_{0.6}Ga_{0.4}As$ material (red line). (C) Integrated QD emission intensity as a function of the inverse of temperature (points). Lines show fits with dependences with one (dashed red, Eq. (6.2)) or two (dashed blue, Eq. (6.3)) energies of escape processes.

Figure 6.10C shows the emission intensity (in logarithmic scale) as a function of temperature inverse. The quenching of emission is associated with stronger impact of non-radiative processes at higher temperatures including losses of carriers confined in the dots (e.g. escape to the barriers). The analysis of the presented relationship allows for estimating the energy necessary for carriers to escape – activation energies. A dependence for a single escape process (red fitting curve) is:

$$I(T) = \frac{I_0}{1 + A \exp\left(-\frac{E_Q}{k_B T}\right)}, \tag{6.2}$$

where $I(T)$ is the PL intensity at temperature T, I_0 is the intensity at 0 K, A is the scaling factor, E_Q is the activation energy for the escape process, and k_B is the Boltzmann constant. The fitting yields an activation energy of about 108 meV. However, this fit does not match experimental data in the low temperature range

[18] According to the calculation results the WL, which is in a very thin quantum well with asymmetric barriers does not confine the electrons, so it could not be a carrier loss channel.

(slight reduction in emission intensity for $1/T$ = 0.02–0.06 1/K, i.e. T = 17–50 K). Thus, an additional fit (blue curve) is made for two escape processes:

$$I(T) = \frac{I_0}{1 + A_1 \exp\left(-\frac{E_{Q,1}}{k_B T}\right) + A_2 \exp\left(-\frac{E_{Q,2}}{k_B T}\right)}, \tag{6.3}$$

where two activation energies, $E_{Q,1}$ and $E_{Q,2}$, are introduced. This fitting gives a similar activation energy for the primary escape process equal to about 111 meV and a low activation energy of about 2.0 meV. This low activation energy can be related to the excitation of carriers to higher states with lower emission intensity (due to lower oscillator strength) as it is too small to release the carriers from the dots.

A similar analysis was performed for all the structures. Figure 6.11 shows peak emission energy and PL broadening plots for the first five structures (In-11%, In-15%, In-20%, In-24%, In-29%).[19] The range of measurements is limited by PL quenching, with a different temperature range effectively available depending on the MBL composition. An analogous deviation of energy from the Varshni relation is always observed. In addition, the FWHM dependencies also show a deviation from the expected increase with temperature. All these results suggest the presence of a redistribution process for all structures [263], but just activated at different temperatures (due to differences in the QD electronic structure). On the other hand, this process is rather not noticeable in quenching with increasing temperature because it does not result in the loss of carriers within the entire distribution of dots. The redistributed carriers reach other QDs with lower energies and they recombine there radiatively resulting only in the demonstrated changes of the PL peak broadening and its energy (corresponding now to smaller subensemble of dots).

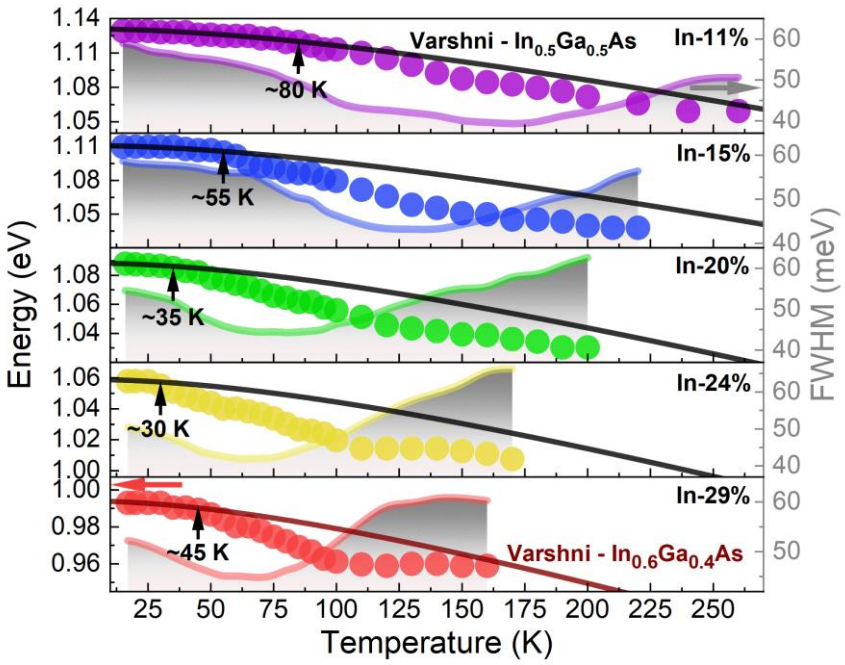

Figure 6.11. Energy (colored points) and FWHM (colored lines) for QD ensemble emission as a function of temperature for the following structures: In-11%, In-15%, In-20%, In-24%, and In-29%. Additional black and brown lines show the Varshni dependences for $In_{0.5}Ga_{0.5}As$ or $In_{0.6}Ga_{0.4}As$. Arrows indicate the starting points of divergence of results from the Varshni relation.

[19] The complex, double band character of the PL spectra of the In-38% structure, modified additionally by the presence of a DBR, made it difficult to analyze the temperature dependence unequivocally, therefore it is not added to Figure 6.11.

A more important issue, also from the application point of view, is the process of complete escape of carriers from the dots, limiting the temperature range at which emission can be observed. As already shown in Figure 6.11, different activation energies for different samples allowed for characterizing the emission in different temperature ranges. Figure 6.12 compares the larger of the activation energies based on Eq. (6.3) with the energy differences between the QDs and the lowest-energy states in the MBL, forming the barrier (in accordance with Figures 6.8 and 6.9). Good agreement of the determined energies indicates the escape of carriers into the MBL as a process responsible for the PL quenching.

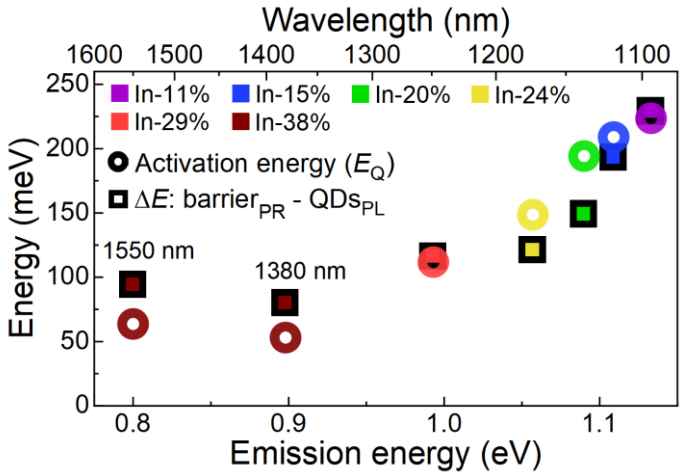

Figure 6.12. The energy difference between the QD ground state and the lowest energy state in the MBL (black-colored squares) and activation energies E_Q (empty circles) as a function of the QD emission energy for successive structures with varying MBL indium content (In-38% emission is split into parts around 1380 nm and 1550 nm).

Based on the calculation results, Figure 6.13 shows the energy diagrams for three selected structures: In-11%, In-29%, and In-38%.[MG] The determined activation energies (especially for the first five structures) are consistent with the sum of energies needed for the electron and the hole in a QD to be excited to the MBL, plus the exciton binding energy (about 13–15 meV). For the In-11% structure, the mentioned sum of energies is about 220 meV which perfectly agrees with the activation energy of 223 meV. Similarly, for the In-29% structure, a good agreement between 106 meV and 112 meV, respectively, is found. These results are in agreement with the mentioned previously property of the wetting layer which in these structure does not confine the carriers therefore cannot operate as the carrier loss channel.

The case of the In-38% structure is more complicated due to the complex QDs' distribution. For QDs emitting around 1380 nm, the higher activation energy is about 53 meV whereas the lower is 18 meV, which may indicate separate electron and hole escape or two different channels for carrier escape. The sum of these two energies is about 71 meV, close to the energy difference between QD and MBL states (about 80 meV presented in Figure 6.12), which seems to agree with the scenario of separate escape of carriers to the MBL. The respective activation energies determined for the second family of QDs within this structure have similar values (about 64 meV and 13 meV, together giving about 77 meV). In this case, the larger of the energies can actually correspond to both, electron activation (confinement energy of 42 meV) or hole activation, with rather lower probability (82 meV of confinement, according to Figure 6.13). In that respect, the smaller activation energy may be responsible for thermal spreading of the occupations to higher QD states mainly in the valence band where the ladder of levels is denser and their separation smaller.

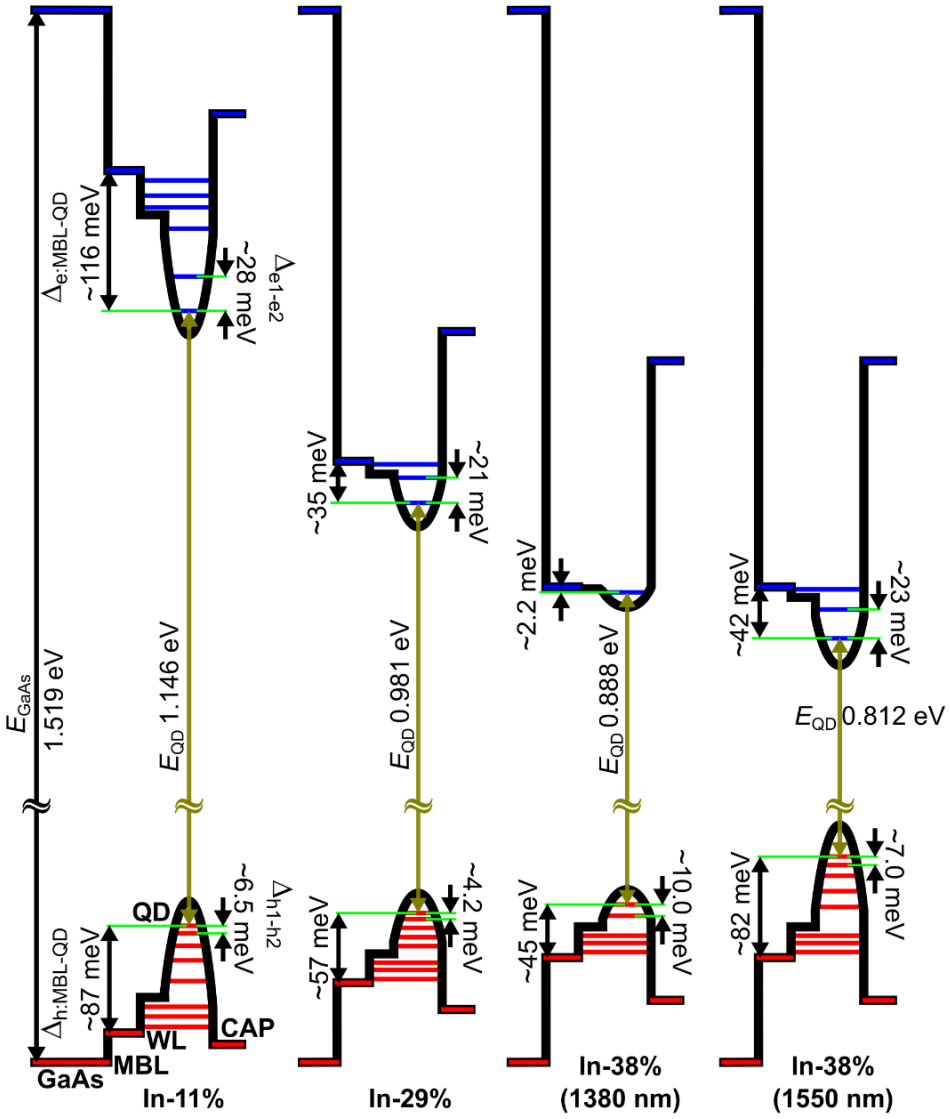

Figure 6.13. A diagram of the energy structure based on the advanced calculations[MG] for the structures of In-11%, In-29%, and QDs emitting at about 1380 nm or about 1550 nm for the In-38% structure.

6.5. Emission Dynamics

Emission dynamics in semiconductor structures, including QDs, results from radiative exciton recombination and non-radiative (energy dissipation without emitting photons from QDs) processes. The characteristic PL decay time is related to the competition between these processes. The radiative lifetime of the exciton depends on the oscillator strength of the optical transition, which is also dependent on the confinement potential. In addition, the carrier supplying processes after the optical excitation also affect the emission decay by modifying the occupation of different excitonic states. These consist of possible thermal escape to surrounding states near QDs (presented in Figure 2.3C) and thermalization of the carriers to the QD ground states. Due to indicated impact of different processes, PL decay time measured at low excitation power and low temperature should be close to radiative lifetime due to limited thermal occupation of the higher states and limited probability of non-radiative processes. Typical PL decay times for InAs QDs emitting below 1200 nm are 0.5–2.0 ns [14,68,69,265–267]. Based on the time-resolved measurements, the PL decay times for the QD ensemble are derived for the studied structures. Exemplary low-temperature results for structure In-29% are presented in Figure 6.14A. A series of decays for different emission

wavelengths was obtained – see Figure 6.14B, showing significant changes in the decay dynamics. Figure 6.14C is a plot of the PL decay times spectral distribution across the QD ensemble PL band for low excitation power. A relatively wide range of times was obtained from almost 0.7 ns for higher emission energies to almost 1.3 ns on the low energy side of the emission band (obtained based on fitting with a single exponential decay). The decay times may vary within the QD ensemble due to several different reasons, which can actually coexist. The first one is a redistribution of carriers from high-energy dots to the lower-energy ones [23,259,261], which is probable, as it agrees with the observations in PL temperature dependence and in PLE spectra. Such transfer works for the high-energy dots as non-radiative losses, so it shortens the PL decay. On the other hand, it delays the emission from the low-energy dots. Other mechanisms involved can be some contribution of exited states to the emission, characterized rather by a faster decay time due to additional relaxation to lower-energy states, and variations in confinement potential within the ensemble (QD size and indium content) causing a spectral distribution of the QD transitions with different oscillator strengths with typically a similar tendency of shorter lifetimes for the higher energy dots (at least in the strong confinement regime).

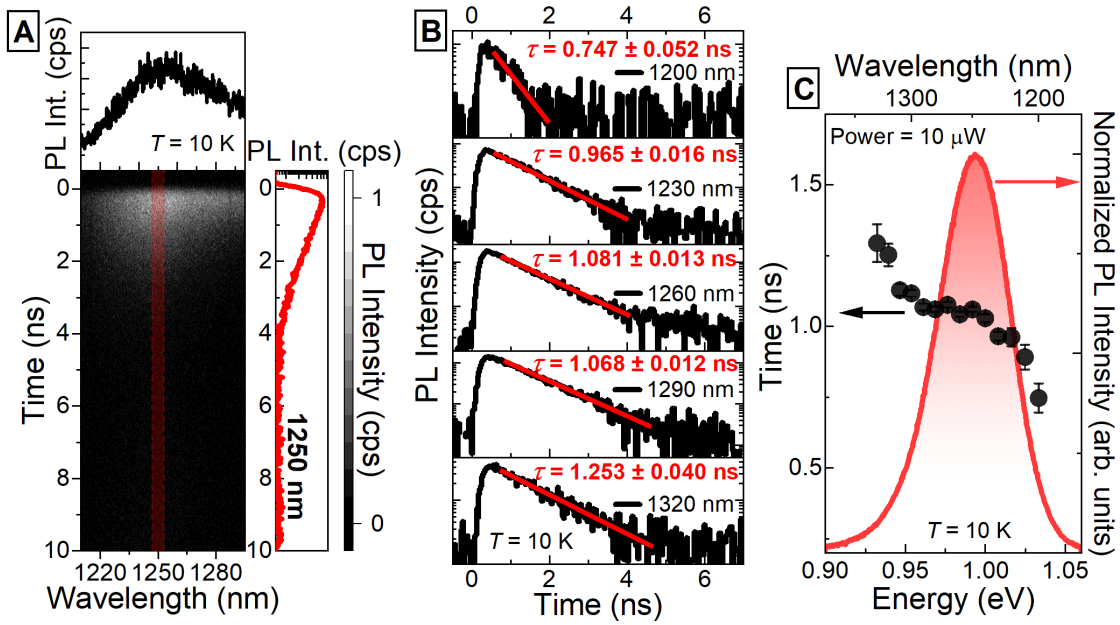

Figure 6.14. (A) Time-resolved emission map from the streak camera, together with the PL spectrum integrated against the entire range of times (top panel) and PL decay (right panel) for the selected emission wavelength (cross-section marked in red). (B) Series of emission decays for successive wavelengths together with decay times based on fitting with an exponential (red lines). (C) Normalized emission spectrum for the In-29% sample (colored line) and decay times for different emission energies for the lowest excitation powers (black dots).

Similar characterization for all the structures allowed determining the decay times in a wide range of the emission energy associated with modification of the MBL, as shown in Figure 6.15. Decay times for PL peak ranging from ~1.0 ns for the In-11% structure to ~1.3 ns for In-38% (within the third telecom window) are obtained. They are comparable to standard InAs QDs emitting below 1200 nm [68,69,265,267]. The decay time increases with emission energy reduction in a manner roughly following the inverse energy trend (marked with the black solid line), characteristic for nanostructures in the strong confinement regime (as described in Section 2.4). In the case of QDs emitting at ~ 0.9 eV (In-38% structure), a different, more steep spectral dispersion of the decay times is observed, with values up to 3 ns. The very long times seems to be consistent with the weak electron confinement within this QD family (as was demonstrated by the calculations shown in Figure 6.13), which can translate into smaller electron-hole wave functions overlap (smaller oscillator strength).

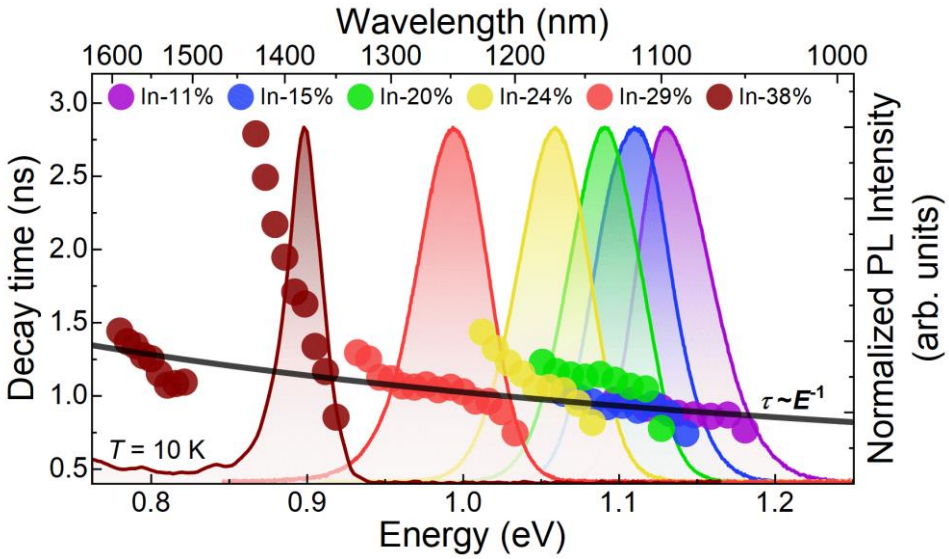

Figure 6.15. Decay times (determined for the lowest excitation powers) as a function of emission energy for successive structures (colored points) together with normalized emission spectra for individual samples (colored lines). Comparison with the dependence of the inverse of the emission energy (black line).

The determined values of decay times, corresponding to the PL peak positions, as a function of emission energy for all the investigated structures seem to match approximately the 1/E dependence, which suggests a small contribution of the non-radiative processes related to defects under these conditions, and indicates similarly good structural quality for all structures.

The influence of temperature on decay times for an example of the In-29% sample was also analyzed, which is shown in Figure 6.16. The temperature dependence of the decay times was determined for three selected energies within the QD ensemble emission band (marked with colored arrows in the inset of Figure 6.16).

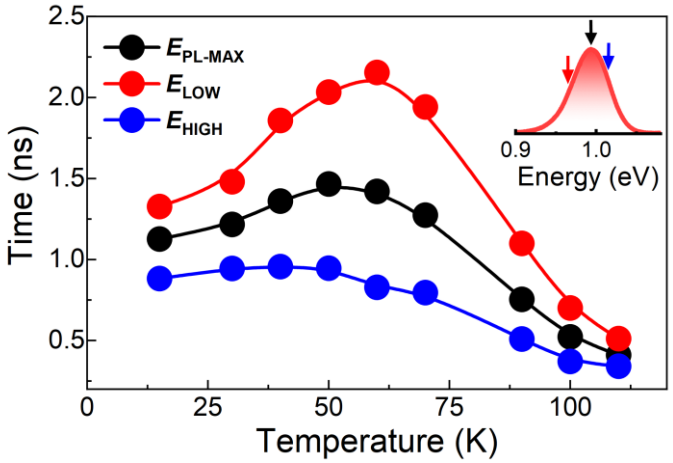

Figure 6.16. Decay times for the QDs emission from the different spectral parts of the ensemble QDs emission (PL spectrum included in the inset) as a function of temperature.

In addition to the expected and common observation of decay time reduction at higher temperatures, resulting from the increased probability of non-radiative processes (e.g., more efficient carrier escape from QDs), an increase in the decay time for temperatures in the range up to approx. 60 K is also observed. The effect is evident for two characterized emission ranges, low-energy (red) and PL peak (black), and less pronounced for the high energy part (blue). Such a trend has already been observed for other self-assembled QDs [268,269] and can be explained thermally activated spreading of carriers (occupation) over higher

energy levels (here mostly the less separated hole states) and the consequent increase in the radiative lifetime (decreased probability of radiative recombination). The effect should be weaker for the higher energy dots with larger energy distances to the excited states, in agreement with the observation in Figure 6.16. In addition, the already mentioned carriers redistribution occurring in similar temperature range (see Figure 6.11) can add up here, as it will cause shortening of the decay times for higher-energy dots (blue arrow on the PL spectrum in the inset) with respect to the low-energy ones (red arrow).

7. EMISSION PROPERTIES OF SINGLE QDS

7.1. SINGLE QD EMISSION IN THE TELECOM RANGE

Devices for quantum technologies, including secure quantum communication based on QDs, require employing single emitters. Thus, the optical properties of individual QDs play a crucial role. In that context, realizing a true single-photon source requires using a single QD emission. It is insufficient only to know the properties of QD ensemble to predict the suitability of particular QDs as emitters of single photons or entangled photon pairs, as it provides only averaged optical information on the system under study. Although the characterization on the ensemble level is necessary when developing new material and understanding the general trends and factors driving the electronic and optical properties, only a comprehensive in-depth study of single QDs allows determining their potential for quantum technology applications.

Investigation of the emission from single QDs has been performed for five structures: In-15%, In-20%, In-24%, In-29%, and In-38%, where the last emits in the range of third telecom window. It allowed detecting spectrally narrow QD emission lines from 1100 nm to 1600 nm. Figure 7.1 demonstrates examples of single QD lines for all these structures.

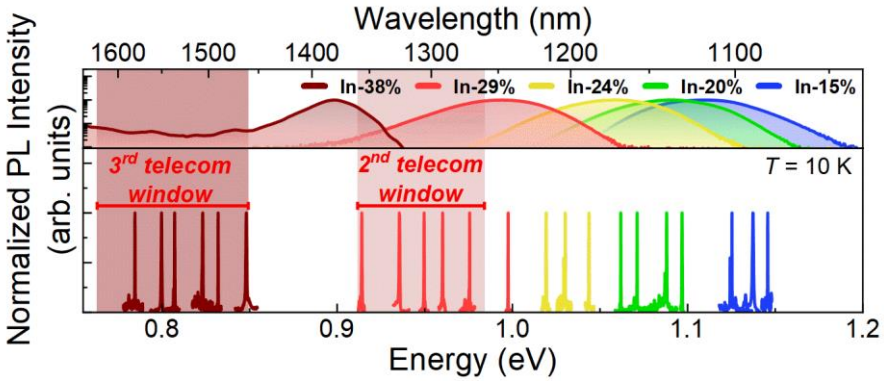

Figure 7.1. Top part - PL spectra of QD ensembles (in log scale). Bottom part - selected single QD emission lines in the 1100–1600 nm range, including the second and third telecom windows (marked by the shaded areas).

This chapter presents below a detailed characterization of the optical properties of single QDs in the selected structures. An important issue (already discussed on the QD ensemble level) is the impact of the MBL properties. Section 7.2 focuses on the quality of QDs (relation between radiative and non-radiative processes) in the context of single QD excitonic emission, including the influence of the environment on the linewidth, due to the MBL and processing necessary for single QD measurements. Section 7.3 presents the analysis of the effect of temperature and related carrier-phonon interaction on single QD emission. Section 7.4 studies the influence of the environment on single QD emission under various excitation conditions. The following Section investigates individual excitonic complexes and their optical properties. The polarization properties and binding energy are analyzed, and a reference to the exciton confinement regime is made. Further, photon cross-correlation spectroscopy measurement results are presented to confirm the origin of lines. Section 7.6 discusses the characteristic PL decay times for single QDs, whereas the last Section 7.7 describes the single-photon emission from QDs under continuous and pulsed excitation (CW and triggered mode), indicating the possibility of implementing the investigated QDs as single-photon sources operating in the second and the third telecom windows.

7.2. MAIN CHARACTERISTICS OF SINGLE QD PHOTOLUMINESCENCE

Single QD emission dynamics directly depends on the oscillator strength of optical transitions, the rates of generation and relaxation of carriers, and the resulting states' occupation. In addition, any degradation of

structural quality of QDs and their surroundings may favor non-radiative recombination processes decreasing the decay time and affecting the internal quantum efficiency (IQE), which is very often assumed to be 100%. The internal quantum efficiency describes the ratio of the radiative recombination rate to the sum of radiative and non-radiative recombination rates. The ideal IQE can be thus reduced due to non-radiative recombination processes [59]. It has been demonstrated that the assumption on IQE ≈ 1 can work well for good quality materials, i.e., QDs obtained within mature technology [57], but its value can be limited for structures where the surrounding layers contain a significant concentration of defects and carrier traps [270]. These may result from strain engineering applied to shift QD emission [59]. As determining the internal quantum efficiency directly from measurements is hardly possible, the emission intensity is analyzed and shown in Figure 7.2A for individual QDs under the excitation conditions assuring saturation, i.e., the maximum emission intensity. The intensity of all emission lines is normalized with respect to the most intense case of all structures. This approach allows comparing quantitatively the emission intensity between successive structures, which should at least partly allow comparing the QD optical quality dependent on IQE, where non-radiative processes play a key influence. However, it is also necessary to take into account the dependence of oscillator strength (exciton lifetime) on emission energy which also affects the QD emission intensity (different number of emission acts per unit time). The median value of the normalized PL intensities is about 0.3–0.4 for the structures emitting in the 1100–1300 nm range and lower for In-38% emitting in the third telecom window (emission at around 1380 nm is not included in the characterization of single QDs). The lack of significant intensity changes for the In-15%, In-20%, In-24%, and In-29% samples confirms their similar optical quality, regardless of the modifications in the strain conditions and the carrier confinement, both induced by changes in the MBL. For the In-38% structure (highest MBL indium content; emission above 1450 nm), the relative median intensity is about 0.15, which suggests decreased material quality. The highest relative intensities reach about 0.4 for these dots, which is about twice lower than the strongest emission for other structures. However, this reduced intensity can be partially explained by increased emission decay times as pre-determined for QD ensembles already (see Figure 6.15) and then characterized for single dots in Section 7.6. But the lifetime changes could explain only at most a 50% decrease in emission intensity, therefore its reduction definitely occurs in part at least due to enhanced non-radiative recombination.

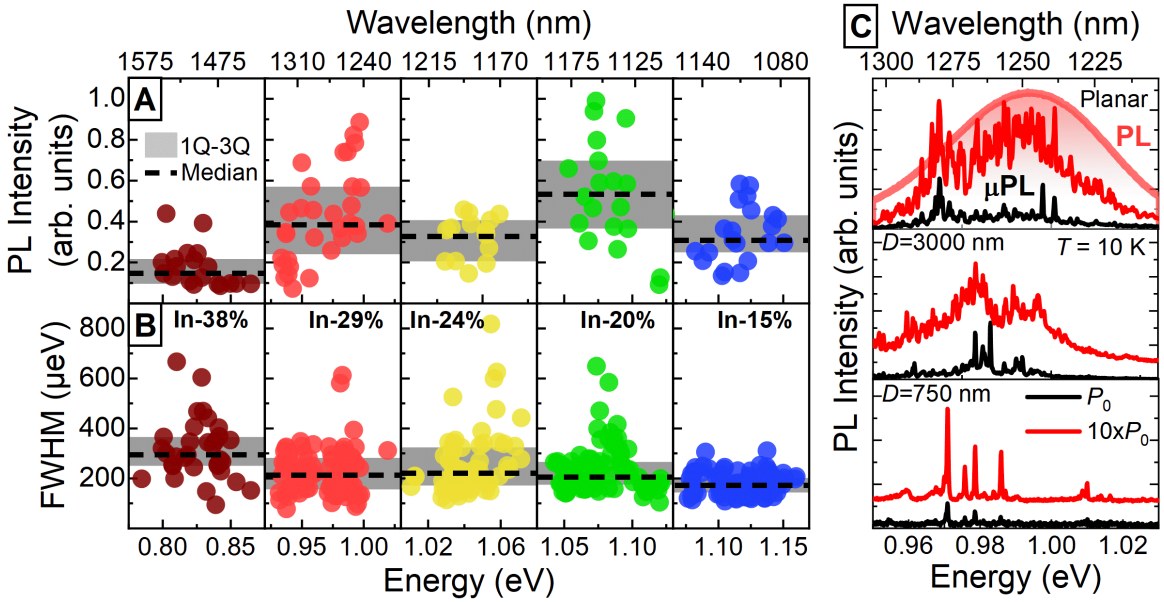

Figure 7.2. (A) The intensity and (B) line broadening for low-temperature single QD emission for studied structures with the first and the third quartiles and median values marked. (C) QD emission spectra for In-29% structure for planar (unmodified surface) and mesa structures (see Section 5.1) with diameters of 3000 nm and 750 nm.

The oscillator strength of optical transitions determines the radiative lifetimes and hence the homogenous part of the PL lines' broadening. For standard InAs QDs with decay times of about 1 ns [14,68,69,265,267], the resulting "natural" spectral broadening should be below 1 μeV. However, especially at elevated temperatures, the interaction with phonons cannot be neglected [71,72,271,272], and additionally broadens the emission lines. In addition, there is also a significant contribution of spectral diffusion, which is actually usually the dominant factor causing inhomogeneous broadening 1–2 orders of magnitude larger than the homogenous one at low temperatures (see Section 2.4 [71]). A summary of the FWHM values for many lines of all the structures is shown in Figure 7.2B. The linewidths range from 70 μeV to 800 μeV, where most cases fall between 100 and 400 μeV. Despite the significant dispersion, the median values of approximately 170 μeV for the In-15% structure and 300 μeV for the In-38% were obtained. Thus, there is a slight tendency for the FWHM to increase with the QD emission shift to longer wavelengths, being a fingerprint of increasing spectral diffusion. These are rather large linewidths compared to the best quality III-V QDs, with values even below 50 μeV reported for non-resonant excitation [157]. It suggests more significant spectral diffusion in the investigated MBL-based samples. On the other hand however, the obtained linewidths are comparable to those reported for other QDs grown on MBL in different technologies [124,153,154], and QDs grown under reduced stress conditions in InAs/InP [80,175] and InAs/GaAs [273,274] material systems. The MBL layer is expected to contain built-in defects and charge traps near the QDs, which are sources of the electric environment fluctuations occurring due to illumination-generated carriers or built-in excess carriers in the structure (unintentional doping). The observed slight trend of increasing linewidth with decreasing emission energy is most likely related to the modification of the indium content and the thickness for the MBL structure, probably favoring larger concentration of defects [124,152,153]. Therefore, the largest FWHM is observed for the In-38% structure. A shallower carrier confinement potential QDs on In-rich MBL (see Figure 6.8 and the related discussion) and possible QD elongation can also cause higher QD sensitivity to the electrical environment.

To characterize the emission of single QDs, fabrication of additional mesa or aperture structures were needed, as explained in Section 5.1. An interesting issue is the possible impact of surface processing (mesa or aperture creation) on the QD emission broadening, especially for the In-38% structure characterized by the largest FWHM values. For this sample, both mesa and aperture structures were fabricated. For the mesas, their sidewalls (etching edges) are able to cumulate charges on the surface states and hence can be a strong source of electric field fluctuations under illumination, which is especially important for QDs located close to the sidewalls. This effect should not be observed in the case of the apertures, where no etching has been carried out and there are now sidewall states. Nevertheless, the deposition of the cover layer and removal of the cover layer for selective deposition of the silver layer may also have an effect on the surface quality, possibly also enhancing the spectral diffusion. Additionally, considering the small thickness of the capping layer of ~60 nm, the effect may not be negligible for the buried, optically active dots. To make a comparison, the emission linewidth is characterized for these structures and compared to the planar (unprocessed) structure while measured in the same setup and maintaining similar excitation conditions. As presented in Figure 7.3A, the single QD lines exhibit larger FWHM for the processed structure. As seen in Figure 7.3B, the median FWHM values of approximately 374 μeV characterize the planar structure, and 417 μeV and 530 μeV is obtained for the apertures and mesas, respectively. These results indicate an effect of processing on the QD charge environment enhancing the spectral diffusion, which should be expected and was very often reported. The difference between the planar structure and the sample with apertures is relatively small, below 40 μeV, most likely because the fabrication process caused less surface modification when compared to the mesas with their sidewalls. Therefore, the determined FWHM increased by about 150 μeV for the latter. The significant spread of the FWHM values can be explained by dependence on the exact location of a given QD, i.e. how close it is to the charge fluctuation source. However, the still

significant FWHM for even the planar structure indicates an impact of the direct QD electric environment associated with the MBL, which seems to be the dominating factor for all samples.

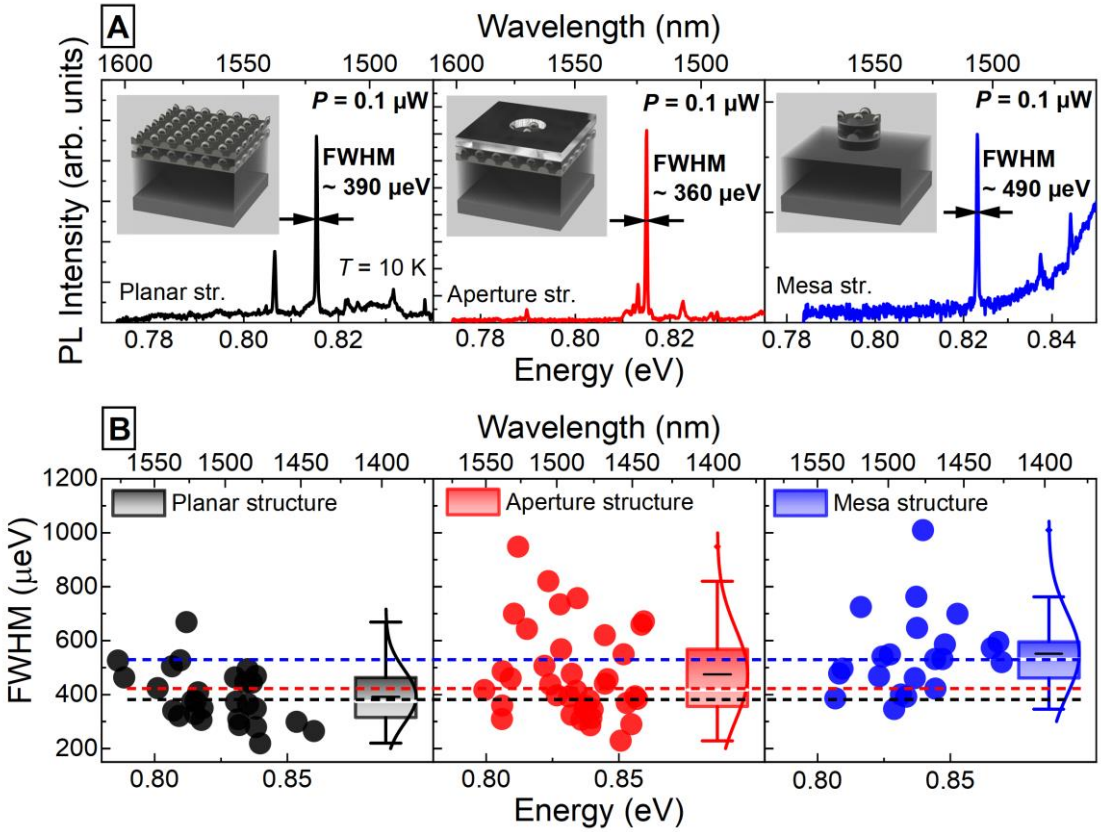

Figure 7.3. (A) Emission spectra for the In-38% sample: for the planar structure (black line), the structure with apertures (red line), and the structure with mesas (blue line). Insets show the type of structure schematically. (B) Emission line broadenings in the corresponding structures. For each structure, the median broadening values (dashed lines), and a box plot characterizing the distribution of values (minimum value, first quartile, median value, mean value, third quantile, maximum value).

Besides additional contribution to inhomogeneous linewidth, mesa or aperture structures ensure the necessary reduction of the number of probed QDs and repeatability of the measurements. The structural characterization shows a surface density of above 10^{10} cm^{-2} (about 100 dots per 1 μm^2) for all the samples. When illuminating the planar structures via a microscope objective (see Subsection 4.2.2 for details), the diffraction-limited spot diameter is about 1–2 μm (1–4 μm^2 area), i.e., the number of excited QDs is usually a few hundred. Fabricating the mesas or apertures allows limiting the actually probed areas to below 1 μm^2 (below 100 QDs). This is a normally employed approach to decrease the number of investigated QDs so that single emission lines can well resolved in the spectra as show the examples in Figure 7.2C. Usually, only 10–20 lines are observed from a mesa, less than the estimated number of QDs. The reasons can be manifold. First of all, the determined QD densities might slightly overestimated due to choosing areas with many dots (instead of those with a small number of QDs) in the AFM characterization, from the strongly nonuniform QD distribution in the structure correlated with the noticeable cross-hatch pattern (as shown in Figure 5.13). So, the density inside the patterned areas fabricated randomly is probably usually lower, down to few tens of dots. Second, the PL measurements may underestimate the number of QDs due to the selection at the initial stage of characterization mainly those mesas or apertures that showed bright and better resolved lines, as opposed to areas showing weak or no emission or those showing too dense emission patterns. Some of QDs can be "switched-off" by the states on the mesa sidewalls, which for the nearest dots can work as non-radiative channels of carrier losses, i.e. some of the dots are excited but are optically inactive and do not contribute to the PL spectrum. In the case of apertures, QDs outside the central region may show weaker

emission due to the limited signal detection partly blocked by the silver layer and due to diffraction at the aperture edges. Finally, it is possible that only part of QDs is optically active even in a structure without additional patterning due to the nonradiative recombination centers associated with defects in the MBL. It is worth underlining here that in the case of the In-38% structure, the density of QDs (based on optical characterization) emitting in the third telecom window is even lower, because the observation range is intentionally limited spectrally to about 1450–1600 nm, i.e. to the very tail of the entire emission band (see, e.g., Figure 7.1). Therefore, measurements on the larger mesas or apertures with diameters above 1 μm could be carried, allowing to still resolve single QD lines. Based on the number of emission lines detected in this range the estimated density of these 3rd telecom window QDs is below 10 per μm^2.

7.3. TEMPERATURE DEPENDENCE OF EMISSION FROM SINGLE QDS

As already mentioned before, the thermally-enhanced interaction of the QD confined excitons with phonons, and the modification of the crystal lattice may affect the QD emission properties. Typically, a reduction in emission energy and intensity is observed with increasing temperature. For single QDs, the interaction of an exciton with phonons may be more apparent than in QD ensembles due to the lack of averaging of properties over the entire set of dots. In particular, for a QD ensemble, the thermally-induced excitation of carriers to excited states or even the wetting layer does not necessarily mean that these carriers were lost for radiative recombination: they can be re-trapped by QDs and still contribute to ensemble PL. It is the opposite for the emission from a specific state in a single nanostructure, where excitation to a higher state can lead to a loss in emission as the carriers escaping from the particular dot and re-trapped by another one is lost for the radiative recombination in the first one.

Single QD emission was measured as a function of temperature for the same sample as in the previous Section (In-29%): see examples in Figure 7.4A (investigated QD emission marked by the red box). The primary effect is the PL peak redshift with temperature (see Figure 7.4B), however, deviating from the standard Varshni dependence for InAs and GaAs bulk material (one would expect that for single InGaAs QDs, it should follow the temperature energy gap dependence for InGaAs bulk, without the impact of possible redistribution processes as it was seen for the ensembles), i.e. for Varshni parameters somewhat in between InAs and GaAs [264]. As shown in Figure 7.4B, the changes in $E_{\mathrm{QD}}(T)$ slower than predicted by Varshni dependence indicate the existence of additional effects partly compensating for the band-gap reduction. This may be connected to energy quantization in a QD, due to which exciton energy is not directly defined by the material band gap. But this difference is usually small, especially for the QD ground states, i.e. deeply confined levels. Therefore, the main factor modifying the trend is suspected to be the influence of carrier-phonon coupling. The number of phonons increases with the temperature, which enhances their impact on the QD emission energy (based on the renormalization of band energies driven by electron-phonon interactions [275]). To analyze the indicated effect, the dependence of emission energy on temperature was fitted using a model including the interaction of carriers in a QD with phonons, taking into account the contribution of both optical and acoustic modes [276]:

$$E_{\mathrm{QD}}(T) = E_{\mathrm{QD}}(0) - S_{\mathrm{ph},1}\left[\coth\left(\frac{E_{\mathrm{ph},1}}{2k_{\mathrm{B}}T}\right) - 1\right] - S_{\mathrm{ph},2}\left[\coth\left(\frac{E_{\mathrm{ph},2}}{2k_{\mathrm{B}}T}\right) - 1\right], \tag{7.1}$$

where, $E_{\mathrm{QD}}(0)$ is the emission energy at $T = 0$ K, k_{B} is the Boltzmann constant, $S_{\mathrm{ph},1}$ and $S_{\mathrm{ph},2}$ are constants of electron-phonon coupling with corresponding average energy for acoustic phonons, $E_{\mathrm{ph},1}$, and optical phonons, $E_{\mathrm{ph},2}$. The value of $E_{\mathrm{ph},2}$ was set at about 30 meV, corresponding to the longitudinal optical phonon (LO) energy in the InGaAs material (ranging from 26 meV in InAs to 36 meV in GaAs [277]). Based on the fitting shown in Figure 7.4B for structure In-29%, the average phonon energy is obtained, $E_{\mathrm{ph},1} = 7.32 \pm 0.39$ meV, comparable to the InGaAs zone-edge transversal acoustic phonon

energy [277]. It seems to confirm the interaction of carriers in the dot with phonons as the main source of deviation from Varshni dependence.

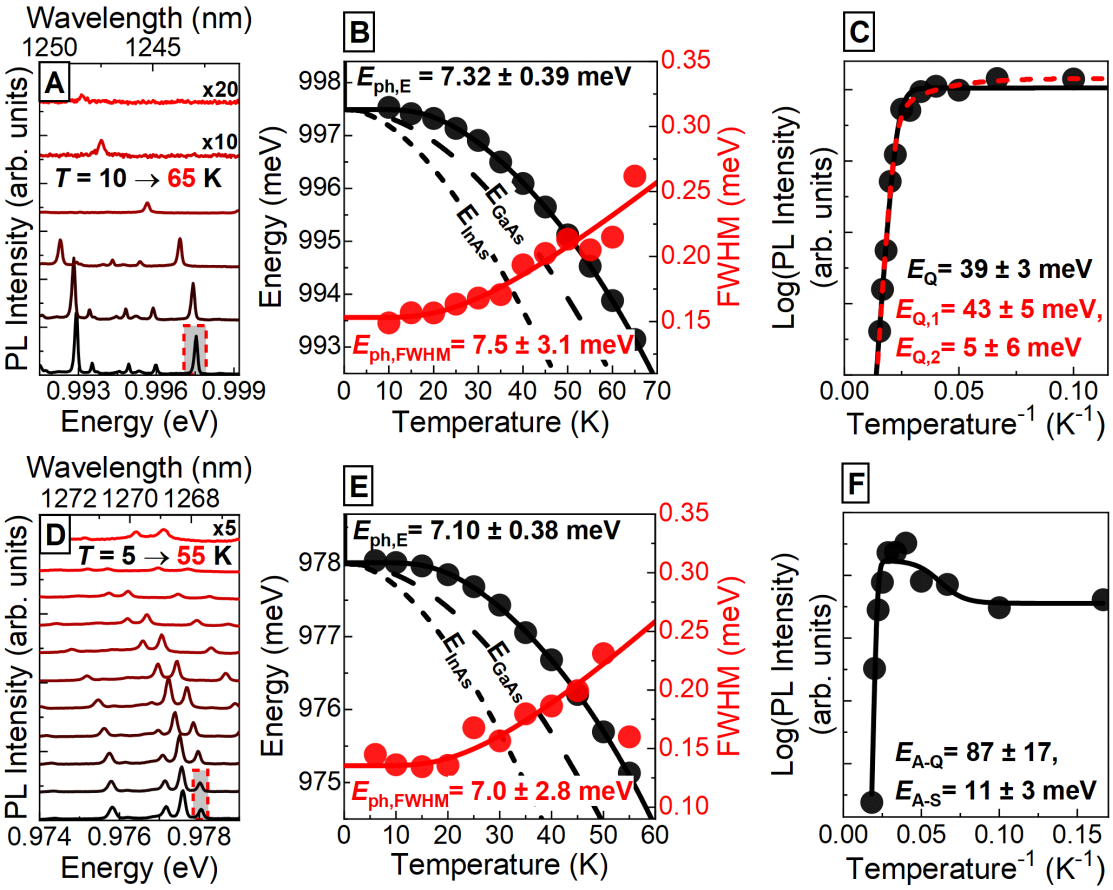

Figure 7.4. (A) PL spectra for the In-29% sample as a function of temperature in the range from 10 to 65 K. The emission line selected for analysis is indicated by the red frame. (B) The temperature dependence of emission energy (black dots) and broadening (red dots) for the selected emission line. Fitting of energy using Eq. (7.1) (black line) and broadening using Eq. (7.2) (red line) is shown; additionally, the Varshni dependences for InAs and GaAs materials are shown (dashed lines). (C) Emission intensity as a function of inverse temperature with fitting using the dependence for a single escaping process (according to Eq. (6.2)) and for two processes (Eq. (6.3)). (D, E, F) Analogous analysis for another emission line showing an increase in emission intensity in the initial temperature range in addition to the processes shown for the previous line. Fitting using the dependence for single escaping process with an additional supplying process (according to Eq. (7.3)).

In addition, Figure 7.4B shows an increase in QD emission line broadening, $\mathrm{FWHM}(T)$, from about 150 μeV at 10 K to about 250 μeV at 65 K, as predicted based on larger number of phonons affecting QD emission. The indicated broadening dependence is fitted using the exciton-phonon coupling model [278,279]:

$$\mathrm{FWHM}(T) = \mathrm{FWHM}(0) + a\left[\exp\left(\frac{E_{\mathrm{ph}}}{k_{\mathrm{B}}T}\right) - 1\right]^{-1}, \tag{7.2}$$

where $\mathrm{FWHM}(0)$ is the emission linewidth at $T = 0$ K, k_{B} is the Boltzmann constant, a is a scaling factor, and E_{ph} is the phonon energy. The average energy of phonons interacting with the carriers is determined to be $E_{\mathrm{ph},\Gamma} = 7.5 \pm 3.1$ meV could be obtained from this fitting. The significant uncertainty is most likely related to large inhomogeneous broadening already occurring at low temperatures (presented in Figure 7.2), which hinders the observation of the additional broadening caused by the coupling with phonons in the temperature range at which the impact of phonons is weak. On the other hand, a rapid decrease in emission

intensity at elevated temperatures results in lower accuracy of the determined line parameters. Nonetheless, similar values for the phonon energy based on changes in the energy emission and broadening were observed, indicating a significant impact of the interaction of carriers/excitons with phonons.

Elevating the sample temperature also leads to the increased carrier escape rates from QDs due to the higher thermal energy, resulting in a decrease in signal intensity with increasing temperature until the emission is completely quenched when the rates related to carrier losses are much higher than the exciton radiative recombination rates. Carriers from a QD can be excited to the QD higher-energy states or escape to the surrounding, i.e., to the WL or barriers or to defect states present there. Figure 7.4C shows the decrease in emission intensity with temperature. Using the dependence for one or two activation processes, Eqs. (6.2) and (6.3), the intensity dependences were fitted, giving the activation energies equal to $E_{\mathrm{Q}} = 39 \pm 3$ meV and $E_{\mathrm{Q},1} = 43 \pm 5$ meV, $E_{\mathrm{Q},2} = 5 \pm 6$ meV. Due to only a slight improvement in the fit (and only in the low-temperature range) and large uncertainty of $E_{\mathrm{Q},2}$ in the second formula, a fit for a single process is used as sufficiently describing the obtained dependencies. The value of about 40 meV is close to the energy separation between the electron ground state in a QD and the MBL conduction band edge equal to about 35 meV, according to Figure 7.5 showing the calculated energy diagrams[MG]. So, the most like process is the escape of electrons from a QD (analogous confinement energy for holes is 57 meV). The demonstrated activation energies are smaller than those determined for the emission of QD ensembles (above 100 meV; presented in Section 6.4). In the case of single QD emission, excitation to higher QD states results directly in a decrease in emission intensity, as the possible emission from higher states within the dot is not collected. In contrast, in the case of QD ensembles, emission from higher states still contributes to the characterized emission intensity, and only the complete escape from the dot can result in an efficient decrease in emission intensity.

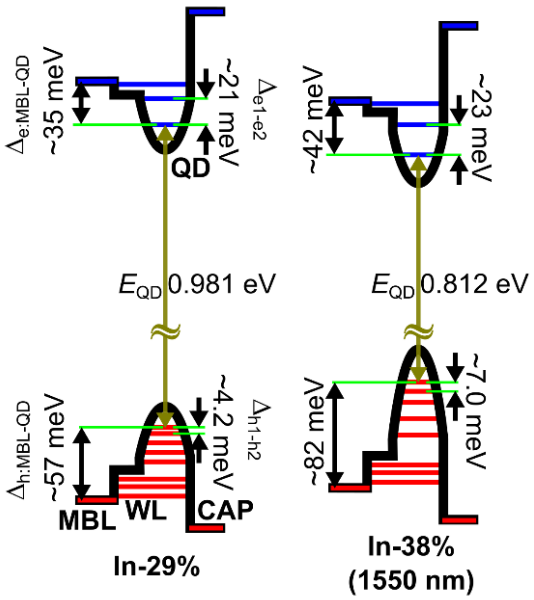

Figure 7.5. A diagram of the energy structure based on the results of the advanced calculations[MG] for the In-29% structure and QD emitting at about 1550 nm for the In-38% structure.

In addition to carrier escape processes as described above, for some of the dots it was possible to observe a fingerprint of supplying QDs with additional carriers, i.e. recapturing of the carriers which could be thermally released from the shallow defects in the surrounding or thermally activated and transferred from other quantum dots. It causes an increase in the PL intensity with temperature in the low-temperature range instead of the expected quenching. Figure 7.4D shows such a case, i.e., an emission line (marked with a red frame) showing an increase in emission intensity for the initial range of temperatures. Analysis of

emission energy and broadening temperature dependences (see Figure 7.4E) showed similar average phonon energies of about 7 meV, as for the case discussed above. The dependence of emission intensity on the temperature is presented in Figure 7.4F. In addition to a decrease in intensity at elevated temperatures, an initial increase of PL signal at around 20 K is observed. The obtained results were fitted using the dependence for a single quenching process together with an additional carrier supply process introduced phenomenologically in Ref. [176]:

$$I(T) = \frac{I_0\left[1 - I_P\left(1 + A_1 \exp\left(-\frac{E_S}{k_B T}\right)\right)^{-1}\right]}{1 + A_2 \exp\left(-\frac{E_Q}{k_B T}\right)}, \tag{7.3}$$

where, I_0 is initial emission intensity at $T = 0$ K, I_P is reservoir-gained intensity (based on additional carrier trapped near the QD), $A_1$and A_2 constants with the meaning of process intensities, E_Q is the activation energy for the escape process and E_S is the activation energy for the supplying process. Based on the fitting, the activation energy for the carrier escape process is found to be about $E_Q = 87 \pm 17$ meV, and the activation energy for the supplying process is $E_S = 11 \pm 3$ meV. The latter can be interpreted as the energy needed to release the carriers from the charge traps surrounding the dot or within the MBL structure. The identified activation energy of about 87 meV corresponds to the escape of carriers to MBL. The sum of energy separations from the confined electron and hole levels to the MBL barrier is around 92 meV (35 meV for electrons and 57 meV for holes, according to Figure 7.5), i.e. close to the determined activation energy.

A similar analysis was carried out for a series of single QD emission lines for the In-29% and In-38% structures, characterized by emission in the second and third telecom windows, respectively. The results of phonon energy analysis based on temperature dependences PL peak position and linewidth are shown in Figures 7.6A and 7.6B. Similar median values were obtained of about 6.8 meV (In-38%) and 7.2 meV (In-29%) from the emission energy dependence and 6.3 meV (In-38%) and 8.6 meV (In-29%) for the linewidth modification. The determined values are close to the 7 meV characteristic for the InGaAs material (ranging from 6.2 meV for InAs to 9.8 meV for GaAs [277]). The observed range of values, especially for emission line broadening, is most likely caused by significant line broadening at low temperatures (due to spectral diffusion), resulting in difficulty in observing changes on top of this, especially at lower temperatures, thus making the fitting less accurate. Activation energies in the range of 3.5 meV to 60 meV (similar analysis to Figures 7.4C and 7.4F) were found for the In-29% and In-38% structures, respectively, as shown in Figures 7.6C and 7.6D. They vary due to significant QD parameter distribution within the ensemble affecting the energy distance of states. The obtained results are consistent with the calculated optically-active higher transitions for the exciton^{MG} (see horizontal lines in Figures 7.6C and 7.6D), which probably confirms the emission quenching due to carrier excitation to higher QD states, (especially for small activation energies insufficient to escape of carriers to the barrier). On the other hand, single carrier escape processes cannot be excluded (especially for the larger of the activation energies) and will be hardly distinguished for the dots with weaker confinement for one type of carriers, electrons or holes (as shown in Figure 7.5). Figures 7.6E and 7.6F also show the determined activation energies related with currier supply from 2 to 22 meV, indicating the presence of this additional carrier exchange processes with charge traps located in the QD environment or additional carriers transferred from other QDs within a redistribution process.

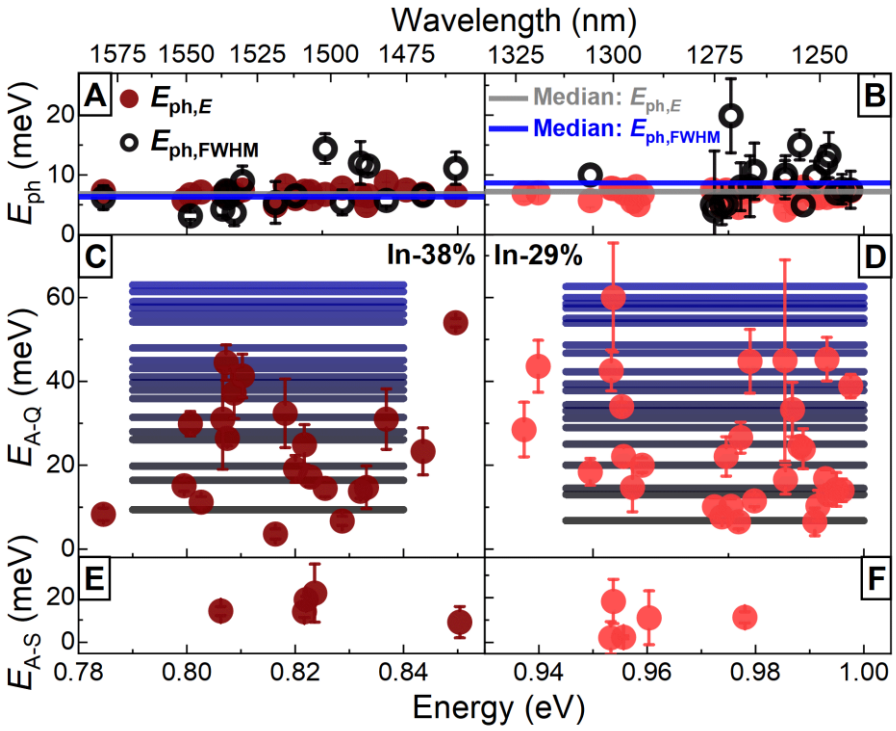

Figure 7.6. Average phonon energy determined based on the temperature dependence of emission energy (black dots; gray line shows median value) and line broadening (red dots; blue line shows median value) for (A) In-38% and (B) In-29% structures. Activation energy of carrier escape for different dots as a function of their emission energy for the sample (C) In-38% and (D) In-29%, with the indication of the calculated[MG] energies of the higher states for QDs showing emission in the second and third telecom windows (lines). Activation energy of the carrier supplying process for various QDs as a function of their emission energies for sample (E) In-38% and (F) In-29%.

7.4. SINGLE QD EMISSION UNDER QUASI-RESONANT EXCITATION

Modifications in the MBL change the entire energy structure of the system, especially the QD-confined levels. The reduction of strain and MBL energy barrier with increasing In content decrease the QD state energies, including the ground state responsible for the emission wavelength and the energy separation between the excited states, making the entire ladder of the confined states denser. On the other hand, the increase of the QD indium content for the In-29% and In-38% structures may lead to an opposite effect due to the complex effect of strain and energy gap modification [53,280]. Considering the low absorption cross-section for QDs, which makes any direct absorption measurement challenging, PLE is a method that allows studying the ladder of QD states. Assuming the relaxation of carriers from higher states to the ground state is possible, the PLE signal can indicate the spectral positions of the higher optically-active transitions, including the separation between the ground and the first excited state.

PLE measurements were carried out for the In-38% sample to probe the spectrum of excited states. Figure 7.7A shows an example of a PLE intensity map. The framed detection energy corresponds to the selected single QD strong emission line marked with the red arrow in Figure 7.7B (PL is shown there with black line). A vertical cross-section of the map gives the PLE spectrum for the selected emission line plotted with the red line in Figure 7.7B. Strong resonances indicate optical transitions involving higher states (from which carriers relax to the emitting state) or correspond to optical phonons. The lowest resonance agrees with the PL spectrum, which probably indicates a direct observation of emission from a higher excitonic state in a QD. However, due to fast thermalization and often quite complex optical spectra, PL

measurements at varying excitation power usually do not allow for easy analysis of higher QD states, especially since a signal from at least several dots usually coexists.

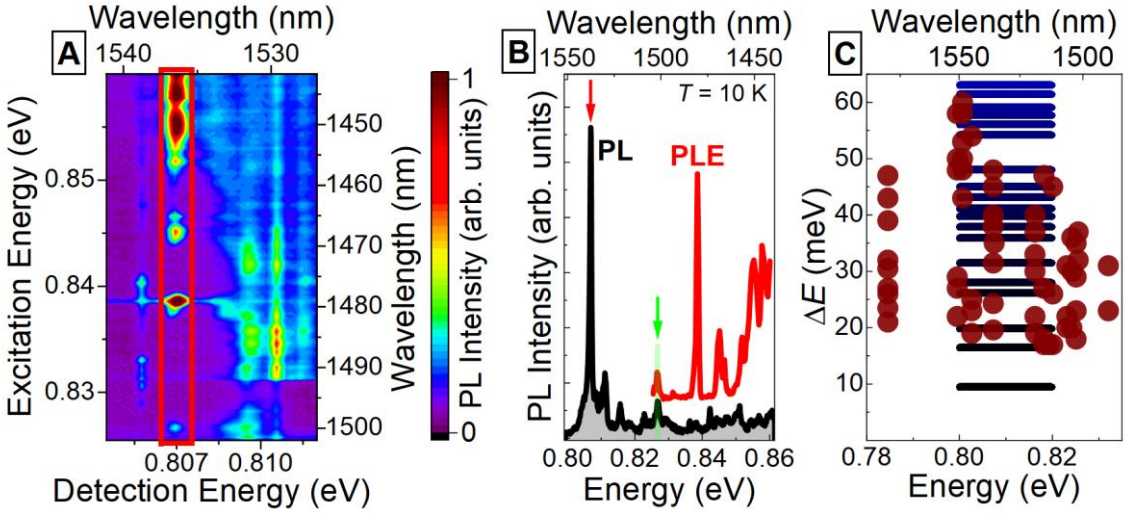

Figure 7.7. (A) PLE map for In-38% structure. The emission line selected for analysis is marked with a red box frame. (B) Comparison of the PL spectrum and emission intensity for the selected emission line (marked with red arrow) as a function of excitation energy (PLE). Matching peaks in the PL and PLE spectra are marked with the green arrow. (C) Energy differences (relative to emission) of PLE maxima for different QDs as a function of their emission energy. Calculated energy levels for a QD with H = 6 nm, D = 30 nm (lines).[MG]

Analogous measurements were made for several QDs emitting in the third telecom window for structure In-38%. Energies of the excited states are found as the difference between the PLE resonance positions and the detection energy of the ground state, as shown in Figure 7.7C. As an outcome, it gives a dense ladder of higher optical transitions (excitonic states) in the range from 15 meV to 60 meV above the ground state. This range is set by experimental limitations: measuring PLE for energy differences lower than 15 meV could not be performed due to the filtering of the excitation laser. On the other hand, energies above 60 meV were not achievable due to the limited tuning range of the laser used. The obtained relative energies of higher optical transitions are compared in Figure 7.7C with the calculations[MG]. In both cases, similarly dense ladders of states are obtained. There are some deviations between the experiment and theory in the absolute values of energies. It is rather normal, as the model cannot consider the exact parameters of the particular dots like the actual size, shape, asymmetry, and indium content and distribution. The calculations showed that the first excited exciton state is about 10 meV above the ground state, which was not reachable experimentally. Nevertheless, the semi-quantitative agreement of the energy level structure has been obtained, which also corresponds well to the dense activation energy distribution in Figure 7.6C. Due to the mentioned limitations and the high density of the confined states in these dots, no clear dependence of the excited states spacing on the ground state energy could be determined.

Information on the higher-energy states from PLE measurements also allows for modifying the excitation scheme from non-resonant (above the confinement barrier) to quasi-resonant (into one of the QD excited states). This excitation scheme should deliver carriers directly into the investigated QD, omitting more complex carrier relaxation and minimizing the photo-excited charge fluctuations in the QD environment. Minimizing fluctuations should, in turn, reduce emission broadening, making single-photon emission observations clearer. For studied QDs (only emission in the range of the third telecom window for structure In-38%), a comparison of the emission line broadening between non-resonant (laser wavelength of about 640 nm, corresponding to ~ 1.94 eV) and quasi-resonant excitation (1440–1540 nm, ~ 0.805–0.860 eV) into higher states (see the description of the PLE setup in Subsection 4.2.2) was made. The corresponding emission spectra are shown in Figure 7.8A. For quasi-resonant excitation, a slight reduction in the line broadening is observed from about 640 μeV down to about 460 μeV.

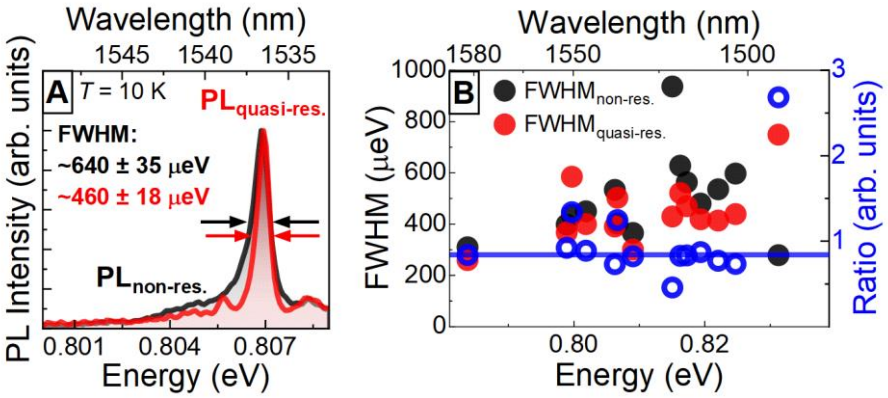

Figure 7.8. (A) Comparison of the QD emission spectrum for non-resonant (black line) and quasi-resonant (red line) excitation with FWHM marked. (B) FWHM (left axis) for individual QDs under non-resonant (black dots) and quasi-resonant (red dots) excitation and the corresponding FWHM ratio (blue dots; right axis) as a function of the emission energy.

Figure 7.8B shows the results for a series of QDs. For most lines, a decrease in the broadening is observed with a median $\mathrm{FWHM_{quasi-res}/FWHM_{nonres}}$ ratio of about 0.84, which indicates a slight reduction in the influence of the charge environment fluctuations. Improvement less significant than expected can be related to embedded trapped carriers in the structure near QDs (on defects) causing spectral diffusion regardless of the excitation. Similar problems with spectral diffusion have been reported for MOVPE-grown dots on MBL [172,220], and other forms of control of the charge environment are needed then, via the use of magnetic [281] or electric field [282] stabilization.

7.5. EXCITONIC COMPLEXES

QD emission origins from to the recombination of electron-hole pairs within various excitonic complexes, i.e. composed of different number of confined carriers, including the possibility of excited states occupation. As a result, a series of emission lines is observed from a single QD, spectrally shifted with respect to the neutral exciton ground state. The Coulomb and exchange interactions result in several properties specific to the respective exciton complexes, including FSS, complex binding energies, emission decay time, or cascaded emission (as described in Chapter 2). All these properties depend on the QD material, structural and geometrical parameters modifying the carrier confinement potential, including the in-plane shape elongation. Analyzing the properties of various excitonic complexes allows one to trace back the QD parameters, particularly to probe the QD potential anisotropy.

To identify particular excitonic complexes, for instance X-XX pairs in a single QD, the emission intensity as a function of excitation power and energy position of emission lines as a function of polarization are characterized in a standard approach. According to kinetic equations presented in Section 2.4, finding the exponents of intensity increase in the low excitation regime of about 1 and 2 for X and XX lines, respectively, separated by a typical value of XX binding energy (<5 meV), is the first indication on the observation of such a pair. This should be consistent with the opposite phase dependence of peak position on the linear polarizer angle of the two lines showing the same value of FSS.

A series of QD emission measurements were carried out for the studied structures to identify exciton complexes and determine their properties. At first, the goal was to pre-identify X-XX pairs from the same QD. Figure 7.9 shows exemplary results in the emission ranges around 1100 nm (structure In-15%), 1300 nm (In-29%), and 1500 nm (In-38%). These results allow characterizing the dependence of exciton complex properties on emission energy in a broad spectral range from 1100 nm to 1600 nm.

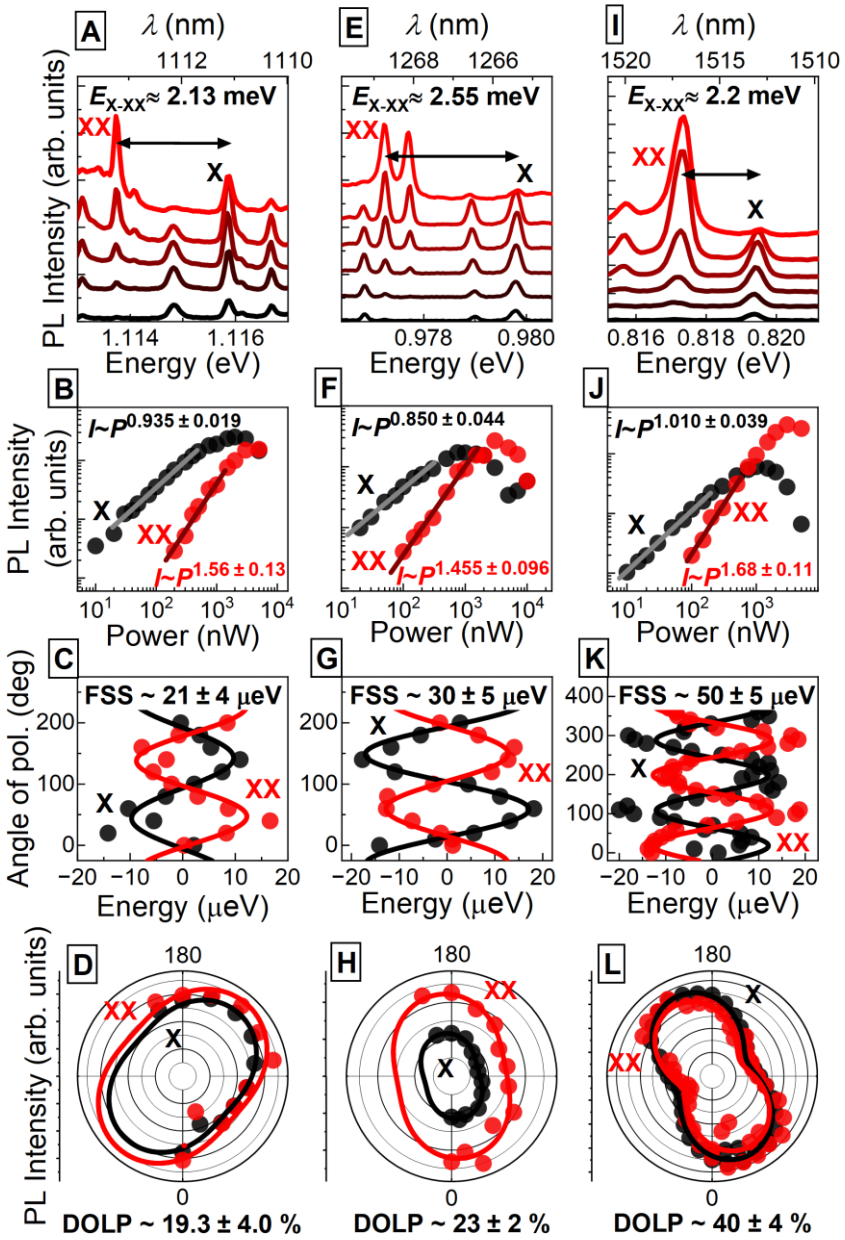

Figure 7.9. Low-temperature QD emission spectra at varying excitation powers (values measured outside the cryostat) for an X-XX pair emitting at approximately (A) 1100 nm, (B) 1300 nm, and (C) 1500 nm. (B), (F), (J) Dependence of emission intensity on excitation power (points), along with the determined exponents (lines). (C), (G), (K) Dependence of emission energy on the angle of linear polarization for individual lines from the X-XX pair (points) with sine fits (lines) and the indication of the FSS value. (D), (H), (L) Dependence of emission intensity on linear polarization (points) and fits with Eq. (6.1) with indicated DOLP value.

Identifying correlated exciton and the biexciton lines allows for determining the XX binding energy, as shown in Figures 7.9A, 7.9E, and 7.9I. Similar values of the biexciton binding energy above 2.0 meV are determined for the examples shown. Based on fitting with a power function, the dependence of line intensity on excitation power (at low excitation) presented in Figures 7.9B, 7.9F, and 7.9J gives exponent values of 0.85–1.0 for X and 1.45–1.7 for XX. Moreover, Figures 7. 9C, 7. 9G, and 7. 9K show that FSS values obtained from the emission peak energy dependence on linear polarization angle are 20–50 μeV (based on fitting with Gaussian peaks). Finally, fitting the integrated emission intensity as a function of polarization angle with Eq. (6.1) allows determining DOLP from about 20% to 40%, as shown in Figures 7.9D, 7.9H, and 7.9L.

In addition to pairs of X and XX lines, emission from excited states and charged exciton complexes can also be detected, depending on QD properties, its electrical environment, and the experimental conditions (mainly the excitation power and temperature). However, due to a relatively large number of emission lines in the spectrum with excitation power dependence similar to the neutral exciton or hardly resolvable FSS (within the possessed experimental capabilities), the characterization of the other complexes confined in these QDs was limited.

7.5.1. DETERMINING THE CONFINEMENT REGIME: POWER-DEPENDENT SINGLE QD EMISSION

Due to different occupations of states, various excitonic complexes exhibit different kinetics of optical transitions (see Section 2.4). Exemplary results are shown in Figure 7.10A. In particular, for the X-XX pair, there is a significant difference in the exponent of the emission intensity increase with excitation power, see Figure 7.10B. Depending on the QD properties (in a simple approach described by confinement regime), a specific ratio of these exponents for the indicated emission cascade can be obtained, as discussed in Section 2.4. For the dependence shown in Figure 7.10B, the slope in double logarithmic scale is about 0.84 for X and about 1.49 for XX, giving the ratio of about 1.77. Fitting with the rate equation model (Eqs. (2.14) in Section 2.4) - see Figure 7.10B, indicates that this pair of lines comes from the same QD.

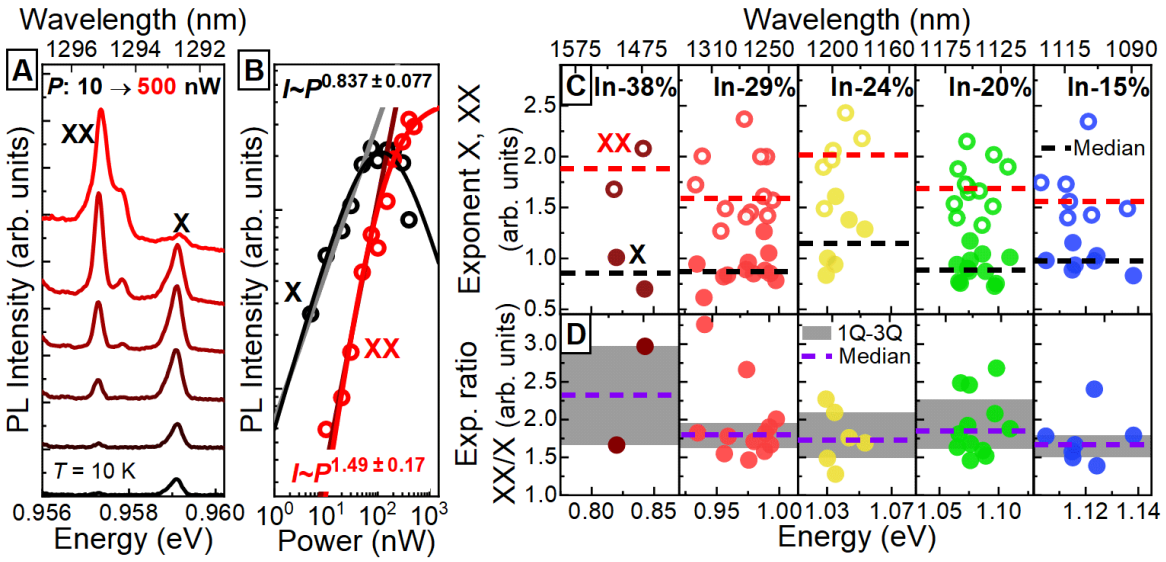

Figure 7.10. (A) QD emission spectra at varying excitation power (values measured outside the cryostat) for an X-XX pair emitting at approximately 1300 nm (In-29%). (B) Dependence of emission intensity on excitation power (points) with the determined increase exponent and fitting with a standard three-level kinetic rate equation model (lines). The determined values of (C) exponents and (D) exponent ratios for studied X-XX pairs. The distance between the first and third quartiles and the median values are marked for each sample.

Fitting a power function to the low-excitation-power part of dependences for a series of single QDs shows median values of exponents of around 0.93 for the exciton and 1.71 for the biexciton. Based on this, median ratio values from 1.67 (for structure In-15%) to 2.32 (In-38%) are obtained, as shown in Figure 7.10C, however it is the least reliable for the latter sample due to very limited statistics. Small number of cases for the In-38% sample is most likely related to the low surface density of QDs emitting in the third telecom window. In addition, for many of the cases it was impossible to resolve any FSS suggesting an increased proportion of charged complexes in this sample, making the characterization of neutral complexes more difficult. It was further complicated by the increased broadening of emission lines and reduced emission intensity for this structure (see Figure 7.2). Vast majority of values this ratio for the identified X-XX pairs are below 2, which suggests an intermediate confinement regime, where the energy levels separation for one type of the carriers is smaller than the electron-hole Coulomb interaction energy (according to Section 2.2).

Based on the more advanced band structure modeling[MG], the exciton binding energies of 12–15 meV were obtained (similar to standard values for InAs QDs [14,17]), while single-particle level splittings for QDs emitting in the second (third) telecom windows were found to be ~21 meV (~23 meV) for the electron, and ~4.3 meV (~7.0 meV) for the hole, for a QD with H = 6 nm, D = 30 nm, and LAR = 1.2. These results confirm the intermediate confinement regime (hole states separation smaller than exciton binding energy) as determined based on power-dependent characterization. In the following Section, a direct comparison of the decay times for individual complexes will further support these results.

7.5.2. ANALYSIS OF THE EXCITON FINE STRUCTURE SPLITTING

For neutral exciton, the electron-hole exchange interaction combined with in-plane asymmetry of the confinement potential causes the FSS (see Chapter 2). Due to the ultra-long lifetimes of the dark states, the QD PL spectrum in zero magnetic field is dominated by the bright states, characterized by shorter lifetimes. FSS is a kind of figure of merit of the confinement potential anisotropy of any origin (shape, composition, strain) and can very often be detected even for its very small values, even below the linewidth, as shown in Figure 7.11A for structure In-29%. The energy shift of the emission maximum as a function of linear polarization, due to the varying contribution of emission from individual bright states, can be fitted with the sine function for a more accurate determination of the FSS, see Figure 7.11B. In addition, biexciton as a complex without a fine structure but recombining to the split exciton states (see Section 2.3) shows identical FSS value, while its polarization angle dependence is in the opposite phase. These properties are used as additional verification of the FSS.

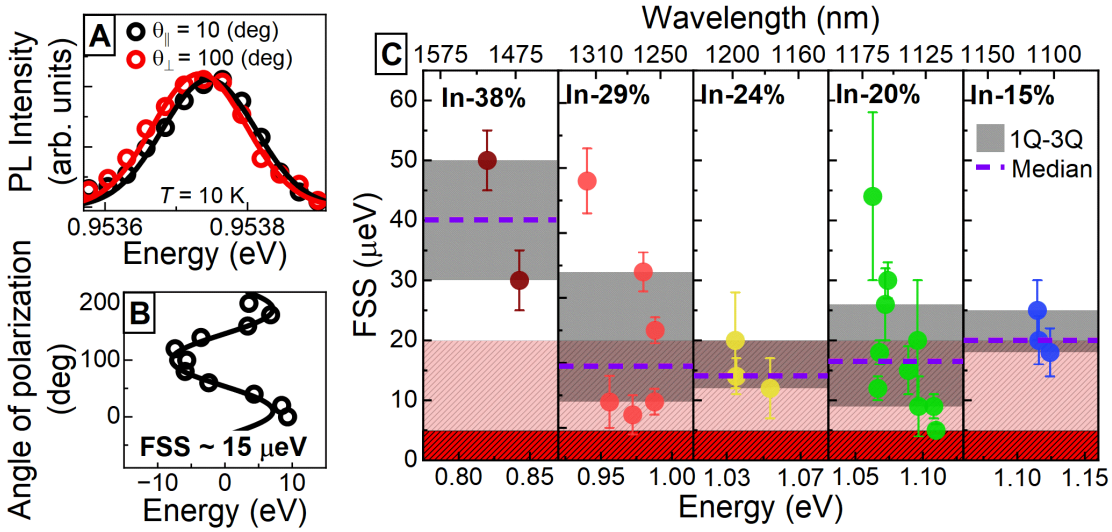

Figure 7.11. (A) Emission spectrum for a QD single line in a narrow energy range for two orthogonal polarizations. (B) The emission energy dependence on polarization. (C) FSS values for X-XX pairs for the studied structures. Ranges from the first to the third quartile and the median value for the determined FSS are shown. The red area indicates the range of values that cannot be determined based on the measurement method used. The light-red area indicates the range below the available resolution of the measurement system.

The polarization dependence of peak positions for a series of QDs in the 1100–1600 nm range was measured, and FSS was determined with values shown in Figure 7.11C. They range from about 5 μeV to 50 μeV, where for QDs with emission below 1350 nm small median values of about 20 μeV are obtained. An increase in FSS is observed for the In-38% structure with the emission from dots above 1450 nm, although the median value is relatively low, around 40 μeV. The presented results indicate a weak FSS increase when shifting the emission energy to the telecom range, suggesting more pronounced in-plane confinement potential asymmetry, especially for the In-38% sample with a modified growth scheme. It can be a fingerprint of the QD elongation in one crystallographic direction, also supported by the results of DOLP and biexciton binding energies shown in the upcoming Subsections. Due to the finite energy

resolution of the measuring system (about 20 μeV for the optical system and approximately 5 μeV in the analysis), the results do not contain the smallest FSS values that may occur for the investigated dots. Therefore the obtained median should be considered as slightly overestimated.

7.5.3. DEGREE OF LINEAR POLARIZATION

The mixing of LH and HH states, as described in Chapter 2, leads to an imbalance in the oscillator strengths of the two orthogonal optical transitions from the bright states of the neutral exciton and causes a non-zero DOLP. The measurements of single QDs can show a broad range of DOLP values, most probably due to the wide distribution of QD parameters, such as size, indium composition, shape asymmetry, or local residual strain in MBL. All these change the confinement potential and modify the HH-LH mixing, hence the oscillator strength imbalance causing a wide spread of DOLP values. However, when taking into account the statistics, median values can represent overall DOLP characteristics. Additionally, in the case of the charged exciton, the mixing of hole states results in a modification of the elliptical polarization basis with similar non-zero DOLP as for neutral exciton (see Section 2.3). Figure 7.12 shows the observation of non-zero DOLP for exemplary lines in the second telecom window for two cases: with non-zero FSS (Figure 7.12A), most likely corresponding to a neutral exciton, and without detectable FSS (Figure 7.12D), most likely corresponding to a charged exciton complex.

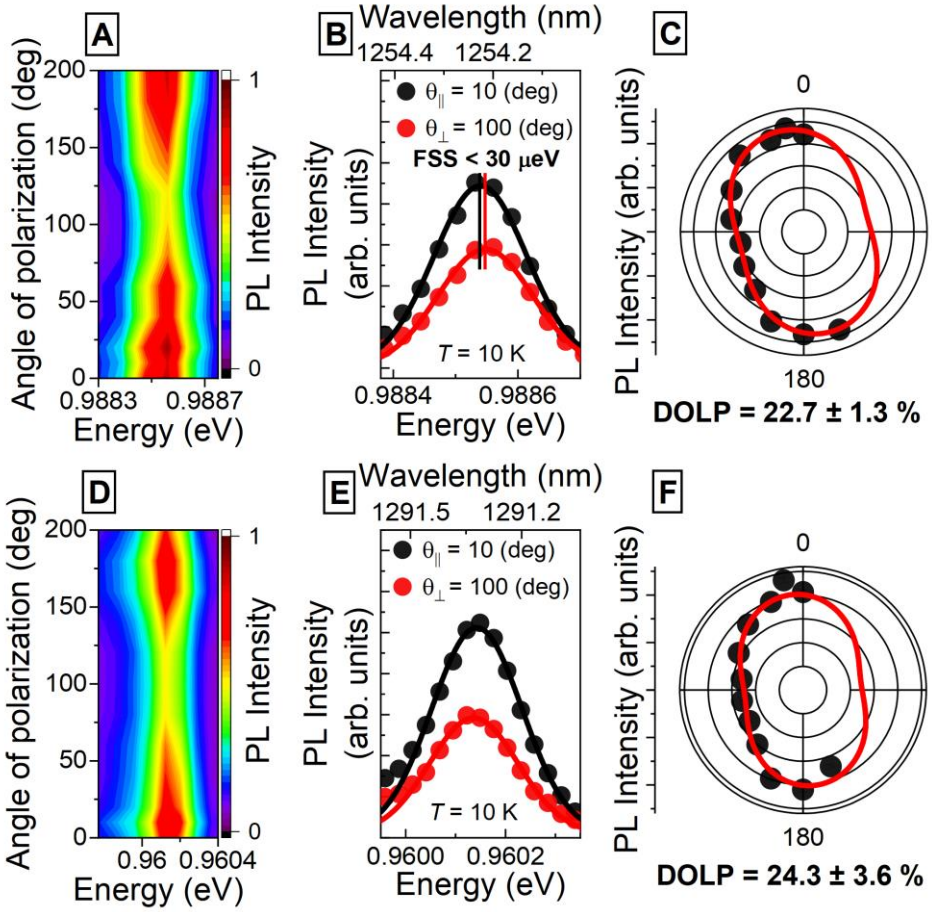

Figure 7.12. (A) Map of emission intensity as a function of linear polarization and energy for a selected QD emission line most likely for exciton emission (structure In-29%) showing non-zero FSS. (B) Emission spectra for two orthogonal polarizations showing the lowest and highest emission intensities. Positions of the maxima are marked to enable FSS observation. (C) Emission intensity as a function of linear polarization angle (points) with the fitting using Eq. (6.1) to determine DOLP values (line). (D), (E), (F) An analogous analysis of DOLP for an emission line not showing FSS most likely associated with a charged exciton.

A significant difference in the emission intensity in orthogonal linear polarizations is observed for both cases, as shown in Figures 7.12B and 7.12E. Fitting the dependence of integrated PL intensity on linear polarization with Eq. (6.1) shows DOLP above 20% in both cases (see Figures 7.12C and 7.12F).

A similar analysis, regardless of the possible complexes type, was carried out for a series of emission lines in the range from 1100 nm to 1600 nm, shown in Figure 7.13. The determined DOLP ranges from nearly 0% to almost 100%. Values close to zero indicate cases with most likely a close to zero contribution of the LH state in the QD ground state. In contrast, DOLP of almost 100% indicate a significant LH contribution. Nevertheless, most values fall into the 20%–30% range (and hence similarly for the median values), regardless of the emission energy and MBL modification.

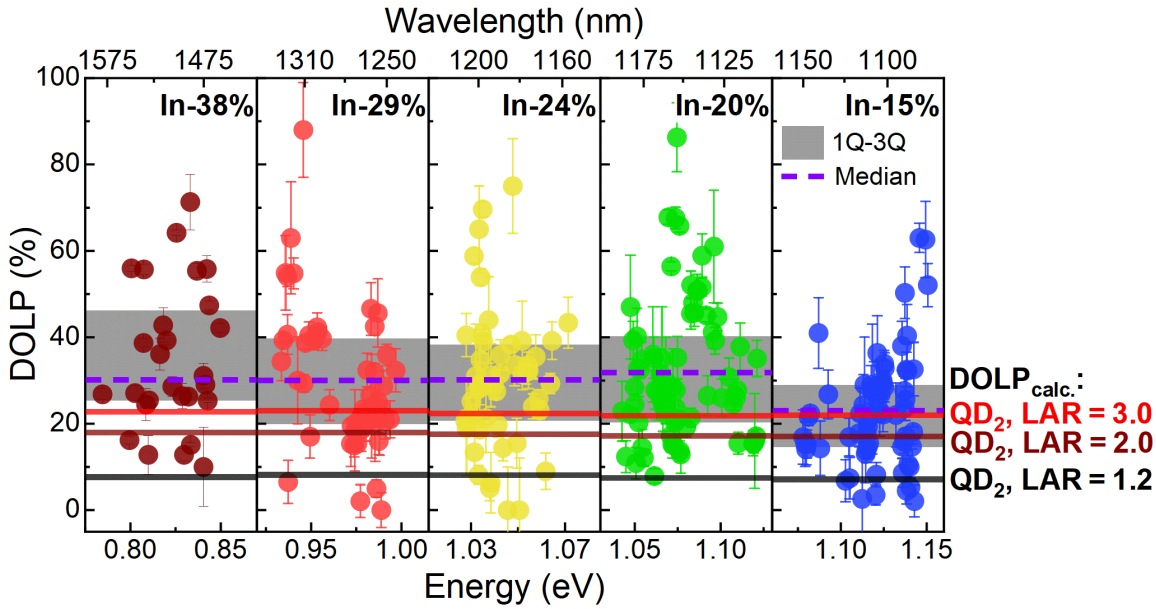

Figure 7.13. DOLP values for each structure determined experimentally (points) and calculated^{MG} for QD_2 model with H = 6 nm, D = 30 nm, and LAR values of 1.2, 2.0, and 3.0. Distances between the first and third quartiles and the median values are marked for each sample.

The obtained results are compared with calculations^{MG} for selected QD geometries (QD_2 model discussed in Section 5.6). For QDs with an almost symmetrical shape of the base (LAR = 1.2), DOLP of about 7% was obtained. Considering the possible elongation of the dot (LAR = 2.0 and LAR = 3.0) yields DOLP above 20%, i.e., closer to the median values from experimental data. The further increase in LAR no longer leads to a significant increase in DOLP as it saturates. All this makes a necessary assumption of some QD asymmetry, which may be in line with the difficulties in STEM measurements for one of the crystallographic directions described in Section 5.5. The lack of conclusive STEM results for the second direction may indicate QD elongation. Signals from several QDs overlapping within the imaging of lamellae about 50–70 nm thick made it difficult to indicate the dot image. Some underestimation of the theoretical DOLP may come for the inability to consider the actual strain in the structure, with possibly an overestimation of its level, which results in lower DOLP. The complicated structure of MBL with gradient growth carried out in the digitally alloyed approach may result in less strain within QDs, e.g., by built-in residual opposite strain in the MBL, which is unknown and cannot be taken into account in the modeling. Independently of that limitation, the the calculation shows similarly close to constant DOLP as a function of emission energy for a fixed QD geometry for all QD shape asymmetries, as in the optical measurement results. These results indicate a similar level of HH-LH mixing, regardless of MBL indium content. In addition, possible fluctuations in the QD, MBL, and cap layer compositions can lead to significant fluctuations in the local strain for the dots modifying the carrier confinement potential and the LH contribution. Another important factor is the aspect of reduced material contrast between a QD and MBL, resulting in a shallower

confinement potential, especially for holes (also contributing to the intermediate confinement regime, according to Figure 6.13, the energy distance between the ground and first excited states is < 10 meV) leading to increased wave function leakage into the QD/MBL interface where the LH and HH subbands cross and hence easily mix. As an effect, enhanced HH-LH mixing and its significant distribution in a QD ensemble may occur.

For QD ensembles, different DOLP tendencies were registered, with an increase at longer wavelengths (see Section 6.2). Those results concerned the averaged properties over the entire family. A key factor shaping these values may be the fluctuations in the dot elongation axis orientation depending on the indium content in the MBL, especially for In-11%–In-29% samples with lower DOLP (below 16%) than for single QDs (about 30%). In contrast, the characterization of emission from single QDs avoids this averaging, as DOLP is characterized separately for each QD against the direction showing the strongest emission intensity instead of the preselected crystallographic direction. An additional factor modifying the value of ensemble DOLP may come from the QD emission background (emission from objects that do not show strong emission in the form of isolated single lines as for QDs), which does not occur is in the case of single dots characterization. In addition, measurements on the mesas and apertures may translate into reduced observations of elongated objects due to the effect of limited mesa (or aperture) sizes.

7.5.4. BIEXCITON BINDING ENERGY

Based on the identification of exciton complexes, it is possible to determine the energy separation between the exciton and biexciton emission lines (see example in Figure 7.14A), which determines the biexciton binding energy. Figure 7.14B plots this binding energy as a function of the exciton ground state energy. The acquired values of about 1–3 meV are typical for InAs QDs grown on the GaAs substrate and comparable to other QDs on an MBL [14,121,124,153,217,218]. The median values for the structures present slight dependence on the emission energy (i.e., on the MBL modifications), with values from 2.14 meV for the In-15% sample down to about 1.85 meV for In-38%.

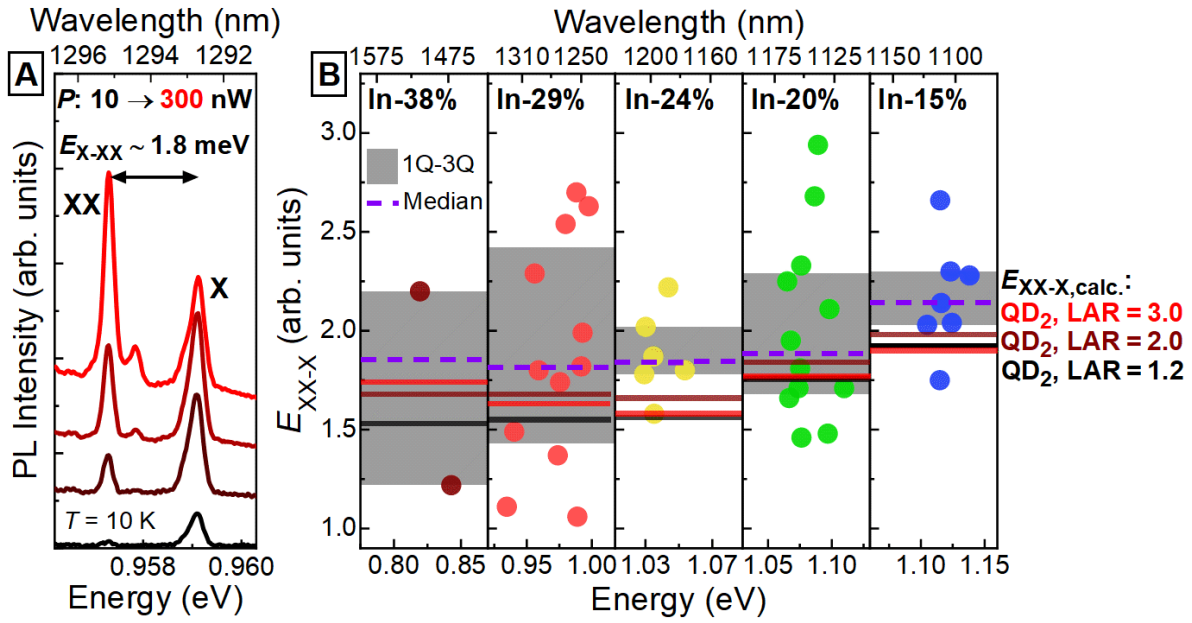

Figure 7.14. (A) QD emission spectra at varying excitation power for an X-XX pair emitting at approximately 1300 nm (In-29%). (B) Biexciton binding energies determined experimentally for each structure (points) and calculated^{MG} for the QD_2 model with H = 6 nm, D = 30 nm, and LAR = 1.2, 2.0, and 3.0. The distance between the first and third quartiles and the median values of the determined values are marked for each sample.

The experimental results were compared with the calculations (within the CI approach)[MG] for selected QD geometries (QD_2 model, Section 5.6). Linking changes in the emission energy with the modification of the QD indium content (for structures In-29% and In-38%) allows reconstructing the approximately flat dependence (changes below 0.5 meV) for calculated binding energy as a function of the emission energy. For most results, the calculated values are lower than the experimental ones, presumably due to limitations on the accuracy of the adopted QD model and the CI method associated with the limited number of single-particle states included in determining the binding energies. However, all the assumed QD parameters showed a similar trend of the XX binding energy reduction with the emission redshift. Better matching is observed for structures showing a more significant asymmetry of the dot shape with LAR = 2.0 or 3.0, in agreement with the results of preceding Sections.

7.5.5. CROSS-CORRELATION MEASUREMENTS

The unequivocal confirmation of the lines origin can be made by measuring the second-order correlation function between the photons' emission from two different lines (see Section 2.5). First of all, some of the lines could not be cross-correlated as they were detected without any coexisting emission. However, they exhibit several properties (lack of FSS, non-zero DOLP, power-dependent emission intensity similar to neutral) that suggests their charged complex character. Figure 7.15 shows such an example of PL spectra for an isolated single line in the third telecom window (structure In-38%). As already discussed above, for these 3rd window QDs, the complex properties of the MBL might favor an increased number of charged complexes (trions) when compared to other samples.

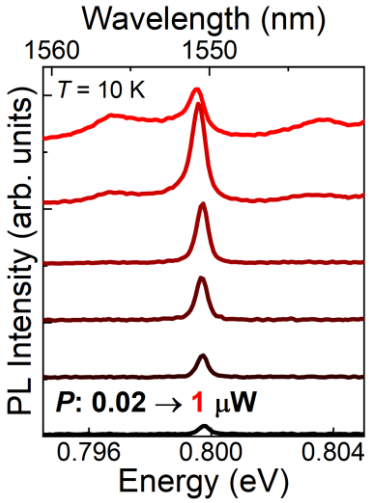

Figure 7.15. Emission spectra of a single QD emission line at varying excitation power (values measured outside the cryostat) without additional emission lines in the range of up to 5 meV.

For the studied structures, cross-correlation measurements were carried out for pre-selected pairs of lines (based on the power end polarization dependences) to confirm the emission from one QD and the origin of character of the emitting complexes. For instance, the observation of significant bunching in $g^{(2)}(t)$ (as presented in Figure 2.5) confirms that the given pair is an exciton and biexciton in the same dot, whereas asymmetric antibunching is expected when correlating exciton and trion emission. Figure 7.16 shows examples of such identification results for QDs emitting in the second and third telecom windows, for which the cross-correlation was measured.

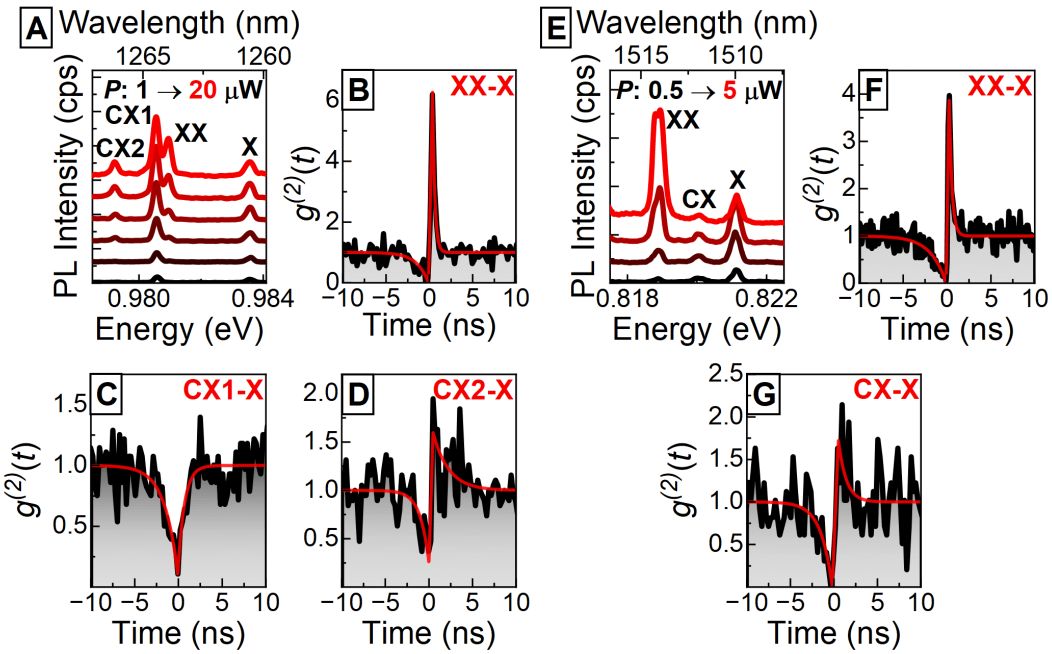

Figure 7.16. (A) Low-temperature emission spectra for a single QD in the second telecom window (In-29% structure) at varying excitation power with individual exciton complexes marked. Cross-correlation for individual emission lines: (B) XX-X, (C) CX1-X, and (D) CX2-X. (E), (F), (G) Analogous analysis for a single QD emitting in the third telecom window (In-38% structure). Fitting with two exponential functions for positive and negative delays is also shown (red solid lines) to just visualize the possible different dynamics $g^{(2)}(t)$ function on both the sides of the zero delay.

For cross-correlations of lines assigned as X and XX, a significant increase in the value of $g^{(2)}(t)$ above 1 is found near zero delays for one of the delay time directions, as shown in Figures 7.16B and 7.16F. For the remaining lines, an asymmetric shape of antibunching is observed in Figures 7.16C (CX1-X), 7.16D (CX2-X), and 7.16G (CX-X), indicating two complexes with different emission dynamics (different times of capturing particular carriers after recombination, accordingly to differences presented in Section 2.5), most likely a neutral and a charged exciton. An increase in $g^{(2)}(t)$ above the value of 1 near $g^{(2)}(0)$ for CX2-X (see Figure 7.16C) and CX-X (Figure 7.16G) cases suggest a relatively fast process of exciton formation and emission after the charged exciton recombination. The low emission intensity of the CX2 and CX lines may indeed indicate a lower rate of formation of such complexes. Thus, higher excitation power is needed to observe these lines, which results in an increased probability of exciton formation. In the case of the CX1 line, the lack of bunching correlates with its stronger emission (comparable to X), which allowed the use lower excitation power in the $g^{(2)}(t)$ measurements, i.e. in the conditions of reduced formation rates of the CX1 and X. The differences in the results in Figures 7.16C and 7.16D and in the CX1 and CX2 emission intensities indicate differences in the carriers forming the respective complexes, where perhaps there is a charge imbalance favoring increased formulation of one type of charged complexes (positive or negative).

A series of cases of QDs emitting at around 1100 nm, 1300 nm, and 1500 nm are characterized using analogous measurements. Thanks to this analysis there could be determined biexciton (empty black circles) and trion (divided into those with lower, blue empty triangles, and higher binding energy, purple empty diamonds) binding energies which are plotted versus the emission energy in Figure 7.17A and 7.17B. The results are placed on those previously obtained from the power- and polarization-dependent emissions series (full colored symbols). A close to energy-independent biexciton binding energy of about 2 meV is observed, which confirms the reliability of the previous data from before verification by cross-correlation that could be done only for selected cases.

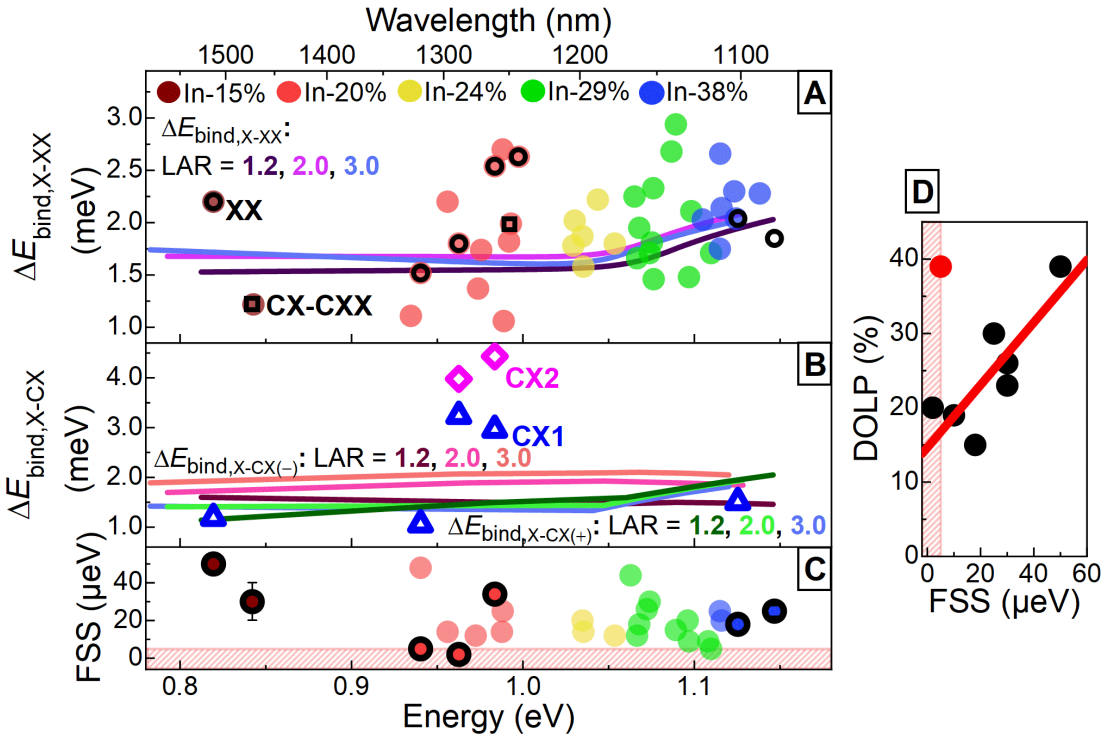

Figure 7.17. Binding energies of the (A) XX, and (B) CX complexes (black empty circles or squares for XX, blue empty triangles and purple empty diamonds for CX1 and CX2, accordingly) determined based on cross-correlation characterization (taking into account power-dependent and polarization-resolved characterization) for individual structures as a function of exciton emission energy. Comparison with calculated results[MG] (solid lines) and XX binding energy based on previous measurements (without cross-correlation verification; colored dots). (C) FSS for complexes confirmed by cross-correlation measurements (black circles). Comparison with the values determined from previous measurements (without cross-correlation verification; colored dots). (D) DOLP as a function of FSS for confirmed pairs of X-XX complexes (points) with a linear fit excluding one outlying measurement point.

A significant spread from 1 meV to above 4 meV is observed for the trion binding energies. It can be related to observations of higher excitonic complexes instead of a trion in some cases, or different geometry of individual QDs. Comparison of the experimental values with calculations[MG] for a QD with H = 6 nm, D = 30 nm, and LAR = 1.2, 2.0, and 3.0 is shown in Figure 7.17B (solid lines). Some cases (binding energy lower than XX binding energy - blue empty triangles) show good agreement with the calculated curves for the positively charged excitons. On the other hand, the calculated binding are larger for the negatively charged complexes, which can explain, in part at least, the origin of the remaining cases. A few complexes (especially purple empty diamonds determined by optical characterization, marked by CX2) show much higher values, even above 3 meV, which may indicate the observation of higher complexes or QDs with entirely different parameters than the adopted in the model.

The observed FSS values (see Subsection 7.5.2) were also verified for the X-XX complexes obtained from cross-correlation characterization, which is shown in Figure 7.17C, which do not exceed 50 μeV. For the confirmed X-XX pairs (based on cross-correlation), changes in the DOLP versus FSS are plotted in Figure 7.17D. An almost linear dependence can be seen (except of one point marked in red). A correlation of these factors is expected for QDs with confinement potential asymmetry, as both DOLP and FSS should increase with the increase of this asymmetry, to some extent at least. As the calculations did not provide FSS values, it is impossible to indicate a more detailed relationship between FSS and DOLP other than their expected positive correlation.

The emission cascade does not have to occur only for neutral excitons. It can concern charged complexes, i.e., charged exciton and charged biexciton or a pair of more complex excitonic states. The

emission cascade between such a pair would show similar $g^{(2)}(t)$ correlation function like for the X-XX pair emission, with the possible lower probability of emission of the lower complex after recombination of the higher complex compared to the X-XX pair based on the need for some additional processes for carriers to form the complex made of more charges [211]. Figure 7.18A shows the emission lines identified as a pair of complexes with a pattern of power-dependent emission (in Figure 7.18B), similar to an X-XX pair, according to Eqs. (2.12). Their energy distance of about 1.22 meV is slightly lower than the biexciton binding energy of about 1.5–2.5 meV for the studied structures (see Figure 7.17A). Cross-correlation results shown in Figure 7.18C confirm that the lines originate from the same QD based on antibunching observation with $g^{(2)}(t)$. However, the low bunching value compared to the results presented in Figures 7.16B or 7.16F indicates probably a different type of cascade with a lower probability of emission due to the need to form a complex, most likely CX-CXX pairs or X-CX cascade emission [121,211,283]. This effect may slightly hinder the identification of X-XX pairs. For individual cases of pairs showing a standard X-XX-like dependence on excitation power (see indicated square points in Figure 7.17A), cross-correlation results with a much smaller value of $g^{(2)}(t)$ were obtained, indicating another type of cascade, probably a pair of charged complexes. Another possibility for such results is the increased XX occupation relative to X (due to strong excitation), resulting in a similarly reduced X emissions, showing a lower bunching value [63].

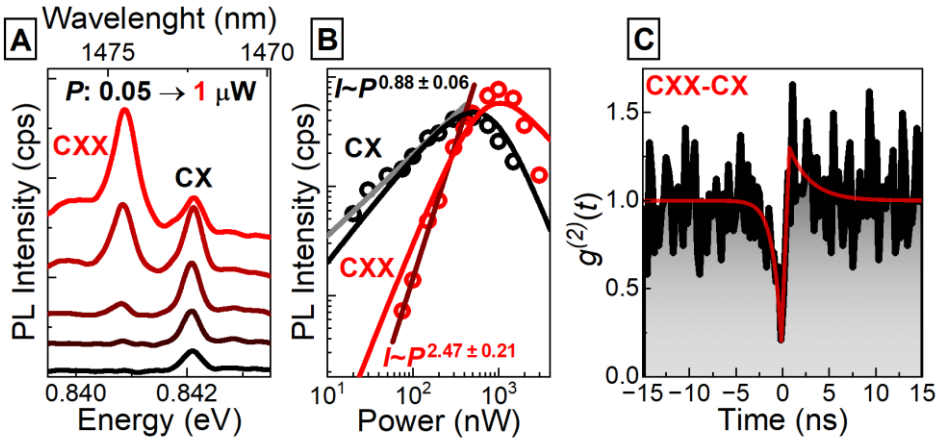

Figure 7.18. (A) Low-temperature QD emission spectra at varying excitation power with two lines labeled CX and CXX corresponding most likely to the CX-CXX emission cascade. (B) Emission intensity as a function of excitation power with the determined increase exponent and fitting with standard three-level kinetic rate equation model (see Section 2.4). (C) Cross-correlation plot for CX-CXX lines. Fitting with two exponential functions for positive and negative delays is also shown (red solid lines) to just visualize the possible different dynamics $g^{(2)}(t)$ function on both the sides of the zero delay.

7.6. TEMPORAL CHARACTERISTICS OF SINGLE QD EMISSION

The decay time of the exciton emission comes from the competition between the radiative recombination and non-radiative processes. Non-radiative transitions and the excitation of carriers to dark exciton states or their escape to trap states and higher states within the MBL or WL lead to faster emission decay times. However, observing decay time at low temperature and low excitation powers should limit the influence of these processes, providing conditions for radiative lifetime characterization. The lifetimes of excitonic transitions involving bright states are defined by the oscillator strengths, which for excitons in structures exhibiting non-zero DOLP, may depend on polarization, as mentioned in Section 6.2. However, these differences may often be too small to observe two separate decay times (especially if they cannot be easily separated spectrally, even for orthogonal polarizations), showing more complex PL decay (in the form

of two combined decays). The confinement potential modification can affect the oscillator strength and the polarization dependence, resulting in an exciton lifetime change.

Characterization of the single QD emission decay times for studied structures showed both single exponential decay and a combination of two decays, fast and slow – examples shown in Figure 7.19A for structure In-29%. Based on fitting with one or two exponential functions a decay time of about 1.38 ns and a pair of times equal to about 2.26 ns and 13.3 ns were determined. The additional slow decay component significantly extends the overall decay beyond 20 ns, in contrast to the single decay case. The determined value of short decay time in the range of about 1–2.5 ns is most likely related to the exciton lifetime, i.e. not far from the values observed for standard InAs/GaAs QDs [14,68,69,265–267].

Another aspect in the PL dynamics analysis is the existence of various exciton complexes. Due to the different oscillator strengths of optical transitions, individual complexes have different emission lifetimes. In particular, the ratio of exciton and biexciton lifetimes can indicate the confinement regime (see Section 2.4). Figure 7.19B shows an exemplary QD PL spectrum with marked emission lines (complexes identified based on the correlation measurements), for which emission dynamics measurements presented in Figure 7.19C show different decay times for individual emission lines.

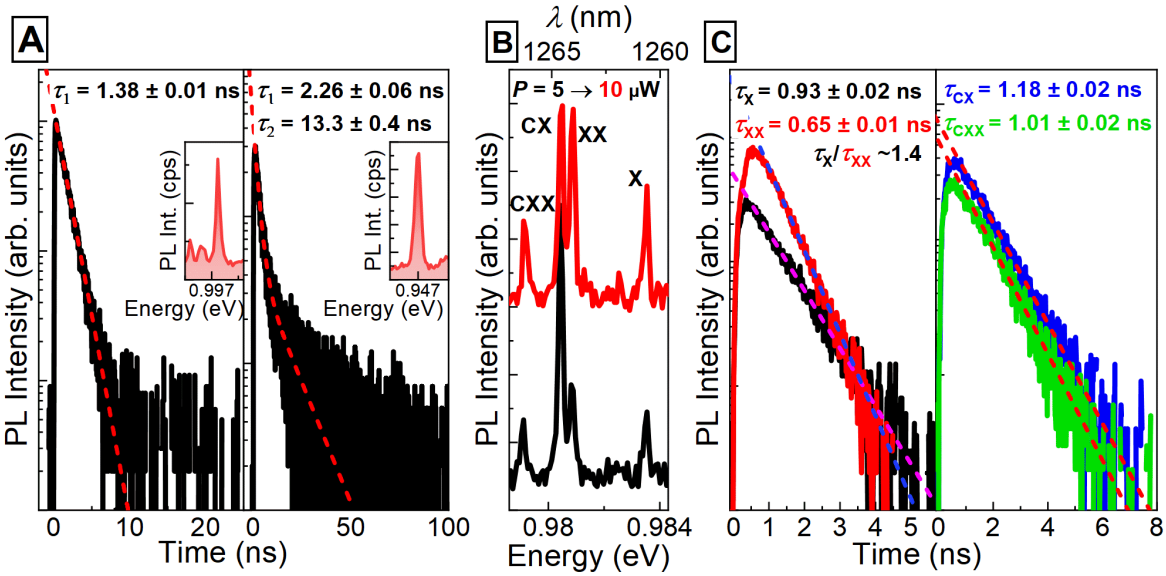

Figure 7.19. (A) Time-resolved PL (at low temperature) for two single QD emission cases in the second telecom window (In-29% structure) with a single short decay time and a combination of short and long decay times with exponential fits (dashed red lines). Insets present corresponding PL spectra of single QD emission. (B) Low-temperature single QD emission spectra at two values of excitation power with four lines labeled X, XX, CX, and CXX. (C) TRPL results for indicated lines with exponential fits (dashed lines).

It is around 0.93 ns for exciton, while for the biexciton it is 0.65 ns. The X to XX lifetime ratio of about 1.4 ns indicates the intermediate confinement regime in this case, in agreement with the results presented in Subsection 7.5.1. Decay times close to the exciton, i.e. approximately 1.01 ns and 1.18 ns are observed for charged complexes.

Similar measurements were performed for a series of lines in the third (structure In-38%) and second (In-29%) telecom windows, and around 1100 nm (In-15%). The results are collected in Figure 7.20A. In the case of short decay times, lines corresponding to exciton or charged exciton emission are selected based on previous characterization of complexes (without correlation; see Section 7.5). There is a chance that some of the values correspond to other complexes due to similar properties, which can cause a slight distortion of the obtained values. On the other hand, in the case of long decay times, all obtained values are considered. Short decay times in the range of 0.5–3.5 ns and long decay times of 2–25 ns are obtained (times longer than 4 ns are considered long or in the case of two times below 4 ns the longer of the two is considered

long). The median short decay times range from 1.55 for QDs emitting at 1100 nm to 1.45 for those emitting close to 1500 nm. The obtained values show rough agreement with the $1/E$ relationship (red line), typical used in the strong confinement regime, however it will be still similar when also entering the intermediate confinement regime. Comparison of these decay times with calculations^{MG} (see Figure 7.20A) shows an excellent agreement with a minimal deviation in the 1100 nm range, probably related to the limitations of the QD model and finite accuracy of the input QD parameters (however based on limited number of measured cases). In addition, since emission most likely from the charged exciton is also included, the decay time may be inconsistent with calculations for the exciton (CX decay time may differ from that for X). Nonetheless, the agreement confirms the assumed QD geometry and is at least not inconsistent with the conclusions on the intermediate confinement regime in the investigated QDs (as e.g. based on calculations presented in Subsection 7.5.1).

As mentioned, some of the characterized lines have an additional slow decay component. However, the corresponding long decay times do not match the decay associated with the imbalance of the two orthogonal bright optical transitions (driven by the HH-LH mixing). For the latter, a difference in the lifetimes of the two bright states of no more than 0.5 ns is expected (based on calculations^{MG}). Therefore, the most likely source of the long decay time is the process of thermal cycling of carrier occupation with higher lying states, like e.g. charge traps in the QD vicinity (see Figure 2.3C) [219]. The slow component is not observed for QDs emitting around 1100 nm, which indicates a lower contribution of this effect (however based on limited number of measured cases), most likely due to the better quality of the MBL structure (lower number defects around QDs).

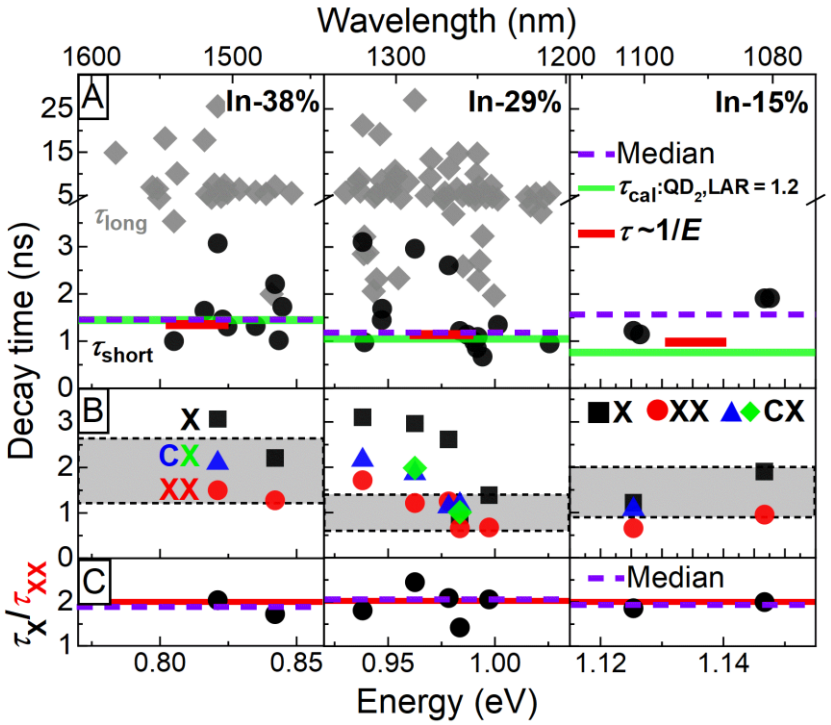

Figure 7.20. (A) Short decay times for emission pre-identified as exciton (black dots) and long decay times for all emission lines (grey diamonds) for In-11%, In-29%, and In-38% structures as a function of emission energy. The median value for short decay times (dashed purple line) and calculated values of decay times^{MG} (green line) for the QD$_2$ model with H = 6 nm, D = 30 nm, and LAR = 1.2. Comparison with the $1/E$ dependence (red line). (B) Decay times for individual X, XX, and CX complexes (black squares, red dots, blue triangles, or green diamonds) confirmed by cross-correlation measurements. The gray areas indicate lifetimes found in the literature for the range around: 1100 nm [14,68,69,265–267], 1300 nm [59,98,155,209,212,284] and 1500 nm [157,217–219]. (C) The ratio of decay times for X and XX (black dots) and the median value of the ratio (dashed purple line). Indication (red line) of ratio equal to 2 (standard value for QDs in strong confinement regime).

Summarizing, the obtained decay times for a number of identified exciton complexes shows a significant variation, as presented in Figure 7.20B. For an exciton, a change from 1 ns to 3 ns is observed for different emission energies. However, a lower value of the biexciton decay time than the exciton (~ 0.5–1.5 ns) and an intermediate one for charged excitons (~ 1.0–2.2 ns) are shown. The exciton decay times are slightly longer than ~ 1–2 ns typical for InAs dots [14,68,69,265–267] and about 0.9–2.6 ns for analogous QDs on the MBL structure [155,157,217–219], which indicated differences in the carrier's confinement potential. In addition, the difference between the short decay time median value (Figure 7.20A) and exciton lifetimes presented in Figure 7.20B seems significant, possibly indicating observations of less standard QDs with different QD parameters and probably confinement potential than those characterized by cross-correlation and decay time measurements. The exciton and biexciton lifetime ratio is also determined (see Figure 7.20C), showing values from 1.4 ns to 2.5 ns, with a median value slightly below 2 ns. This result confirms the intermediate confinement regime regardless of the emission range, indicating similar carrier confinement in all QDs.

7.7. SINGLE-PHOTON EMISSION

Photon autocorrelation measurements were carried out to analyze the second $g^{(2)}(t)$ function, and verify the single-photon emission from the studied dots under CW excitation. Figure 7.21 shows exemplary results for a QD neutral exciton emitting around 1500 nm (see the PL spectra in Figure 7.21A). Photon autocorrelation measured for different excitation powers and presented in Figure 7.21B shows the as-measured values of $g^{(2)}(0)$ always well below 0.5, confirming the single-photon character of the emission.

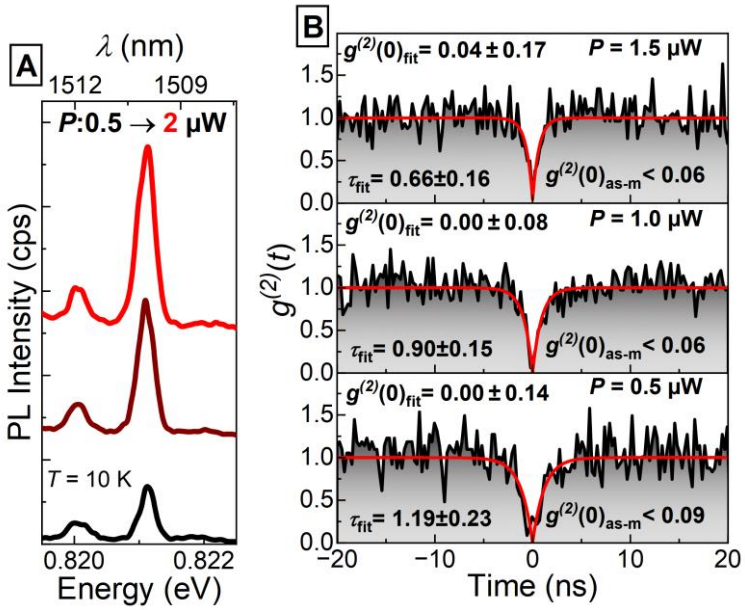

Figure 7.21. (A) Single QD emission spectra at varying excitation power for structure In-38%. (B) Second-order correlation function $g^{(2)}(t)$ for single QD emission line at varying excitation power with fitting based on Eq. (7.4). Values directly from the measurement, $g^{(2)}(0)_{as-m}$, and from the fit, $g^{(2)}(0)_{\mathrm{fit}}$, are indicated.

The as-measured values suffer from inaccuracies caused by finite temporal resolution and the signal to noise ratio which can partly eliminated by fitting the $g^{(2)}(t)$ with the following dependence, allowing better estimation of $g^{(2)}(0)$ (as introduced in Section 2.5 for an almost ideal single-photon source):

$$g^{(2)}(t) = 1 - \left(1 - g^{(2)}(0)\right) e^{\frac{|t|}{\tau_D}}, \tag{7.4}$$

where τ_D is the rise time related to the radiative lifetime and the generation rate of an excitonic complex. Using the fits shown in Figure 7.21B, the values of $g^{(2)}(0)$ close to 0 are found for lower excitation powers (with limited accuracy due to the low number of coincidences, not more than 40). The purity is worse for higher excitation power (1.5 μW) which is probably connected to the increased influence of the background emission. A reduction of τ_D from about 1.2 ns to 0.7 ns (reducing the time width the antibunching dip) due to the increased exciton generation rate is observed, which is the standard impact of the excitation power [171,187,285].

The obtained $g^{(2)}(0)$ values (as-measured and fitted) as a function of the excitation power are plotted in Figure 7.22A, together with the determined values of the signal rise time and the emission linewidth shown in Figure 7.22B. An increase in the excitation power causes an increase in $g^{(2)}(0)$ and a decrease in $g^{(2)}(t)$ rise times (associated with the mentioned increased exciton generation rate). The presented results indicate a common and expected negative influence of increasing the excitation power, causing a reduction of the single-photon emission purity, usually mainly due to larger background. In addition, the increased PL linewidth reflecting enhanced influence of the electrical environment fluctuations for larger powers also affects the $g^{(2)}(t)$. The electric environment always limits emission coherence but it should not spoil the purity of the single-photon emission as itself, apart from the technical effects of the increased background emission contribution in the recorded signal (in the spectral window of detection).

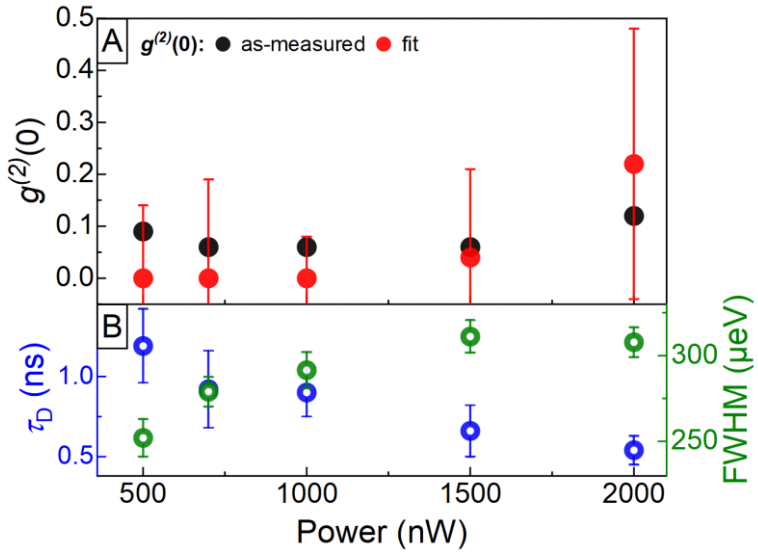

Figure 7.22. Excitation power dependence for single QD emission lines of: (A) $g^{(2)}(0)$ values, as measured - black dots, fitted - red dots; (B) rise time of $g^{(2)}(t)$ (blue empty circles) and FWHM (green empty circles).

The measurements of the single-photon emission purity based on CW excitation for a series of QDs in the second and third telecom windows allow for the analysis of the impact of changes in emission energy and MBL structure on the obtained values of $g^{(2)}(0)$, summarized in Figure 7.23A. The determined values are 0–0.3, confirming a successful demonstration of single-photon emission in the telecom range. The lack of any clear correlation with the emission energy indicates no significant and no systematic effect of MBL modification on the purity of single-photon emission. The distribution of the $g^{(2)}(0)$ is apparently random defined rather by the properties of a certain QD. The main limitations in determining $g^{(2)}(0)$ can come from the measurement time resolution and the effect of the background emission. Additionally, there is also an indirect effect of the emission intensity – when it is low it limits the use of better emission spectral filtering (a narrower spectral range of detection allows minimizing the contribution of background emissions) and forces to use worse time resolution. The as-measured $g^{(2)}(0)$ obtained for non-resonant

CW excitation are very comparable with those reported for InAs/InP QDs and InAs/InGaAlAs/InP [171,175,177,182,183,186–188] and even those on GaAs. The best fit-corrected values below 0.005 were reported for MBE-grown QDs with used SRL to shift their emission towards the second telecom window [98,212] and below 0.005 for QDs using MBL approach in MOVPE and emitting in the third telecom window [157]. In that respect, the QDs studied here exhibit very good single-photon emission purity and hence these results are very promising as for a new type of QD material structure, especially without the use of any dedicated photonic structures that would increase the extraction efficiency.

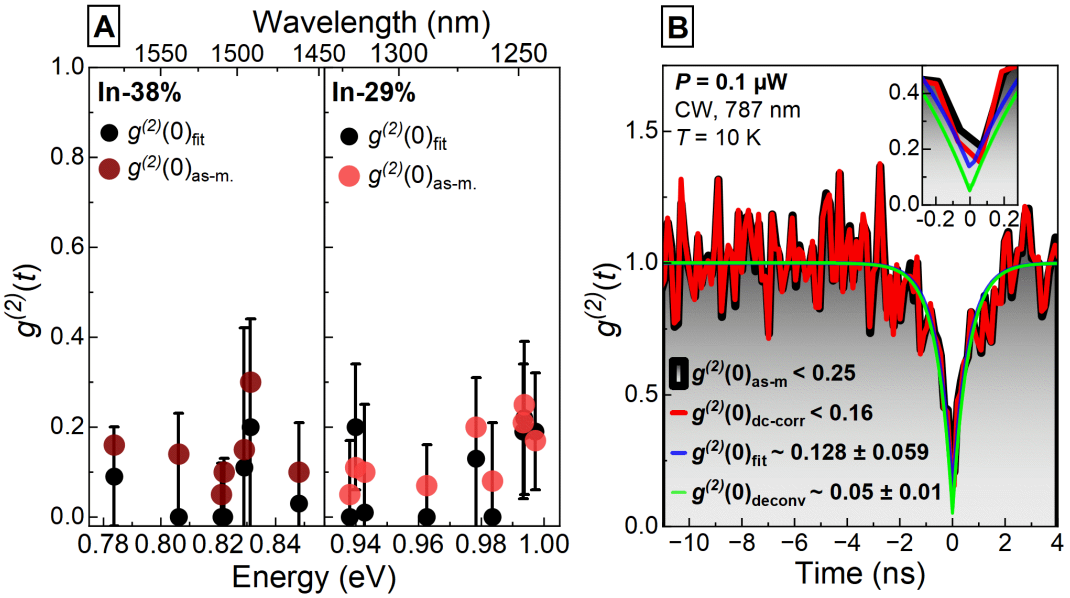

Figure 7.23. (A) As measured (colored dots) and fitted (black dots) $g^{(2)}(0)$ values for single QD emission lines for structures In-38% and In-29%. (B) Second-order correlation function $g^{(2)}(t)$ for a single QD emission line with results of correction for dark counts (red line) and deconvolution with temporal response function of the system (blue line), including fitting based on Eq. (7.4).

Other factors the accuracy in determination of $g^{(2)}(0)$ are associated with detector dark counts (constant background) and the finite temporal resolution of the system (convolution of the autocorrelation signal with the setup response function). Using these corrections will not have strong impact when low $g^{(2)}(0)$ values are obtained directly from the experiment or after fitting with Eq. (7.4), which was usually the case, but they make a difference for lines showing larger multiphoton events probabilities. For instance, as shown in Figure 7.23B, for as-measured $g^{(2)}(0) \sim 0.25$, it is possible to obtain a value of about 0.05 using the correction for dark counts and deconvolution with the time characteristic of the system. The correction for dark counts takes into account the parameter $\rho = S/(S+D)$ equal to about 0.942 related to the signal to dark count ratio (S/D), where the autocorrelation value is determined based on the $g^{(2)}(0)$ as-measured value ($g^{(2)}(0)_{as-m.}$) [79,286]:

$$g^{(2)}(0)_{dc-corr.} = \left[g^{(2)}(0)_{as-m.} - (1-\rho^2)\right]/\rho^2. \tag{7.5}$$

Taking into account the finite temporal resolution of the system, the deconvolution of the fitted $g^{(2)}(t)$ dependence with a function imitating the temporal response function of the system, $e^{(-|t|/\tau_{IRF})}$, assuming $\tau_{IRF} \approx 80$ ps, gives the $g^{(2)}(0)_{deconv}$ value. With the above-mentioned corrections, it is possible to achieve a significant improvement in the $g^{(2)}(0)$ value below 0.1.

There were also made attempts to detect triggered single-photon emission, i.e. under pulsed excitation – see Figure 7.24 with example in the 2nd and 3rd telecom windows. In both excitation schemes, an evident

antibunching is observed. Fitting the $g^{(2)}(0)$ for CW excitation shows values close to 0, confirming very good sources purity (low multiphoton events probability) similarly to previous examples. As explained in Section 2.5, the triggered realization of single-photon emission is more application-relevant. However, using pulsed excitation results in lower signal levels and thus requires higher excitation powers for measuring autocorrelation signals comparable the CW case. In addition, if the consecutive pulses are separated by time intervals shorter than the characteristic PL decay times it is impossible to obtain a zero level in $g^{(2)}(t)$ between the pulses and then lower repetition rates need to be used. For the studied structures, due to the slow decay component (in the 2–25 ns range with emission still observed even after 50 ns, as presented in Figure 7.19A), the repetition frequency of 40 MHz (pulses every 25 ns) for emission in the second telecom window and 20 MHz (pulses every 50 ns) for the third window were used. The difference in pulse repetition rates is related to the optimization of measurement time and the additional rise of $g^{(2)}(t)$ for emission in the third telecom window. Increasing the pulses' time distance was necessary to better separate the possible emission acts between individual pulses. In spite of that, the counts for the delays between pulses did not reach exactly zero (or the level of dark counts[20]) and was about 0.21 for QDs emitting in the second telecom window, see Figure 7.24C, and 0.31 for the third telecom window, see Figure 7.24F. Unfortunately, reducing the repetition rates further is limited by the amount of signal (decreasing for smaller repetition rates), so the conditions as in Figures 7.24 C and F were a kind of compromise between these two.

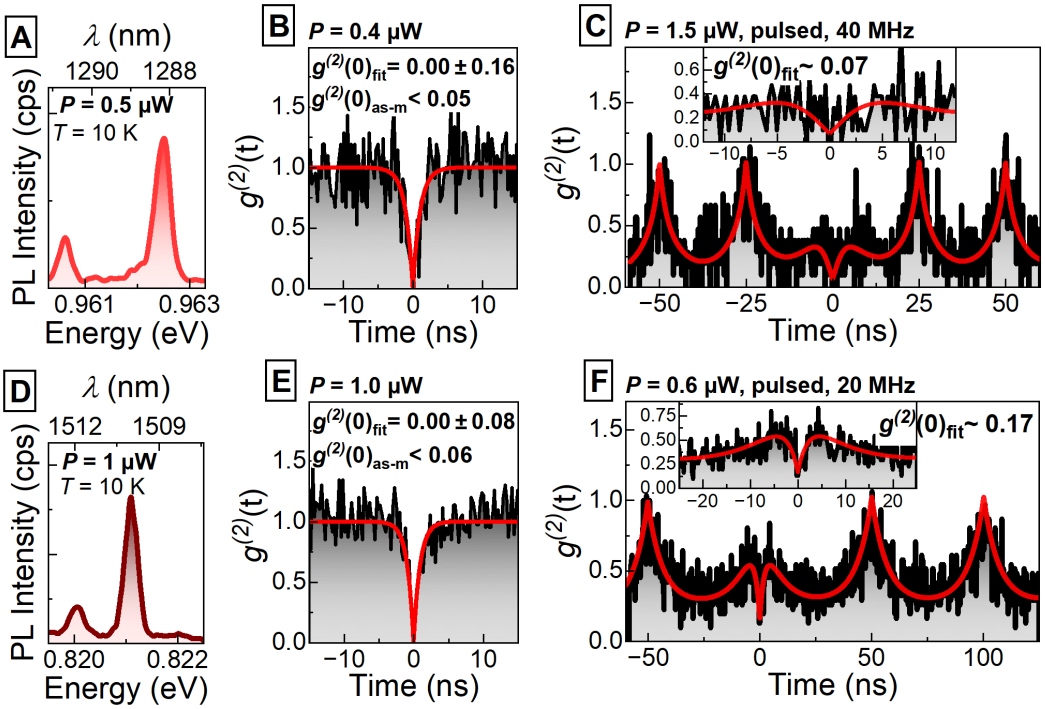

Figure 7.24. (A) PL spectrum for a single QD emission line in the second telecom window for structure In-29%. (B) Second-order correlation function $g^{(2)}(t)$ for the single QD emission line for CW excitation with fitting based on Eq. (7.4). Values directly from the measurement, $g^{(2)}(0)_{as-m}$, and from the fit, $g^{(2)}(0)_{\text{fit}}$, are indicated. (C) $g^{(2)}(t)$ for the single QD emission line for pulsed excitation with fitting based on Eq. (7.6). Inset presents a close-up of the near zero-delay range. (D), (E), (F) Analogous analysis for a single QD emitting in the third telecom window (In-38% structure).

[20] $g^{(2)}(t)_{dark-counts}$ should be below 0.1 based on signal of dark counts in PL

Independently of the discussed background level problem an increase in the value of $g^{(2)}(t)$ around the zero delay is observed for delay $|t| < 10$ ns (second telecom window, see Figure 7.24C) or $|t| < 20$ ns (third telecom window, see Figure 7.24F). The indicated effect is related to the delivery of more than a single pair of carriers to a QD within a single pulse and it is due to the so called carriers recapture (e.g. from surrounding defects in MBL, or from another QD nearby [78]), where the next exciton is formed some time after the recombination of the first one but before the next pulse comes [287]. A stronger increase of $g^{(2)}(t)$ around zero is observed for emission in the third telecom window, indicating a higher probability of carrier recapturing and, thus, more charge traps in this structure. Regardless of the observed recapturing processes and slow decay time components, a significant reduction towards zero level in the $g^{(2)}(t)$ function at zero delay was observed for both measurements, confirming the single-photon character of emission.

The $g^{(2)}(t)$ dependences obtained with the pulsed excitation were fitted with the following function, taking into account two components of decay time due to occurrence of the slow decay (according to Ref. [77]) and the additional increase of $g^{(2)}(t)$ due to recapturing process (according to Ref. [171]):

$$f(t) = \alpha e^{-\frac{t}{\tau_{\text{fast}}}} + (1-\alpha)e^{-\frac{t}{\tau_{\text{slow}}}},$$
$$g^{(2)}(t) = A_{\text{bg}} + A_{\text{auto}}\left\{f(|t|) - e^{-\frac{|t|}{\tau_{\text{cap}}}}\right\} + A_{\text{peak}}\sum_{n\neq 0} f(|t-nT|), \tag{7.6}$$

where $f(t)$ reproduces the decay of emission involving the fast component τ_{fast} and the slow component τ_{slow}, with different contributions based on the scaling parameter α. The parameters A_{bg}, A_{auto}, and A_{peak} relate to the level of background counts, the contribution of secondary photon emission, and the autocorrelation signal associated with successive peaks for delays equal to nT (T is the period of occurrence of successive excitation pulses), while τ_{cap} corresponds to the time of capture of successive carriers resulting in the observation of secondary photon emission. The values of $g^{(2)}(0)$ from fitting are about 0.07 for ~1.3 μm emission and about 0.17 for the ~1.5 μm emission. Both are close to g_{bg} of about 0.1 (based on the dark counts), confirming the observation of the triggered single-photon emission in both telecom windows. Nevertheless, problems with the recapturing processes as well as the slow decay component occurrence, seem to hinder the performance of these QDs as triggered sources, where not only single-photon emission strictly for zero delays matters, but also for a range around zero time delay of a single pulse [78]. Comparing the integrated peak area for the zero delay (A_0) with the average peak area for delays different from zero ($\bar{A}$) results in $g^{(2)}(0)_{\text{area}} = \frac{A_0}{\bar{A}}$ equal to about 0.74 for emission in the second telecom window and about 0.88 for the third window, which clearly shows that further optimization of the structural and material quality is needed to reduce this effect.

SUMMARY

The main aim of this work was to investigate fundamental optical and electronic properties of In(Ga)As quantum dots fabricated on a gradual-composition InGaAs metamorphic buffer layer on GaAs substrate by using molecular-beam epitaxy, in the context of their application potential for single-photon emitters in the telecommunication spectral range. To realize that, a number of complementary spectroscopic experiments were carried out, supported by the structural data and the results of electronic structure calculations.

The obtained results demonstrated spectral tunability of the photoluminescence from such dots in a broad range from approximately 1.1 μm to even above 1.6 μm, i.e., covering also the telecom bands. The optical transitions shift is driven by changes in the composition profile of the metamorphic layer, also affecting the strain conditions. The information on the QD morphology allowed for calculating the electronic structure details and explaining the experimental observations. Strain reduction due to increased indium content in the metamorphic buffer layer combined with increase in the quantum dots indium content have been shown as the main factors shifting emission to longer wavelengths.

Spectroscopic characterization of QD ensembles allowed also analyzing other optical properties. The measured degree of linear polarization indicated a significant heavy and light hole mixing. Characterization of photoluminescence thermal quenching showed the carriers' escape to the MBL as the most efficient carrier loss mechanism. In addition, changes in the QD ensemble emission spectra showed fingerprints of the thermally activated carrier redistribution. Existence of excitation transfer between different dots was also supported by other observations in PLE spectra and carrier dynamics. Analysis of the emission intensity and the PL dynamics confirmed good structural quality with slight deterioration with the increase of the indium content in the MBL.

Properties of individual quantum dots were also studied by microphotoluminescence measurements. Single-dot emission lines in the entire 1100–1600 nm range could be detected. Analysis of the emission intensity and the line broadening confirmed a slight degradation of the QD material when shifting to longer wavelengths caused by changes in the MBL composition, presumably due to the increased concentration of non-radiative carrier recombination centers. The determined large PL linewidths of single QD lines were explained by strong spectral diffusion due to fluctuations of the charge environment caused by charge traps around the dots. Changing the excitation conditions from non-resonant above-barrier to a quasi-resonant scheme into one of the QD excited states showed a reduction of the broadening, but only by about 16%, which suggests a significant number of built-in carriers in the direct QD vicinity. The obtained carrier activation energies indicated the escape of carriers to the barriers as the primary reason of the PL quenching, plus thermal excitation to higher QD states causing also some emission decrease at low temperatures. In some cases, the PL intensity enhancement was observed instead, with the temperature increase in the low-temperature range, indicating a process of supplying the carriers which were thermally released from shallow defects.

Combining PL excitation power density dependence, linear-polarization-resolved measurements, time-resolved data, and photon cross-correlation spectroscopy allowed identifying various excitonic complexes and investigate their properties. The fine structure splitting of the exciton bright states of below 50 μeV was found, with a weak tendency to increase towards longer wavelengths, indicating on some asymmetry of the QD confinement potential. It agrees with rather large values of the degree of linear polarization with its median value of about 30%, independently of the emission energy. The shape anisotropy was also confirmed by the results of numerical simulations, which, however, gave slightly lower values of the DOLP, suggesting that some effects, like residual strain or composition fluctuations, were not taken into account in the model. The binding energies of excitonic complexes have been determined. In particular, values in the range of 1 meV to 3 meV were found for the biexciton and from 1 meV to 5 meV for charged excitons. A slight

biexciton binding energy reduction with emission redshift has been observed, which is semi-quantitatively in line with the theoretical results. The obtained decay times measured at low temperature and low excitation, hence approximating the radiative lifetimes, were 1–3 ns for excitons and charged excitons and from 0.5 to 1.5 ns for biexcitons, for all structures, slightly increasing toward longer wavelengths. The average ratio of the exciton and biexciton decay times is slightly below 2, which, combined with the obtained ratio of the exponential increase of exciton and biexciton PL intensities, seems to indicate the intermediate confinement regime for the investigated QDs. This assessment agrees with small energy separation of the hole states in comparison to the Coulomb interaction energy obtained from the calculations.

Photon autocorrelation statistics measurements were also carried out, with continuous wave or pulsed excitation. For both, it was possible to demonstrate the possibility of obtaining single-photon emission in the second and third telecommunication windows, showing clear antibunching at a zero delay with $g^{(2)}(0)$ significantly below the 0.5 threshold. The main experimental limitation was insufficient signal intensity forcing higher excitation powers and longer integration times. In addition, an increase in the counts around the zero delay was observed for pulsed excitation, which is a common fingerprint of the carrier recapturing from the neighboring traps, as already suggested by other results. Fighting the latter can be considered one of the main routes for improvements in the single-photon characteristics of the investigated dots. Despite that, the results of this work allowed demonstration of the application potential of QDs on metamorphic buffers grown by MBE on GaAs substrate for secure quantum communication schemes in the fiber networks, including especially the most demanded third telecommunication window.

BIBLIOGRAPHY:

[1] Y. Arakawa and M. J. Holmes, *Progress in Quantum-Dot Single Photon Sources for Quantum Information Technologies: A Broad Spectrum Overview*, Appl. Phys. Rev. **7**, 1 (2020).

[2] S. Buckley, K. Rivoire, and J. Vučković, *Engineered Quantum Dot Single-Photon Sources*, Reports Prog. Phys. **75**, 126503 (2012).

[3] Ł. Dusanowski, C. Nawrath, S. L. Portalupi, M. Jetter, T. Huber, S. Klembt, P. Michler, and S. Höfling, *Optical Charge Injection and Coherent Control of a Quantum-Dot Spin-Qubit Emitting at Telecom Wavelengths*, Nat. Commun. **13**, 748 (2022).

[4] L. Seravalli, *Metamorphic InAs/InGaAs Quantum Dots for Optoelectronic Devices: A Review*, Microelectron. Eng. **276**, 111996 (2023).

[5] S. L. Portalupi, M. Jetter, and P. Michler, *InAs Quantum Dots Grown on Metamorphic Buffers as Non-Classical Light Sources at Telecom C-Band: A Review*, Semicond. Sci. Technol. **34**, 053001 (2019).

[6] X. Cao, M. Zopf, and F. Ding, *Telecom Wavelength Single Photon Sources*, J. Semicond. **40**, 071901 (2019).

[7] S. Franchi, G. Trevisi, L. Seravalli, and P. Frigeri, *Quantum Dot Nanostructures and Molecular Beam Epitaxy*, Prog. Cryst. Growth Charact. Mater. **47**, 166 (2003).

[8] P. Michler, *Single Semiconductor Quantum Dots* (Springer Berlin Heidelberg, Berlin, Heidelberg, 2009).

[9] D. Bimberg, *Semiconductor Nanostructures* (Springer Berlin Heidelberg, Berlin, Heidelberg, 2008).

[10] R. Dingle, W. Wiegmann, and C. H. Henry, *Quantum States of Confined Carriers in Very Thin $Al_xGa_{1-x}As$-GaAs-$Al_xGa_{1-x}As$ Heterostructures*, Phys. Rev. Lett. **33**, 827 (1974).

[11] H. Eisele, A. Lenz, R. Heitz, R. Timm, M. Dähne, Y. Temko, T. Suzuki, and K. Jacobi, *Change of InAs/GaAs Quantum Dot Shape and Composition during Capping*, J. Appl. Phys. **104**, 1 (2008).

[12] R. Nötzel, *Self-Organized Growth of Quantum-Dot Structures*, Semicond. Sci. Technol. **11**, 1365 (1996).

[13] R. Heitz, F. Guffarth, K. Pötschke, A. Schliwa, D. Bimberg, N. D. Zakharov, and P. Werner, *Shell-like Formation of Self-Organized InAs/GaAs Quantum Dots*, Phys. Rev. B **71**, 045325 (2005).

[14] G. A. Narvaez, G. Bester, and A. Zunger, *Excitons, Biexcitons, and Trions in Self-Assembled (In,Ga)As/GaAs Quantum Dots: Recombination Energies, Polarization, and Radiative Lifetimes versus Dot Height*, Phys. Rev. B **72**, 245318 (2005).

[15] H. Vural, S. L. Portalupi, and P. Michler, *Perspective of Self-Assembled InGaAs Quantum-Dots for Multi-Source Quantum Implementations*, Appl. Phys. Lett. **117**, 030501 (2020).

[16] C. Tonin, R. Hostein, V. Voliotis, R. Grousson, A. Lemaitre, and A. Martinez, *Polarization Properties of Excitonic Qubits in Single Self-Assembled Quantum Dots*, Phys. Rev. B **85**, 155303 (2012).

[17] M. Gong, K. Duan, C.-F. Li, R. Magri, G. A. Narvaez, and L. He, *Electronic structure of self-assembled InAs/InP quantum dots: Comparison with self-assembled InAs/GaAs quantum dots*, Phys. Rev. B **77**, 045326 (2008).

[18] P. Senellart, G. Solomon, and A. White, *High-Performance Semiconductor Quantum-Dot Single-Photon Sources*, Nat. Nanotechnol. **12**, 1026 (2017).

[19] M. Z. M. Khan, T. K. Ng, and B. S. Ooi, *Self-Assembled InAs/InP Quantum Dots and Quantum Dashes: Material Structures and Devices*, Prog. Quantum Electron. **38**, 237 (2014).

[20] S. Bauer, D. Wang, N. Hoppe, C. Nawrath, J. Fischer, N. Witz, S. L. Portalupi, M. Jetter, M. Berroth, and P. Michler, *Efficient and Stable Fiber-to-Chip Coupling Enabling the Injection of Telecom Quantum Dot Photons into a Silicon Photonic Chip*, in *2021 Conference on Lasers and Electro-Optics Europe, European Quantum Electronics Conference (CLEO/Europe-EQEC)*, Vol. 023103 (IEEE, 2021), pp. 1–1.

[21] N. Ozaki, K. Takeuchi, S. Ohkouchi, N. Ikeda, Y. Sugimoto, H. Oda, K. Asakawa, and R. A. Hogg, *Monolithically Grown Multi-Color InAs Quantum Dots as a Spectral-Shape-Controllable near-Infrared Broadband Light Source*, Appl. Phys. Lett. **103**, 1 (2013).

[22] L. Seravalli, M. Gioannini, F. Cappelluti, F. Sacconi, G. Trevisi, and P. Frigeri, *Broadband Light Sources Based on InAs/InGaAs Metamorphic Quantum Dots*, J. Appl. Phys. **119**, 143102 (2016).

[23] P. Holewa, M. Gawelczyk, A. Maryński, P. Wyborski, J. P. Reithmaier, G. Sęk, M. Benyoucef, and M. Syperek, *Optical and Electronic Properties of Symmetric InAs/(In,Al,Ga)As/InP Quantum Dots Formed by Ripening in Molecular Beam Epitaxy: A Potential System for Broad-Range Single-Photon Telecom Emitters*, Phys. Rev. Appl. **14**, 064054 (2020).

[24] N. N. Ledentsov, V. M. Ustinov, V. A. Shchukin, P. S. Kop'ev, Z. I. Alferov, and D. Bimberg, *Quantum Dot Heterostructures: Fabrication, Properties, Lasers (Review)*, Semiconductors **32**, 343 (1998).

[25] P. Bhattacharya and Z. Mi, *Quantum-Dot Optoelectronic Devices*, Proc. IEEE **95**, 1723 (2007).

[26] C. Shang, Y. Wan, J. Selvidge, E. Hughes, R. Herrick, K. Mukherjee, J. Duan, F. Grillot, W. W. Chow, and J. E. Bowers, *Perspectives on Advances in Quantum Dot Lasers and Integration with Si Photonic Integrated Circuits*, ACS

Photonics **8**, 2555 (2021).

[27] Z. Yao, C. Jiang, X. Wang, H. Chen, H. Wang, L. Qin, and Z. Zhang, *Recent Developments of Quantum Dot Materials for High Speed and Ultrafast Lasers*, Nanomaterials **12**, 1058 (2022).

[28] A. Yadav, N. B. Chichkov, E. A. Avrutin, A. Gorodetsky, and E. U. Rafailov, *Edge Emitting Mode-Locked Quantum Dot Lasers*, Prog. Quantum Electron. **87**, 100451 (2023).

[29] R. Oshima, A. Takata, and Y. Okada, *Strain-Compensated InAs/GaNAs Quantum Dots for Use in High-Efficiency Solar Cells*, Appl. Phys. Lett. **93**, 083111 (2008).

[30] S. R. Tatavarti, Z. S. Bittner, A. Wibowo, M. A. Slocum, G. Nelson, H. Kum, S. P. Ahrenkiel, and S. M. Hubbard, *Epitaxial Lift-off (ELO) of InGaP/GaAs/InGaAs Solar Cells with Quantum Dots in GaAs Middle Sub-Cell*, Sol. Energy Mater. Sol. Cells **185**, 153 (2018).

[31] H. Kalt, *Optical Properties of III–V Semiconductors*, Vol. 120 (Springer Berlin Heidelberg, Berlin, Heidelberg, 1996).

[32] C. Schimpf, M. Reindl, F. Basso Basset, K. D. Jöns, R. Trotta, and A. Rastelli, *Quantum Dots as Potential Sources of Strongly Entangled Photons: Perspectives and Challenges for Applications in Quantum Networks*, Appl. Phys. Lett. **118**, 100502 (2021).

[33] V. Cerletti, W. A. Coish, O. Gywat, and D. Loss, *Recipes for Spin-Based Quantum Computing*, Nanotechnology **16**, R27 (2005).

[34] A. J. Williamson, L. W. Wang, and A. Zunger, *Theoretical Interpretation of the Experimental Electronic Structure of Lens-Shaped Self-Assembled InAs/GaAs Quantum Dots*, Phys. Rev. B **62**, 12963 (2000).

[35] P. Mrowiński, M. Zieliński, M. Świderski, J. Misiewicz, A. Somers, J. P. Reithmaier, S. Höfling, and G. Sęk, *Excitonic Fine Structure and Binding Energies of Excitonic Complexes in Single InAs Quantum Dashes*, Phys. Rev. B **94**, 115434 (2016).

[36] M. Bayer et al., *Fine Structure of Neutral and Charged Excitons in Self-Assembled In(Ga)As/(Al)GaAs Quantum Dots*, Phys. Rev. B **65**, 195315 (2002).

[37] V. Mlinar and A. Zunger, *Internal Electronic Structure and Fine Structure of Multiexcitons in Semiconductor Quantum Dots*, Phys. Rev. B **80**, 205311 (2009).

[38] R. Seguin, A. Schliwa, S. Rodt, K. Pötschke, U. W. Pohl, and D. Bimberg, *Size-Dependent Fine-Structure Splitting in Self-Organized InAs/GaAs Quantum Dots*, Phys. Rev. Lett. **95**, 257402 (2005).

[39] L. He, M. Gong, C.-F. Li, G.-C. Guo, and A. Zunger, *Highly Reduced Fine-Structure Splitting in InAs/InP Quantum Dots Offering an Efficient On-Demand Entangled 1.55-μm Photon Emitter*, Phys. Rev. Lett. **101**, 157405 (2008).

[40] K. Kowalik, O. Krebs, A. Lemaître, S. Laurent, P. Senellart, P. Voisin, and J. A. Gaj, *Influence of an In-Plane Electric Field on Exciton Fine Structure in InAs-GaAs Self-Assembled Quantum Dots*, Appl. Phys. Lett. **86**, 041907 (2005).

[41] J. D. Mar, X. L. Xu, J. S. Sandhu, A. C. Irvine, M. Hopkinson, and D. A. Williams, *Electrical Control of Fine-Structure Splitting in Self-Assembled Quantum Dots for Entangled Photon Pair Creation*, Appl. Phys. Lett. **97**, 221108 (2010).

[42] J.-W. Luo, R. Singh, A. Zunger, and G. Bester, *Influence of the Atomic-Scale Structure on the Exciton Fine-Structure Splitting in InGaAs and GaAs Quantum Dots in a Vertical Electric Field*, Phys. Rev. B **86**, 161302 (2012).

[43] M. Ghali, K. Ohtani, Y. Ohno, and H. Ohno, *Generation and Control of Polarization-Entangled Photons from GaAs Island Quantum Dots by an Electric Field*, Nat. Commun. **3**, 661 (2012).

[44] S. Seidl, M. Kroner, A. Högele, K. Karrai, R. J. Warburton, A. Badolato, and P. M. Petroff, *Effect of Uniaxial Stress on Excitons in a Self-Assembled Quantum Dot*, Appl. Phys. Lett. **88**, 203113 (2006).

[45] J. Zhang, J. S. Wildmann, F. Ding, R. Trotta, Y. Huo, E. Zallo, D. Huber, A. Rastelli, and O. G. Schmidt, *High Yield and Ultrafast Sources of Electrically Triggered Entangled-Photon Pairs Based on Strain-Tunable Quantum Dots*, Nat. Commun. **6**, 10067 (2015).

[46] T. Lettner et al., *Strain-Controlled Quantum Dot Fine Structure for Entangled Photon Generation at 1550 nm*, Nano Lett. **21**, 10501 (2021).

[47] E. Kadantsev and P. Hawrylak, *Theory of Exciton Fine Structure in Semiconductor Quantum Dots: Quantum Dot Anisotropy and Lateral Electric Field*, Phys. Rev. B **81**, 045311 (2010).

[48] H. Haug and S. W. Koch, *Quantum Theory of the Optical and Electronic Properties of Semiconductors* (WORLD SCIENTIFIC, 2009).

[49] A. Musiał, P. Kaczmarkiewicz, G. Sęk, P. Podemski, P. Machnikowski, J. Misiewicz, S. Hein, S. Höfling, and A. Forchel, *Carrier Trapping and Luminescence Polarization in Quantum Dashes*, Phys. Rev. B **85**, 035314 (2012).

[50] A. Musiał et al., *Height-Driven Linear Polarization of the Surface Emission from Quantum Dashes*, Semicond. Sci. Technol. **27**, 105022 (2012).

[51] A. L. Efros and A. L. Efros, *Interband Light Absorption in Semiconductor Spheres*, Sov. Physics. Semicond. **16**, 772 (1982).

[52] M. Gawełczyk, *Excitons in Asymmetric Nanostructures: Confinement Regime*, Acta Phys. Pol. A **134**, 930 (2018).

[53] M. Gawełczyk, *Atypical Dependence of Excited Exciton Energy Levels and Electron-Hole Correlation on Emission Energy in Pyramidal InP-Based Quantum Dots*, Sci. Rep. **12**, 164 (2022).

[54] S. Rodt, R. Seguin, A. Schliwa, F. Guffarth, K. Pötschke, U. W. Pohl, and D. Bimberg, *Size-Dependent Binding Energies and Fine-Structure Splitting of Excitonic Complexes in Single InAs/GaAs Quantum Dots*, J. Lumin. **122–123**, 735 (2007).

[55] W. Rudno-Rudziński, M. Burakowski, J. P. Reithmaier, A. Musiał, and M. Benyoucef, *Magneto-Optical Characterization of Trions in Symmetric InP-Based Quantum Dots for Quantum Communication Applications*, Materials (Basel). **14**, 942 (2021).

[56] M. Wimmer, S. V. Nair, and J. Shumway, *Biexciton Recombination Rates in Self-Assembled Quantum Dots*, Phys. Rev. B **73**, 165305 (2006).

[57] J. Johansen, S. Stobbe, I. S. Nikolaev, T. Lund-Hansen, P. T. Kristensen, J. M. Hvam, W. L. Vos, and P. Lodahl, *Size Dependence of the Wavefunction of Self-Assembled InAs Quantum Dots from Time-Resolved Optical Measurements*, Phys. Rev. B **77**, 073303 (2008).

[58] S. Stobbe, T. W. Schlereth, S. Höfling, A. Forchel, J. M. Hvam, and P. Lodahl, *Large Quantum Dots with Small Oscillator Strength*, Phys. Rev. B **82**, 233302 (2010).

[59] J. Große, P. Mrowiński, N. Srocka, and S. Reitzenstein, *Quantum Efficiency and Oscillator Strength of InGaAs Quantum Dots for Single-Photon Sources Emitting in the Telecommunication O-Band*, Appl. Phys. Lett. **119**, 061103 (2021).

[60] P. A. Dalgarno, J. M. Smith, J. McFarlane, B. D. Gerardot, K. Karrai, A. Badolato, P. M. Petroff, and R. J. Warburton, *Coulomb Interactions in Single Charged Self-Assembled Quantum Dots: Radiative Lifetime and Recombination Energy*, Phys. Rev. B **77**, 245311 (2008).

[61] E. Dekel, D. Gershoni, E. Ehrenfreund, J. M. Garcia, and P. M. Petroff, *Carrier-Carrier Correlations in an Optically Excited Single Semiconductor Quantum Dot*, Phys. Rev. B **61**, 11009 (2000).

[62] P. Senellart, E. Peter, J. Hours, A. Cavanna, and J. Bloch, *Few Particle Effects in the Emission of Short-Radiative-Lifetime Single Quantum Dots*, Phys. Rev. B **72**, 115302 (2005).

[63] M. H. Baier, A. Malko, E. Pelucchi, D. Y. Oberli, and E. Kapon, *Quantum-Dot Exciton Dynamics Probed by Photon-Correlation Spectroscopy*, Phys. Rev. B **73**, 205321 (2006).

[64] G. Sęk, A. Musiał, P. Podemski, M. Syperek, J. Misiewicz, A. Löffler, S. Höfling, L. Worschech, and A. Forchel, *Exciton Kinetics and Few Particle Effects in Self-Assembled GaAs-Based Quantum Dashes*, J. Appl. Phys. **107**, (2010).

[65] Ł. Dusanowski, G. Sęk, A. Musiał, P. Podemski, J. Misiewicz, A. Löffler, S. Höfling, S. Reitzenstein, and A. Forchel, *Multiexcitonic Emission from Single Elongated InGaAs/GaAs Quantum Dots*, J. Appl. Phys. **111**, 063522 (2012).

[66] G. Sęk, A. Musiał, P. Podemski, and J. Misiewicz, *On the Applicability of a Few Level Rate Equation Model to the Determination of Exciton versus Biexciton Kinetics in Quasi-Zero-Dimensional Structures*, J. Appl. Phys. **108**, 033507 (2010).

[67] J. Suffczyński et al., *Excitation mechanisms of individual CdTe/ZnTe quantum dots studied by photon correlation spectroscopy*, Phys. Rev. B **74**, 085319 (2006).

[68] G. Wang, S. Fafard, D. Leonard, J. E. Bowers, J. L. Merz, and P. M. Petroff, *Time-Resolved Optical Characterization of InGaAs/GaAs Quantum Dots*, Appl. Phys. Lett. **64**, 2815 (1994).

[69] P. D. Buckle, P. Dawson, S. A. Hall, X. Chen, M. J. Steer, D. J. Mowbray, M. S. Skolnick, and M. Hopkinson, *Photoluminescence Decay Time Measurements from Self-Organized InAs/GaAs Quantum Dots*, J. Appl. Phys. **86**, 2555 (1999).

[70] J. Seufert, R. Weigand, G. Bacher, T. Kümmell, A. Forchel, K. Leonardi, and D. Hommel, *Spectral Diffusion of the Exciton Transition in a Single Self-Organized Quantum Dot*, Appl. Phys. Lett. **76**, 1872 (2000).

[71] Ł. Dusanowski et al., *Phonon-Assisted Radiative Recombination of Excitons Confined in Strongly Anisotropic Nanostructures*, Phys. Rev. B **90**, 125424 (2014).

[72] L. Besombes, K. Kheng, L. Marsal, and H. Mariette, *Acoustic Phonon Broadening Mechanism in Single Quantum Dot Emission*, Phys. Rev. B **63**, 155307 (2001).

[73] P. Michler, *Quantum Dots for Quantum Information Technologies* (Springer International Publishing, Cham, 2017).

[74] M. D. Eisaman, J. Fan, A. Migdall, and S. V. Polyakov, *Invited Review Article: Single-Photon Sources and Detectors*, Rev. Sci. Instrum. **82**, 071101 (2011).

[75] Ł. Dusanowski, M. Syperek, W. Rudno-Rudziński, P. Mrowiński, G. Sęk, J. Misiewicz, A. Somers, J. P. Reithmaier, S. Höfling, and A. Forchel, *Exciton and Biexciton Dynamics in Single Self-Assembled InAs/InGaAlAs/InP Quantum Dash Emitting near 1.55 μm*, Appl. Phys. Lett. **103**, 253113 (2013).

[76] D. Regelman, U. Mizrahi, D. Gershoni, E. Ehrenfreund, W. Schoenfeld, and P. Petroff, *Semiconductor Quantum*

Dot: A Quantum Light Source of Multicolor Photons with Tunable Statistics, Phys. Rev. Lett. **87**, 257401 (2001).

[77] T. Miyazawa et al., *Single-Photon Emission at 1.5 μm from an InAs/InP Quantum Dot with Highly Suppressed Multi-Photon Emission Probabilities*, Appl. Phys. Lett. **109**, 132106 (2016).

[78] S. Fischbach et al., *Single Quantum Dot with Microlens and 3D-Printed Micro-Objective as Integrated Bright Single-Photon Source*, ACS Photonics **4**, 1327 (2017).

[79] G. Sallen, A. Tribu, T. Aichele, R. André, L. Besombes, C. Bougerol, S. Tatarenko, K. Kheng, and J. P. Poizat, *Exciton Dynamics of a Single Quantum Dot Embedded in a Nanowire*, Phys. Rev. B **80**, 085310 (2009).

[80] Ł. Dusanowski, M. Syperek, P. Mrowiński, W. Rudno-Rudziński, J. Misiewicz, A. Somers, S. Höfling, M. Kamp, J. P. Reithmaier, and G. Sęk, *Single Photon Emission at 1.55 μm from Charged and Neutral Exciton Confined in a Single Quantum Dash*, Appl. Phys. Lett. **105**, 021909 (2014).

[81] D. A. Vajner, L. Rickert, T. Gao, K. Kaymazlar, and T. Heindel, *Quantum Communication Using Semiconductor Quantum Dots*, Adv. Quantum Technol. **5**, 2100116 (2022).

[82] A. Fiore, J. X. Chen, and M. Ilegems, *Scaling Quantum-Dot Light-Emitting Diodes to Submicrometer Sizes*, Appl. Phys. Lett. **81**, 1756 (2002).

[83] E. B. Desurvire, *Capacity Demand and Technology Challenges for Lightwave Systems in the Next Two Decades*, J. Light. Technol. **24**, 4697 (2006).

[84] D. Giggenbach and A. Shrestha, *Atmospheric Absorption and Scattering Impact on Optical Satellite-ground Links*, Int. J. Satell. Commun. Netw. **40**, 157 (2022).

[85] A. W. Elshaari, W. Pernice, K. Srinivasan, O. Benson, and V. Zwiller, *Hybrid Integrated Quantum Photonic Circuits*, Nat. Photonics **14**, 285 (2020).

[86] L. Feng, M. Zhang, J. Wang, X. Zhou, X. Qiang, G. Guo, and X. Ren, *Silicon Photonic Devices for Scalable Quantum Information Applications*, Photonics Res. **10**, A135 (2022).

[87] J. C. Norman, D. Jung, Y. Wan, and J. E. Bowers, *Perspective: The Future of Quantum Dot Photonic Integrated Circuits*, APL Photonics **3**, (2018).

[88] R. Helkey, A. A. M. Saleh, J. Buckwalter, and J. E. Bowers, *High-Performance Photonic Integrated Circuits on Silicon*, IEEE J. Sel. Top. Quantum Electron. **25**, 1 (2019).

[89] S. Hepp, M. Jetter, S. L. Portalupi, and P. Michler, *Semiconductor Quantum Dots for Integrated Quantum Photonics*, Adv. Quantum Technol. **2**, 1900020 (2019).

[90] *Corning, Optical Communications, Corning, USA, 2023*, https://www.corning.com/optical-communications/emea/en/home.html.

[91] L. Seravalli and F. Sacconi, *Reviewing Quantum Dots for Single-Photon Emission at 1.55 μm: A Quantitative Comparison of Materials*, J. Phys. Mater. **3**, 042005 (2020).

[92] G. Giesecke, *Chapter 4 Lattice Constants*, *Semiconductors and Semimetals* (Elsevier, Vol. 2 1966), pp. 63–73.

[93] A. Löffler, J.-P. Reithmaier, A. Forchel, A. Sauerwald, D. Peskes, T. Kümmell, and G. Bacher, *Influence of the Strain on the Formation of GaInAs/GaAs Quantum Structures*, J. Cryst. Growth **286**, 6 (2006).

[94] P. Poloczek, G. Sęk, J. Misiewicz, A. Löffler, J. P. Reithmaier, and A. Forchel, *Optical Properties of Low-Strained $In_xGa_{1-x}As$/GaAs Quantum Dot Structures at the Two-Dimensional–Three-Dimensional Growth Transition*, J. Appl. Phys. **100**, 013503 (2006).

[95] V. M. Ustinov et al., *InAs/InGaAs Quantum Dot Structures on GaAs Substrates Emitting at 1.3 μm*, Appl. Phys. Lett. **74**, 2815 (1999).

[96] K. Nishi, H. Saito, S. Sugou, and J.-S. Lee, *A Narrow Photoluminescence Linewidth of 21 meV at 1.35 μm from Strain-Reduced InAs Quantum Dots Covered by $In_{0.2}Ga_{0.8}As$ Grown on GaAs Substrates*, Appl. Phys. Lett. **74**, 1111 (1999).

[97] S. Maier, K. Berschneider, T. Steinl, A. Forchel, S. Höfling, C. Schneider, and M. Kamp, *Site-Controlled InAs/GaAs Quantum Dots Emitting at Telecommunication Wavelength*, Semicond. Sci. Technol. **29**, 052001 (2014).

[98] J. Kettler, M. Paul, F. Olbrich, K. Zeuner, M. Jetter, and P. Michler, *Single-Photon and Photon Pair Emission from MOVPE-Grown In(Ga)As Quantum Dots: Shifting the Emission Wavelength from 1.0 to 1.3 μm*, Appl. Phys. B **122**, 48 (2016).

[99] J. Bloch, J. Shah, W. S. Hobson, J. Lopata, and S. N. G. Chu, *Room-Temperature 1.3 μm Emission from InAs Quantum Dots Grown by Metal Organic Chemical Vapor Deposition*, Appl. Phys. Lett. **75**, 2199 (1999).

[100] A. Fiore et al., *Structural and Electrooptical Characteristics of Quantum Dots Emitting at 1.3 μm on Gallium Arsenide*, IEEE J. Quantum Electron. **37**, 1050 (2001).

[101] F. Guffarth, R. Heitz, A. Schliwa, O. Stier, N. N. Ledentsov, A. R. Kovsh, V. M. Ustinov, and D. Bimberg, *Strain Engineering of Self-Organized InAs Quantum Dots*, Phys. Rev. B **64**, 085305 (2001).

[102] H. Y. Liu, M. Hopkinson, C. N. Harrison, M. J. Steer, R. Frith, I. R. Sellers, D. J. Mowbray, and M. S. Skolnick, *Optimizing the Growth of 1.3 μm InAs/InGaAs Dots-in-a-Well Structure*, J. Appl. Phys. **93**, 2931 (2003).

[103] N. I. Cade, H. Gotoh, H. Kamada, H. Nakano, and H. Okamoto, *Fine structure and magneto-optics of exciton, trion,*

and charged biexciton states in single InAs quantum dots emitting at 1.3 μm, Phys. Rev. B **73**, 115322 (2006).

[104] G. Trevisi, L. Seravalli, P. Frigeri, and S. Franchi, *Low Density InAs/(In)GaAs Quantum Dots Emitting at Long Wavelengths*, Nanotechnology **20**, 415607 (2009).

[105] L. Seravalli, C. Bocchi, G. Trevisi, and P. Frigeri, *Properties of Wetting Layer States in Low Density InAs Quantum Dot Nanostructures Emitting at 1.3 μm: Effects of InGaAs Capping*, J. Appl. Phys. **108**, (2010).

[106] E. Goldmann, S. Barthel, M. Florian, K. Schuh, and F. Jahnke, *Excitonic Fine-Structure Splitting in Telecom-Wavelength InAs/GaAs Quantum Dots: Statistical Distribution and Height-Dependence*, Appl. Phys. Lett. **103**, 242102 (2013).

[107] E. Goldmann, M. Paul, F. F. Krause, K. Müller, J. Kettler, T. Mehrtens, A. Rosenauer, M. Jetter, P. Michler, and F. Jahnke, *Structural and Emission Properties of InGaAs/GaAs Quantum Dots Emitting at 1.3 μm*, Appl. Phys. Lett. **105**, 1 (2014).

[108] P. Mrowiński et al., *Excitonic Complexes in MOCVD-Grown InGaAs/GaAs Quantum Dots Emitting at Telecom Wavelengths*, Phys. Rev. B **100**, 115310 (2019).

[109] J. Tatebayashi, M. Nishioka, and Y. Arakawa, *Over 1.5 μm Light Emission from InAs Quantum Dots Embedded in InGaAs Strain-Reducing Layer Grown by Metalorganic Chemical Vapor Deposition*, Appl. Phys. Lett. **78**, 3469 (2001).

[110] J. M. Ripalda, D. Granados, Y. González, A. M. Sánchez, S. I. Molina, and J. M. García, *Room Temperature Emission at 1.6 μm from InGaAs Quantum Dots Capped with GaAsSb*, Appl. Phys. Lett. **87**, 202108 (2005).

[111] A. Hospodková, E. Hulicius, J. Pangrác, J. Oswald, J. Vyskočil, K. Kuldová, T. Šimeček, P. Hazdra, and O. Caha, *InGaAs and GaAsSb Strain Reducing Layers Covering InAs/GaAs Quantum Dots*, J. Cryst. Growth **312**, 1383 (2010).

[112] A. Salhi, S. Alshaibani, B. Ilahi, M. Alhamdan, A. Alyamani, H. Albrithen, and M. El-Desouki, *Tailoring the Optical Properties of InAs/GaAs Quantum Dots by Means of GaAsSb, InGaAs and InGaAsSb Strain Reducing Layers*, J. Alloys Compd. **714**, 331 (2017).

[113] A. Salhi, S. Alshaibani, Y. Alaskar, H. Albrithen, A. Albadri, A. Alyamani, and M. Missous, *Altering the Optical Properties of GaAsSb-Capped InAs Quantum Dots by Means of InAlAs Interlayers*, Nanoscale Res. Lett. **14**, 41 (2019).

[114] K. Akahane, N. Yamamoto, S. Gozu, A. Ueta, and N. Ohtani, *1.5 μm Emission from InAs Quantum Dots with InGaAsSb Strain-Reducing Layer Grown on GaAs Substrates*, Phys. E Low-Dimensional Syst. Nanostructures **32**, 81 (2006).

[115] A. Stintz, G. T. Liu, A. L. Gray, R. Spillers, S. M. Delgado, and K. J. Malloy, *Characterization of InAs Quantum Dots in Strained $In_xGa_{1-x}As$ Quantum Wells*, J. Vac. Sci. Technol. B Microelectron. Nanom. Struct. **18**, 1496 (2000).

[116] L. Seravalli, M. Minelli, P. Frigeri, P. Allegri, V. Avanzini, and S. Franchi, *The Effect of Strain on Tuning of Light Emission Energy of InAs/InGaAs Quantum-Dot Nanostructures*, Appl. Phys. Lett. **82**, 2341 (2003).

[117] N. N. Ledentsov et al., *High Performance Quantum Dot Lasers on GaAs Substrates Operating in 1.5 μm Range*, Electron. Lett. **39**, 1126 (2003).

[118] A. E. Zhukov et al., *Lasing at 1.5 μm in Quantum Dot Structures on GaAs Substrates*, Semiconductors **37**, 1411 (2003).

[119] E. S. Semenova et al., *Metamorphic Growth for Application in Long-Wavelength (1.3–1.55 μm) Lasers and MODFET-Type Structures on GaAs Substrates*, Nanotechnology **15**, S283 (2004).

[120] L. Seravalli, P. Frigeri, M. Minelli, P. Allegri, V. Avanzini, and S. Franchi, *Quantum Dot Strain Engineering for Light Emission at 1.3, 1.4 and 1.5 μm*, Appl. Phys. Lett. **87**, (2005).

[121] C. Carmesin et al., *Structural and Optical Properties of InAs/(In)GaAs/GaAs Quantum Dots with Single-Photon Emission in the Telecom C-Band up to 77 K*, Phys. Rev. B **98**, 125407 (2018).

[122] P. M. J. Marée, J. C. Barbour, J. F. van der Veen, K. L. Kavanagh, C. W. T. Bulle-Lieuwma, and M. P. A. Viegers, *Generation of Misfit Dislocations in Semiconductors*, J. Appl. Phys. **62**, 4413 (1987).

[123] M. Geddo, G. Guizzetti, M. Patrini, T. Ciabattoni, L. Seravalli, P. Frigeri, and S. Franchi, *Metamorphic Buffers and Optical Measurement of Residual Strain*, Appl. Phys. Lett. **87**, 263120 (2005).

[124] L. Seravalli, G. Trevisi, G. Muñoz-Matutano, D. Rivas, J. Martinez-Pastor, and P. Frigeri, *Sub-Critical InAs Layers on Metamorphic InGaAs for Single Quantum Dot Emission at Telecom Wavelengths*, Cryst. Res. Technol. **49**, 540 (2014).

[125] S. Golovynskyi, L. Seravalli, O. Datsenko, G. Trevisi, P. Frigeri, E. Gombia, I. Golovynska, S. V. Kondratenko, J. Qu, and T. Y. Ohulchanskyy, *Comparative Study of Photoelectric Properties of Metamorphic InAs/InGaAs and InAs/GaAs Quantum Dot Structures*, Nanoscale Res. Lett. **12**, 335 (2017).

[126] A. Bosacchi et al., *Continuously Graded Buffers for Structures Grown on GaAs*, J. Cryst. Growth **175–176**, 1009 (1997).

[127] L. Seravalli, P. Frigeri, G. Trevisi, and S. Franchi, *1.59 μm Room Temperature Emission from Metamorphic InAs/InGaAs Quantum Dots Grown on GaAs Substrates*, Appl. Phys. Lett. **92**, 213104 (2008).

[128] H. Y. Liu, Y. Qiu, C. Y. Jin, T. Walther, and A. G. Cullis, *1.55 μm InAs Quantum Dots Grown on a GaAs Substrate Using a GaAsSb Metamorphic Buffer Layer*, Appl. Phys. Lett. **92**, 111906 (2008).

[129] Y.-C. Xin, L. G. Vaughn, L. R. Dawson, A. Stintz, Y. Lin, L. F. Lester, and D. L. Huffaker, *InAs Quantum-Dot GaAs-Based Lasers Grown on AlGaAsSb Metamorphic Buffers*, J. Appl. Phys. **94**, 2133 (2003).

[130] A. . Zhukov et al., *High External Differential Efficiency and High Optical Gain of Long-Wavelength Quantum Dot Diode Laser*, Phys. E Low-Dimensional Syst. Nanostructures **17**, 589 (2003).

[131] E. C. Le Ru, P. Howe, T. S. Jones, and R. Murray, *Strain Engineered InAs/GaAs Quantum Dots for 1.5 μm Emitters*, Phys. Status Solidi **1224**, 1221 (2003).

[132] L. H. Li, M. Rossetti, A. Fiore, and G. Patriarche, *1.43 μm InAs Bilayer Quantum Dot Lasers on GaAs Substrate*, Electron. Lett. **42**, 638 (2006).

[133] G. Sęk, K. Ryczko, M. Motyka, J. Andrzejewski, K. Wysocka, J. Misiewicz, L. H. Li, A. Fiore, and G. Patriarche, *Wetting Layer States of InAs/GaAs Self-Assembled Quantum Dot Structures: Effect of Intermixing and Capping Layer*, J. Appl. Phys. **101**, 063539 (2007).

[134] S. Sengupta, S. Y. Shah, N. Halder, and S. Chakrabarti, *Comparison of Single-Layer and Bilayer InAs/GaAs Quantum Dots with a Higher InAs Coverage*, Opto-Electronics Rev. **18**, 295 (2010).

[135] M. A. Majid, D. T. D. Childs, K. Kennedy, R. Airey, R. A. Hogg, E. Clarke, P. Spencer, and R. Murray, *O-Band Excited State Quantum Dot Bilayer Lasers*, Appl. Phys. Lett. **99**, 051101 (2011).

[136] K. Shimomura and I. Kamiya, *Strain Engineering of Quantum Dots for Long Wavelength Emission: Photoluminescence from Self-Assembled InAs Quantum Dots Grown on GaAs(001) at Wavelengths over 1.55 μm*, Appl. Phys. Lett. **106**, 082103 (2015).

[137] R. Murray, D. Childs, S. Malik, P. Siverns, C. Roberts, J.-M. Hartmann, and P. Stavrinou, *1.3 μm Room Temperature Emission from InAs/GaAs Self-Assembled Quantum Dots*, Jpn. J. Appl. Phys. **38**, 528 (1999).

[138] M. J. da Silva, A. A. Quivy, S. Martini, T. E. Lamas, E. C. F. da Silva, and J. R. Leite, *InAs/GaAs Quantum Dots Optically Active at 1.5 μm*, Appl. Phys. Lett. **82**, 2646 (2003).

[139] B. Alloing, C. Zinoni, V. Zwiller, L. H. Li, C. Monat, M. Gobet, G. Buchs, A. Fiore, E. Pelucchi, and E. Kapon, *Growth and Characterization of Single Quantum Dots Emitting at 1300 nm*, Appl. Phys. Lett. **86**, 101908 (2005).

[140] D. Guimard, H. Lee, M. Nishioka, and Y. Arakawa, *Growth of High-Uniformity InAs/GaAs Quantum Dots with Ultralow Density below $10^7 cm^{-2}$ and Emission above 1.3 μm*, Appl. Phys. Lett. **92**, (2008).

[141] M. B. Ward, O. Z. Karimov, D. C. Unitt, Z. L. Yuan, P. See, D. G. Gevaux, A. J. Shields, P. Atkinson, and D. A. Ritchie, *On-Demand Single-Photon Source for 1.3 μm Telecom Fiber*, Appl. Phys. Lett. **86**, 1 (2005).

[142] W. Rudno-Rudziński, G. Sęk, J. Misiewicz, T. E. Lamas, and A. A. Quivy, *The Formation of Self-Assembled InAs/GaAs Quantum Dots Emitting at 1.3 μm Followed by Photoreflectance Spectroscopy*, J. Appl. Phys. **101**, 073518 (2007).

[143] R. P. Mirin, J. P. Ibbetson, J. E. Bowers, and A. C. Gossard, *Overgrowth of InGaAs Quantum Dots Formed by Alternating Molecular Beam Epitaxy*, J. Cryst. Growth **175–176**, 696 (1997).

[144] K. Mukai, N. Ohtsuka, M. S. Mitsuru Sugawara, and S. Y. Susumu Yamazaki, *Self-Formed $In_{0.5}Ga_{0.5}As$ Quantum Dots on GaAs Substrates Emitting at 1.3 μm*, Jpn. J. Appl. Phys. **33**, L1710 (1994).

[145] R. P. Mirin, J. P. Ibbetson, K. Nishi, A. C. Gossard, and J. E. Bowers, *1.3 μm Photoluminescence from InGaAs Quantum Dots on GaAs*, Appl. Phys. Lett. **67**, 3795 (1995).

[146] D. L. Huffaker, H. Deng, and D. G. Deepe, *1.15-μm Wavelength Oxide-Confined Quantum-Dot Vertical-Cavity Surface-Emitting Laser*, IEEE Photonics Technol. Lett. **10**, 185 (1998).

[147] S. Krishna, D. Zhu, J. Xu, K. K. Linder, O. Qasaimeh, P. Bhattacharya, and D. L. Huffaker, *Structural and Luminescence Characteristics of Cycled Submonolayer InAs/GaAs Quantum Dots with Room-Temperature Emission at 1.3 μm*, J. Appl. Phys. **86**, 6135 (1999).

[148] M. Sopanen, H. P. Xin, and C. W. Tu, *Self-Assembled GaInNAs Quantum Dots for 1.3 and 1.55 μm Emission on GaAs*, Appl. Phys. Lett. **76**, 994 (2000).

[149] Y. D. Jang, N. J. Kim, J. S. Yim, D. Lee, S. H. Pyun, W. G. Jeong, and J. W. Jang, *Strong Photoluminescence at 1.3 μm with a Narrow Linewidth from Nitridized InAs/GaAs Quantum Dots*, Appl. Phys. Lett. **88**, 8 (2006).

[150] M. Motyka, R. Kudrawiec, G. Sęk, J. Misiewicz, D. Bisping, B. Marquardt, A. Forchel, and M. Fischer, *Contactless Electroreflectance Investigation of Energy Levels in a 1.3 μm Emitting Laser Structure with the Gain Medium Composed of InAsN Quantum Dots Embedded in GaInNAs/GaAs Quantum Wells*, Appl. Phys. Lett. **90**, 2005 (2007).

[151] M. Strauss, S. Höfling, and A. Forchel, *InAs/GaInAs(N) Quantum Dots on GaAs Substrate for Single Photon Emitters above 1300 nm*, Nanotechnology **20**, 505601 (2009).

[152] L. Seravalli, P. Frigeri, L. Nasi, G. Trevisi, and C. Bocchi, *Metamorphic Quantum Dots: Quite Different Nanostructures*, J. Appl. Phys. **108**, 064324 (2010).

[153] L. Seravalli, G. Trevisi, P. Frigeri, D. Rivas, G. Muñoz-Matutano, I. Suárez, B. Alén, J. Canet-Ferrer, and J. P. Martínez-Pastor, *Single Quantum Dot Emission at Telecom Wavelengths from Metamorphic InAs/InGaAs Nanostructures*

Grown on GaAs Substrates, Appl. Phys. Lett. **98**, 173112 (2011).

[154] G. Muñoz-Matutano, D. Rivas, A. L. Ricchiuti, D. Barrera, C. R. Fernández-Pousa, J. Martínez-Pastor, L. Seravalli, G. Trevisi, P. Frigeri, and S. Sales, *Time Resolved Emission at 1.3 μm of a Single InAs Quantum Dot by Using a Tunable Fibre Bragg Grating*, Nanotechnology **25**, 035204 (2014).

[155] G. Muñoz-Matutano, D. Barrera, C. R. Fernández-Pousa, R. Chulia-Jordan, L. Seravalli, G. Trevisi, P. Frigeri, S. Sales, and J. Martínez-Pastor, *All-Optical Fiber Hanbury Brown and Twiss Interferometer to Study 1300 nm Single Photon Emission of a Metamorphic InAs Quantum Dot*, Sci. Rep. **6**, 27214 (2016).

[156] E. S. Semenova, R. Hostein, G. Patriarche, O. Mauguin, L. Largeau, I. Robert-Philip, A. Beveratos, and A. Lemaître, *Metamorphic Approach to Single Quantum Dot Emission at 1.55 μm on GaAs Substrate*, J. Appl. Phys. **103**, 103533 (2008).

[157] M. Paul, F. Olbrich, J. Höschele, S. Schreier, J. Kettler, S. L. Portalupi, M. Jetter, and P. Michler, *Single-Photon Emission at 1.55 μm from MOVPE-Grown InAs Quantum Dots on InGaAs/GaAs Metamorphic Buffers*, Appl. Phys. Lett. **111**, 033102 (2017).

[158] K. D. Zeuner et al., *A Stable Wavelength-Tunable Triggered Source of Single Photons and Cascaded Photon Pairs at the Telecom C-Band*, Appl. Phys. Lett. **112**, 173102 (2018).

[159] S. Castelletto and A. Boretti, *Perspective on Solid-State Single-Photon Sources in the Infrared for Quantum Technology*, Adv. Quantum Technol. **2300145**, 1 (2023).

[160] M. Bock, A. Lenhard, C. Chunnilall, and C. Becher, *Highly Efficient Heralded Single-Photon Source for Telecom Wavelengths Based on a PPLN Waveguide*, Opt. Express **24**, 23992 (2016).

[161] L. A. Ngah, O. Alibart, L. Labonté, V. D'Auria, and S. Tanzilli, *Ultra-Fast Heralded Single Photon Source Based on Telecom Technology*, Laser Photon. Rev. **9**, L1 (2015).

[162] R. T. Willis, F. E. Becerra, L. A. Orozco, and S. L. Rolston, *Photon Statistics and Polarization Correlations at Telecommunications Wavelengths from a Warm Atomic Ensemble*, Opt. Express **19**, 14632 (2011).

[163] X. He et al., *Tunable Room-Temperature Single-Photon Emission at Telecom Wavelengths from sp3 Defects in Carbon Nanotubes*, Nat. Photonics **11**, 577 (2017).

[164] J. Wang, Y. Zhou, Z. Wang, A. Rasmita, J. Yang, X. Li, H. J. von Bardeleben, and W. Gao, *Bright Room Temperature Single Photon Source at Telecom Range in Cubic Silicon Carbide*, Nat. Commun. **9**, 4106 (2018).

[165] Y. Zhou, Z. Wang, A. Rasmita, S. Kim, A. Berhane, Z. Bodrog, G. Adamo, A. Gali, I. Aharonovich, and W. Gao, *Room Temperature Solid-State Quantum Emitters in the Telecom Range*, Sci. Adv. **4**, 1 (2018).

[166] M. W. Doherty, N. B. Manson, P. Delaney, F. Jelezko, J. Wrachtrup, and L. C. L. Hollenberg, *The Nitrogen-Vacancy Colour Centre in Diamond*, Phys. Rep. **528**, 1 (2013).

[167] M. Schwartz, E. Schmidt, U. Rengstl, F. Hornung, S. Hepp, S. L. Portalupi, K. Llin, M. Jetter, M. Siegel, and P. Michler, *Fully On-Chip Single-Photon Hanbury-Brown and Twiss Experiment on a Monolithic Semiconductor–Superconductor Platform*, Nano Lett. **18**, 6892 (2018).

[168] K. Żołnacz et al., *Method for Direct Coupling of a Semiconductor Quantum Dot to an Optical Fiber for Single-Photon Source Applications*, Opt. Express **27**, 26772 (2019).

[169] S. Liu, K. Srinivasan, and J. Liu, *Nanoscale Positioning Approaches for Integrating Single Solid-State Quantum Emitters with Photonic Nanostructures*, Laser Photon. Rev. **15**, 2100223 (2021).

[170] A. Musiał, M. Mikulicz, P. Mrowiński, A. Zielińska, P. Sitarek, P. Wyborski, M. Kuniej, J. P. Reithmaier, G. Sęk, and M. Benyoucef, *InP-Based Single-Photon Sources Operating at Telecom C-Band with Increased Extraction Efficiency*, Appl. Phys. Lett. **118**, 221101 (2021).

[171] P. Holewa et al., *Bright Quantum Dot Single-Photon Emitters at Telecom Bands Heterogeneously Integrated on Si*, ACS Photonics **9**, 2273 (2022).

[172] C. Nawrath et al., *High Emission Rate from a Purcell-Enhanced, Triggered Source of Pure Single Photons in the Telecom C-Band*, ArXiv:2207.12898 1 (2022).

[173] P. Holewa et al., *Scalable Quantum Photonic Devices Emitting Indistinguishable Photons in the Telecom C-Band*, ArXiv:2304.02515 (2023).

[174] S. Rodt, S. Reitzenstein, and T. Heindel, *Deterministically Fabricated Solid-State Quantum-Light Sources*, J. Phys. Condens. Matter **32**, 153003 (2020).

[175] Ł. Dusanowski, M. Syperek, J. Misiewicz, A. Somers, S. Höfling, M. Kamp, J. P. Reithmaier, and G. Sęk, *Single-Photon Emission of InAs/InP Quantum Dashes at 1.55 μm and Temperatures up to 80 K*, Appl. Phys. Lett. **108**, 163108 (2016).

[176] F. Olbrich, J. Kettler, M. Bayerbach, M. Paul, J. Höschele, S. L. Portalupi, M. Jetter, and P. Michler, *Temperature-Dependent Properties of Single Long-Wavelength InGaAs Quantum Dots Embedded in a Strain Reducing Layer*, J. Appl. Phys. **121**, 184302 (2017).

[177] T. Müller, J. Skiba-Szymanska, A. B. Krysa, J. Huwer, M. Felle, M. Anderson, R. M. Stevenson, J. Heffernan,

D. A. Ritchie, and A. J. Shields, *A Quantum Light-Emitting Diode for the Standard Telecom Window around 1550 nm*, Nat. Commun. **9**, 862 (2018).

[178] P. Holewa, M. Burakowski, A. Musiał, N. Srocka, D. Quandt, A. Strittmatter, S. Rodt, S. Reitzenstein, and G. Sęk, *Thermal Stability of Emission from Single InGaAs/GaAs Quantum Dots at the Telecom O-Band*, Sci. Rep. **10**, 21816 (2020).

[179] A. Musiał et al., *Plug(and)Play Fiber-Coupled 73 kHz Single-Photon Source Operating in the Telecom O-Band*, Adv. Quantum Technol. **3**, 1 (2020).

[180] K. Takemoto, Y. Sakuma, S. Hirose, T. Usuki, N. Yokoyama, T. Miyazawa, M. Takatsu, and Y. Arakawa, *Non-Classical Photon Emission from a Single InAs/InP Quantum Dot in the 1.3-μm Optical-Fiber Band*, Jpn. J. Appl. Phys. **43**, L993 (2004).

[181] M. D. Birowosuto, H. Sumikura, S. Matsuo, H. Taniyama, P. J. Van Veldhoven, R. Nötzel, and M. Notomi, *Fast Purcell-Enhanced Single Photon Source in 1550-nm Telecom Band from a Resonant Quantum Dot-Cavity Coupling*, Sci. Rep. **2**, 1 (2012).

[182] X. Liu, K. Akahane, N. A. Jahan, N. Kobayashi, M. Sasaki, H. Kumano, and I. Suemune, *Single-Photon Emission in Telecommunication Band from an InAs Quantum Dot Grown on InP with Molecular-Beam Epitaxy*, Appl. Phys. Lett. **103**, 061114 (2013).

[183] M. Benyoucef, M. Yacob, J. P. Reithmaier, J. Kettler, and P. Michler, *Telecom-Wavelength (1.5 μm) Single-Photon Emission from InP-Based Quantum Dots*, Appl. Phys. Lett. **103**, 162101 (2013).

[184] K. Takemoto, Y. Nambu, T. Miyazawa, Y. Sakuma, T. Yamamoto, S. Yorozu, and Y. Arakawa, *Quantum Key Distribution over 120 km Using Ultrahigh Purity Single-Photon Source and Superconducting Single-Photon Detectors*, Sci. Rep. **5**, 14383 (2015).

[185] A. Musiał, P. Holewa, P. Wyborski, M. Syperek, A. Kors, J. P. Reithmaier, G. Sęk, and M. Benyoucef, *High-Purity Triggered Single-Photon Emission from Symmetric Single InAs/InP Quantum Dots around the Telecom C-Band Window*, Adv. Quantum Technol. **3**, 1900082 (2020).

[186] P. Wyborski, A. Musiał, P. Mrowiński, P. Podemski, V. Baumann, P. Wroński, F. Jabeen, S. Höfling, and G. Sęk, *InP-Substrate-Based Quantum Dashes on a DBR as Single-Photon Emitters at the Third Telecommunication Window*, Materials (Basel). **14**, 759 (2021).

[187] N. Ha, T. Mano, S. Dubos, T. Kuroda, Y. Sakuma, and K. Sakoda, *Single Photon Emission from Droplet Epitaxial Quantum Dots in the Standard Telecom Window around a Wavelength of 1.55 μm*, Appl. Phys. Express **13**, 025002 (2020).

[188] P. Holewa, S. Kadkhodazadeh, M. Gawełczyk, P. Baluta, A. Musiał, V. G. Dubrovskii, M. Syperek, and E. Semenova, *Droplet Epitaxy Symmetric InAs/InP Quantum Dots for Quantum Emission in the Third Telecom Window: Morphology, Optical and Electronic Properties*, Nanophotonics **11**, 1515 (2022).

[189] J. Skiba-Szymanska et al., *Universal Growth Scheme for Quantum Dots with Low Fine-Structure Splitting at Various Emission Wavelengths*, Phys. Rev. Appl. **8**, 014013 (2017).

[190] A. Sauerwald, T. Kümmell, G. Bacher, A. Somers, R. Schwertberger, J. P. Reithmaier, and A. Forchel, *Size Control of InAs Quantum Dashes*, Appl. Phys. Lett. **86**, 253112 (2005).

[191] G. Sęk, P. Podemski, A. Musiał, J. Misiewicz, S. Hein, S. Höfling, and A. Forchel, *Exciton and Biexciton Emission from a Single InAs/InP Quantum Dash*, J. Appl. Phys. **105**, 086104 (2009).

[192] M. Syperek, Ł. Dusanowski, M. Gawełczyk, G. Sęk, A. Somers, J. P. Reithmaier, S. Höfling, and J. Misiewicz, *Exciton Spin Relaxation in InAs/InGaAlAs/InP(001) Quantum Dashes Emitting near 1.55 μm*, Appl. Phys. Lett. **109**, 193108 (2016).

[193] M. Gawełczyk, P. Wyborski, P. Podemski, J. P. Reithmaier, S. Höfling, and G. Sęk, *Excited States of Neutral and Charged Excitons in Single Strongly Asymmetric InP-Based Nanostructures Emitting in the Telecom C Band*, Phys. Rev. B **100**, 241304 (2019).

[194] M. Yacob, J. P. Reithmaier, and M. Benyoucef, *Low-Density InP-Based Quantum Dots Emitting around the 1.5 μm Telecom Wavelength Range*, Appl. Phys. Lett. **104**, 022113 (2014).

[195] A. Kors, J. P. Reithmaier, and M. Benyoucef, *Telecom Wavelength Single Quantum Dots with Very Small Excitonic Fine-Structure Splitting*, Appl. Phys. Lett. **112**, 172102 (2018).

[196] T. Miyazawa, K. Takemoto, Y. Sakuma, S. Hirose, T. Usuki, N. Yokoyama, M. Takatsu, and Y. Arakawa, *Single-Photon Generation in the 1.55-μm Optical-Fiber Band from an InAs/InP Quantum Dot*, Jpn. J. Appl. Phys. **44**, L620 (2005).

[197] T. Usuki, Y. Sakuma, S. Hirose, K. Takemoto, N. Yokoyama, T. Miyazawa, M. Takatsu, and Y. Arakawa, *Single-Photon Generator for Optical Telecommunication Wavelength*, J. Phys. Conf. Ser. **38**, 140 (2006).

[198] K. Takemoto, M. Takatsu, S. Hirose, N. Yokoyama, Y. Sakuma, T. Usuki, T. Miyazawa, and Y. Arakawa, *An Optical Horn Structure for Single-Photon Source Using Quantum Dots at Telecommunication Wavelength*, J. Appl. Phys. **101**, 081720 (2007).

[199] T. Miyazawa, S. Okumura, S. Hirose, K. Takemoto, M. Takatsu, T. Usuki, N. Yokoyama, and Y. Arakawa, *First Demonstration of Electrically Driven 1.55 μm Single-Photon Generator*, Jpn. J. Appl. Phys. **47**, 2880 (2008).

[200] K. Takemoto, S. Hirose, M. Takatsu, N. Yokoyama, Y. Sakuma, T. Usuki, T. Miyazawa, and Y. Arakawa, *Telecom Single-photon Source with Horn Structure*, Phys. Status Solidi C **5**, 2699 (2008).

[201] T. Miyazawa, K. Takemoto, T. Nakaoka, T. Saito, S. Hirose, Y. Sakuma, N. Yokoyama, and Y. Arakawa, *Effect of Electronic Structure on Single-photon Emission in InAs/InP Quantum Dot with Quasi-resonant Excitation*, Phys. Status Solidi C **8**, 417 (2011).

[202] G. Shooter et al., *1GHz Clocked Distribution of Electrically Generated Entangled Photon Pairs*, Opt. Express **28**, 36838 (2020).

[203] M. Anderson, T. Müller, J. Skiba-Szymanska, A. B. Krysa, J. Huwer, R. M. Stevenson, J. Heffernan, D. A. Ritchie, and A. J. Shields, *Gigahertz-Clocked Teleportation of Time-Bin Qubits with a Quantum Dot in the Telecommunication C Band*, Phys. Rev. Appl. **13**, 054052 (2020).

[204] M. Anderson, T. Müller, J. Huwer, J. Skiba-Szymanska, A. B. Krysa, R. M. Stevenson, J. Heffernan, D. A. Ritchie, and A. J. Shields, *Quantum Teleportation Using Highly Coherent Emission from Telecom C-Band Quantum Dots*, Npj Quantum Inf. **6**, 14 (2020).

[205] M. Anderson, T. Müller, J. Skiba-Szymanska, A. B. Krysa, J. Huwer, R. M. Stevenson, J. Heffernan, D. A. Ritchie, and A. J. Shields, *Coherence in Single Photon Emission from Droplet Epitaxy and Stranski–Krastanov Quantum Dots in the Telecom C-Band*, Appl. Phys. Lett. **118**, 014003 (2021).

[206] L. Wells, T. Müller, R. M. Stevenson, J. Skiba-Szymanska, D. A. Ritchie, and A. J. Shields, *Coherent Light Scattering from a Telecom C-Band Quantum Dot*, ArXiv:2205.07997 1 (2022).

[207] A. Barbiero, J. Huwer, J. Skiba-Szymanska, T. Müller, R. M. Stevenson, and A. J. Shields, *Design Study for an Efficient Semiconductor Quantum Light Source Operating in the Telecom C-Band Based on an Electrically-Driven Circular Bragg Grating*, Opt. Express **30**, 10919 (2022).

[208] A. Barbiero, J. Huwer, J. Skiba-Szymanska, D. J. P. Ellis, R. M. Stevenson, T. Müller, G. Shooter, L. E. Goff, D. A. Ritchie, and A. J. Shields, *High-Performance Single-Photon Sources at Telecom Wavelength Based on Broadband Hybrid Circular Bragg Gratings*, ACS Photonics **9**, 3060 (2022).

[209] C. Zinoni et al., *Time-Resolved and Antibunching Experiments on Single Quantum Dots at 1300 nm*, Appl. Phys. Lett. **88**, 86 (2006).

[210] M. Paul, J. Kettler, K. Zeuner, C. Clausen, M. Jetter, and P. Michler, *Metal-Organic Vapor-Phase Epitaxy-Grown Ultra-Low Density InGaAs/GaAs Quantum Dots Exhibiting Cascaded Single-Photon Emission at 1.3 μm*, Appl. Phys. Lett. **106**, 122105 (2015).

[211] J. Kettler, M. Paul, F. Olbrich, K. Zeuner, M. Jetter, P. Michler, M. Florian, C. Carmesin, and F. Jahnke, *Neutral and Charged Biexciton-Exciton Cascade in near-Telecom-Wavelength Quantum Dots*, Phys. Rev. B **94**, 1 (2016).

[212] Ł. Dusanowski et al., *Triggered High-Purity Telecom-Wavelength Single-Photon Generation from p-Shell-Driven InGaAs/GaAs Quantum Dot*, Opt. Express **25**, 31122 (2017).

[213] M. B. Ward, M. C. Dean, R. M. Stevenson, A. J. Bennett, D. J. P. Ellis, K. Cooper, I. Farrer, C. A. Nicoll, D. A. Ritchie, and A. J. Shields, *Coherent Dynamics of a Telecom-Wavelength Entangled Photon Source*, Nat. Commun. **5**, 3316 (2014).

[214] J. Große, M. von Helversen, A. Koulas-Simos, M. Hermann, and S. Reitzenstein, *Development of Site-Controlled Quantum Dot Arrays Acting as Scalable Sources of Indistinguishable Photons*, APL Photonics **5**, 096107 (2020).

[215] N. Srocka et al., *Enhanced Photon-Extraction Efficiency from InGaAs/GaAs Quantum Dots in Deterministic Photonic Structures at 1.3 μm Fabricated by in-Situ Electron-Beam Lithography*, AIP Adv. **8**, 085205 (2018).

[216] N. Srocka, P. Mrowiński, J. Große, M. Schmidt, S. Rodt, and S. Reitzenstein, *Deterministically Fabricated Strain-Tunable Quantum Dot Single-Photon Sources Emitting in the Telecom O-Band*, Appl. Phys. Lett. **117**, 224001 (2020).

[217] F. Olbrich, J. Höschele, M. Müller, J. Kettler, S. Luca Portalupi, M. Paul, M. Jetter, and P. Michler, *Polarization-Entangled Photons from an InGaAs-Based Quantum Dot Emitting in the Telecom C-Band*, Appl. Phys. Lett. **111**, 133106 (2017).

[218] K. D. Zeuner et al., *On-Demand Generation of Entangled Photon Pairs in the Telecom C-Band with InAs Quantum Dots*, ACS Photonics **8**, 2337 (2021).

[219] C. Nawrath, F. Olbrich, M. Paul, S. L. Portalupi, M. Jetter, and P. Michler, *Coherence and Indistinguishability of Highly Pure Single Photons from Non-Resonantly and Resonantly Excited Telecom C-Band Quantum Dots*, Appl. Phys. Lett. **115**, 023103 (2019).

[220] C. Nawrath, H. Vural, J. Fischer, R. Schaber, S. L. Portalupi, M. Jetter, and P. Michler, *Resonance Fluorescence of Single In(Ga)As Quantum Dots Emitting in the Telecom C-Band*, Appl. Phys. Lett. **118**, 244002 (2021).

[221] R. Sittig et al., *Thin-Film InGaAs Metamorphic Buffer for Telecom C-Band InAs Quantum Dots and Optical Resonators on GaAs Platform*, Nanophotonics **11**, 1109 (2022).

[222] R. M. Langford and A. K. Petford-Long, *Preparation of Transmission Electron Microscopy Cross-Section Specimens Using Focused Ion Beam Milling*, J. Vac. Sci. Technol. A Vacuum, Surfaces, Film. **19**, 2186 (2001).

[223] M. Pawlyta, M. Szindler, and D. Łukowiec, *Zastosowanie Skaningowej Mikroskopii Elektronowej w Badaniach Materiałów Inżynierskich*, LAB Lab. Apar. Badania **22**, 6 (2017).

[224] F. H. Pollak and H. Shen, *Modulation Spectroscopy of Semiconductors: Bulk/Thin Film, Microstructures, Surfaces/Interfaces and Devices*, Mater. Sci. Eng. R Reports **10**, xv (1993).

[225] C. Hamaguchi, *Basic Semiconductor Physics* (Springer Berlin Heidelberg, Berlin, Heidelberg, 2001).

[226] J. Misiewicz, P. Sitarek, G. Sęk, and R. Kudrawiec, *Semiconductor Heterostructures and Device Structures Investigated by Photoreflectance Spectroscopy*, Mater. Sci. Pol. **21**, 263 (2003).

[227] R. Kudrawiec and W. Walukiewicz, *Electromodulation Spectroscopy of Highly Mismatched Alloys*, J. Appl. Phys. **126**, 141102 (2019).

[228] B. O. Seraphin and N. Bottka, *Band-Structure Analysis from Electro-Reflectance Studies*, Phys. Rev. **145**, 628 (1966).

[229] D. E. Aspnes and J. E. Rowe, *Resonant Nonlinear Optical Susceptibility: Electroreflectance in the Low-Field Limit*, Phys. Rev. B **5**, 4022 (1972).

[230] D. E. Aspnes, *Third-Derivative Modulation Spectroscopy with Low-Field Electroreflectance*, Surf. Sci. **37**, 418 (1973).

[231] D. E. Aspnes and A. A. Studna, *Schottky-Barrier Electroreflectance: Application to GaAs*, Phys. Rev. B **7**, 4605 (1973).

[232] D. E. Aspnes, *Band Nonparabolicities, Broadening, and Internal Field Distributions: The Spectroscopy of Franz-Keldysh Oscillations*, Phys. Rev. B **10**, 4228 (1974).

[233] H. Shen and F. H. Pollak, *Generalized Franz-Keldysh Theory of Electromodulation*, Phys. Rev. B **42**, 7097 (1990).

[234] B. V. Shanabrook, O. J. Glembocki, and W. T. Beard, *Photoreflectance Modulation Mechanisms in GaAs-$Al_xGa_{1-x}As$ Multiple Quantum Wells*, Phys. Rev. B **35**, 2540 (1987).

[235] *Nextnano, Software for Semiconductor Nanodevices, Nextnano GmbH, München, Germany, 2023*, https://www.nextnano.com/.

[236] S. Birner, T. Zibold, T. Andlauer, T. Kubis, M. Sabathil, A. Trellakis, and P. Vogl, *Nextnano: General Purpose 3-D Simulations*, IEEE Trans. Electron Devices **54**, 2137 (2007).

[237] A. Trellakis, T. Zibold, T. Andlauer, S. Birner, R. K. Smith, R. Morschl, and P. Vogl, *The 3D Nanometer Device Project Nextnano: Concepts, Methods, Results*, J. Comput. Electron. **5**, 285 (2006).

[238] S. Birner, S. Hackenbuchner, M. Sabathil, G. Zandler, J. A. Majewski, T. Andlauer, T. Zibold, R. Morschl, A. Trellakis, and P. Vogl, *Modeling of Semiconductor Nanostructures with Nextnano 3*, Acta Phys. Pol. A **110**, 111 (2006).

[239] T. B. Bahder, *Eight-Band $k \cdot p$ Model of Strained Zinc-Blende Crystals*, Phys. Rev. B **41**, 11992 (1990).

[240] J. Stangl, V. Holý, and G. Bauer, *Structural Properties of Self-Organized Semiconductor Nanostructures*, Rev. Mod. Phys. **76**, 725 (2004).

[241] R. J. Warburton, *Single Spins in Self-Assembled Quantum Dots*, Nat. Mater. **12**, 483 (2013).

[242] J. G. Cody, D. L. Mathine, R. Droopad, G. N. Maracas, R. Rajesh, and R. W. Carpenter, *Application of the Digital Alloy Composition Grading Technique to Strained InGaAs/GaAs/AlGaAs Diode Laser Active Regions*, J. Vac. Sci. Technol. B Microelectron. Nanom. Struct. Process. Meas. Phenom. **12**, 1075 (1994).

[243] R. Kudrawiec, G. Sęk, J. Misiewicz, L. H. Li, and J. C. Harmand, *Influence of Carrier Localization on Modulation Mechanism in Photoreflectance of GaAsN and GaInAsN*, Appl. Phys. Lett. **83**, 1379 (2003).

[244] I. Vurgaftman, J. R. Meyer, and L. R. Ram-Mohan, *Band Parameters for III–V Compound Semiconductors and Their Alloys*, J. Appl. Phys. **89**, 5815 (2001).

[245] J. P. Reithmaier et al., *InP Based Lasers and Optical Amplifiers with Wire-/Dot-like Active Regions*, J. Phys. D. Appl. Phys. **38**, 2088 (2005).

[246] K. Gawarecki, P. Machnikowski, and T. Kuhn, *Electron States in a Double Quantum Dot with Broken Axial Symmetry*, Phys. Rev. B **90**, 085437 (2014).

[247] A. Mielnik-Pyszczorski, K. Gawarecki, M. Gawełczyk, and P. Machnikowski, *Dominant Role of the Shear Strain Induced Admixture in Spin-Flip Processes in Self-Assembled Quantum Dots*, Phys. Rev. B **97**, 245313 (2018).

[248] J. Andrzejewski, G. Sęk, E. O'Reilly, A. Fiore, and J. Misiewicz, *Eight-Band $k \cdot p$ Calculations of the Composition Contrast Effect on the Linear Polarization Properties of Columnar Quantum Dots*, J. Appl. Phys. **107**, 073509 (2010).

[249] A. Thränhardt, C. Ell, G. Khitrova, and H. M. Gibbs, *Relation between Dipole Moment and Radiative Lifetime in Interface Fluctuation Quantum Dots*, Phys. Rev. B **65**, 035327 (2002).

[250] M. Gawełczyk et al., *Exciton Lifetime and Emission Polarization Dispersion in Strongly In-Plane Asymmetric Nanostructures*, Phys. Rev. B **96**, 245425 (2017).

[251] A. V. Koudinov, I. A. Akimov, Y. G. Kusrayev, and F. Henneberger, *Optical and Magnetic Anisotropies of the Hole States in Stranski-Krastanov Quantum Dots*, Phys. Rev. B **70**, 241305 (2004).

[252] F. H. Pollak, W. Krystek, M. Leibovitch, L. Malikova, M. S. Hybertsen, R. Lum, J. M. Vandenberg, and C. L. Reynolds, Jr., *Room-Temperature Contactless Electromodulation Investigation of Wafer-Sized Quantum Well Laser*

Structures, in *Proc. SPIE 2693, Physics and Simulation of Optoelectronic Devices IV*, edited by W. W. Chow and M. Osinski, Vol. 2693 (1996), p. 455.

[253] W. Rudno-Rudziński, R. Kudrawiec, P. Podemski, G. Sęk, J. Misiewicz, A. Somers, R. Schwertberger, J. P. Reithmaier, and A. Forchel, *Photoreflectance-Probed Excited States in InAs/InGaAlAs Quantum Dashes Grown on InP Substrate*, Appl. Phys. Lett. **89**, 031908 (2006).

[254] P. D. Berger, C. Bru, T. Benyattou, A. L. Chenevas-Paule, and P. Grosse, *Investigations of Vertical Cavity Surface Emitting Lasers (VCSEL) Resonant Cavities by Photoreflectance Spectroscopy*, in *Proc. SPIE 2397, Optoelectronic Integrated Circuit Materials, Physics, and Devices*, edited by M. Razeghi, Y.-S. Park, and G. L. Witt, Vol. 2397 (1995), p. 726.

[255] F. V. de Sales, S. W. da Silva, J. M. R. Cruz, A. F. G. Monte, M. A. G. Soler, P. C. Morais, M. J. da Silva, and A. A. Quivy, *Indications of Amplified Spontaneous Emission in the Energy Transfer between InAs Self-Assembled Quantum Dots*, Phys. Rev. B **70**, 235318 (2004).

[256] T. Kazimierczuk, J. Suffczyński, A. Golnik, J. A. Gaj, P. Kossacki, and P. Wojnar, *Optically Induced Energy and Spin Transfer in Nonresonantly Coupled Pairs of Self-Assembled CdTe/ZnTe Quantum Dots*, Phys. Rev. B **79**, 153301 (2009).

[257] T. Kazimierczuk, A. Golnik, P. Wojnar, J. A. Gaj, and P. Kossacki, *Clustering in a Self-Assembled CdTe/ZnTe Quantum Dot Plane Revealed by Inter-Dot Coupling*, Phys. Status Solidi **247**, 1409 (2010).

[258] M. Motyka, R. Kudrawiec, G. Sęk, J. Misiewicz, D. Bisping, B. Marquardt, A. Forchel, and M. Fischer, *Photoluminescence from InAsN Quantum Dots Embedded in GaInNAs/GaAs Quantum Wells*, J. Appl. Phys. **101**, 113539 (2007).

[259] M. Syperek, M. Baranowski, G. Sęk, J. Misiewicz, A. Löffler, S. Höfling, S. Reitzenstein, M. Kamp, and A. Forchel, *Impact of Wetting-Layer Density of States on the Carrier Relaxation Process in Low Indium Content Self-Assembled (In,Ga)As/GaAs Quantum Dots*, Phys. Rev. B **87**, 125305 (2013).

[260] A. Musiał, G. Sęk, A. Maryński, P. Podemski, J. Misiewicz, A. Löffler, S. Höfling, S. Reitzenstein, J. P. Reithmaier, and A. Forchel, *Temperature Dependence of Photoluminescence from Epitaxial InGaAs/GaAs Quantum Dots with High Lateral Aspect Ratio*, Acta Phys. Pol. A **120**, 883 (2011).

[261] P. Holewa, M. Gawełczyk, C. Ciostek, P. Wyborski, S. Kadkhodazadeh, E. Semenova, and M. Syperek, *Optical and Electronic Properties of Low-Density InAs/InP Quantum-Dot-like Structures Designed for Single-Photon Emitters at Telecom Wavelengths*, Phys. Rev. B **101**, 195304 (2020).

[262] H. Lee, W. Yang, and P. C. Sercel, *Temperature and Excitation Dependence of Photoluminescence Line Shapein InAs/GaAs Quantum-Dot Structures*, Phys. Rev. B **55**, 9757 (1997).

[263] S. Sanguinetti, M. Henini, M. Grassi Alessi, M. Capizzi, P. Frigeri, and S. Franchi, *Carrier Thermal Escape and Retrapping in Self-Assembled Quantum Dots*, Phys. Rev. B **60**, 8276 (1999).

[264] Y. P. Varshni, *Temperature Dependence of the Energy Gap in Semiconductors*, Physica **34**, 149 (1967).

[265] A. Tackeuchi, Y. Nakata, S. Muto, Y. Sugiyama, T. Usuki, Y. Nishikawa, N. Yokoyama, and O. Wada, *Time-Resolved Study of Carrier Transfer among InAs/GaAs Multi-Coupled Quantum Dots*, Jpn. J. Appl. Phys. **34**, L1439 (1995).

[266] D. Bimberg et al., *InAs–GaAs Quantum Pyramid Lasers: In Situ Growth, Radiative Lifetimes and Polarization Properties*, Jpn. J. Appl. Phys. **35**, 1311 (1996).

[267] W. Yang, R. R. Lowe-Webb, H. Lee, and P. C. Sercel, *Effect of Carrier Emission and Retrapping on Luminescence Time Decays in InAs/GaAs Quantum Dots*, Phys. Rev. B **56**, 13314 (1997).

[268] A. Fiore, P. Borri, W. Langbein, J. M. Hvam, U. Oesterle, R. Houdré, R. P. Stanley, and M. Ilegems, *Time-Resolved Optical Characterization of InAs/InGaAs Quantum Dots Emitting at 1.3 μm*, Appl. Phys. Lett. **76**, 3430 (2000).

[269] M. Rossetti, A. Fiore, G. Sęk, C. Zinoni, and L. Li, *Modeling the Temperature Characteristics of InAs/GaAs Quantum Dot Lasers*, J. Appl. Phys. **106**, (2009).

[270] F. Albert, S. Stobbe, C. Schneider, T. Heindel, S. Reitzenstein, S. Höfling, P. Lodahl, L. Worschech, and A. Forchel, *Quantum Efficiency and Oscillator Strength of Site-Controlled InAs Quantum Dots*, Appl. Phys. Lett. **96**, 151102 (2010).

[271] P. Borri, W. Langbein, S. Schneider, U. Woggon, R. Sellin, D. Ouyang, and D. Bimberg, *Ultralong Dephasing Time in InGaAs Quantum Dots*, Phys. Rev. Lett. **87**, 157401 (2001).

[272] B. Krummheuer, V. M. Axt, and T. Kuhn, *Theory of Pure Dephasing and the Resulting Absorption Line Shape in Semiconductor Quantum Dots*, Phys. Rev. B **65**, 195313 (2002).

[273] A. Musiał, G. Sęk, P. Podemski, M. Syperek, J. Misiewicz, A. Löffler, S. Höfling, and A. Forchel, *Excitonic Complexes in InGaAs/GaAs Quantum Dash Structures*, J. Phys. Conf. Ser. **245**, 012054 (2010).

[274] Ł. Dusanowski, M. Syperek, A. Maryński, L. H. Li, J. Misiewicz, S. Höfling, M. Kamp, A. Fiore, and G. Sęk, *Single Photon Emission up to Liquid Nitrogen Temperature from Charged Excitons Confined in GaAs-Based Epitaxial*

Nanostructures, Appl. Phys. Lett. **106**, 233107 (2015).

[275] P. B. Allen and M. Cardona, *Temperature Dependence of the Direct Gap of Si and Ge*, Phys. Rev. B **27**, 4760 (1983).

[276] K. P. O'Donnell and X. Chen, *Temperature Dependence of Semiconductor Band Gaps*, Appl. Phys. Lett. **58**, 2924 (1991).

[277] D. Ghodsi Nahri and C. H. Raymond Ooi, *Modeling Temperature-Dependent Shift of Photoluminescence Peak of In(Ga)As Quantum Dots with Acoustic and Optical Phonons as Two Oscillators*, J. Opt. Soc. Am. B **31**, 1182 (2014).

[278] D. Gammon, E. S. Snow, B. V. Shanabrook, D. S. Katzer, and D. Park, *Homogeneous Linewidths in the Optical Spectrum of a Single Gallium Arsenide Quantum Dot*, Science **273**, 87 (1996).

[279] G. Moody, M. E. Siemens, A. D. Bristow, X. Dai, D. Karaiskaj, A. S. Bracker, D. Gammon, and S. T. Cundiff, *Exciton-Exciton and Exciton-Phonon Interactions in an Interfacial GaAs Quantum Dot Ensemble*, Phys. Rev. B **83**, 115324 (2011).

[280] P. Podemski et al., *Interplay between Emission Wavelength and s-p Splitting in MOCVD-Grown InGaAs/GaAs Quantum Dots Emitting above 1.3 μm*, Appl. Phys. Lett. **116**, 023102 (2020).

[281] R. N. E. Malein, T. S. Santana, J. M. Zajac, A. C. Dada, E. M. Gauger, P. M. Petroff, J. Y. Lim, J. D. Song, and B. D. Gerardot, *Screening Nuclear Field Fluctuations in Quantum Dots for Indistinguishable Photon Generation*, Phys. Rev. Lett. **116**, 257401 (2016).

[282] A. V. Kuhlmann, J. H. Prechtel, J. Houel, A. Ludwig, D. Reuter, A. D. Wieck, and R. J. Warburton, *Transform-Limited Single Photons from a Single Quantum Dot*, Nat. Commun. **6**, 8204 (2015).

[283] S. M. Ulrich et al., *Correlated Photon-Pair Emission from a Charged Single Quantum Dot*, Phys. Rev. B **71**, 235328 (2005).

[284] M. B. Ward, T. Farrow, P. See, Z. L. Yuan, O. Z. Karimov, A. J. Bennett, A. J. Shields, P. Atkinson, K. Cooper, and D. A. Ritchie, *Electrically Driven Telecommunication Wavelength Single-Photon Source*, Appl. Phys. Lett. **90**, 8 (2007).

[285] P. Michler, A. Imamoğlu, M. D. Mason, P. J. Carson, G. F. Strouse, and S. K. Buratto, *Quantum Correlation among Photons from a Single Quantum Dot at Room Temperature*, Nature **406**, 968 (2000).

[286] R. Brouri, A. Beveratos, J.-P. Poizat, and P. Grangier, *Photon Antibunching in the Fluorescence of Individual Color Centers in Diamond*, Opt. Lett. **25**, 1294 (2000).

[287] P. A. Dalgarno, J. McFarlane, D. Brunner, R. W. Lambert, B. D. Gerardot, R. J. Warburton, K. Karrai, A. Badolato, and P. M. Petroff, *Hole Recapture Limited Single Photon Generation from a Single n-Type Charge-Tunable Quantum Dot*, Appl. Phys. Lett. **92**, 90 (2008).

LIST OF PUBLICATIONS

PART OF THE THESIS RESULTS ARE INCLUDED IN THE FOLLOWING ARTICLES:

1. P. A. WROŃSKI, **P. WYBORSKI**, A. MUSIAŁ, P. PODEMSKI, G. SĘK, S. HÖFLING, F. JABEEN, Metamorphic buffer layer platform for 1550 nm single-photon sources, **Materials**, 14, 18, s. 1-9 (2021).
2. **P. WYBORSKI**, P. J. PODEMSKI, P. A. WROŃSKI, F. JABEEN, S. HÖFLING, G. SĘK, Electronic and optical properties of InAs QDs grown by MBE on InGaAs metamorphic buffer, **Materials**, 15, 3, s. 1-16 (2022).
3. **P. WYBORSKI**, M. GAWEŁCZYK, P. PODEMSKI, P. A. WROŃSKI, M. PAWLYTA, S. GORANTLA, F. JABEEN, S. HÖFLING, G. SĘK, InGaAs metamorphic buffers grown by MBE on GaAs affect the excitonic and optical properties of single InAs quantum dots while tuning their single photon emission to the telecom range, arXiv:2305.00289 (2023). In the process of reviewing in the journal: **Physical Review Applied**.

OTHER PUBLICATIONS:

4. **P. WYBORSKI**, Advanced perpendicular excitation-detection experimental configuration for light-hole excitons investigation in nanostructures, **15th Students' Science Conference proceedings**, Wroclaw University of Technology Publishing House, s. 309-314 (2017).
5. P. PODEMSKI, A. MARYŃSKI, **P. WYBORSKI**, A. BERCHA, W. TRZECIAKOWSKI, G. SĘK, Single dot photoluminescence excitation spectroscopy in the telecommunication spectral range, **Journal of Luminescence** 212, s. 300–305 (2019).
6. M. GAWEŁCZYK, **P. WYBORSKI**, P. PODEMSKI, J. P. REITHMAIER, S. HÖFLING, G. SĘK, Excited states of neutral and charged excitons in single strongly asymmetric InP-based nanostructures emitting in the telecom C band, **Physical Review B**, 100, 24, s. 1-6 (2019).
7. A. MUSIAŁ, P. HOLEWA, **P. WYBORSKI**, M. SYPEREK, A. KORS, J. P. REITHMAIER, G. SĘK, AND M. BENYOUCEF, High-purity triggered single-photon emission from symmetric single InAs/InP quantum dots around the telecom C-band window, **Advanced Quantum Technologies**, 3, 2, s. 1-6 (2020).
8. P. HOLEWA, M. GAWEŁCZYK, C. CIOSTEK, **P. WYBORSKI**, S. KADKHODAZADEH, E. SEMENOVA, M. SYPEREK, Optical and electronic properties of low-density InAs/InP quantum dot-like structures devoted to single-photon emitters at telecom wavelength, **Physical Review B**, 101, 19, s. 1-14 (2020).
9. P. HOLEWA, M. GAWEŁCZYK, A. MARYŃSKI, **P. WYBORSKI**, J.P. REITHMAIER, G. SĘK, M. BENYOUCEF, M. SYPEREK, Optical and electronic properties of symmetric InAs/(In,Al,Ga)As/InP quantum dots formed by ripening in molecular beam epitaxy: a potential system for broad-range single-photon telecom emitters, **Physical Review Applied**, 14, 6, s. 1-13 (2020).
10. **P. WYBORSKI**, A. J. MUSIAŁ, P. MROWIŃSKI, P. J. PODEMSKI, V. BAUMANN, P. A. WROŃSKI, F. JABEEN, S. HÖFLING, G. SĘK, InP-substrate-based quantum dashes on a DBR as single-photon emitters at the third telecommunication window, **Materials**, 14, 4, s. 1-12 (2021)
11. A. MUSIAŁ, M. MIKULICZ, P. MROWIŃSKI, A. ZIELIŃSKA, P. SITAREK, **P. WYBORSKI**, M. KUNIEJ, J. P. REITHMAIER, G. SĘK, M. BENYOUCEF, InP-based single-photon sources operating at telecom C-band with increased extraction efficiency, **Applied Physics Letters**, 118, 22, s. 1-6, (2021).
12. P. PODEMSKI, M. GAWEŁCZYK, **P. WYBORSKI**, H. SALAMON, M. BURAKOWSKI, A. MUSIAŁ, J.P. REITHMAIER, M. BENYOUCEF, G. SĘK, Spin memory effect in charged single telecom quantum dots, 26.07.2021, **Optics Express**, 29, 21, s. 34024-34034 (2021).

13. T. SMOŁKA, K. Z. POSMYK, M. WASILUK, **P. WYBORSKI**, M. GAWEŁCZYK, P. MROWIŃSKI, M. MIKULICZ, A. D. ZIELIŃSKA, J. P. REITHMAIER, A. J. MUSIAŁ, M. BENYOUCEF, Optical quality of InAs/InP quantum dots on distributed Bragg reflector emitting at 3rd telecom window grown by molecular beam epitaxy, **Materials**, 14, 21, s. 1-22 (2021).
14. A. D. ZIELIŃSKA, A. J. MUSIAŁ, **P. WYBORSKI**, M. KUNIEJ, T. HEUSER, N. SROCKA, J. GROßE, J. P. REITHMAIER, M. BENYOUCEF, S. RODT, S. REITZENSTEIN, W. RUDNO-RUDZIŃSKI, Temperature dependence of refractive indices of Al0.9Ga0.1As and In0.53Al0.1Ga0.37As in the telecommunication spectral range., **Optics Express**, 30, 12, s. 20225-20240 (2022).
15. M. SYPEREK, R. STUHLER, A. CONSIGLIO, P. HOLEWA, **P. WYBORSKI**, Ł. DUSANOWSKI, F. REIS, S. HOFLING, R. THOMALE, W. HANKE, R. CLAESSEN, D. D. SANTE, C. SCHNEIDER, Observation of room temperature excitons in an atomically thin topological insulator, **Nature Communications**, 13, 6313, s. 1-7 (2022).

CONFERENCE PRESENTATIONS

1. **P. WYBORSKI**, Advanced perpendicular excitation-detection experimental configuration for light-hole excitons investigation in nanostructures, **15th Students' Scientific Conference**, Jelenia Góra, Poland, 09.2017, contributed talk.
2. **P. WYBORSKI**, A. MARYŃSKI, P. PODEMSKI, A. MUSIAŁ, J. MISIEWICZ, J. H. SCHULZE, S. STRITTMATTER, S. RODT, S. REITZENSTEIN, G. SĘK, , Development of experimental approach for investigating light-hole excitons in III-V nanostructures, **5th International Workshop on the Optical Properties of Nanostructures (OPON)**, Münster, Germany, 02.2018, poster presentation.
3. **P. WYBORSKI**, A. MARYŃSKI, P. PODEMSKI, A. MUSIAŁ, J. MISIEWICZ, A. LÖFFLER, S. HÖFLING, A. FORCHEL, M. KAMP, S. REITZENSTEIN, G. SĘK, Investigation of valence band mixing in quantum dots by polarization-resolved photoluminescence, **14th International Seminar on Surface and Thin-film Structures "SemPiSC2018"**, Szklarska Poręba, Poland, 04.2018, poster presentation.
4. **P. WYBORSKI**, A. MARYŃSKI, P. PODEMSKI, A. MUSIAŁ, G. SĘK, Reguły wyboru przejść optycznych oraz mieszanie stanów walencyjnych w nanostrukturach (Optical transitions selection rules and valence band states mixing in nanostructures), **III Międzyuczelniana Konferencja Zawansowanych Materiałów i Nanotechnologii**, Wrocław University Science and Technology, Poland, 05.2018, contributed talk.
5. **P. WYBORSKI**, A. MARYŃSKI, P. PODEMSKI, A. MUSIAŁ, J. MISIEWICZ, A. LÖFFLER, S. HÖFLING, A. FORCHEL, M. KAMP, S. REITZENSTEIN, G. SĘK, Investigation of light-hole/heavy-hole mixing in self-assembled quantum dots emitting in telecommunication spectral range, **47th International School & Conference on the Physics of Semiconductors "Jaszowiec 2018"**, Szczyrk, Poland, 06.2018, poster presentation.
6. **P. WYBORSKI**, M. GAWEŁCZYK, H. SALAMON, P. PODEMSKI, J. MISIEWICZ, J. P. REITHMAIER, S. HÖFLING, G. SĘK, Photoluminescence excitation spectroscopy of single nanostructures in the 1.55 μm range, **Winter School on "Quantum Dots: from growth to fundamental properties"**, University of Würzburg, Germany, 02.2019, poster presentation.
7. **P. WYBORSKI**, M. GAWEŁCZYK, H. SALAMON, P. PODEMSKI, J. MISIEWICZ, J. P. REITHMAIER, S. HÖFLING, G. SĘK, Probing the excited states spectrum in single, strongly elongated InP-based nanostructures emitting in the telecommunication spectral range, **48th International School & Conference on the Physics of Semiconductors "Jaszowiec 2019"**, Szczyrk, Poland, 06.2019, poster presentation.
8. **P. WYBORSKI**, M. GAWEŁCZYK, H. SALAMON, P. PODEMSKI, J. P. REITHMAIER, S. HÖFLING, G. SĘK, Photoluminescence excitation spectroscopy of single InAs/InP quantum dots emitting at the telecom C band, **Summer School on "Quantum devices for non-classical light generation and manipulation"**, Erice, Italy, 10.2019, poster presentation.
9. **P. WYBORSKI**, M. GAWEŁCZYK, P. PODEMSKI, J. P. REITHMAIER, S. HÖFLING, G. SĘK, Excited exciton states in single strongly asymmetric InP based nanostructures emitting in C band, **International Workshop on the Optical Properties of Nanostructures "OPON 2020"**, 02.2020, Warszawa, Poland, poster presentation.
10. M. GAWEŁCZYK, **P. WYBORSKI**, P. PODEMSKI, J. P. REITHMAIER, S. HÖFLING, G. SĘK, Excited exciton states in single strongly asymmetric InP based nanostructures emitting in C band, **International Conference on Nonlinear Optics and Excitation Kinetics in Semiconductors (NOEKS 15)**, 09.2020, Münster, Germany, virtual environment, poster presentation.
11. **P. WYBORSKI**, P.A. WROŃSKI, A. MUSIAŁ, P. PODEMSKI, F. JABEEN, S. HÖFLING, G. SĘK, Metamorphic buffer layer platform for 1550 nm single-photon sources grown on [001] GaAs, **49th International School & Conference on the Physics of Semiconductors "Jaszowiec 2021"**, Poland, 09.2021, virtual environment, poster presentation.

12. **P. WYBORSKI**, A. MUSIAŁ, P. PODEMSKI, P. A. WROŃSKI, F. JABEEN, S. HÖFLING, G. SĘK, Kropki kwantowe InAs na metamorficznej warstwie buforowej z InGaAs jako źródła pojedynczych fotonów w zakresie telekomunikacyjnym (InAs QDs on InGaAs metamorphic buffer layer as single-photon sources in the telecom range), **X Krajowa Konferencja Nanotechnologii „KK-Nano 2022"**, Kraków, Poland, 07.2022, poster presentation.
13. **P. WYBORSKI**, M. GAWEŁCZYK, P. PODEMSKI, A. MUSIAŁ, P. A. WROŃSKI, F. JABEEN, S. HÖFLING, G. SĘK, GaAs-based quantum dots grown by MBE on metamorphic buffers as a platform for single-photon sources at telecom range, **8th International workshop on "Engineering of Quantum Emitter Properties",** University of Stuttgart, Niemcy, 12.2022, poster presentation.
14. **P. WYBORSKI**, W. RUDNO-RUDZIŃSKI, P. PODEMSKI, V. SICHKOVSKYI, J. P. REITHMAIER, G. SĘK, Własności optyczne kropek kwantowych InAs/InP wzrastanych na podłożach krzemowych (Optical properties of InAs/InP quantum dots grown on silicon substrates), **XXII Krajowa Konferencja Elektroniki,** Darłowo, Poland, 06.2023, poster presentation.
15. **P. WYBORSKI**, M. GAWEŁCZYK, A. MUSIAŁ, P. PODEMSKI, P. A. WROŃSKI, F. JABEEN, S. HÖFLING, G. SĘK, Kropki kwantowe na podłożu GaAs z buforami metamorficznymi do zastosowań w telekomunikacyjnych emiterach pojedynczych fotonów (GaAs-based quantum dots on metamorphic buffers for applications in telecom single photon sources), **XXII Krajowa Konferencja Elektroniki,** Darłowo, Poland, 06.2023, contributed talk.

LIST OF ABBREVIATIONS

µPL	microphotoluminescence
0D	zero-dimensional
3D	three-dimensional
AFM	atomic force microscopy
AR	aspect ratio
CI	configuration interaction
CW	continuous-wave
CX	charged exciton, or trion
D	diameter
DBR	distributed Bragg reflector
DOLP	degree of linear polarization
EDS	energy dispersion spectrometer
EDX	energy-dispersive x-ray spectroscopy
FKO	Franz-Keldysh oscillation
FM	Frank-van der Merwe
FSS	fine structure splitting
FWHM	full width at half maximum
H	height
HAADF	High-Angle Annular Dark Field
HBT	Hanbury Brown and Twiss
HF	Hartree-Fock
HH	heavy hole
IRF	instrument response function
IQE	internal quantum efficiency
LAR	lateral aspect ratio
LH	light hole
MBE	molecular beam epitaxy
MBL	metamorphic buffer layer
ML	monolayers
MOVPE	metalorganic vapour-phase epitaxy
NEP	noise equivalent power
PL	photoluminescence
PLE	photoluminescence excitation
PR	photomodulated reflectance
QD	quantum dot
QDash	quantum dash
SK	Stranski-Krastanow
SEM	scanning electron microscopy
SPD	single-photon detector
SSPD	superconducting single-photon detector
SPS	single-photon source
STEM	scanning transmission electron microscopy
TEM	transmission electron microscopy
TRPL	time-resolved photoluminescence
VW	Volmer-Weber
WL	wetting layer
X	exciton
X^+	positively-charged exciton
X^-	negatively-charged exciton
XX	biexciton
ZPL	zero-phonon-linewidth